

Preface

Special Issue on Up-to-Date Problems in Modern Railways and Optimization in Engineering Structures

The current issue is the third part of the Special Issue series in Acta Polytechnica Hungarica, the scientific journal of Óbuda University. The first issue has been published in Vol. 19, No. 3 (2022) (<http://acta.uni-obuda.hu/Issue121.htm>), the second was the Vol. 19, No. 6 (2022) (<http://acta.uni-obuda.hu/Issue124.htm>). In the first two issues 32 papers are available. Altogether with the third issue, the authors are from more than 5 foreign countries, e.g., among others Bosnia and Herzegovina, China, Germany, Iran, Jordan, Poland, Serbia, etc. The published topics have a significant wide range in railways. The most papers have been prepared in railway permanent ways, however, there are many articles about mechanical engineering. Current issue is a mixed one because the civil and structural engineering field with the engineering structures' optimization has been connected to railways. From now, the Special Issue Series will be organized with the extended content.

We are very grateful to all the authors for their contribution to the Special Issue and for sharing their results with Acta Polytechnica Hungarica.

The Special Issue Series cannot be organized without the help of Anikó Szakál and Prof. Péter Baranyi. A huge thank you for their help and support.

Dragan Marinkovic, Dmytro Kurhan, Mykola Sysyn, Majid Movahedi Rad and Szabolcs Fischer

Guest Editors

An Easy Way for the Generation of Structural Topologies under Random Loads Using Cellular Automata

Bogdan Bochenek

Faculty of Mechanical Engineering, Cracow University of Technology,
Jana Pawla II 37, 31-864 Kraków, Poland, e-mail: bogdan.bochenek@pk.edu.pl

Abstract: The topology optimization, is a dynamically developing research area, with numerous applications, to many research and engineering fields and despite the decades of progress, still remains one of the most important research tasks, within the area of structural and material design. The implementation of innovative, efficient and versatile optimization approaches and methods, stimulate this process. Among many research problems, where topology optimization is present, there is generation of topologies for structures under random loads. As reported in the literature, random changes in load magnitude, angle of load application, as well as its position can affect resulting topologies. The idea of the paper is to propose an easy to implement numerical approach, which allows for the prediction of resulting topologies of structures, in the case of load uncertainty. This simple, but effective technique, based on transforming random loads into deterministic problem of multiple loads, is discussed, its numerical implementation based on the idea of Cellular Automata, is described and some examples are presented to illustrate the concept. Based on obtained results, it can be concluded that the approach discussed in the paper can be a useful tool to support the research within structural topology optimization, under random loads.

Keywords: structural topology optimization; random loads; Cellular Automata

1 Introduction

The papers by Bendsoe and Kikuchi [1] and Bendsoe [2], dated back to the late 80s of the 20th Century, are broadly treated as the pioneering ones within the field of structural topology optimization. Since then, the intensive research on this subject has been conducted for decades and the results have been widely presented in engineering literature. The numerous approaches to generation of optimal topology have been presented together with appearing concepts which have been implemented in various engineering and research fields. A broad discussion on various aspects of topology optimization has been provided by many survey papers: e.g. [3-6] with the recent ones by Ribeiro et al. [7], Logo and Ismail [8].

Despite a long lasting development the topology optimization still remains one of the most important research fields within the area of structural and material design. Novel ideas and formulations emerge simultaneously with new fields of their application. The researchers community continuously works on innovative and efficient topology optimization methods and algorithms, what stimulates that progress. The spectrum of numerous solutions of topology optimization problems ranges from classic Michell structures to sophisticated contemporary engineering ones.

Among many research problems where topology optimization is present there is structural topology optimization with consideration of load uncertainties. This subject has received for the recent decades increasing interest within the design optimization community. The variety of approaches and techniques has been proposed to handle with random and uncertain loads and the comprehensive study of associated problems has been provided in numerous publications. Among them, there are problems of reliability-based topology optimization and robust topology optimization. The recent papers [9-13] and the newly published by Yin et al. [14], Shen et al. [15], Wang et al. [16], Tazowski et al. [17], along with presentation of particular subjects, bring extensive literature review on topology optimization under uncertainty.

The idea of this paper is to present an easy to implement numerical approach which allows to predict resulting topologies of structures in the case of random loads. The simple but effective technique based on transforming random loads into deterministic problem of multiple loads is implemented. From computational point of view the applied approach is based on the concept of Cellular Automata. Cellular Automata (CA) are developed to represent behavior of complicated systems in a relatively easy way. The special local rules are implemented with a view to mimic the performance of a considered system. Then, local physical quantities are respectively updated, what allows to describe the global behavior of the system.

Since the late 1940s when von Neumann and Ulam proposed the concept of Cellular Automata this idea has been found interesting by researchers representing various fields. In the paper by Inou et al. [18] probably for the first time topology optimization has been discussed within CA approach. Since then many papers have been published on that subject. The majority of them have appeared during last two decades, see e.g. [19-22] or [23]. The efficient CA algorithm has been also proposed and then developed by Bochenek and Tajs-Zielińska [24] [25] and recently [26] [27].

The outline of the paper is as follows. In Section 2.1, the topology optimization problem is formulated with extension to multiple load case described in Section 2.2. The concept of Cellular Automata is introduced in Section 2.3, together with the detailed description of numerical algorithm built based on this idea. The illustrative introductory example discussed in Section 2.4 presents implementation of the paper concept. Next, utilizing results of the preliminary

analysis, the Cellular Automaton is applied in Section 3 to solve the selected tasks of topology generation under random loads. Where available, the obtained topologies are compared with those works reported in the literature. Based on the results of performed tests, the paper ends in Section 4, with concluding remarks.

2 Problem Formulation and Numerical Treatment

2.1 Structural Topology Optimization

The idea of performing topology optimization is to generate within a specified design domain a material layout so as to meet the assumed optimality criteria. The optimized structure gains a new shape and material layout since some parts of material are relocated and others are selectively removed. This allows, for example, creating a stiffer construction with minimal amount of material. Generated this way concept solutions can be the inspiration for further efforts of engineers and designers. Over years many formulations of topology optimization problems have been proposed. The discussion on this subject one can find for example in the paper by Lewiński et al. [28]

When searching for the stiffest design, it is very often that the structure compliance is minimized, since minimal compliance results in maximal stiffness of the optimized structure. The compliance can be defined as the work done by the applied external forces, as proposed in the early papers [1] [2]. Along with the development of topology optimization, especially within the power law approach, the problem has been formulated also as minimization of the elastic strain energy stored in the deforming structure. The compliance has been defined then as twice the total strain energy, see e.g. Stolpe and Svanberg [29]. The problem of equivalence of these two forms of objective function has been discussed together with proposals of new approaches and fields of implementation. Hence, it is important that the structure is elastic, subjected to specified external forces and fixed structural support. In more complex cases, including mixed boundary conditions or various types of loading, modifications of the above formulations are required. The papers by Niu et al. [30], Zhang et al. [31] or Araujo et al. [32] may serve here as examples.

The finite element based strategy for structural topology optimization has gained strong attention of researchers and engineers and considerable progress within this area has been observed. This paper follows the structural topology optimization problem formulated in widely recognized paper by Sigmund [33]. The objective function and constraints are defined within the finite element approach. The objective is to minimize compliance c represented by Eq. (1). The available material volume fraction κ is defined and treated as the constraint imposed on structure volume V in the optimization process, Eq. (2):

Minimize...

$$c(\mathbf{d}) = \mathbf{u}^T \mathbf{k} \mathbf{u} = \sum_{n=1}^N d_n^p \mathbf{u}_n^T \mathbf{k}_n \mathbf{u}_n \quad (1)$$

subject to:

$$V(\mathbf{d}) = \kappa V_0 \quad (2)$$

$$\mathbf{k} \mathbf{u} = \mathbf{f} \quad (3)$$

$$0 < d_{\min} \leq d_n \leq 1 \quad (4)$$

The quantity \mathbf{u}_n represents displacement vector whereas \mathbf{k}_n stands for the stiffness matrix. Both are defined for N elements. The design variable d_n which represents the material relative density is assigned to each element. In Eq. (3) \mathbf{k} is the global stiffness matrix, \mathbf{u} stands for the global displacement vector and \mathbf{f} represents vector of forces. Singularity of d_n is avoided due to the simple bounds imposed in Eq. (4) on the design variables with d_{\min} as a non-zero minimal value of relative density.

The SIMP - solid isotropic material with penalization, see e.g. Bendsoe and Sigmund [34], in the form of power law is adapted as the material representation. For each finite element the modulus of elasticity E_n is a function of the design variable d_n :

$$E_n = d_n^p E_0 \quad \rho_n = d_n \rho_0 \quad (5)$$

In Eq. (5) p (typically $p=3$) is responsible for penalization of intermediate densities what allows controlling the design process and leads to obtaining black-and-white resulting structures. The quantities E_0 and ρ_0 stand for modulus of elasticity and material density, both defined for a solid material. The topology generation process leads to a redistribution of material within design domain, which results in removing parts unnecessary from design criterion point of view.

2.2 Topology Optimization for Multiple Load Case and Paper Concept

As described in the papers by Bendsoe [35], Bendsoe and Sigmund [34], Sigmund [33] the compliance minimization problem formulated in the previous section can be extended to multiple load case. Similarly to the formulation of multi-objective optimization problem, the case of multiple load case can be implemented to the formulation of the topology optimization problem by using the weighted sum of objectives/compliances subjected to all considered load cases. The topology optimization algorithm has to be therefore only slightly modified to cope with this problem, what was illustrated in [33] by the two load case example, see Fig. 1, which is recalled below.

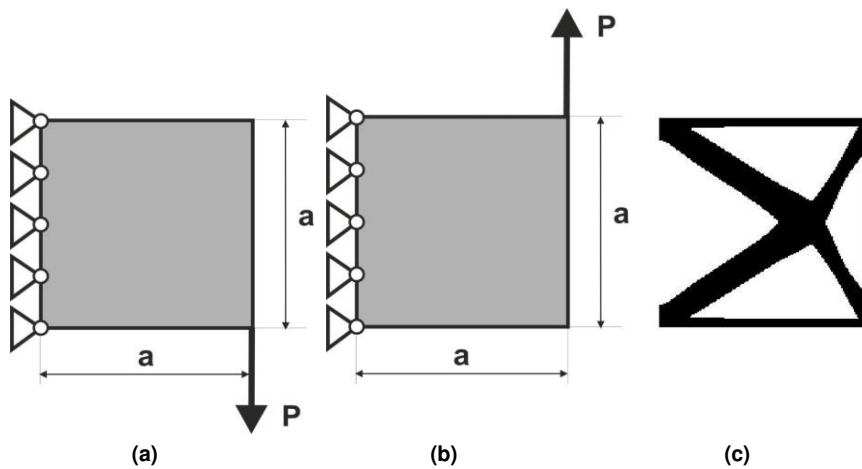


Figure 1

(a) The square structure: support and two loads (b) The resulting topology for the two load case

Dealing with the above problem, the equilibrium equations are solved for both load cases and the objective is defined as the sum of compliances referring to each case. The numerical implementation, as described in detail in [33], requires only modification of a few lines of numerical code, namely insertion of the sum of compliances which replaces the single one.

The idea of the present paper is to adapt the above approach to deal with random loads. These are treated here as sets of loads for which topology is generated. The values, positions or angles of application are generated from particular random distributions.

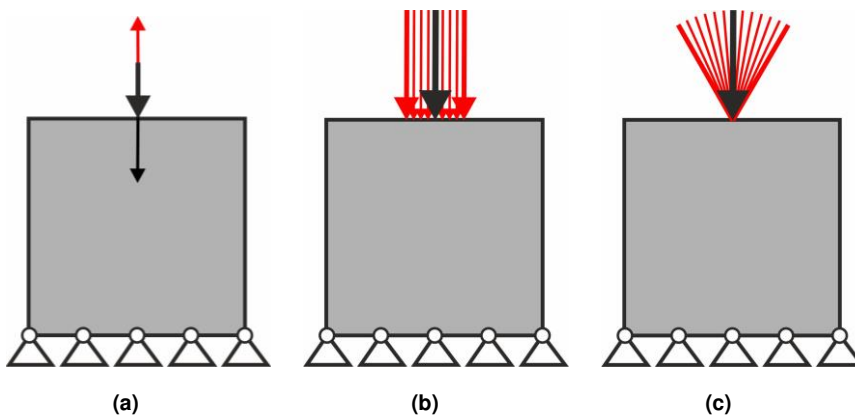


Figure 2

(a) Random magnitude of load (b) Random load position (c) Random angle of load application

Allowing for random changes of load magnitude, angle or position of load application, see Fig. 2, the formulations (1)-(4) has to be slightly modified. In what follows, the objective is now represented by the sum of compliances, Eq. (5), calculated for each load case

$$\sum_{i=1}^L c^{(i)} \quad (5)$$

whereas $\mathbf{u}^{(i)}$ and $\mathbf{f}^{(i)}$ refer to displacement and force vectors representing each load case.

The sets of loads are randomly generated according to the following:

$$P^{(i)} = P + r\Delta_p, \text{ or } P^{(i)} = P + (2r-1)\Delta_p \quad (6)$$

for random load value,

$$x_p^{(i)} = x_p + r\Delta_x, \text{ or } x_p^{(i)} = x_p + (2r-1)\Delta_x \quad (7)$$

for random load position with load value unchanged, and

$$\alpha^{(i)} = r\Delta_\alpha \text{ or } \alpha^{(i)} = (2r-1)\Delta_\alpha \text{ and } P_1^{(i)} = P \cos \alpha^{(i)} \quad P_2^{(i)} = P \sin \alpha^{(i)} \quad (8)$$

for random angle of load application.

In Eqs. (6-8) the Δ_p , Δ_x , Δ_α represent admissible change of load magnitude, position and angle of application, respectively. The random value r is taken from uniform distribution or from the normal one. In numerical implementation the *rand* and *randn* Matlab functions have been applied.

2.3 Cellular Automata Rules for Topology Optimization

The effectiveness of topology optimization process is determined by selecting a proper method of topology generation. Heuristic optimization techniques are gaining popularity among researchers because they are easy for numerical implementation, do not require gradient information, and one can easily combine this type of algorithm with any finite element structural analysis code.

In this paper an efficient heuristic approach based on the concept of Cellular Automata is proposed. The implementation of CA requires decomposition of the design domain usually into uniform lattice of cells which are usually equivalent to finite elements while performing analysis and topology optimization. It is assumed that the interaction between cells takes place only within the neighboring cells and is governed by local rules. The rules are identical for all cells and are applied simultaneously to each of them.

In this paper, a heuristic local update rule [27] is implemented utilizing the Jacobi update scheme, where updating is based on the states of the surrounding cells determined in the previous iteration, see Eq. (9):

$$d_n^{new} = d_n + [F(n) + \sum_{k=1}^M F(k)] \frac{m}{M+1} \quad (9)$$

In Eq. (9), m denotes move limit (e.g. $m=0.2$). The values of F for a central cell (n) and for M neighboring ones (k) are calculated based on local compliance values. In what follows, the structural analysis is performed first and based on obtained results the values of local compliances are calculated for all cells/elements. Then, compliances are sorted in ascending order and those having the lowest and the highest values are identified. As the next step, N_1 , N_2 are selected and values of $F(n)$ are assigned according to Eq. (10):

$$F(n) = \begin{cases} -C_\alpha & \text{if } n < N_1 \\ f(n) & \text{if } N_1 \leq n \leq N_2 \\ -C_\alpha & \text{if } n > N_2 \end{cases} \quad (10)$$

As to the intermediate interval $N_1 \leq n \leq N_2$ a monotonically increasing function representing elements compliances is selected and then its values are assigned to the design elements, respectively. Here, the linear function in Eq. (11) is built to fulfill the conditions $f(N_1) = -C_\alpha$ and $f(N_2) = C_\alpha$, thus:

$$f(n) = 2C_\alpha \frac{n}{N_2 - N_1} - C_\alpha \frac{N_2 + N_1}{N_2 - N_1} \quad (11)$$

The quantity C_α is a user-specified parameter, usually equal to 1.

The numerical algorithm was built in order to implement the above proposed design rule. As for the optimization procedure, the sequential approach was adapted, meaning that for each iteration, the structural analysis performed for the optimized element is followed by a local updating process. Simultaneously, a global volume constraint is applied for a specified volume fraction. As a result, the generated topologies preserve a specified volume fraction of a solid material during the optimization process.

2.4 Introductory Example

The rectangular structure, discussed by many authors, shown in the Fig. 3 has been chosen as the introductory example.

Volume fraction has been selected as 0.2. The regular mesh of 2500 (50×50) elements has been implemented to perform structural analysis and topology optimization, for $E=1$, $P=1$, $\nu=0.3$. The Moore type neighborhood has been applied. Generation of topology has been performed for a single deterministic load as well as for the increasing number of random ones. In the subsequent figures the resulting structures are presented.

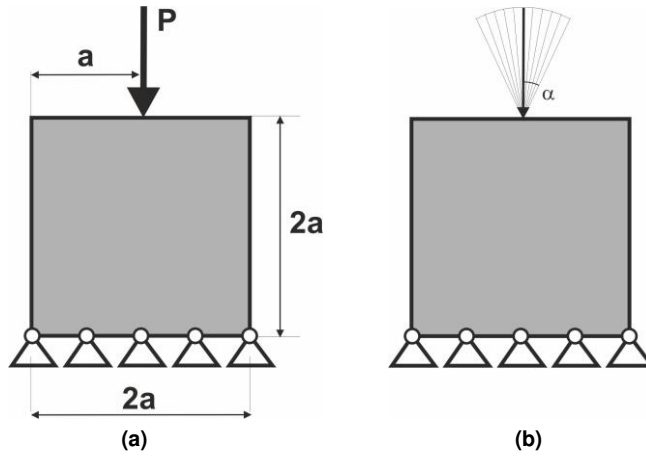


Figure 3

(a) The square structure under single (deterministic) load (b) The structure under random loads

It can be seen from the results shown in the Fig. 4 that there is no significant difference between topologies generated under increasing number of loads. Moreover, the average values of compliances are close each other.

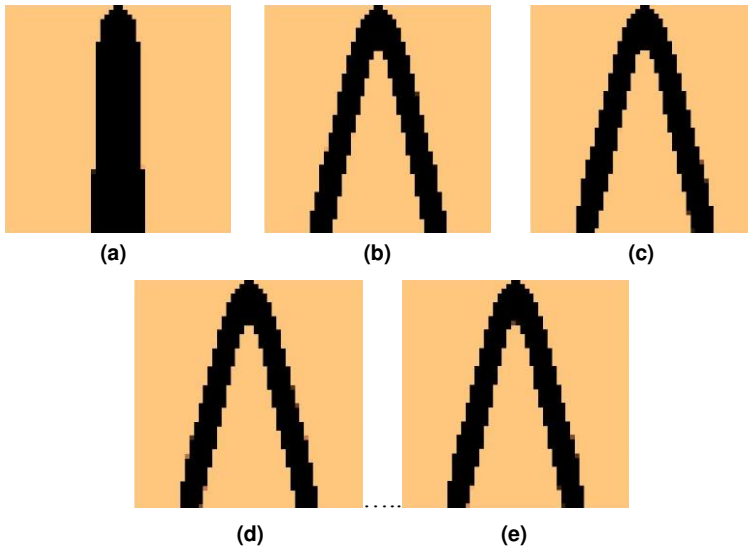


Figure 4

The square structure 50x50 cells. Topologies obtained for: (a) Deterministic load (b) Random 100 loads (c) Random 1000 loads (d) Random 10000 loads (e) Random 100000 loads. Uniform distribution $\Delta_\alpha = \pi/18$

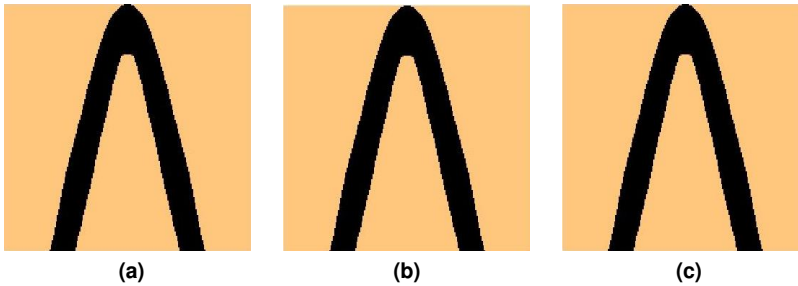


Figure 5

The square structure 100×100 cells. Topologies obtained for: (a) Random 100 loads
(b) Random 1000 loads (c) Random 10000 loads. Uniform distribution $\Delta_\alpha = \pi/18$

The calculations have been repeated for the square structure which has been discretized with mesh of 100×100 cells. The topologies obtained for 100, 1000 and 10000 applied random loads are shown in the Fig. 5.

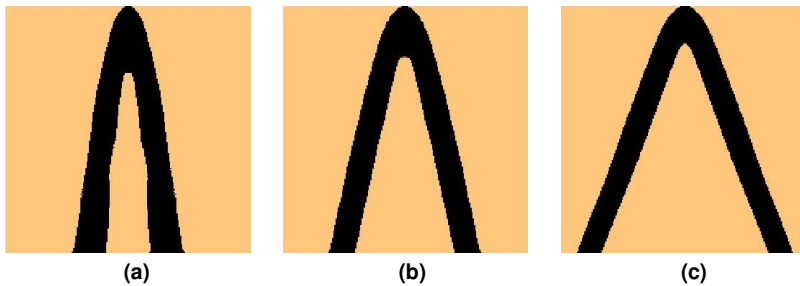


Figure 6

The square structure 200×200 cells. Topologies obtained for: (a) Random 1000 loads, $\Delta_\alpha = \pi/36$
(b) Random 1000 loads, $\Delta_\alpha = \pi/18$. (b) Random 1000 loads. Uniform distribution $\Delta_\alpha = \pi/9$

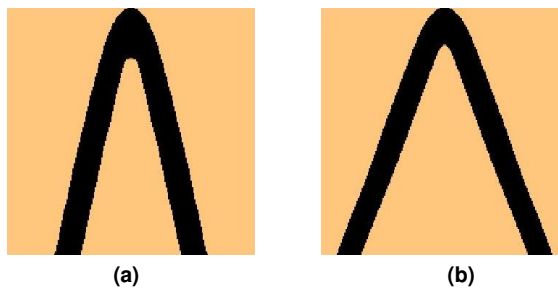


Figure 7

The square structure 200×200 cells. Topologies obtained for: (a) Random 1000 loads, $\Delta_\alpha = \pi/18$
(b) Random 1000 loads, $\Delta_\alpha = \pi/9$. Normal distribution.

Another comparison regards topologies generated for various Δ_α . The considered structure has been discretized with mesh of 200×200 cells. The topologies obtained for $\Delta_\alpha = \pi/36, \pi/18, \pi/9$ and 1000 applied random loads are shown in the Fig. 6.

The topologies obtained for $\Delta_\alpha = \pi/18, \pi/9$ and 1000 applied random loads from normal distribution are shown in the Fig. 7.

As can be seen from the results of the test example discussed in this section the implemented strategy which mimics random loads allows to generate topologies in an easier way.

3 Results of Topology Generation under Random Loads

In order to illustrate the paper concept more thorough some numerical test examples have been selected. Below presented are the results of numerical calculations. The attention has been focused mainly on the case of random angle of load application.

3.1 The Michell Structure

The structure shown in the Fig. 8 has been selected as the test example. The angle of applied load, see Fig. 8b, is treated as the random value which is generated according to uniform or normal distribution.

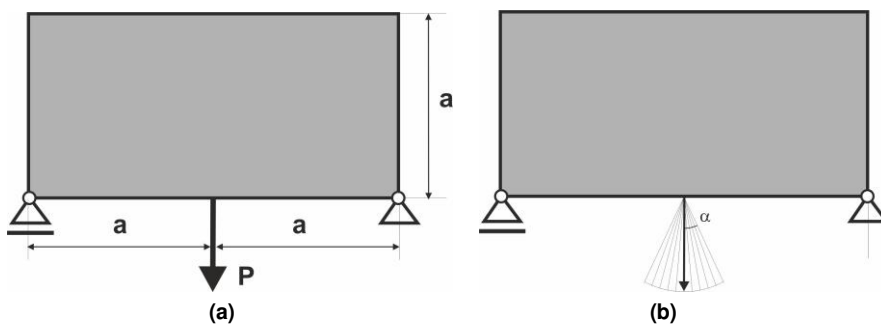


Figure 8

The rectangular Michell structure: (a) load and support (b) random angle of applied load

Volume fraction has been selected as 0.3. The regular mesh of 20000 (200×100) elements has been implemented to perform structural analysis and topology optimization, for $E=1, P=1, \nu=0.3$. The Moore type neighborhood has been

applied. The topology generation has been performed for a single deterministic load as well as for selected random ones. In the Fig. 9a the resulting structure obtained for the single load case is presented.

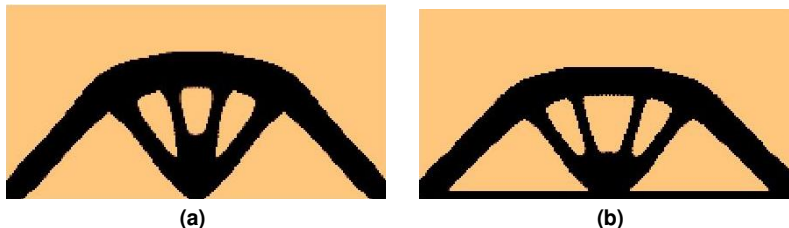


Figure 9

The Michell structure 200×100 cells. (a) Topology obtained for the deterministic load. (b) Random 100 loads. Uniform distribution $\Delta_\alpha = \pi/6$

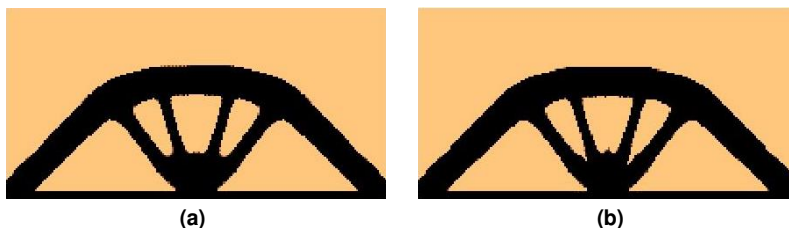


Figure 10

The Michell structure 200×100 cells. Topologies obtained for: (a) Random 1000 loads (b) Random 10000 loads. Uniform distribution $\Delta_\alpha = \pi/6$

The topologies generated under random loads are shown in the Figs. 9b, 10. The number of loads has been selected as 100, 1000 and 10000, and random values have been generated from uniform distribution for $\Delta_\alpha = \pi/6$.

The topology obtained for $\Delta_\alpha = \pi/6$ and 1000 applied random loads taken from normal distribution are shown in the Fig. 11.



Figure 11

The Michell structure 200×100 cells. Topology obtained for random 1000 loads. Normal distribution $\Delta_\alpha = \pi/6$

For the structure under random load the additional line connecting supports has been generated. The obtained results can be compared with the ones reported in [36] [16].

3.2 The Tower Structure

The second example is the tower structure shown in the Fig. 12. The angle of applied load, see Fig. 12b, is treated as the random value which is generated according to uniform or normal distribution.

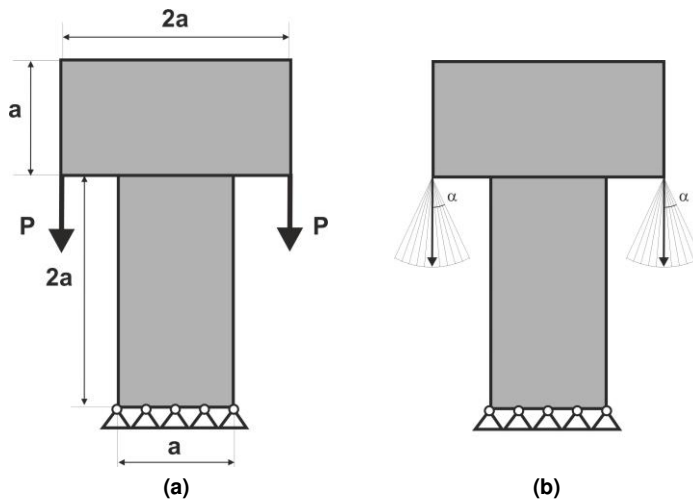


Figure 12

The tower structure (a) Load and support (b) Random angle of applied load

Volume fraction has been selected as 0.25. The regular mesh of 38400 elements has been implemented. The data are the same as for other examples. The Moore type neighborhood has been applied. The topology generation has been performed for a single deterministic load as well as for selected random ones.

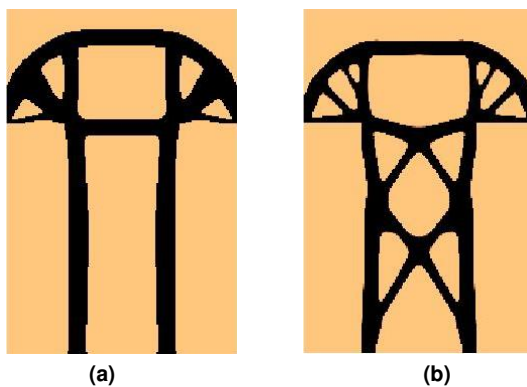


Figure 13

The tower structure 240×160 cells. (a) Single load case, deterministic solution (b) Random 100 loads.

Uniform distribution $\Delta\alpha = \pi/4$

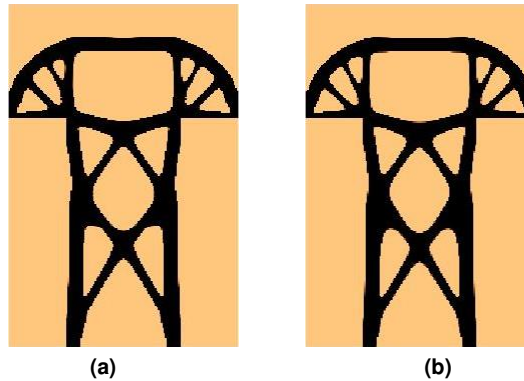


Figure 14

The tower structure. Topologies obtained for: (a) Random 1000 loads (b) Random 10000 loads.
Uniform distribution $\Delta_\alpha = \pi/4$

In the Fig. 13a the resulting structure obtained for the single load case is presented, whereas the Figs. 13b, 14 show topologies found for uniform random loads

The topology obtained for $\Delta_\alpha = \pi/9$ and 1000 applied random loads taken from normal distribution are shown in the Fig. 15.

For the structure under random load the additional stiffening within column part has been generated. The above solution can be compared with the one presented in [37] and [38], where similar changes in topology layout are observed when comparing deterministic and randomized results.

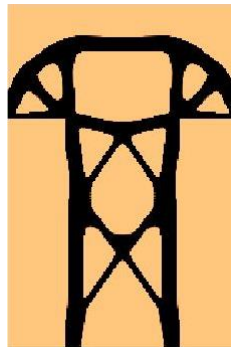


Figure 15

The tower structure. Topology obtained for random 1000 loads. Normal distribution $\Delta_\alpha = \pi/9$

3.3 The Foot Structure

The structure shown in the Fig. 16 has been selected as the next test example.

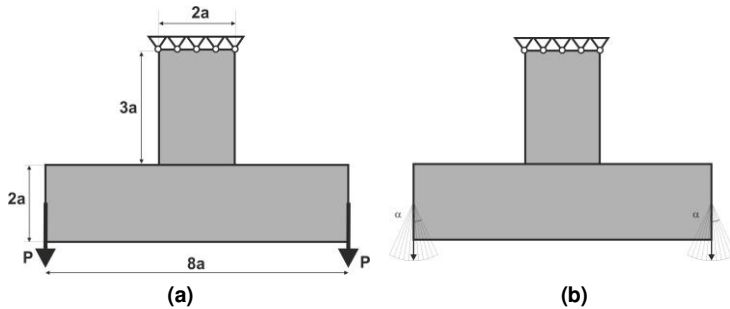


Figure 16

The foot structure. (a) Load and support (b) Random angle of applied load

The angle of applied load, see Fig. 16b, is treated as the random value which is generated according to uniform or normal distribution. Volume fraction has been selected as 0.25. The regular mesh of 25000 elements has been implemented. The Moore type neighborhood has been applied. The topology generation has been performed for a single deterministic load as well as for selected random ones. In the Fig. 17a the resulting structure obtained for the single load case is presented.

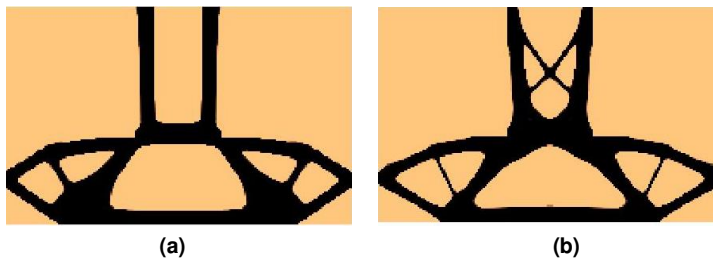


Figure 17

The foot structure. 200×125 cells. (a) Single load case, deterministic solution (b) Random 100 loads.

Uniform distribution $\Delta_\alpha = \pi/4$

The topologies generated for random loads are shown in the Figs. 17b, 18. The number of loads has been selected as 100, 1000 and 10000, random values have been generated from uniform distribution and $\Delta_\alpha = \pi/4$.

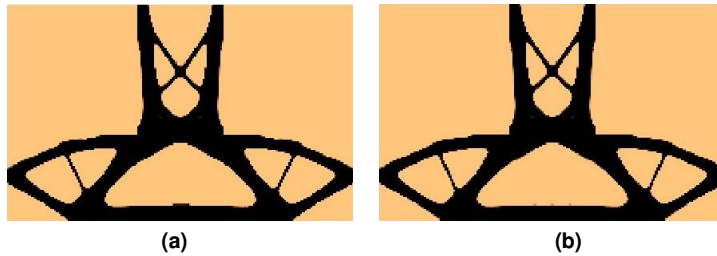


Figure 18

The foot structure. Topologies obtained for: (a) Random 1000 loads (b) Random 10000 loads.
Uniform distribution $\Delta_\alpha = \pi/4$

The topology obtained for $\Delta_\alpha = \pi/9$ and 1000 applied random loads taken from normal distribution are shown in the Fig. 19.

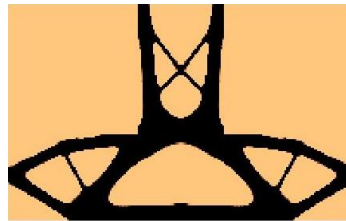


Figure 19

The foot structure. Topology obtained for random 1000 loads. Normal distribution $\Delta_\alpha = \pi/9$

For the structure under random load the additional stiffening within middle part of the structure has been generated. The results of this section can be compared with the one presented in [37] and [39].

3.4 The Structures under Random Load Position or Magnitude

As stated within introduction the load magnitude and its position can be also random variables. The numerical approach of this paper allows considering such cases therefore two additional, simple examples are presented to slightly broaden the discussion of this section.

As to the random load position, the structure used as introductory example is revisited, see Fig. 20. This time horizontal position of load can vary within a specified range defined by Δ_x .

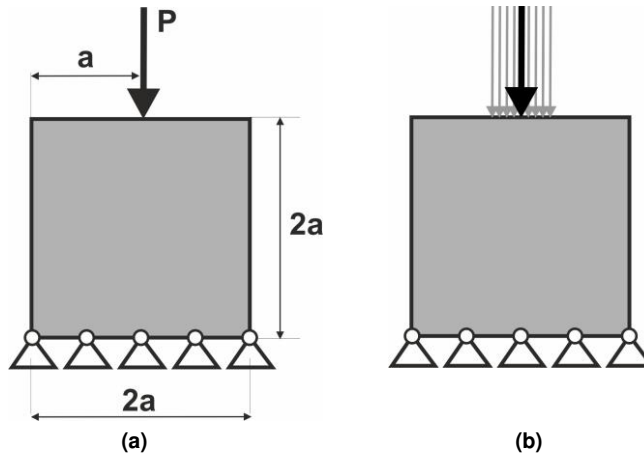


Figure 20

(a) The square structure under single (deterministic) load (b) The structure under random load position



Figure 21

The square structure. (a) Single load case, deterministic solution (b) Topology obtained for random 1000 loads and $\Delta_x=0.2a$. Uniform distribution

The topology has been generated and the result is presented in the Fig. 21b. One can see that it is different from these obtained under random angle of load application.

The final example regards illustration of generation of topology in the case of load magnitude changing at random. These changes usually do not affect significantly resulting topologies, however if the load orientation can vary results can be different from deterministic ones. The test example discussed in [40] is here revisited and resulting topologies are presented in the Fig. 22. The obtained structures comply with the ones reported in [40].

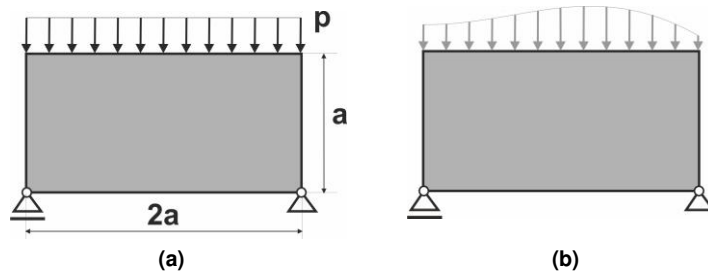


Figure 22

The rectangular structure. (a) Load and support (b) Random load magnitude

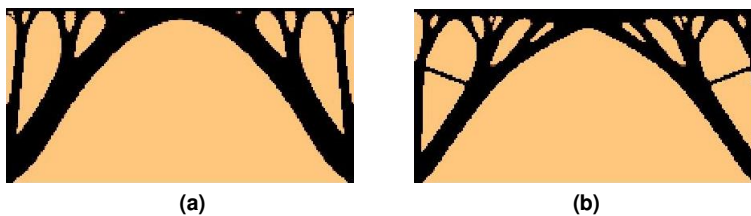


Figure 23

The rectangular structure. (a) Single load case, deterministic solution (b) Topology obtained for random 1000 loads. Normal distribution, mean of load magnitude equals 0.

Conclusions

In this paper, an easy to implement, numerical approach, which allows for the prediction of resulting topologies of structures, in the case of random loads, has been introduced and implemented. Based on obtained results, of selected test examples, it can be concluded that reasonably low number of load cases, can mimic load acting at random and is enough to obtain final topologies. The topologies generated under random loads, represent the same layout changes, compared to other deterministic solutions, as those reported in the literature. It seems that the approach discussed in this paper, can be a useful tool, supporting the research within structural topology optimization under random loads.

The benefit of the proposed approach based on a CA generator, besides the possibility of obtaining fine optimal topologies, is also that mesh dependency, and the “grey areas” can be eliminated without using any additional filtering. Moreover, the presented algorithm is versatile, which allows for its easy combination with any structural analysis solver, built on the finite element method (FEM). The presented approach can also be applied to 3D problems.

References

- [1] M. P. Bendsoe and N. Kikuchi, Generating optimal topologies in optimal design using a homogenization method, *Computer Methods in Applied Mechanics and Engineering*, Vol. 71, 1988, pp. 197-224

-
- [2] M. P. Bendsoe, Optimal shape design as a material distribution problem, *Structural Optimization*, Vol. 1, 1989, pp.193-202
- [3] O. Sigmund, K. Maute, Topology optimization approaches, *Structural and Multidisciplinary Optimization*, Vol. 48, 2013, pp. 1031-1055
- [4] J. D. Deaton, R. V. Grandhi, A survey of structural and multidisciplinary continuum topology optimization: post 2000, *Structural and Multidisciplinary Optimization*, Vol. 49, 2014, pp. 1-38
- [5] J. Liu, A. T. Gaynor, S. Chen, Z. Kang, K. Suresh, A. Takezawa, L. Li, J. Kato, J. Tang, C. C. L. Wang, L. Cheng, X. Liang, A. C. To, Current and future trends in topology optimization for additive manufacturing, *Structural and Multidisciplinary Optimization*, Vol. 57, 2018, pp. 2457-2483
- [6] A. Kentli, Topology optimization applications on engineering structures, in: *Truss and Frames - Recent Advances and New Perspectives*, IntechOpen, 2020, doi: 10.5772/intechopen.80173
- [7] T. P. Ribeiro, L. F. A. Bernardo, J. M. A. Andrade, Topology optimisation in structural steel design for additive manufacturing, *Applied Sciences*, Vol. 11, 2021, 2112
- [8] J. Logo, H. Ismail, Milestones in the 150-year history of topology optimization: a review, *CAMES*, Vol. 27(2-3), 2020, pp. 97-132
- [9] A. Csebfalvi, Robust topology optimization: A new algorithm for volume-constrained expected compliance minimization with probabilistic loading directions using exact analytical objective and gradient, *Periodica Polytechnica, Civil Engineering*, Vol. 61(1), 2017, pp. 154-163
- [10] J. Martínez-Frutos, D. Herrero-Pérez, Evolutionary topology optimization of continuum structures under uncertainty using sensitivity analysis and smooth boundary representation, *Computers and Structures*, Vol. 205, 2018, pp. 15-27
- [11] D. Wang, W. Gao, Robust topology optimization under load position uncertainty, *International Journal for Numerical Methods in Engineering*, Vol. 120, 2019, pp. 1249-1272
- [12] Ch. Mang, J. Cortial, Ch. Nardoni, F. Bordeu, A deterministic approach for shape and topology optimization under uncertain loads, *Eurogen 2019*, Sep. 2019, Giumares, Portugal, hal-02471986
- [13] S. De, J. Hampton, K. Maute, A. Doostan, Topology optimization under uncertainty using a stochastic gradient-based approach, *Structural and Multidisciplinary Optimization*, Vol. 62, 2020, pp. 2255-2278
- [14] F. Yin, K. Dang, W. Yang, Y. Ding, P. Xie, An efficient approach to reliability-based topology optimization for the structural lightweight design of planar continuum structures, *Journal of Mechanics*, Vol. 37, 2021, pp. 270-281

- [15] W. Shen, M. Ohsaki, M. Yamakawa, Quantile-based sequential optimization and reliability assessment for shape and topology optimization of plane frames using L-moments, *Structural Safety*, Vol. 94, 2022, 102153, pp.1-16
- [16] H. Wang, W. Cheng, M. Zhang, R. Du, W. Xiang, Non-gradient robust topology optimization method considering loading uncertainty, *Arabian Journal for Science and Engineering*, Vol.46, 2021, pp. 12599-12611
- [17] P. Tazowski, B. Blachowski, J. Logo, Topology optimization of elasto-plastic structures under reability constraints: A first order approach, *Computers and Structures*, Vol. 243, 2021, 106406, pp.1-15
- [18] N. Inou, N. Shimotai, T. Uesugi, A cellular automaton generating topological structures, in *Proc. 2nd European Conference on Smart Structures and Materials*, 1994, 2361, pp. 47-50
- [19] A. Tovar, N. M. Patel, G. L. Niebur, M. Sen. J. E. Renaud, Topology optimization using a hybrid cellular automaton method with local control rules, *Journal of Mechanical Design*, Vol. 128, 2006, pp. 1205-1216
- [20] B. Hassani, M. Tavakkoli, A multi-objective structural optimization using optimality criteria and cellular automata, *Asian Journal of Civil Engineering Building and Housing*, Vol. 8, 2007, pp. 77-88
- [21] C. L. Penninger, A. Tovar, L. T. Watson, J. E. Renaud, KKT conditions satisfied using adaptive neighboring in hybrid cellular automata for topology optimization, *International Journal of Pure and Applied Mathematics*, Vol. 66, 2011, pp. 245-262
- [22] M. Afrousheh, J. Marzbanrad, D. Gohlich, Topology optimization of energy absorbers under crashworthiness using modified hybrid cellular automata (MHCA) algorithm, *Structural and Multidisciplinary Optimization*, Vol. 60, 2019, pp. 1024-1034
- [23] J. Jia, D., Da, C. L. Loh, H. Zhao, S. Yin, J.Xu, Multiscale topology optimization for non-uniform microstructures with hybrid cellular automata, *Structural and Multidisciplinary Optimization*, Vol. 62, pp. 757-770, 2020
- [24] B. Bochenek, K. Tajs-Zielińska, Minimal compliance topologies for maximal buckling load of columns, *Structural and Multidisciplinary Optimization*, Vol. 51, 2015, pp. 1149-1157
- [25] B. Bochenek, K. Tajs-Zielińska, GOTICA -generation of optimal topologies by irregular cellular automata, *Structural and Multidisciplinary Optimization*, Vol. 55, 2017, pp. 1989-2001
- [26] K. Tajs-Zielińska, B. Bochenek, Multi-domain and multi-material topology optimization in design and strengthening of innovative sustainable structures. *Sustainability*, Vol. 13, 2021, 3435, pp. 1-24

-
- [27] K. Tajs-Zielińska, B. Bochenek, Topology algorithm built as automaton with flexible rules, *Bulletin of the Polish Academy of Sciences, Technical Sciences*, Vol. 69(5), 2021, pp. 1-15
- [28] T. Lewiński, S. Czarnecki, G. Dzierżanowski, T. Sokół, Topology optimization in structural mechanics, *Bulletin of the Polish Academy of Sciences, Technical Sciences*, Vol. 61(1), 2013, pp. 23-37
- [29] M. Stolpe, K. Svanberg, An alternative interpolation scheme for minimum compliance topology optimization, *Structural and Multidisciplinary Optimization*, Vol. 22, 2001, pp. 116-124
- [30] F. Niu, S. Xu, G. Cheng, A general formulation of structural topology optimization for maximizing structural stiffness, *Structural and Multidisciplinary Optimization*, Vol. 43, 2011, pp. 561-572
- [31] W. Zhang, J. Yang, Y. Xu, T. Gao, Topology optimization of thermoelastic structures: mean compliance minimization or elastic strain energy minimization, *Structural and Multidisciplinary Optimization*, Vol. 49, 2014, pp. 417-429
- [32] M. V. O. Araujo, E. N. Lages, M. A. A. Cavalvante, Checkerboard-free topology optimization for compliance minimization of continuum elastic structures based on the generalized finite-volume theory, *Latin American Journal of Solids and Structures*, Vol. 17, 2020, pp. 1-21
- [33] O. Sigmund, A 99 line topology optimization code written in MATLAB, *Structural and Multidisciplinary Optimization*, Vol. 21, 2001, pp. 120-127
- [34] M. P. Bendsoe, *Optimization of Structural Topology, Shape, and Material*, Springer-Verlag Berlin Heidelberg 1995
- [35] M. P. Bendsoe, O. Sigmund, *Topology Optimization: Theory, Methods and Applications*, Springer-Verlag Berlin Heidelberg 2003
- [36] J. Zhao, Ch. Wang, Robust topology optimization of structures under load uncertainty, *AIAA Journal*, Vol. 52(2), 2014, pp. 398-407
- [37] P. D. Dunning, H. A. Kim, G. Mullineux, Introducing loading uncertainty in topology optimization, *AIAA Journal*, Vol. 49(4), 2011, pp. 760-768
- [38] J. Martinez-Frutos, D. Herrero-Perez, M. Kessler, F. Periago, Robust shape optimization of continuous structures via the level set method, *Computer Methods in Applied Mechanics and Engineering*, Vol. 305, 2016, pp. 271-291
- [39] Y. Zheng, L. Gao, M. Xiao, H. Li, Robust topology optimization considering load uncertainty based on semi-analytical method, *International Journal of Advanced Manufacturing Technology*, 2017, pp. 1-15
- [40] J. Zhao, Ch. Wang, Robust structural topology optimization under random field loading uncertainty, *Structural and Multidisciplinary Optimization*, Vol. 50, 2014, pp. 517-522
-

Topology Optimization for Loads with Multiple Points of Application

Hussein Ismail*, Matteo Bruggi, János Lógó*****

*Budapest University of Technology and Economics, Department of Structural Mechanics, Műegyetem rkp. 3, H-1111 Budapest, Hungary and Politecnico di Milano, Department of Civil and Environmental Engineering, P.zza Leonardo da Vinci, 32 20133 Milano Italy, hussein.ismail@emk.bme.hu, hussein.ismail@polimi.it

**Politecnico di Milano, Department of Civil and Environmental Engineering, P.zza Leonardo da Vinci, 32 20133 Milano Italy, matteo.bruggi@polimi.it

***Budapest University of Technology and Economics, Department of Structural Mechanics, Műegyetem rkp. 3, H-1111 Budapest, Hungary, logo.janos@emk.bme.hu

Abstract: The optimal design for loads with multiple points of application is herein investigated by using a formulation of displacement-constrained minimum volume topology optimization. For each one of the several points in which a moving force may be applied, a static load case is introduced, and a local enforcement is implemented to control the relevant displacement. Inspired by some recent contributions in stress-based topology optimization of large-scale structures, an Augmented Lagrangian approach, is adopted to handle efficiently the arising multi-constrained problem, in conjunction with mathematical programming. The results of some numerical simulations are shown to comment on optimal shapes for loads with multiple points of application, as compared to classical solutions for fixed loads.

Keywords: topology optimization; moving loads; local constraints; structural optimization

1 Introduction

Topology optimization is a design technique that allows investigating the optimal shape of structural components by distributing material within a given design domain, given a goal and a set of constraints [1] [2]. Among the others, the design performed by distribution of isotropic material is extensively adopted to investigate lightweight structures [3-5]. By selecting the density field as the unknown that governs pointwise the elastic modulus of the material, a minimization problem can be formulated adopting as objective function the work of the external loads at

equilibrium (the so-called structural compliance), while enforcing a constraint on the allowed amount of material (the available volume fraction). This is the well-known volume-constrained minimum compliance problem [6]. Since the structural compliance equals twice the strain energy stored in the design domain, under the effect of any given load, this problem is in turn equivalent to searching for the distribution of an available amount of material that minimizes the strain energy, i.e. maximizes the overall structural stiffness. Minimum compliance problems may be solved very efficiently, see the recent contribution given in [7].

The design of two-dimensional structural components is addressed in the present work as a displacement-constrained minimum volume problem, focusing on the implementation of multiple constraints and load cases. Among the others, reference is made to [8-11] for discussions and reviews on displacement constraints in topology optimization, and to [12] for an insight on the optimal design including multiple loading. A displacement-constrained minimum volume formulation is ideally conceived to investigate lightweight design at the serviceability limit state. Indeed, displacement limits are prescribed for structural elements by technical codes, whereas the amount of material needed to fulfil these constraints is an outcome of the design problem. When the controlled displacement is that at the loaded point along the direction of the applied force, the work of the external load at equilibrium equals the scalar product of the controlled displacement and the applied force. In this case, the displacement-constrained minimum volume problem is equivalent to a classical volume-constrained minimum compliance problem. As discussed in [13], the same solution (up to a scaling) is expected to arise when considering either problem. This rationale does not apply when multiple loading or distributed loads are dealt with.

Recent contributions in stress-constrained topology optimization, see in particular [14] [15], have shown that very large sets of local enforcements can be efficiently tackled by combining sequential convex programming and Augmented Lagrangian (AL) strategies, as an effective alternative to aggregation methods. Within the family of sequential programming approaches, the Method of Moving Asymptotes (MMA) [16] is widely adopted in structural optimization since it may linearize the objective function and the constraints not only in the direct variables but also in the reciprocal ones, see e.g. the discussion on topology optimization of elastic trusses in [17] and the application in [18]. In [14] an Augmented Lagrangian approach is proposed in which the original penalization term, see [19], is normalized with respect to the number of stress constraints. This approach is implemented herein to enforce a local control of the deflection when addressing loads with multiple points of application. When dynamic effects can be neglected, the case of a moving force may be handled as a set of several static load cases (describing successive positions of the load). A displacement constraint may be therefore implemented for each one of the load cases, to control the relevant displacement at the loaded node. Reference is also made to [20] [21], for examples of application of structural optimization on this topic.

While most of the methods available in topology optimization deal with volume-constrained minimum compliance optimization, the proposed approach is concerned with the application of multiple local constraints to control the displacement field. Indeed, when dealing with the design of structural components at the serviceability limit state, prescriptions on the admissible deflection must be fulfilled. A peculiarity of the proposed approach consists in the adoption of the AL strategy to handle large sets of displacement constraints. Leveraging this framework, it is possible to control the deflection at each one of the loaded points when addressing distributed loads and (static) moving loads. The former case is frequently encountered in problems of structural design, see Figure 1(left): given a geometric domain with prescribed supports, the best shape is sought to carry a distributed load while fulfilling constraint for the deflection along the edge where the load is applied. The latter case is peculiar to the conceptual design of bridges or elements supporting overhead cranes, see Figure 1(right): the desired optimal shape must carry a load with multiple points of application, with full control of the deflection caused by the load in each one of its possible positions.



Figure 1

Design domain and boundary conditions for two problems of structural design: the case of distributed loads (left), and the case of (static) moving forces (right)

It is finally stated that, accounting for the wide variety of topology optimization methods for structural design, see in particular [1, 3, 5], alternative strategies may be successfully implemented when modelling the problem and enforcing constraints. Among the others, reference is made to the use of polygonal finite elements in topology optimization to solve the elastic problem [22], thus minimizing any mesh-related polarization in the research of optimal distributions of material when using standard four-node elements, see also [23]. It is finally remarked that the uncertainty inherent in material properties, loads, and boundary conditions of any structural design problem can be conveniently embedded in the optimization, see e.g., the reliability-based topology optimization with displacement limit state function discussed in [24]. This topic will be object of future extensions of the method.

The organization of the paper is as follows. Section 2.1 presents the displacement-constrained formulation, whereas Section 2.2 gives details on the numerical implementation, including the computation of the sensitivity information by means of the adjoint method. In Section 3 numerical applications are shown pointing out mechanical features of the achieved optimal layouts. They are focused on simple examples (rather than industrial applications), due to the main goal of preliminary assessing the proposed method through benchmark. Finally, conclusions are drawn based on the outcome of the numerical tests.

2 Problem Formulation and Implementation

When dealing with the considered multi-constrained problem of topology optimization, the finite element method is used to solve the governing equation, herein the linear elastic equilibrium. The element-wise constitutive properties of the material depend on the set of optimization unknowns through an interpolation law. A gradient-based minimization algorithm is used to iteratively update the unknowns in order to find the set that minimizes the objective function, accounting for the enforced constraints. In each step, a finite element analysis is performed to solve the elasticity problem with the current distribution of unknowns to compute updated information for the minimizer.

2.1 Problem Statement

Standard four-node displacement-based elements are used to get a discretization of a given design domain. A discrete design variable is assigned to each element. In the e -th of the n elements belonging to the mesh, $0 \leq \rho_e \leq 1$ is the so-called “density” of the material. Using the Solid Isotropic Material with Penalization (SIMP) [6][25], the constitutive matrix $\mathbf{C}(\rho_e)$ reads:

$$\mathbf{C}(\rho_e) = \rho_e^p \mathbf{C}_0 + \mathbf{C}_{min} \quad (1)$$

where \mathbf{C}_0 is the plane stress constitutive matrix at full density, $\mathbf{C}_{min} = 10^{-9} \mathbf{C}_0$ stands for “void” and p is an interpolation parameter that penalizes intermediate densities, see in particular [7]. In the numerical simulations, p is increased from 3 to 9 during the optimization by means of the continuation approach used in the referenced work.

The statement of the displacement-constrained problem of minimum volume topology optimization [12] is:

$$\left\{ \begin{array}{l} \min_{0 \leq \rho_e \leq 1} V = \sum_{e=1}^n \rho_e V_{0,e} \\ \text{subject to } \left(\sum_{e=1}^n \rho_e^p \mathbf{K}_{0,e} \right) \mathbf{U}_j = \mathbf{F}_j, \quad \text{for } j = 1, \dots, l \\ u_i \leq u_{lim,i}, \quad \text{for } i = 1, \dots, m \end{array} \right. \quad (2)$$

In the above problem, the objective function is the volume of the structural element V . This may be computed through the sum over the contributions $\rho_e V_{0,e}$, being $V_{0,e}$ the volume of the e -th element at full density, that is for $\rho_e = 1$.

The first constraint in Eqn. (2) prescribes the static equilibrium of the structural element under multiple load cases. The global stiffness matrix is given by the element contributions accounting for the constitutive law of Eq. (1). The element stiffness matrix reads $\rho_e^p \mathbf{K}_{0,e}$, where $\mathbf{K}_{0,e}$ refers to $\rho_e = 1$. For the j -th of the l load cases, \mathbf{F}_j is the load vector, and \mathbf{U}_j is the relevant nodal displacement vector. Design-independent loads are dealt with in the numerical investigations that follow.

The i -th of the m displacement components to be controlled is denoted by u_i . The second constraint in Eqn. (2) enforces a prescribed limit $u_{lim,i}$. This quantity $u_{lim,i}$ stands for the maximum value that the i -th displacement component is allowed to undergo at the serviceability limit state. Assuming that u_i is an entry of \mathbf{U}_j , meaning that the i -th constraint refers to the j -th load case, one has:

$$u_i = \mathbf{L}_i^T \mathbf{U}_j \quad (3)$$

where \mathbf{L}_i is a vector made of zeros with the exception of the entry referring to the i -th displacement degree of freedom, which takes unitary value.

2.2 Numerical Details

In this section, an insight is given on the treatment of the density field to avoid well-known numerical instabilities while achieving crisp black/white layouts, and on the gradient-based approach used to handle the arising multi-constrained problem.

2.2.1 Filtering and Projection

A linear filter [26] [27] is implemented on the element variables ρ_e to avoid the arising of checkerboard patterns and mesh dependence. The original variables ρ_e are mapped to the new set of $\tilde{\rho}_e$ as:

$$\begin{aligned} \tilde{\rho}_e &= \frac{1}{\sum_n H_{es}} \sum_n H_{es} \rho_s \\ H_{es} &= \max(0, r_{min} - \text{dist}(e, s)) \end{aligned} \quad (4)$$

where $\text{dist}(e, s)$ is the distance between the centroid of the e -th and s -th element, and r_{min} is the filter radius, both entering the weight factor H_{es} . The filtered densities $\tilde{\rho}_e$ are subsequently mapped to the set of physical densities $\hat{\rho}_e$ to get crisp black/white solutions, see the projection proposed in [28]:

$$\hat{\rho}_e = \frac{\tanh(\beta\eta) + \tanh(\beta(\tilde{\rho}_e - \eta))}{\tanh(\beta\eta) + \tanh(\beta(1 - \eta))} \quad (5)$$

with $\eta = [0, 1]$ and $\beta = [1, \infty]$. In the numerical simulations, $\eta = 0.5$, whereas β is smoothly increased during the run from 2 to 16, by means of the continuation approach used in [7]. The layout of the optimal solution is given using maps of $\hat{\rho}_e$.

2.2.2 Solving Algorithm

The optimization problem in Eqn. (2) is solved via mathematical programming, using the Method of Moving Asymptotes (MMA) [16] as minimizer. Displacement constraints are treated following the Augmented Lagrangian method implemented in [14]. Constraints are gathered in a modified version of the objective function such that the problem is turned into an unconstrained minimization. At the k -th AL step, this objective function reads:

$$V = V + \frac{1}{m} \sum_{i=1}^m \left(a_i^{(k)} \frac{u_i}{u_{lim,i}} + \frac{1}{2} b^{(k)} \left(\frac{u_i}{u_{lim,i}} \right)^2 \right) \quad (6)$$

where $a_i^{(k)}$ is the i -th entry of the vector of the Lagrangian multiplier estimators and $b^{(k)} > 0$ is a penalty factor. MMA is used to find an approximate solution of the normalized function in Eqn. (6). This solution allows updating the current values of the estimators of the Lagrangian multipliers and the penalty factor for the subsequent AL step. In the numerical simulations, the number of MMA iterations per AL step has been set to 5.

The overall process is repeated until convergence is met, i.e. the maximum difference in terms of the minimization unknowns between two subsequent steps is less than 10^{-3} .

2.2.3 Sensitivity Computation

The adjoint method is used to compute derivatives in order to provide the gradient-based minimizer with the sensitivity with respect to the design variables, see e.g. [1]. Accordingly, u_i of Eqn. (3) does not change when a zero function is added at the right hand side. Exploiting the discrete equilibrium in Eqn. (2), denoting by $\mathbf{K}(\boldsymbol{\rho})$ the overall stiffness matrix depending on the vector gathering the element unknowns, one may write:

$$-\boldsymbol{\lambda}_i^T (\mathbf{K}(\boldsymbol{\rho}) \mathbf{U}_j - \mathbf{F}_j) \quad (7)$$

where $\boldsymbol{\lambda}_i$ is any arbitrary but fixed vector. After re-arrangement of terms, the derivative of u_i with respect to the h -th entry of $\boldsymbol{\rho}$ may be computed as:

$$\frac{\partial u_i}{\partial \rho_h} = \left(\mathbf{L}_i^T - \boldsymbol{\lambda}_i^T \mathbf{K}(\boldsymbol{\rho}) \right) \frac{\partial \mathbf{U}_j}{\partial \rho_h} - \boldsymbol{\lambda}_i^T \frac{\partial \mathbf{K}(\boldsymbol{\rho})}{\partial \rho_h} \mathbf{U}_j \quad (8)$$

that can be in turn written as:

$$\frac{\partial u_i}{\partial \rho_h} = -\boldsymbol{\lambda}_i^T \frac{\partial \mathbf{K}(\boldsymbol{\rho})}{\partial \rho_h} \mathbf{U}_j \quad (9)$$

In the above expression, $\boldsymbol{\lambda}_i$ satisfies the adjoint equation:

$$\mathbf{K}(\boldsymbol{\rho}) \boldsymbol{\lambda}_i = \left(\frac{\partial u_i}{\partial \mathbf{U}_j} \right)^T = \mathbf{L}_i \quad (10)$$

Eqn. (9) can be evaluated recalling that the derivative of the e -th element stiffness matrix with respect to ρ_h is equal to $p \rho_e^{p-1} \mathbf{K}_{0,e}$, being $\mathbf{K}_{0,e}$ the element stiffness matrix at full density. This sensitivity is null if $e \neq h$.

The derivatives with respect to the filtered variables $\tilde{\rho}_e$ and the physical ones $\hat{\rho}_e$ can be evaluated by applying the chain rule to Eqn. (4) and Eqn. (5), respectively. At each iteration in the process, only one matrix inverse must be computed to evaluate constraints and their sensitivities. This is because the linear systems in the first constraint of Eqn. (2) and Eqn. (11) share the same coefficient matrix $\mathbf{K}(\boldsymbol{\rho})$.

It is also remarked that this framework is ideally conceived for a straightforward implementation within commercial finite element codes, exploding their application programming interfaces, see e.g. [29].

3 Numerical Simulations

Numerical simulations considering the optimal design under displacement constraints are presented in this section, dealing with fixed point forces, uniformly distributed loads, and forces with multiple points of application. The latter are referred to as moving point forces in the discussion that follows.

In all the examples, the controlled displacements u_i are those read at the m loaded nodes in the direction of the acting force. The limit $u_{lim,i}$ is defined either as $\alpha u_{0,i}$, i.e. α times the value found at the same point in case of full material beam $u_{0,i}$, or as $\alpha \max_m u_{0,i}$. In the former case, the goal is reproducing the stiffness provided by a full material beam, with the scaling given by α . In the latter case, the bound of the displacement is the same for all the controlled points, as conventionally done in the assessment of structures at the serviceability limit state. In the numerical simulations that follow $\alpha = 1.50$.

Rectangular domain analyzed next have height equal to L and filter radius $r_{min}=L/10$. All the layouts presented next are respectful of all the enforced local constraints. Each solution is endowed with the value of the volume fraction of the material at convergence v_f , that is the ratio of the last value of the objective function in Eqn. (2) to the volume of a full material beam.

3.1 Cantilever Beam

The first numerical investigation refers to a $3L \times L$ cantilever beam that is fully clamped at the left side. A mesh of 300×100 four-node elements is used. At first, it is assumed that the specimen is acted upon by a vertical force located at the bottom right corner of the rectangular domain. According to Maxwell's principle for elements in bending having constant cross-section, this is the location of a vertical force moving along the bottom side of the rectangular domain, such that the deflection of the element is the largest one. The formulation in Eqn. (2) is implemented considering one load case ($l = 1$) and controlling the vertical component of the displacement read at the loaded point, that is the lower corner of the tip ($m = 1$). The achieved design is the truss-like structure shown in Figure 2. The volume fraction is $v_f = 0.50$. This means that only half of the material making a full material beam is needed if an increase by half in the deflection is allowed.



Figure 2

Cantilever beam: optimal design considering a force applied at the tip ($v_f = 0.50$)

A second investigation is performed considering a uniformly distributed load acting all over the lower side of the rectangular domain. A set of constraints is enforced in the formulation of Eqn. (2) to control the vertical displacement at each one of the loaded nodes within the same load case ($l = 1, m = 300$). The optimal layouts that are found by enforcing the same u_{lim} throughout the span ($\alpha \max_m u_{0,i}$) and by implementing the varying u_{lim} ($\alpha u_{0,i}$), are shown in the left and right picture of Figure 3, respectively.



Figure 3

Cantilever beam: optimal design considering a uniformly distributed load, for the same u_{lim} all over the span (left, $v_f = 0.40$), and varying u_{lim} to approximate the deflection of a full beam (right, $v_f = 0.50$)

The relevant deformed shapes are sketched in Figure 4, along with a horizontal line representing the quantity $\alpha \max_m u_{0,i}$. In the latter case, the design is heavier than in the former ($v_f = 0.50$ vs. 0.40) due to the stricter displacement constraints. Indeed, almost one half of the bottom side of the domain lies along the line representing the quantity $\alpha \max_m u_{0,i}$ in the former case, whereas in the latter such a deflection is allowed at the tip only.



Figure 4

Cantilever beam: deformed shapes of the layouts achieved considering a uniformly distributed load: same u_{lim} all over the span (left), and varying u_{lim} to approximate the deflection of a full beam (right)

Two additional simulations are set to investigate the difference between displacement-constrained minimum volume optimization and volume-constrained minimum compliance design. Minimum compliance layouts are found using as

input the volume fractions found in output for the minimum volume layouts of Figure 3. The optimal layouts (in their deformed configuration) for $v_f = 0.40$ and $v_f = 0.50$ are represented in the left and right picture of Figure 5, respectively. In both pictures, the horizontal line representing the quantity $\alpha \max_m u_{0,i}$ already used in Figure 4 is reported to check the deformability. The achieved minimum compliance layouts have some similarity with the minimum volume design approximating the deflection of a full material beam, see Figure 3 (right). However, as expected, neither of them is stiff as the solutions found by enforcing a local control of the displacement field.

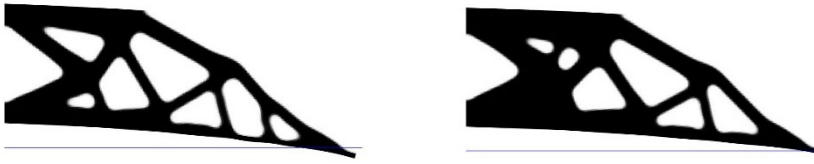


Figure 5

Cantilever beam: deformed shapes of the minimum compliance layouts achieved considering a uniformly distributed load and prescribing: $v_f = 0.40$ (left), and $v_f = 0.50$ (right)

Finally, the optimal design in case of a point force moving along the lower side of the geometrical domain of the cantilever is considered. This may be simply implemented in Eqn. (2) by defining a load case for each one of the nodes belong to the load path of the point force ($l = 300$), and by controlling the relevant displacement at the loaded node ($m = 300$). Along the lines of the simulations performed in case of uniformly distributed load, two optimization strategies have been tested. The picture on the left in Figure 6, is the layout achieved by enforcing the same displacement limit all over the load cases ($\alpha \max_m u_{0,i}$). The optimal design has the same volume fraction of the optimal design found in the case of a specimen loaded by a vertical force at the tip. However, it has less and thicker members than the layout in Figure 2. Dealing with the moving force, a subsequent optimization is performed using the varying u_{lim} that is aimed at reproducing the deflection of a full material beam ($\alpha u_{0,i}$). A much heavier design arises in this case to fulfil the stricter deflection constraints, see the picture on the right in Figure 6.



Figure 6

Cantilever beam: optimal design considering a moving vertical force, for the same u_{lim} throughout the span (left, $v_f = 0.50$), and varying u_{lim} to approximate the deflection of a full beam (right, $v_f = 0.58$)

3.2 Single Span Beams

In this section the displacement-constrained minimum volume design is investigated dealing with single span beams occupying a rectangular domain with size $6L \times L$. A mesh of 600×100 four-node elements are used. Forces are applied at the lower side of the rectangular domain.

At first, the case of simply supported beam is considered. Figure 7 gathers pictures representing the optimal layouts found when considering a force applied at midspan (top), a uniformly distributed load (center), and a moving vertical force (bottom). The last two layouts have been found by enforcing the same displacement limit all over the loaded points ($\alpha \max_m u_{0,i}$). The optimal design achieved in case of uniformly distributed load takes full advantage of the symmetry of the load and of the low value of the shear force around midspan. The solution found for the moving force is a more branched variation of that found considering a force applied at midspan. Indeed, this is the location of the point force for which the deflection is the largest in a beam with uniform cross section. The achieved design costs a very minor increase in terms of volume fraction ($v_f = 0.52$ vs. 0.50).

Then, the case of a two hinged beam is analyzed, considering the same loads and optimization problems already implemented for the simply supported beam. The achieved results are given in Figure 8. The optimal layout found for the uniformly distributed load is an efficient arch-like structure with inclined ties, a widely implemented solution in bridge design. In the solution found considering a force applied at midspan, the point load hangs from a central stiff region that is supported by two inclined struts. This layout cannot accommodate effectively forces with different point of applications. Indeed, the optimal solution found for the moving point force is a much heavier structure: the arch already exploited in the design for the uniformly distributed load is here endowed with a strut-and-tie sub-structure that supports the point force all over its path.

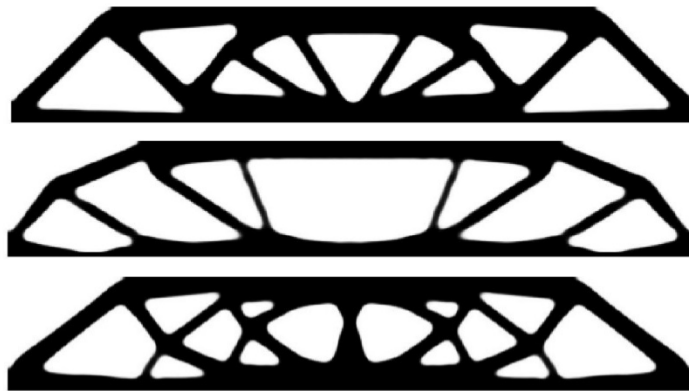


Figure 7

Simply supported beam: optimal design considering a force applied at midspan (top, $v_f = 0.50$), a uniformly distributed load (center, $v_f = 0.37$), and a moving vertical force (bottom, $v_f = 0.52$)

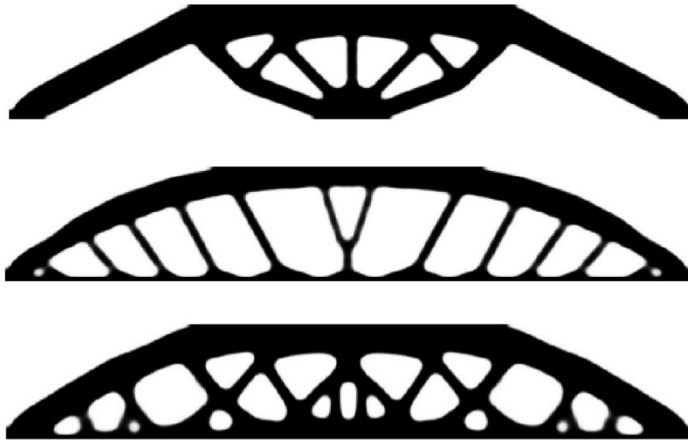


Figure 8

Hinged beam: optimal design considering a force applied at midspan (top, $v_r=0.42$), a uniformly distributed load (center, $v_r=0.36$), and a moving vertical force (bottom, $v_r=0.53$)

3.3 Two-Span Beam

A two-span beam is considered adopting the same mesh used in the previous example. An additional support is added in the middle of the lower side. At first the optimal design is dealt with considering a uniformly distributed load applied at the lower edge all over the two spans ($l=1$ and $m=598$). The same displacement limit ($\alpha \max_m u_{0,i}$) is enforced at all the loaded points. The optimal design is represented in the top picture of Figure 9. The arm between the upper and the lower chord of the structure is in good agreement with the diagram of the bending moment of a two-span beam made of full material. To maximize the deflection, an alternative load scenario could be conveniently considered. The optimal design shown in the bottom picture of Figure 9 concerns the implementation of two load cases. The uniformly distributed load acts in one span at a time, i.e. $l=2$ and $m=598$, with half of the constraints referring to the points loaded in the left span (first load case) and half to the points loaded in the right span (second load case). In each of the two spans the design is quite similar to that found for the simply supported beam, see Figure 7 (center).

The last set of investigations refers to a moving point force whose path is the lower side of the rectangular domain. This is implemented in Eqn. (2) by defining a load case for each one of the nodes belonging to the path followed by the point force ($l=598$) and by controlling the relevant displacement at the loaded node ($m=598$). As done in Section 3.1, two optimization strategies have been tested.

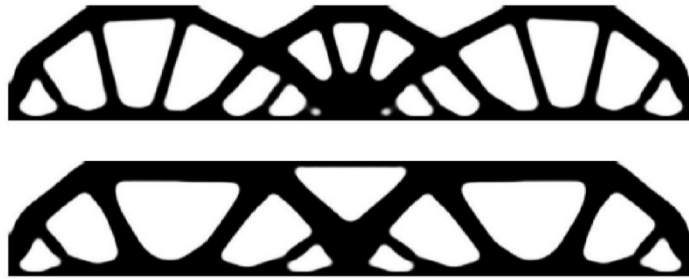


Figure 9

Two-span beam: optimal design considering a uniformly distributed load acting on both spans simultaneously (top, $v_f = 0.46$), and acting in one span at a time (bottom, $v_f = 0.50$)

In Figure 10 the optimal layout achieved by enforcing the same displacement limit all over the load cases ($\alpha \max_m u_{0,i}$) is represented. In Figure 11 the optimal design achieved by enforcing the varying u_{lim} that is aimed at reproducing the deflection of a full material beam ($\alpha u_{0,i}$) is given. In both figures a map of the vertical displacements computed at the varying loaded point is provided, along with a plot of the fixed/ varying u_{lim} . Although the optimal layouts are quite similar in terms of topology and volume fraction ($v_f = 0.62$ vs 0.65), the relevant displacement plots are quite different. While most of the deck undergoes the maximum allowed displacement in the former case, a smoother variation is found, as expected, in the latter.

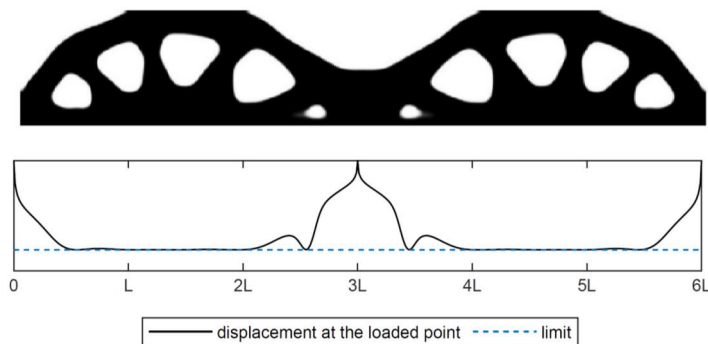


Figure 10

Two-span beam: design considering a moving vertical force and the same u_{lim} throughout the spans ($v_f = 0.62$): optimal layout and displacement computed at the varying loaded point

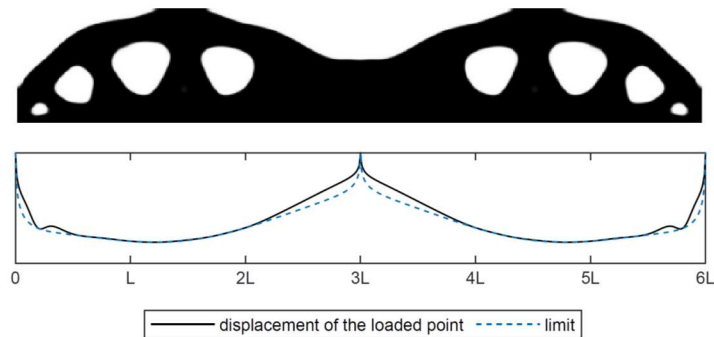


Figure 11

Two-span beam: design considering a moving vertical force and a varying u_{lim} aimed at approximating the deflection of a full beam ($v_f = 0.65$): optimal layout and displacement computed at the varying loaded point

Conclusions

A formulation of topology optimization, by distribution of isotropic material, has been proposed, searching for structures of minimum volume subjected to multiple displacement constraints. The same problem can deal with fixed point or distributed loads and forces with multiple points of application. Indeed, for each one of the several points, in which a moving force may be applied, a local enforcement may be used to control the relevant displacement.

Following recent contributions addressing stress-based topology optimization of large-scale structures, a modified Augmented Lagrangian approach has been implemented, in conjunction with sequential convex programming, to handle the arising multi-constrained problem, in an efficient way.

Numerical simulations have been shown to elaborate on optimal design with multiple displacement constraints. Two strategies have been tested to formulate enforcements regarding the deflection: as conventionally done at the serviceability limit state, the same upper bound of the displacement can be used for all the controlled points. Alternatively, a varying limit may be used to mimic the stiffness provided by a full material beam. Optimal solutions for moving loads have been compared to classical solutions for fixed loads, both point forces and distributed loads. In a few examples, the optimal topology for moving loads was found to be a slightly heavier variation of the topology obtained for a single force applied where the maximum deflection was expected (see results concerning the cantilever beam and the simply supported beam). However, alternative layouts may arise to provide the required support along the entire load path (see results on the two hinged beam). It is also remarked, that the strategy adopted to enforce deflection constraints remarkably affects, as expected, the displacement read under the moving force (see results on the two-span beam).

The proposed design tool can be conveniently used to sketch preliminary solutions for any load conditions and restraint configurations. It is finally remarked that the considered multi-constrained formulation could be effectively augmented with other types of enforcements, such as buckling constraints and stress constraints, with the main aim of designing effective structural components [30]. The ongoing research is devoted to the extension of the proposed approach to multiscale design, moving from a deterministic framework, to a probabilistic one, implementing the methods proposed in [31-33].

Acknowledgement

The authors wish to thank the National Research, Development and Innovation Office of Hungary (grant K 138615).

References

- [1] M. P. Bendsøe, O. Sigmund, *Topology Optimization: Theory, Methods and Applications*. Berlin: Springer, 2003
- [2] T. Lewiński, T. Sokół, C. Graczykowski, *Michell structures*. Berlin: Springer, 2018
- [3] O. Sigmund, K. Maute, “Topology optimization approaches: A comparative review”, *Struct. Multidiscip. Opt.*, Vol. 48(6), pp. 1031-1055, 2013
- [4] W. Zhang, J. Zhu, T. Gao, *Topology Optimization in Engineering Structure Design*. London: Elsevier; 2016
- [5] J. Lógó, H. Ismail, “Milestones in the 150-year history of topology optimization: A review”, *Comput. Assist. Methods Eng. Sci.*, Vol. 27(2-3), pp. 97-132, 2020
- [6] M. P. Bendsøe, N. Kikuchi, “Generating optimal topologies in structural design using a homogenization method”, *Comput. Methods Appl. Mech. Eng.*, Vol. 71(2), pp. 197-224, 1988
- [7] F. Ferrari, O. Sigmund, “A new generation 99 line Matlab code for compliance topology optimization and its extension to 3D”, *Struct. Multidiscip. Optim.*, Vol. 62, pp. 2211-2228, 2020
- [8] M. Kočvara, “Topology optimization with displacement constraints: A bilevel programming approach”, *Struct. Opt.*, Vol. 14(4), pp. 256-263, 1997
- [9] L. Yin, W. Yang, “Optimality criteria method for topology optimization under multiple constraints”, *Comput. Struct.*, Vol. 79(20-21), pp. 1839-1850, 2001
- [10] J. H. Rong, X. H. Liu, J. J. Yi, J. H. Yi, “An efficient structural topological optimization method for continuum structures with multiple displacement constraints”, *Finite Elem. Anal. Des.*, Vol. 47(8), pp. 913-921, 2011

- [11] A. Csébfalvi, “Volume minimization with displacement constraints in topology optimization of continuum structures”, *Int. J. Optim.*, Vol. 6(3), pp. 447-453, 2016
- [12] J. Lógó, B. Balogh, E. Pintér, “Topology optimization considering multiple loading”, *Comput. Struct.*, Vol. 207, pp. 233-244, 2018
- [13] W. Aichtziger, “Topology Optimization of Discrete Structures”, in *Topology Optimization in Structural Mechanics*, Rozvany G.I.N. Ed., International Centre for Mechanical Sciences (Courses and Lectures), Vol. 374, Vienna: Springer, 1997
- [14] O. Giraldo-Londoño, G. H. Paulino, “PolyStress: A matlab implementation for local stress-constrained topology optimization using the augmented lagrangian method”, *Struct. Multidiscip. Optim.*, Vol. 63(4), pp. 2065-2097, 2021
- [15] G. A. da Silva, N. Aage, A. T. Beck, O. Sigmund, “Three-dimensional manufacturing tolerant topology optimization with hundreds of millions of local stress constraints”, *Int. J. Numer. Methods Eng.*, Vol. 122(2), pp. 548-578, 2021
- [16] K. Svanberg, “Method of moving asymptotes - A new method for structural optimization”, *Int. J. Numer. Methods Eng.*, Vol. 24(2), pp. 359-373, 1987
- [17] P. W. Christensen, A. Klarbring, *An introduction to structural optimization*. Berlin: Springer, 2008
- [18] M. Bruggi, “A constrained force density method for the funicular analysis and design of arches, domes and vaults”, *Int. J. Solids Struct.*, Vol. 193-194, pp. 251-269, 2020
- [19] D. P. Bertsekas, *Nonlinear programming*, 2nd edn. Nashua: Athena Scientific, 1999
- [20] R. H. Zuberi, Z. Zhengxing, L. Kai, L. Wen, “Topological optimization of constant beam section under moving load condition”, *2010 International Conference on Mechanic Automation and Control Engineering*, pp. 354-359, 2010
- [21] S. Zhang, J. Yin, Y. Liu, F. Ma, Z. Sha, D. Yang, “Structural topology optimization of brake disc using the equivalent moving load method”, *J. Eng. Tech. Sci.*, Vol. 51(6), pp. 791-804, 2019
- [22] C. Talischi, G. H. Paulino, A. Pereira, I. F. M. Menezes, “Polygonal finite elements for topology optimization: A unifying paradigm”, *Int. J. Numer. Methods Eng.*, Vol. 82(6), pp. 671-698, 2010
- [23] K. Chandrasekhar, V. Bhikshma, S. Mohi, “On the Six Node Hexagon Elements for Continuum Topology Optimization of Plates Carrying in Plane Loading and Shell Structures Carrying out of Plane Loading”, *J. Appl. Comput. Mech.*, Vol. 6(3), pp. 617-639, 2020

- [24] R. Amaral, J. Borges, H. Gomes, “Proportional Topology Optimization under Reliability-based Constraints”, *J. Appl. Comput. Mech.*, Vol. 8(1), pp. 319-330, 2022
- [25] M. Zhou, G. I. N. Rozvany, “The COC algorithm, Part II: Topological, geometrical and generalized shape optimization”, *Comput. Methods. Appl. Mech. Eng.*, Vol. 89(1-3), pp. 309-336, 1991
- [26] T. Borrvall, J. Petersson, “Topology optimization using regularized intermediate density control”, *Comput. Methods. Appl. Mech. Eng.*, Vol. 190(37-38), pp. 4911-4928, 2001
- [27] B. Bourdin, “Filters in topology optimization”, *Int. J. Numer. Methods Eng.*, Vol. 50(9), pp. 2143-2158, 2001
- [28] F. Wang, B. Lazarov, O. Sigmund, “On projection methods, convergence and robust formulations in topology optimization”, *Struct. Multidiscip. Optim.*, Vol. 43(6), pp. 767-784, 2011
- [29] D. Briccola, M. Bruggi, “Analysis of 3D linear elastic masonry-like structures through the API of a finite element software”, *Adv. Eng. Softw.*, Vol. 133, pp. 60-75, 2019
- [30] B. Blachowski, P. Tazowski, J. Lógó, “Yield limited optimal topology design of elastoplastic structures”, *Struct. Multidiscip. Opt.*, Vol. 61(5), pp. 1953-1976, 2020
- [31] M. Bruggi, A. Taliercio, “Hierarchical infills for additive manufacturing through a multiscale approach”, *J. Optim. Theory Appl.*, Vol. 187(3), pp. 654-682, 2020
- [32] B. Balogh, M. Bruggi, J. Lógó, “Optimal design accounting for uncertainty in loading amplitudes: A numerical investigation”, *Mech. Based Des. Struct. Mach.*, Vol. 46(5), pp. 552-566, 2018
- [33] P. Tazowski, B. Blachowski, J. Lógó, “Topology optimization of elastoplastic structures under reliability constraints: A first order approach”, *Comput. Struct.*, Vol(243), n. 106406, 2021

Optimal Elasto-Plastic Analysis of Reinforced Concrete Structures under Residual Plastic Deformation Limitations

Sarah Khaleel Ibrahim, Majid Movahedi Rad*, Szabolcs Fischer

Széchenyi István University, Egyetem tér 1, 9026 Győr, Hungary
e-mail: sarah.khaleel.ibrahim@hallgato.sze.hu; majidmr@sze.hu;
fischersz@sze.hu

Abstract: In this study, an investigation regarding optimal elastic-plastic analysis method of different reinforced concrete (RC) structures is held by applying the residual plastic deformations limitations on the steel bars inside the reinforced concrete. Where different structures, including simple beam and slab, are selected as benchmarks and modelled numerically using ABAQUS in order to calibrate their experimental behaviour according to laboratory tests. Furthermore, concrete damage plasticity (CDP) constitutive model was applied to represent concrete behaviour in the numerical models considered. Then, an objective function was established for optimizing the applied plastic loads for each structure where the process of controlling plastic deformations was carried out by applying constraints on the complementary strain energy of the residual internal forces initiated inside the steel bars. This methodology was applied by authors by writing MATLAB code and linking it with ABAQUS to determine the corresponding applied plastic load for each entered complementary strain energy. Generally, applying optimization problem for each model showed that the complementary strain energy of the residual forces reflects the general behaviour of the structures and may be assumed as a constraint controlling the plastic behaviour of the structures whereas the obtained results indicated how structures acted differently when possessing different complementary strain energy values turning from elastic into elasto-plastic condition and then reaching plastic state.

Keywords: optimal analysis; non-linear elasto-plastic analysis; complementary strain energy; reinforced concrete beam; reinforced concrete slab; limited residual plastic deformations

1 Introduction

Composite steel-concrete structures represent an efficient and economical form of construction for building and bridge applications leading to economical and efficient structural solutions. Therefore, steel behaviour is carried out in different cases and investigations [1, 2, 3, 4, 5]. On the other hand, controlling steel deformation is one of the most typical problems within metals processing where the

influence of residual stresses on fatigue behaviour is regarded as an essential issue to control the steel behaviour. Over the last few years, an increasing number of investigations have been held out to understand the effects of residual stresses and deformations on mechanical performance, Christidis *et al.*, [6] proposed an efficient and simple method for specifying ultimate seismic displacements generated in steel frames caused by the residual deformation by investigating the non-elastic behaviour of various steel frames subjected to powerful ground movements. Therefore, based on comprehensive parametric investigations, observed equations are made to determine the seismic displacement that can be calculated after powerful seismic possibilities. And as a result, the usage of residual deformations could be effectively employed to estimate the performance status of steel structures after an earthquake. Generally, Residual stresses appear in numerous simulated structures and features so a large number of researches investigated this phenomenon. Gradually, various techniques have been created to calculate residual stress for diverse kinds of elements to get a dependable estimation. The different techniques have developed over many years and their applications have significantly aided by the growth of complementary methods like computing power and numerical methods. Rossini *et al.*, [7] classified the various residual stresses measuring techniques and provided a summary of some recent advancements to assist investigators in choosing their methods between destructive, semi-destructive, and non-destructive methods depending on the application and the availabilities of the methods. Considering extensive parametric research on structures with a single degree of freedom structures, Hatzigeorgiou *et al.* [8], constructed practical formulas for an uncomplicated and adequate calculation of the maximum seismic deformation using residual displacements, that can be computed after powerful seismic events.

As for concrete, it is major to understand the behavior of this essential material, that is why, different researchers considered studying concrete properties experimentally and numerically [9, 10, 11]. The concrete damaged plasticity model (CDP) is presently one of the considerable concrete models employed for concrete simulation in ABAQUS. This model was described theoretically by Lubliner *et al.* in 1989 [12] then developed by Lee and Fenves in 1998 [13]. Where the model basically illustrates that there are two damage mechanisms including tensile cracking and compressive crushing of concrete, where the stiffness of the material is decreased by two damage parameters, individually for tension and compression, also the yield function is defined according to Lubliner [12] while the flow potential is a hyperbolic function [14]. Michał and Andrzej, [15] used the concrete damaged plasticity model (CDP) for modeling reinforced concrete structures using ABAQUS software. Performing numerical simulations concerning uniaxial and biaxial compression and uniaxial tension of a sample concrete specimen to be compared with experimental results. While, Shafieifar *et al.*, [16] determined the tensile and compressive behaviour of ultra-high-performance concrete using the Concrete Damage Plasticity model (CDP) to define concrete performance in the absence of sufficient experimental data.

Plastic analysis and design methods are used when there are several engineering issues during the analysis and design of structures subjected to normal loads supplying details of the collapse and the post-yield behaviour benefiting in savings in materials. The optimal plastic design aims to make use of the plastic reserve of structures and to specify the optimal configuration of the material leading to a decrease in the overall weight or improving the load-carrying capacity. However, repeated plastic deformations and extreme residual displacements could be gathered and the structure might become unworkable. That is why limitations for the residual strains and displacements have to be involved in plastic analysis and design enabling the controlling of the plastic behaviour in structures.

As one of the oldest branches of mathematics, optimization theory catalyzed the development of geometry and differential calculus as it finds applications in a myriad of scientific and engineering disciplines [17, 18, 19]. Kaliszky and Logo, [20] presented three appropriate methods for the finding the optimal material form in the case of elasto-plastic structures under extreme loading. In meanwhile, Rohan and Whiteman [21] stated that the problem of optimal design belongs to a branch of the optimal control hypothesis that the control variable specifies the geometry of the issue aiming to find the shape of a compliant body so that an objective function reaches its minimum over an admissible set, where the general objective function affects both the state variables and the control variables as design parameters. As shape optimization for elastic deformation is easier than the elasto-plastic case, sensitivity analysis and optimization of elasto-plastic bodies are held as isotropic strain hardening takes place where the elasto-plastic behaviour of the material is controlled by a non-linear complementarity problem. Wang and Ohmori [22] utilized a cumulative elasto-plastic analysis approach forecasting the factor of the collapse load applied on a truss. The acquired factor of the collapse load is included in truss optimization used to develop the truss that keeps load-carrying capacity underneath standard load conditions and avoids collapse.

On the other hand, some applications of nonlinearity and concrete behavior were considered where Sae-Long et al. [23] suggested an efficient frame model with the inclusion of shear-flexure interaction for nonlinear analyses of columns normally presented in reinforced concrete (RC) frame buildings built prior to the introduction of modern seismic codes in the Seventies. While He et al. [24] considered the 3D printing procedure as a discontinuous control system and gave a straightforward and readable bond stress-slip model for a new and intelligent building 3-D printed concrete.

Besides, delivering a method for efficient prediction of areas in the structure as high stresses that lead to plastic deformation will occur. Where Strzalka et al. [25] proposed an investigation concentrated on the exploration of an efficient method for the a priori detection of a structural component's highly stressed areas. While an efficient method for the a priori detection of highly stressed areas of force-excited components was presented by Strzalka and Zehn [26], based on modal stress superposition. As the component's dynamic response and related stress are always

a function of its excitation, where certain attention is paid to the effect of the loading position.

This study aims to introduce a novel optimal elasto-plastic analysis method aiming to put the plastic behaviour of reinforced concrete structures under control by restraining the residual plastic deformations initiating inside the steel bars of two selected models, a reinforced concrete beam [27] and a reinforced concrete slab [28], employing complementary strain energy of residual forces which is considered globally displacement limitation. Thereafter, these chosen structures were numerically calibrated using ABAQUS and CDP model [14], which defines the concrete damage developed in the structures. The used method is extended from the work originally produced by Kaliszky and Lógó [29]. Generally, the work in this study includes considering an objective function to optimize the applied plastic load assuming that the complementary strain energy is a constraint controlling the plastic behaviour of steel bars. Then, the authors created a non-linear optimization programming code using MATLAB and this was connected to the numerical models calibrated in ABAQUS where residual stresses were calculated after running the code for each increment in order to achieve the optimal load values, after that, the complementary strain energy was calculated and a comparison with the allowed value set in the MATLAB code was considered to investigate the influence of the complementary strain energy on the plastic limit of structures loading bearing capacity.

The structure of this paper includes the numerical modelling procedure of the two benchmarks in Section 2, while Section 3 has a clear description of the limited residual plastic deformation approach applied on steel bars. Furthermore, Section 4 contains the formulations of the optimization problem, while Section 5 presents a summary of results and explanations of the optimized structures. Eventually, conclusions are demonstrated in Section 6.

2 Numerical Calibration of the Structures

2.1 Simple Reinforced Concrete Beam Case

Simply supported reinforced concrete beam model having concrete strength of 25 MPa was considered in this section [27]. The test programs consisted of manufacturing and testing RC beam with rectangular cross-section of 250 mm x 350 mm and a length of 2500 mm, under four-point load as displayed in Fig. 1 where the details of the chosen model S20-1 are clarified. Sequentially, this beam was calibrated by ABAQUS as indicated in Fig. 2 using the CDP model to define concrete behavior where a 3D eight nodes solid element (C3D8) was used to represent concrete, while the reinforcement bars were represented as a 3D beam element with a 2-node linear beam in space (B31). Consequently, crack patterns and

load-deflection curves were acquired as illustrated in Figs. 3 and 4, which clearly show that the numerical results are agreeing with the experimental results given by the study.

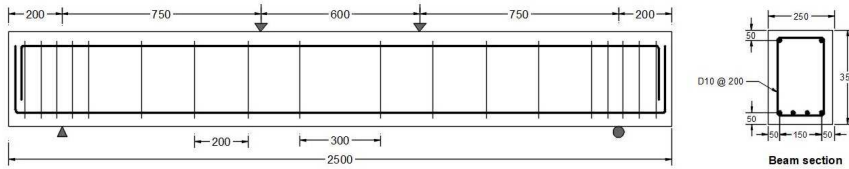


Figure 1
Details of S20-1 model

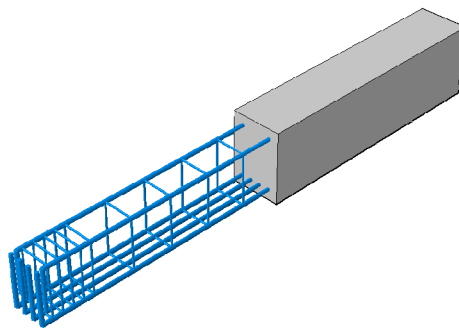


Figure 2
S20-1 numerical modelling

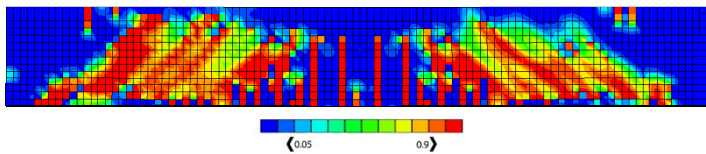


Figure 3
Crack patterns of S20-1 model

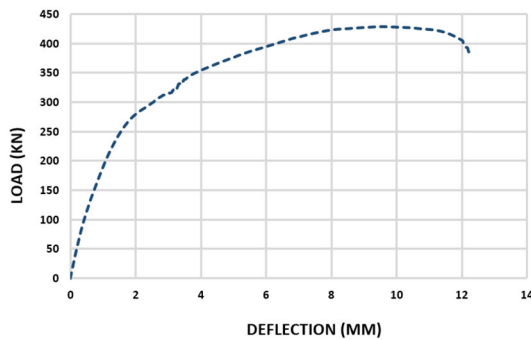


Figure 4
Load-Deflection relationship for S20-1 model

2.2 Reinforced Concrete Slab Case

In this section, a one-way reinforced concrete slab model (SP1) was considered [28] with 1750 mm in length, 700 mm in width, and 100 mm in depth. The slab was tested under two-point load with 500 mm load distance, and supported with a clear span of 1725 mm, also, the reinforcement bars were 8 mm in diameter. Fig. 5 shows the model properties where this model was calibrated using ABAQUS by applying a 3D eight nodes solid element (C3D8) to represent the concrete, while as the reinforcement bars were represented as a 3D beam element with a 2-node linear beam in space (B31) as shown in Fig. 6. As a result, crack patterns and load-deflection curves were obtained for the slab as displayed in Figs. 7 and 8, and these results are compatible with the experimental results offered by the study.

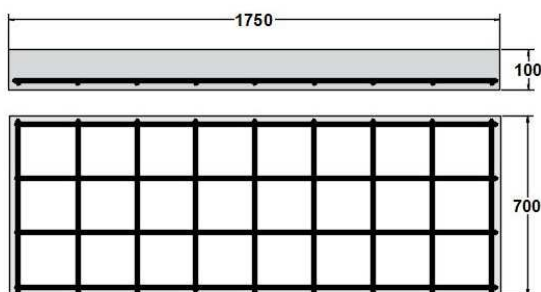


Figure 5
Details of SP1 model

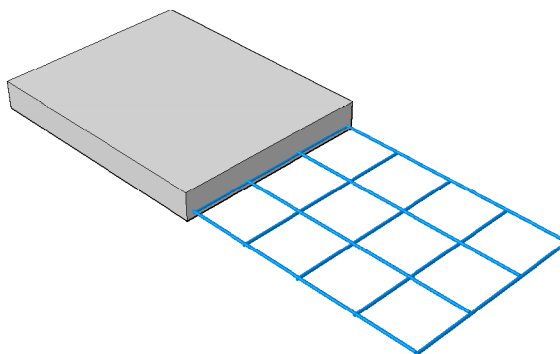


Figure 6
Numerical modelling of SP1

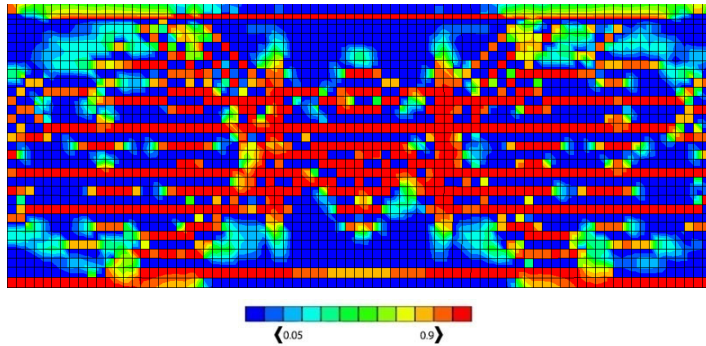


Figure 7

Crack patterns for SP1 model

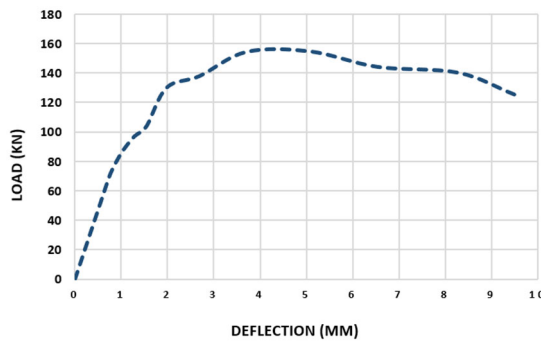


Figure 8

Load-Deflection relationship for SP1 model

3 Limited Residual Plastic Deformation Theory Applied on Steel Bars

Presenting the Euler notation, assume a body formed of elasto-plastic, time- and temperature-independent material with volume V and surface S . A part of S , S_u is under zero surface displacements, whilst the remaining part S_q , is under quasi-static surface tractions $q_i(t)$. The subsequent amounts regarding the surface tractions $q_i(t)$ are described at time t , as [30, 31]:

$\sigma_{ij}(t)$ = actual stresses,

$\epsilon_{ij}(t)$ and $u_i(t)$ = actual strains and displacements,

$\sigma_{ij}^{el}(t)$ = fictitious stresses that would occur if the material were purely elastic,

$\epsilon_{ij}^{el}(t)$ and $u_i^{el}(t)$ = fictitious elastic strains and displacements corresponding to $\sigma_{ij}^{el}(t)$, besides, the following different self-stress distributions are introduced:

$\sigma_{ij}^R(t)$ = actual residual stress distribution,

$\bar{\sigma}_{ij}^R$ = any arbitrary, time-independent self-stress distribution.

The real strain is divided into elastic and plastic parts, as shown in Eq. (1). Devoting the latest notation, the elastic strain parts are linked to real stresses by the constitutive law,

$$\epsilon_{ij} = \epsilon_{ij}^{el} + \epsilon_{ij}^{pl} \quad (1)$$

$$\epsilon_{ij}^{el} = C_{ijkl} \sigma_{kl}^{el} \quad (2)$$

As the plastic strain ϵ_{ij}^{pl} and the elastic tensor C_{ijkl} are expressed by the accompanied flow rule,

$$\epsilon_{ij}^{pl} = \lambda \frac{\partial f}{\partial \sigma_{ij}}, \quad \lambda \geq 0 \text{ if } f = 0 \text{ and } \dot{f} = 0, \quad \text{otherwise } \lambda = 0 \quad (3)$$

here $f(\sigma_{ij})$ is the yield function and $f(\sigma_{ij}) = 0$ defines a convex surface in the stress space.

Yet, the fictitious elastic stresses $\sigma_{ij}^{el}(t)$, the actual stresses $\sigma_{ij}(t)$, and the actual residual stresses σ_{ij}^R should fulfill the next relation:

$$\sigma_{ij}(t) = \sigma_{ij}^{el}(t) + \sigma_{ij}^R \quad (4)$$

here $\sigma_{ij}^{el}(t)$ is related to the fictitious elastic strain $\epsilon_{ij}^{el}(t)$ by the constitutive law,

$$\epsilon_{ij}^{el}(t) = C_{ijkl} \sigma_{kl}^{el}(t). \quad (5)$$

Assume the entire complementary plastic work $W_p(\tau)$ achieved during a load path from the undisturbed state at $t = 0$ up to $t = \tau$. This outcome could be regarded as an appropriate measurement in evaluating the plastic behaviour and general plastic deformation of an elasto-plastic body. Its upper bound can be acquired by the subsequent theory presented by Capurso [32, 33] and Capurso et al. [34, 35].

If any time-independent distribution of self-stresses $\bar{\sigma}_{ij}^R$ could be discovered so that the situation:

$$f(\sigma_{ij}^E(t) + \bar{\sigma}_{ij}^R) \leq 0 \quad (6)$$

is satisfied in V at any time $t \leq \tau$, then the total complementary plastic work is upper bounded by the condition:

$$W_p(\tau) \leq \frac{1}{2} \int C_{ijkl} \bar{\sigma}_{ij}^R \bar{\sigma}_{kl}^R dV. \quad (7)$$

It can be seen that the bound may be enhanced using the proper selection of $(\bar{\sigma}_{ij}^R)$ [32, 33]. Considering the bound on the complementary plastic work illustrated by Eq. (7). To stop excessive plastic deformations, set a suitably selected allowed W_{p0} on the plastic work W_p . The boundaries of the plastic deformations are defined by the existent residual stresses; i.e., it is assumed that:

$$\bar{\sigma}_{ij}^R \equiv \sigma_{ij}^R. \quad (8)$$

This assumption delivers a reasonable upper bound and permits a proper form of the issue. Thus, the plastic deformation constraint will be:

$$W_p(\tau) = \frac{1}{2} \int_V C_{ijkl} \sigma_{ij}^R \sigma_{kl}^R dV - W_{p0} \leq 0. \quad (9)$$

Consequently, a proper computational approach was suggested that the complementary strain energy of the residual forces may be described as a general measure of the plastic behaviour of structures whereas the residual deformations are needed to be restrained using boundaries for such energy amount. Eq. (9) were created regarding the case of bar elements, the complementary strain energy is calculated by the residual forces as the following:

$$W_p = \frac{1}{2E} \sum_{i=1}^n \frac{l_i}{A_i} N_i^R{}^2 \leq W_{p0} \quad (10)$$

where W_{p0} is a suitable permissible energy value for W_p and can be derived from the elastic strain energy of the structure (see, e.g., Kaliszky and Lógó [36]). Also, l_i , ($i = 1, 2, \dots, n$) represents the length of the member (bar elements), while the area of bar elements cross-section is represented by, A_i , ($i = 1, 2, \dots, n$) while N_i^R denotes the residual force of the bar members and E is Young's modulus of the material of bars. By applying Eq. (10), the plastic deformations of bar elements are limited as a suitable limited value W_{p0} is presented.

Besides, the residual forces N^R that held in the structure after finishing the unloading are introduced by the internal plastic force N^{pl} which will occur in the structure by applying the loading P_0 and the elastic internal force— N^{el} :

$$N^R = N^{pl} - N^{el} \quad (11)$$

where:

$$N^{el} = F^{-1} G^T K^{-1} P_0 \quad (12)$$

Where the flexibility matrix is represented by F ; whilst the geometrical matrix is denoted by G ; moreover, the stiffness matrix is represented by K . Mainly, this approach will be used on the steel bars used to reinforce the RC structures for controlling the plastic deformation developed within, nevertheless, the internal forces generated in the concrete are not counted during the optimization problem because of its weak contribution in tension if compared with steel.

4 Optimization Problem

The mathematical equation to determine the optimal load value of RC structures is arranged in this part. A non-linear optimization approach is proposed to obtain the maximum optimal plastic load (F^{pl}) applied to the selected models, employing the extremum plasticity principles, the step-by-step redeveloped constitutive elements are not needed. The next equations represent the elements employed in the optimization code where the purpose is to maximize the applied load (F^{pl}) whilst the plastic deformation is controlled (W_{p0} value) using the constraints provided, also, A_i and l_i describe the cross-section area and length of each steel element, respectively.

$$\text{Max.} \rightarrow F^{pl} \quad (13a)$$

$$\text{Subjected to: } N^{el} = F^{-1}GK^{-1}P_0; \quad (13b)$$

$$-\overline{N^{pl}} \leq N^{pl} \leq \overline{N^{pl}}; \quad (13c)$$

$$\frac{1}{2E} \sum_{i=1}^n \frac{l_i}{A_i} N_i^{R2} \leq W_{p0}. \quad (13d)$$

Eq. (13b) shows the estimation of the elastic fictitious internal normal forces developed in the steel elements, whilst the inequality Eq. (13c) indicates the lower- and upper-plastic limit conditions, whereas $\overline{N^{pl}}$ represents the ultimate plastic limit load. Furthermore, boundary Eq. (13d) shows the complementary strain energy of residual forces employed for controlling the plastic deformations in steel elements as a globally known measurement of plastic behaviour of the structures. Fig. 9 describes the procedure of the optimization problem as the CDP parameters used in the optimization problem are regarded constants.

Essentially, the boundary of plastic deformation employing complementary strain energy is used on steel bars located inside RC structures for controlling the plastic deformation developed within. However, the internal forces developed in the concrete are not included during the optimization process due to its weak contribution in tension in comparison with steel where it is comprehended that tension strain in steel is higher than tension strain in concrete that can drive the early collapse of concrete subjected to tension condition.

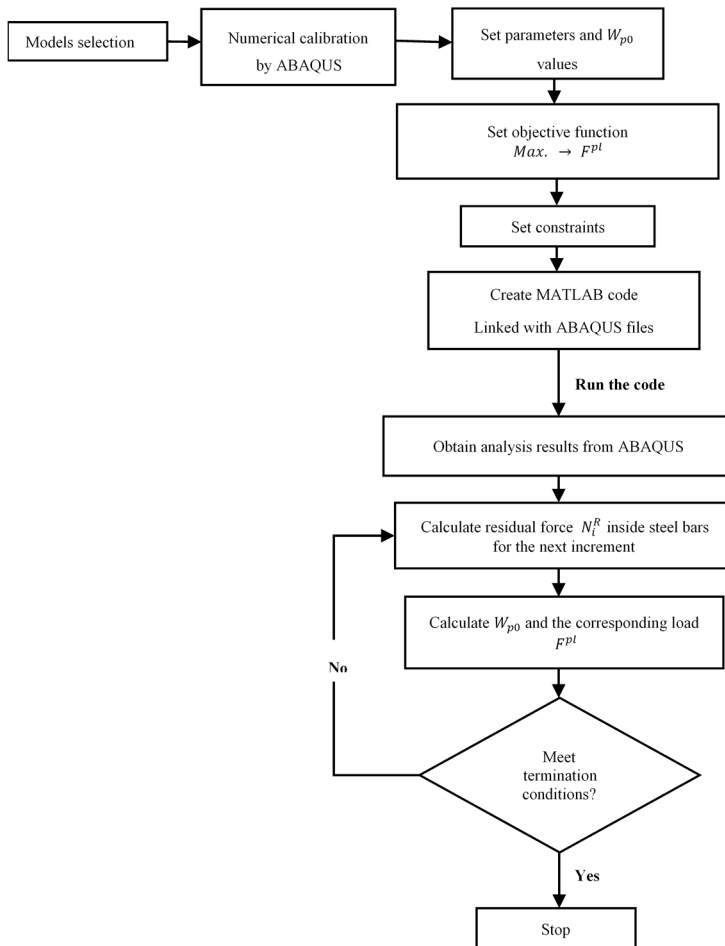


Figure 9
Optimization problem process

5 Results and Discussions

5.1 Simple Reinforced Concrete Beam Case

In this part, the results of having reinforced concrete beam are presented and discussed. Apparently, Fig. 10 displays the load- W_{p0} relationship for S20-1 beam noting that as W_{p0} value increases, the related load is increasing too showing a higher plasticity condition. When W_{p0} value is zero, the curve is within an elastic

state, nevertheless, the curve starts pushing towards the plastic state when W_{p0} value increases.

Additionally, Table 1 demonstrates steel stress intensity for the model assuming different cases of W_{p0} , and it is clear that the red spots that symbolize high-stress intensity in steel are increasing as W_{p0} value increases as the colour varies from blue (low-stress intensity in steel) into red (high-stress intensity in steel). Eventually, having such results proves the effectiveness of the complementary strain energy as a plasticity controller that makes it possible in expecting and controlling the plastic failure behaviour of the beam.

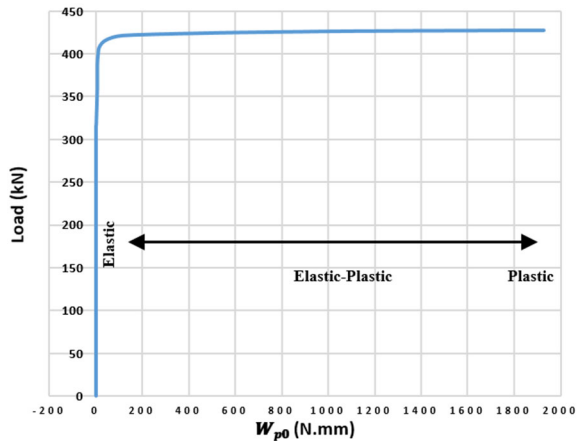
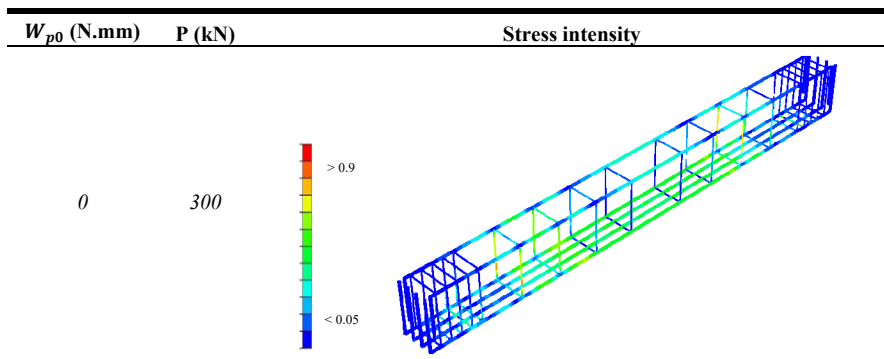
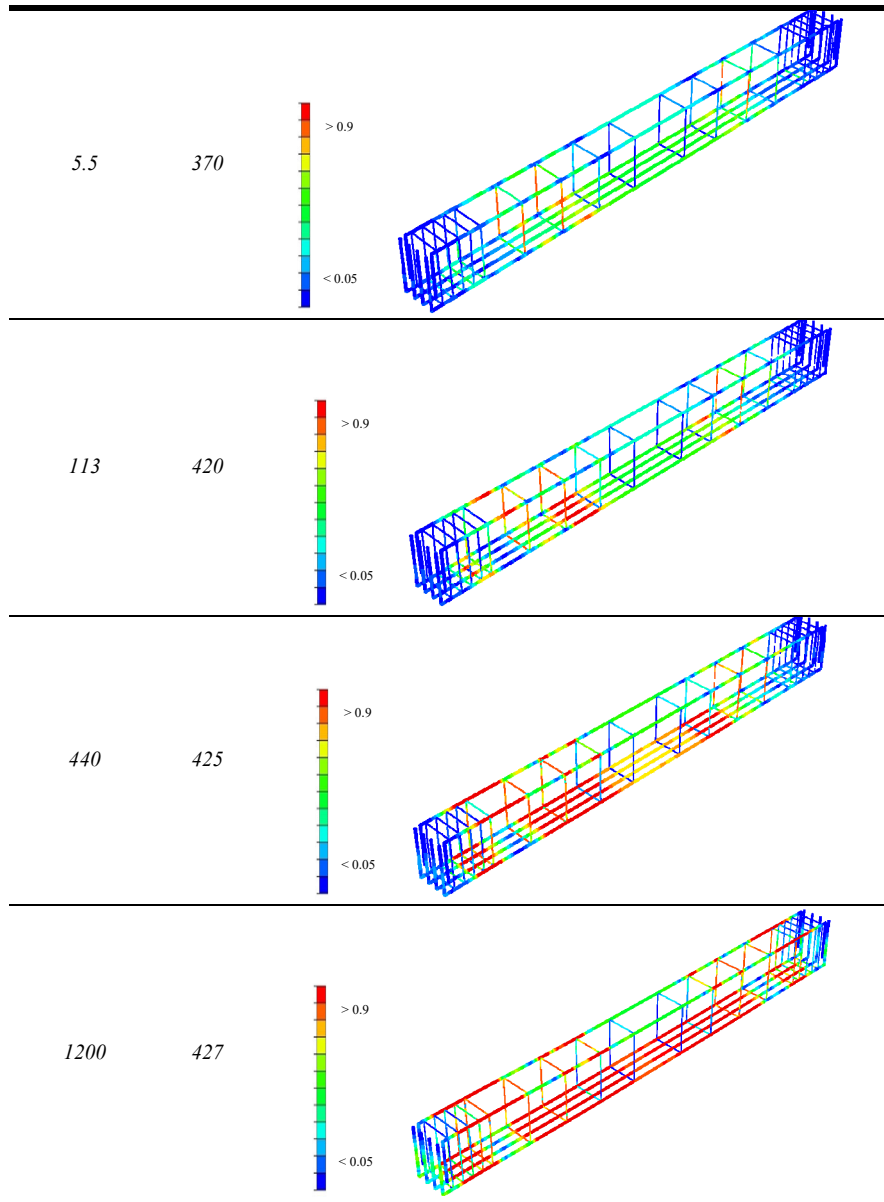


Figure 10
Load- W_{p0} relationship for S20-1 model

Table 1
 W_{p0} - load effect on the stress intensity of S20-1 model





5.2 Reinforced Concrete Slab Case

The results of having reinforced concrete slab are illustrated and discussed in this section where it is worth mentioning that the bars in the long direction are not yielded in this case as the slab is working as a one-way slab. Apparently, Fig. 11 shows the load- W_{p0} relationship for the selected slab noting that by the increment

of W_{p0} value, the corresponding load is increasing too indicating that higher plasticity state is acquired that when W_{p0} value is zero, the curve act in elastic condition, yet, the curve begins proceeding towards plastic state as W_{p0} value grows.

For more explanations, Table 2 displays steel stress intensity for SP1 model considering various possibilities of W_{p0} , and by comparison, it is detected that the red spots that shows high-stress intensity in steel, increase when W_{p0} value increases as the colour goes from blue (low-stress intensity in steel) into red (high-stress intensity in steel). So, having such outcomes proves the usefulness of the complementary strain energy as a plasticity controller which makes it likely in predicting and controlling the plastic failure behaviour of the slab.

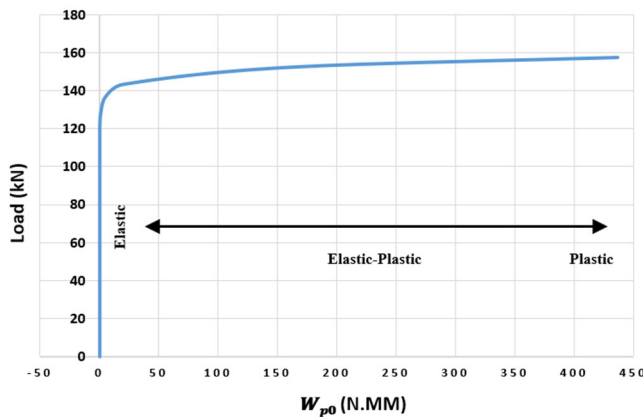
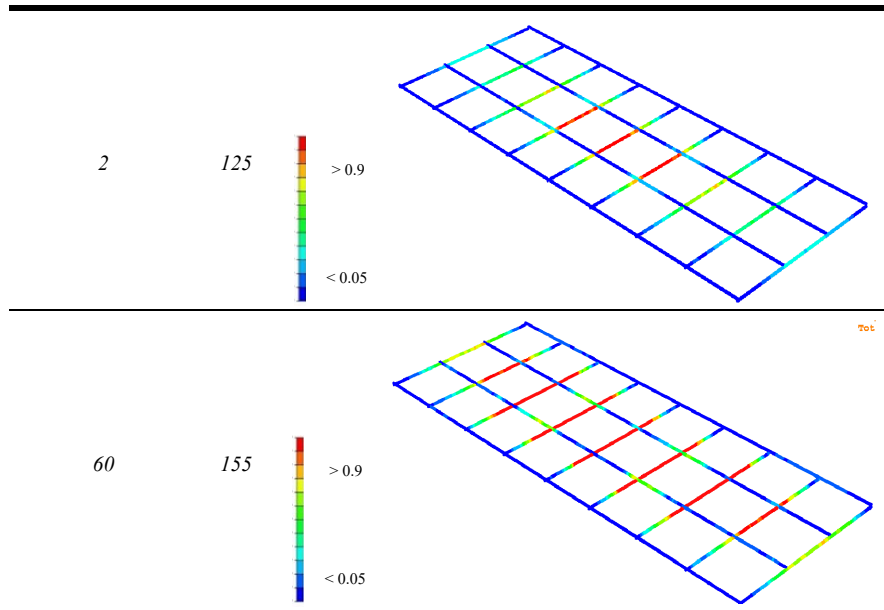


Figure 11
Load- W_{p0} relationship for SP1 model

Table 2
 W_{p0} - load effect on the stress intensity of SP1 model

W_{p0} (N.mm)	P (kN)	Stress intensity
0	70	



Conclusions

In this investigation, the optimal analysis problem of RC structures was studied. Thus, a numerical calibration process was carried out in order to validate the two benchmarks selected from earlier studies [27, 28] where the concrete damage plasticity (CDP) constitutive model was employed to define the behaviour of the used concrete. Sequentially, an optimization problem was used to maximize the plastic loading while controlling the plastic deformations by employing the complementary strain energy of the residual internal forces W_{p0} as a constraint. Eventually, different points were concluded whereas W_{p0} value increases, the corresponding load is increasing too indicating that a higher plasticity state is acquired. Moreover, when W_{p0} value is small, the curves are within elastic region, nonetheless, the curves start moving towards plastic region as W_{p0} value increases.

References

- [1] Kurhan, D., Kurhan, M. and Husak, M., 2020, November. Impact of the variable stiffness section on the conditions of track and rolling stock interaction. In IOP Conference Series: Materials Science and Engineering (Vol. 985, No. 1, p. 012005) IOP Publishing
- [2] Kurhan, M., Kurhan, D., Novik, R., Baydak, S. and Hmelevska, N., 2020, November. Improvement of the railway track efficiency by minimizing the rail wear in curves. In IOP Conference Series: Materials Science and Engineering (Vol. 985, No. 1, p. 012001) IOP Publishing

-
- [3] Mahmood, T., Haleemzai, I., Ali, Z., Pamucar, D. and Marinkovic, D., 2022. Power Muirhead Mean Operators for Interval-Valued Linear Diophantine Fuzzy Sets and Their Application in Decision-Making Strategies. *Mathematics*, 10(1), p.70
- [4] Kuchak, A. J. T., Marinkovic, D. and Zehn, M., 2021. Parametric investigation of a rail damper design based on a lab-scaled model. *Journal of Vibration Engineering & Technologies*, 9(1), pp. 51-60
- [5] Németh, A. and Fischer, S., 2021. Investigation of the glued insulated rail joints applied to CWR tracks. *Facta Universitatis, Series: Mechanical Engineering*, 19(4), pp. 681-704, <https://doi.org/10.22190/FUME210331040N>
- [6] Christidis, A. A., Dimitroudi, E. G., Hatzigeorgiou, G. D. and Beskos, D. E., 2013. Maximum seismic displacements evaluation of steel frames from their post-earthquake residual deformation. *Bulletin of Earthquake Engineering*, 11(6), pp. 2233-2248, <https://doi.org/10.1007/s10518-013-9490-z>
- [7] Rossini, N. S., Dassisti, M., Benyounis, K. Y. and Olabi, A. G., 2012. Methods of measuring residual stresses in components. *Materials & Design*, 35, pp. 572-588, <https://doi.org/10.1016/j.matdes.2011.08.022>
- [8] Hatzigeorgiou, G. D., Papagiannopoulos, G. A. and Beskos, D. E., 2011. Evaluation of maximum seismic displacements of SDOF systems from their residual deformation. *Engineering structures*, 33(12), pp. 3422-3431, <https://doi.org/10.1016/j.engstruct.2011.07.006>
- [9] Saberi Varzaneh, A. and Naderi, M., 2020. Experimental and Finite Element Study to Determine the Mechanical Properties and Bond Between Repair Mortars and Concrete Substrates. *Journal of Applied and Computational Mechanics*
- [10] Di Re, P. and Addessi, D., 2021. Computational Enhancement of a Mixed 3D Beam Finite Element with Warping and Damage. *Journal of Applied and Computational Mechanics*
- [11] He, C. H., Liu, C., He, J. H., Mohammad-Sedighi, H., Shokri, A. and Gepreel, K. A., 2021. A fractal model for the internal temperature response of a porous concrete. *Appl. Comput. Math*, 20(2)
- [12] Lubliner, J., Oliver, J., Oller, S. and Oñate, E., 1989. A plastic-damage model for concrete. *International Journal of solids and structures*, 25(3), pp. 299-326, [https://doi.org/10.1016/0020-7683\(89\)90050-4](https://doi.org/10.1016/0020-7683(89)90050-4)
- [13] Lee, J. and Fenves, G. L., 1998. Plastic-damage model for cyclic loading of concrete structures. *Journal of engineering mechanics*, 124(8), pp. 892-900, [https://doi.org/10.1061/\(ASCE\)0733-9399\(1998\)124:8\(892\)](https://doi.org/10.1061/(ASCE)0733-9399(1998)124:8(892))
- [14] Abaqus/CAE ver. 6-12.2, Dassault Systemes Simulia Corp., 2012

- [15] Michał, S. and Andrzej, W., 2015. Calibration of the CDP model parameters in Abaqus. World Congr. Adv. Struct. Eng. Mech.(ASEM 15), Incheon Korea
- [16] Shafieifar, M., Farzad, M. and Azizinamini, A., 2017. Experimental and numerical study on mechanical properties of Ultra High Performance Concrete (UHPC). *Construction and Building Materials*, 156, pp. 402-411, <https://doi.org/10.1016/j.conbuildmat.2017.08.170>
- [17] Tazowski, P., Blachowski, B. and Lógó, J., 2021. Topology optimization of elasto-plastic structures under reliability constraints: A first order approach. *Computers & Structures*, 243, p. 106406, <https://doi.org/10.1016/j.compstruc.2020.106406>
- [18] Blachowski, B., Świercz, A., Ostrowski, M., Tazowski, P., Olaszek, P. and Jankowski, Ł., 2020. Convex relaxation for efficient sensor layout optimization in large - scale structures subjected to moving loads. *Computer - Aided Civil and Infrastructure Engineering*, 35(10), pp. 1085-1100, <https://doi.org/10.1111/mice.12553>
- [19] Blachowski, B., Tazowski, P. and Lógó, J., 2020. Yield limited optimal topology design of elastoplastic structures. *Structural and Multidisciplinary Optimization*, 61(5), pp. 1953-1976, <https://doi.org/10.1007/s00158-019-02447-9>
- [20] Kaliszky, S. and Logo, J., 2006. Optimal design of elasto-plastic structures subjected to normal and extreme loads. *Computers & structures*, 84(28), pp. 1770-1779, <https://doi.org/10.1016/j.compstruc.2006.04.009>
- [21] Rohan, E. and Whiteman, J. R., 2000. Shape optimization of elasto-plastic structures and continua. *Computer Methods in Applied Mechanics and Engineering*, 187(1-2), pp. 261-288, [https://doi.org/10.1016/S0045-7825\(99\)00134-6](https://doi.org/10.1016/S0045-7825(99)00134-6)
- [22] Holzer, S. M. and Yosibash, Z., 1996. The p - version of the finite element method in incremental elasto - plastic analysis. *International journal for numerical methods in engineering*, 39(11), pp. 1859-1878, [https://doi.org/10.1002/\(SICI\)1097-0207\(19960615\)39:11<1859::AID-NME932>3.0.CO;2-7](https://doi.org/10.1002/(SICI)1097-0207(19960615)39:11<1859::AID-NME932>3.0.CO;2-7)
- [23] Sae-Long, W., Limkatanyu, S., Hansapinyo, C., Imjai, T. and Kwon, M., 2020. Forced-based shear-flexure-interaction frame element for nonlinear analysis of non-ductile reinforced concrete columns. *Journal of Applied and Computational Mechanics*. doi: 10.22055/jacm.2020.32731.2065
- [24] He, C. H., Liu, S. H., Liu, C. and Mohammad-Sedighi, H., 2021. A novel bond stress-slip model for 3-D printed concretes. *Discrete & Continuous Dynamical Systems-S*. doi: 10.3934/dcdss.2021161

-
- [25] Strzalka, C., Marinkovic, D. and Zehn, M. W., 2021. Stress mode superposition for a priori detection of highly stressed areas: Mode normalisation and loading influence
- [26] Strzalka, C. and Zehn, M., 2020. The influence of loading position in a priori high stress detection using mode superposition. *Reports in Mechanical Engineering*, 1(1), pp. 93-102, <https://doi.org/10.31181/rme200101093s>
- [27] Lee, J. Y., Choi, I. J. and Kim, S. W., 2011. Shear Behavior of Reinforced Concrete Beams with High-Strength Stirrups. *ACI Structural Journal*, 108(5)
- [28] Adam, M. A., Erfan, A. M., Habib, F. A. and El-Sayed, T. A., 2021. Structural Behavior of High-Strength Concrete Slabs Reinforced with GFRP Bars. *Polymers*, 13(17), p. 2997, <https://doi.org/10.3390/polym13172997>
- [29] Kaliszky, S. and Lógó, J., 1995. Elasto-plastic analysis and optimal design with limited plastic deformations and displacements. In: *Structural and Multidisciplinary Optimization*, ed. by N. Olhoff, G. I. N. Rozvany, Pergamon Press, 465-470
- [30] Rahmanian, I., Lucet, Y. and Tesfamariam, S., 2014. Optimal design of reinforced concrete beams: A review. *Computers and Concrete*, 13(4), pp. 457-482
- [31] Kaliszky S. Elastoplastic analysis with limited plastic deformations and displacements. *Journal of Structural Mechanics*. 1996, 24(1):39-50, <https://doi.org/10.1080/08905459608905254>
- [32] Capurso M. A displacement bounding principle in shakedown of structures subjected to cyclic loads. *International Journal of Solids and Structures*. 1974, 10(1):77-92, [https://doi.org/10.1016/0020-7683\(74\)90102-4](https://doi.org/10.1016/0020-7683(74)90102-4)
- [33] Chutani, S. and Singh, J., 2017. Design optimization of reinforced concrete beams. *Journal of The Institution of Engineers (India): Series A*, 98(4), pp. 429-435
- [34] Capurso M, Corradi L, Maier G. Bounds on deformations and displacements in shakedown theory. *Proc. Materiaux et Structures sous Chargement Cyclique*. Palaiseau. ass. amicale des ingénieursanciens élèves de l'E.N.P.C., Paris, France. 1978, 231-244
- [35] Tin-Loi F. Optimum shakedown design under residual displacement constraints. *Structural and Multidisciplinary Optimization*. 2000, 19(2):130-139, <https://doi.org/10.1007/s001580050093>
- [36] Kaliszky S, Lógó J. Optimal plastic limit and shake-down design of bar structures with constraints on plastic deformation. *Engineering Structures*. 1997, 19(1):19-27

Entropy Application for Simulation the Ballast State as a Railway Element

Dmytro Kurhan

Department of Transport Infrastructure, Ukrainian State University of Science and Technologies, Lazaryan st. 2, 49010 Dnipro, Ukraine; d.m.kurhan@ust.edu.ua

Abstract: The purpose of the paper is to develop methods of entropy application for simulation of the ballast layer operation of a railway track in the tasks of predicting and controlling the service life. The author developed a method for determining the entropy of the ballast layer as an element of a railway track through calculations of the mechanical work performed by ballast as a result of the reaction to an external load. To determine the array of stresses and deformations operating in the ballast layer space, the spatial model of the stress-strained state of a railway track based was used on the elastodynamic problem. The major part of the developed method is supplemented by the technique of assessing the entropy of a system according to the deviation measuring results in its geometric position. The geometric position of a railway track was measured by a track renewal train. Files archiving to determine the randomness of data recorded in them were carried out using the LZMA algorithm. The tasks of predicting and controlling the service life of ballast have been further developed. The usage of entropy has allowed simulating the ballast degradation as a random process that depends on cyclic stresses and deformations arising in ballast from rolling stock. For the first time, the method of assessing the quality of the track surfacing through the entropy of the ballast layer is proposed. The developed mathematical tool may be used to compare the service life of ballast in various operating conditions, which allows optimizing consistency between the track design and parameters of train movements.

Keywords: railway; ballast; entropy; stress-strained state; track state

1 Introduction

The railway track, like any engineering structure, has a certain operational resource. Forecasting resource exhaustion is a key tool for planning the frequency of repairs, organizing current maintenance, and, in general, establishing reasonable operating conditions that could meet both the technical capabilities of the railway and economic feasibility.

At present, the main criterion for justifying the compliance of the railway structure with the operating conditions and forecasting inter-repair time is the passed tonnage. However, this approach does not take into consideration the structure of the train flow and excludes the possibility of assessing the impact of certain categories of trains. It is clear that there are cases when, with the same general load intensity, the impact of rolling stock on the track, and, accordingly, the timing of the disorder in its elements, would be different. First of all, it concerns main directions with the movement of passenger trains at high speeds, or freight trains with a large axle load, or tracks at industrial enterprises with special-purpose rolling stock.

To take such features into consideration, there is a need to substantiate the appropriate estimation tool.

2 Statement of the Problem

Today, there is a wealth of experience in scientific research on the issues related to diagnosing, estimating, and forecasting the state of the railway track. Thus, works [1-3] provide a fairly detailed overview of such studies with their advantages and disadvantages.

Given that the section of a railway track has uniform design characteristics and established operating conditions at a large length, the occurrence of deviations in its condition can be considered as a random process subordinated to the law of large numbers.

Methods of probability theory in the research of railway operations are increasingly used. It is shown in [4] that the accuracy of the source data has a significant impact on the results of the forecast of the geometric state of the track. Most often, specially equipped track measuring cars are used to measure the geometry of the track. They produce a large amount of information, but both the mechanics of its acquisition and subsequent mathematical processing algorithms lead to a certain uncertainty of the full-on position of the track, which necessitates the application of approaches from probability theory.

Current procedures for predicting failures of the railway track should take into consideration the likelihood of the appearance of a particular event, which makes it possible to reduce operational risks [5].

Taking into consideration various factors, including those of a random nature, makes it possible to devise system methods for optimal management of a transport enterprise. Thus, work [6] proposed an approach to determining the effective management system of a transport enterprise on the example of mining and metallurgical companies based on the theory of mass service.

The presence of changes in the state of the track directly affects its interaction with the rolling stock. This is especially true of difficult operating conditions, for example, for braking processes along sections with significant slopes [7].

Some general approaches to describing deviations in the geometry of the track using the normal law of distribution of random variables are shown in work [8]. Of the elements that make up the upper structure of the railway track, probably more difficult in terms of forecasting the state change over time is a ballast layer [9, 10]. Thus, the rail, with an adequacy enough for most problems, can be described as a homogeneous beam that works at bending. Reinforced concrete sleeper transfers the load from the rail to the ballast almost without compression or bending and has the largest established service life among other elements of the upper structure of the track. Deformation of the ballast layer as a loose material [11, 12], when working under load, is more difficult – due to the elastic movement of individual particles, which leads to their gradual destruction and mixing [13]. That causes changes in elastic properties in some places and, as a result, leads to uneven deflection and the formation of residual strains [14]. Irregularities in the ballast layer are reflected at the position of the rail-sleeper mesh and form indentation in the geometry of the track in general.

Deviations in the vast majority do not appear as a result of stress outside the permissible ones but are the result of fluctuations induced by relatively small but repeated loads. The measure of system order violation due to such random fluctuations can be described through entropy.

Entropy makes it possible to numerically determine the state of the system and predict its "aging". This approach is used in many areas [15-17].

The author of the paper [18] provides a justification for determining the entropy of the railway track as a system in general, by calculating mechanical work. However, the issue of the detailed description to transition to the likelihood of destruction and service life of individual elements, such as the ballast layer, and the question of determining entropy by natural geometric deviations remain unresolved.

To calculate the entropy of the full-on position of the system, it is necessary to determine the probabilities of all possible variations of its condition. With the increase in the size of the system, the complexity of the problem quickly increases, and, for most cases, solving it is impossible even for modern computing devices. In work [19], a creative solution to such a problem was proposed and substantiated. The authors of the cited work proved that the entropy of the system is proportional to the degree to which it is possible to compress a lossless byte sequence describing the predefined system configuration through discrete levels of connections of all degrees of freedom. That proves the uniformity of the approach to modeling the development (aging) of systems through entropy for various industries: from gas thermodynamics to solid-state physics, biology, chemistry, as well as information applications. The procedure proposed in [19] can be used,

with a certain adaptation, as one of the elements in the entropy calculations of railway tracks.

3 Methods and Results

The condition of the track can be estimated according to different criteria. For most problems, they primarily include the geometric deviations of an actual position of the track elements relative to the values set by the project. The main ones are the position of the rail threads in the horizontal plane (plan), in the vertical plane (sagging), the width of the track, and the mutual position of rail threads in the vertical plane (distortions). These indicators refer to those that are restored during the relevant repair work and do not require direct replacement of elements of the railway track. The list of indicators reflecting the condition of the track includes another group: the wear of rails, damage to fasteners, destruction of sleepers, ballast layer diseases (clogging, abrasion of gravel, uneven sealing). Some of these deviations can be attributed to partially restorable by executing special operations (for example, grinding rails, cleaning ballast), while the elimination of others is possible only through replacement. All indicators that characterize the state of the track, either directly or indirectly are reduced to a set of linear geometric characteristics at the level of several units or several tens of millimeters. Depending on the operating conditions established in a given section, regulatory documents regulate the permissible values of such deviations. The presence of deviations to certain established limits would determine the serviceable state of the track that is, one that does not require operational restrictions. Further increase in the level of deviations would lead to the transition to a partially working state when a further operation could be possible with certain restrictions (usually the permissible speed of movement). Large values of deviations can lead to an inoperable state when further operation without their elimination is not allowed due to a threat to traffic safety. Carrying out timely scheduled repairs and proper current maintenance of the track typically makes it impossible for an inoperable state to occur, except for sudden failures such as, for example, breaking the rail.

For each of these indicators, the state of the track can be described as a set of values of its geometric position, measured in a certain step $\{\omega_i\}$, where the difference of ω_i from zero would show the level of deviation. Most deviations would be within a certain range. The presence of individual deviations beyond its boundaries is possible but their probability is insignificant $P(\omega_i \in [-\varepsilon; \varepsilon]) \rightarrow 1$, where ε is the permissible level of deviations in accordance with the established speed of movement. Then there should be an average deviation indicator

$$\exists \mu : \sum_{i=1}^n |\omega_i - \mu| = 0 \quad (1)$$

Taking into consideration the design and operation of the railway track $\mu \in \varepsilon$, based on expression (1) $P(\omega_i \approx \mu) = \max$, the further process of development of deviations mainly occurs due to an increase in μ and only to some extent due to an increase in ε .

A set of values that reflects the state of the track can be represented in a discrete form

$$\Omega \in \left\{ \delta \left[\frac{\omega_i}{\delta} \right] \right\}, \quad (2)$$

where δ is the smallest difference in the geometric position of the track.

Then the indicator of its condition may be the weight of such a set

$$Z = \sum \left[\frac{\omega_i}{\delta} \right]. \quad (3)$$

The process of further degradation of the section of the railway track can be described as

$$Z_t = Z_{t-1} + \delta f(t, P), \quad (4)$$

where $f(t, P)$ is the function that shows how many discrete deviations can be added, as a result of the next external action, taking into consideration the probability that not all potential residual deformations will be implemented.

The above definitions of gradual degradation of the railway track match the principle of entropy.

In a general form, the entropy of the system is described by the following equation

$$S = k_1 \ln W, \quad (5)$$

where k_1 is the coefficient showing elementary entropy (in the classical approach – a Boltzmann constant); W is the weight of the system state, namely the number of micro conditions (variations of the interaction of its elements), corresponding to the general macrostate of the system. That is $Z \equiv W$, or, in other words, the set Ω with a metric Z is one of the possible implementations of the state of the system with entropy S , and $\Delta Z = f(\Delta S)$.

Further considerations will apply to the ballast layer as the most complex but also the most indicative element of the railway track as part of this study.

Violations of the state of ballast under the influence of external load can be considered changes in the integrity of this layer as a system that perceives pressure from sleepers and, reacting with elastic strains, transfers it to the soil bed. Such changes occur both directly due to the destruction of gravel and due to the irreversible movement of its particles. An event in which mechanical violations should be observed is an excess of permissible stresses. However, it is known that the destruction of connections between the particles of ballast and even the degradation of gravel has also happened at a much lower level of stress.

As an elementary component of external action, it is appropriate to adopt the travel of one wheel along the track. A one-time application of such a load, and at the level of stresses that do not reach the permissible values, cannot lead to the occurrence of residual deformations. However, having dozens of wheelsets in each train, dozens of trains running per day, and several years of operation, researcher shall obtain the transformation of some minor fluctuations into significant geometric irregularities.

If researcher consider a specific cross-section of the section, taking into consideration its isotropic length along the track and meeting the condition of non-exceeding permissible stresses, the occurrence of an irregularity in this very cross-section is almost zero. With an increased length of the observed section, the frequency of deviations would approach the theoretical probability predetermined by entropy. Thus, there is no exact mapping of the calculated entropy into a set that recognizes the state of the section ($S \rightarrow \Omega$), although the number of such mappings is finite and depends on W . But for the set tasks of comparing the operating conditions over a sufficiently long period, it is possible to predict changes in the state of the section (equation (4)) relative to the increase in entropy (ΔS).

A ballast layer can be described as a set of objects; their number would depend on the degree of detail of the model. Each element has several degrees of freedom of potential change in position relative to the project, related to movement, rotation, or 3D strain. Such a system works on the perception of the load transmitted to it by other elements of the railway track from the rolling stock; its entropy then would depend on a change in internal energy, which can be expressed through mechanical work. The increase in entropy (ΔS) is proportional to a change in the energy of the system exerted by external influence (δQ)

$$\Delta S = k_2 \delta Q, \quad (6)$$

where k_2 is the proportionality coefficient (for Boltzmann entropy – the value opposite to the temperature value).

The equivalent of a single energy change cycle to be adopted is the mechanical work of the ballast cross-section (A^*) when one wheel travels over it (t)

$$\delta Q = k_3 \int_t A^*(t) dt, \quad (7)$$

where k_3 is the proportionality coefficient; for the elements of the railway track, accepted to equal 0.066 [18].

The mechanical operation of the system is defined as the sum of mechanical works of each element, which describe the ballast layer when modeling its stressed-strained state

$$\begin{aligned} A^* &= \sum A_i; \\ A_i &= f(\sigma_i, \varepsilon_i). \end{aligned} \quad (8)$$

where σ_i, ε_i are, respectively, the stresses and elastic deformations of the i th element of the ballast layer.

Then the state of the system after a certain period of operation over years (T) can be determined as follows

$$\begin{aligned} W &= e^{k_3 A}; \\ A &= 365T \sum_j N_d N_c N_w \sum_i \int_t f(\sigma_{ij}, \varepsilon_{ij}, t_j) dt \end{aligned} \quad (9)$$

where N_w is the number of wheelsets in a railway car; N_c is the number of cars of the j -th type; N_d – the number of trains with such cars per day.

The above approach is convenient to use to compare variants of different train flows. If the base variant has a term of operation (T_0), then, for an alternative, it can be determined through the following ratio of system states

$$T_x = T_0 \frac{W_0}{W_x} \quad (10)$$

or

$$T_x = T_0 e^{k_3(A_0 - A_x)} \quad (11)$$

To determine the stressed-strained state of the ballast layer, an arbitrary mathematical model can be used, which makes it possible to obtain the necessary array of data $\{\sigma_i, \varepsilon_i, t\}$ with details sufficient for the problem being solved. For further research, within the framework of this work, a model of the stressed-strained state of the railway track was used, based on the dynamic problem of elasticity theory whose basic provisions are given in works [20, 21]. The feature of this model is the calculation of dynamic stresses and deformations using the propagation of elastic waves through the objects of the railway track. The sites of the application of external load are used to start building a set of vectors in all

directions of the semi-space. The results of calculations according to such a mathematical model are the values of stresses and deformations, required for equation (9), for each time step.

Typically, a train flow moving along a given section of the railway track consists of trains that have different set speeds, weight, length, etc. This is especially inherent in mainline tracks. Moreover, this difference is not limited to simple separation into passenger and freight traffic. Both freight trains can have different purposes, different cargo, and, accordingly, different loads on the axle and other characteristics, and passenger trains can be divided into intercity, high-speed, and others. It is known that the introduction of trains in the train flow, which differ from others by the increased axle load or speed, increases the intensity of accumulation of residual deformations of the tracks, despite the fact that the stresses from their wheels in the elements of the track do not exceed the permissible values, and the total volume of transportation (cargo intensity) does not change significantly. Our method makes it possible to take into consideration such differences to some extent.

As an illustration, let us consider a problem on comparing the operational time of a ballast layer for different variants of the train flow using a numerical example.

Author accept that the train flow consists of freight cars (with an axle load of 18 t/axle, 42 cars per train) and passenger trains (15 cars per train), moving at speeds of 80 km/h and 120 km/h, respectively. Option 1: 25 freight and 8 passenger trains per day. Option 2: 16 freight and 40 passenger trains per day. The initial data are simplified and selected in such a way that both options could produce a load capacity of 30 million tons gross per km per year, which implies the same inter-repair terms.

The following structure of a railway track is adopted: rails UIC60; reinforced concrete sleepers; gravel ballast with a thickness of 0.5 m with a deformation module of 200 MPa; soil bed with a deformation module of 35 MPa. With the specified composition, the general module of deformation of the under-rail base obtained was at the level of 52 MPa.

The results of calculations according to the proposed method for both options, such as the values of stresses and mechanical work in the elements of the ballast layer, are shown in Figs. 1-4. The stress plots demonstrate the maximum values – when the wheel is passing directly above the estimated cross-section. The plots of mechanical work show the total values when a wheel travels over the estimated cross-section from the beginning of the track deflection, when the wheel is at a certain distance, to the end of the action when the wheel has already traveled further by a symmetrical distance.

The calculation results corresponding to the values of stresses in cross-section (Figs. 1 and 2) and mechanical work (Figs. 3 and 4) are given on the same scale for the possibility of comparing the effect exerted by a freight car and passenger

car both in terms of values and quality. The difference is observed not only in the absolute values of stresses in the elements of the track (in this case, in the ballast layer) but also in the propagation of stresses in different zones.

According to the calculations according to equation (9), the total annual mechanical work of the ballast layer cross-section would equal 20.78 MN·m and 16.20 MN·m for the first and second options, respectively. Then, equation (11) can be represented as a ratio $T_2 = 1.35T_1$. Thus, for the considered initial data for option 2 of the train flow (dominated by passenger traffic), the accumulation of residual deformations in the ballast would occur 35% slower.

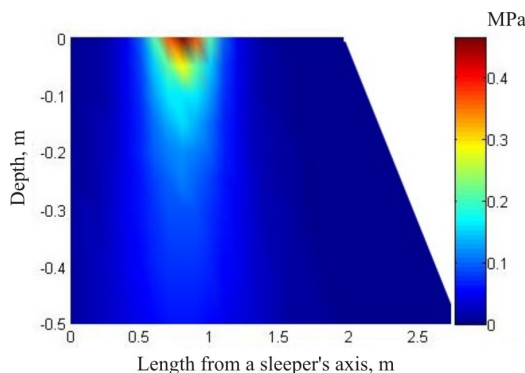


Figure 1

Propagation of maximum vertical stresses in the ballast induced by a freight car wheel in cross section (18 t/s, 80 km/h)

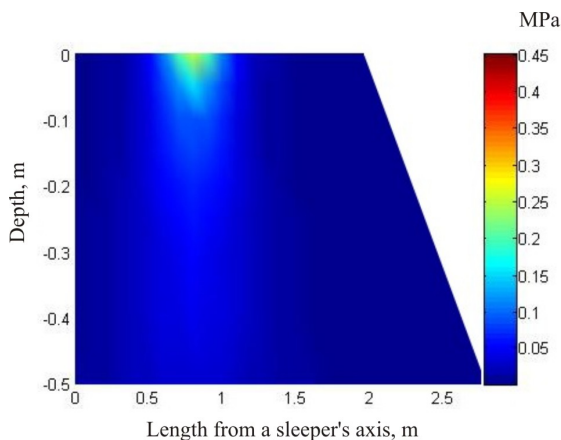


Figure 2

Propagation of maximum vertical stresses in the ballast induced by a passenger car wheel in cross section (120 km/h)

Entropy can be used not only for forecasting tasks but also to assess the current state of the system or the quality of repair work. However, the problem of calculating the entropy of a complex system based on its condition has no direct unambiguous solution.

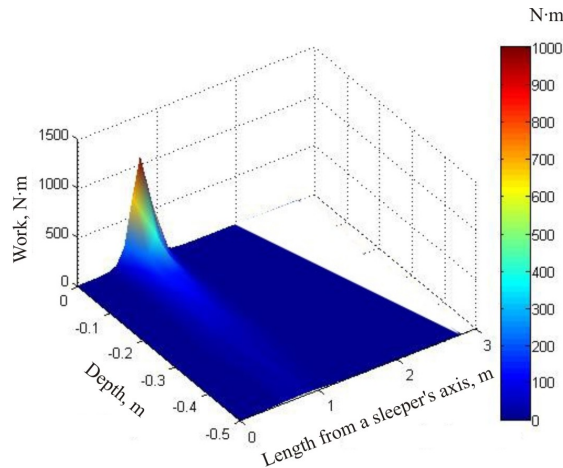


Figure 3

Distribution of mechanical work in the ballast cross-section space induced by a freight car wheel

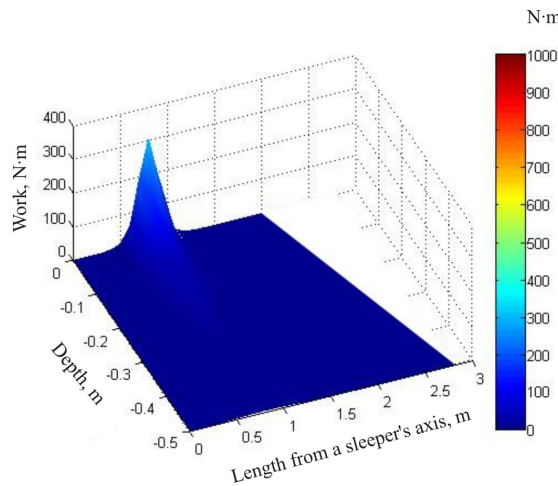


Figure 4

Distribution of mechanical work in the ballast cross-section space induced by a passenger car wheel

A hypothesis is proposed in [19] that such a problem can be solved by switching to information entropy. To this end, one determines the number of degrees of freedom of the system (D), as minimally sufficient, given the number of elements of which it consists, their possible fluctuations, and ties. Each degree of freedom

is described by the required number of discrete states (n_s). A set of states of all degrees of freedom is converted to a chain of numbers (bytes). A file that is a sequence of such bytes is archived without data loss. According to the authors of work [19], the degree of archiving does reflect the entropy of the system, given that the size of the archive depends on the chaoticity of the data

$$S = \frac{CFS - ZFS}{RFS - ZFS} K_1 D \text{Log} n_s, \quad (12)$$

where CFS is the size of the archive file describing the state of the system; ZFS is the archive of the file, in which all degrees of freedom are in zero position (the system is in a state of minimal entropy); RFS is the archive of the file with "white noise" – all degrees of freedom have a random value from the possible ones (the system is in a state of maximum entropy).

This approach does not contradict the understanding of ballast entropy, given that the deterioration of its condition should be characterized precisely by the unevenness of deviations of adjacent elements while uniform compaction (loosening) is not reflected in the irregularity of the track.

Irregularities in the ballast layer can be tracked for deviations in the vertical position of the rail. There are machine-based means for measuring this value along the section – by a track measuring car or a straightening-tamping machine. Paper [22] provides an example of such an entry before and after the track correction. Based on these examples, Fig. 5 shows ballast deviations in a vertical plane along a 500-m long section. The array has 800 points, the distance between points is 0.625 m.

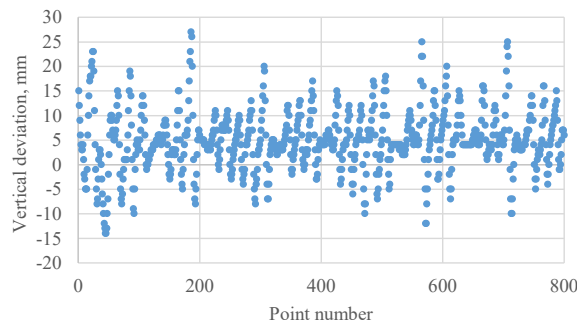


Figure 5

Registering track deviations in a vertical plane

The data given in Fig. 5, consisting of a sequence of deviations in the position of the track, indirectly reflect the position of the rail in the vertical plane. For the correct perception of the picture, it should be noted that the horizontal and vertical scales vary greatly – variations in the range from -15 mm to +30 mm (vertical axis) occur along a 500-m long section (horizontal axis). That is, the considered section has certain deviations but, in general, its profile is quite even.

To create files according to equation (12), the position of each point was written in one byte with a sampling level of 1 mm through the conversion $[-127...128] \rightarrow [0...255]$. The LZMA algorithm was used for archiving. Given that ballast is considered as a system that obeys the law of large numbers and has approximately the same state in its length, the sample size should ensure that the ratio of data archiving is approximated to a constant value, Fig. 6.

If researcher talk about the correction and not about repairs with a complete replacement of the upper structure of the track, then its execution does not imply the return of the outline of the section to the design position. This is due to the inability to significantly lower the level of the track, which requires cutting ballast, and other technical limitations of track machines. Thus, the correction work requires preliminary calculations, which are the solution to the optimization problem of finding a compromise between the quality of the track outline and the magnitude of its displacement, with restrictions on ballast volumes, machine capabilities, and others. Such an optimization problem does not have an unambiguous solution, and, therefore, requires the existence of a method for assessing the position of the track both at the stage of calculations and immediately after work.

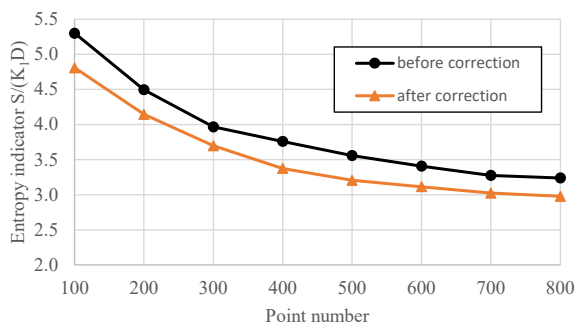


Figure 6

Entropy indicator dependence on a sample size

Figure 6 shows, in addition to entropy calculations for the data reflecting the actual state of the section before the correction (Fig. 5), the corresponding results for the state of the section after correction.

The method of correction and the numerical data on its application are given in [22]. Regarding the example under consideration (Fig. 6), it can be concluded that the entropy of the ballast is reduced after correction. According to equation (11), its lifetime has been restored by $e^{(3.238-2.977)}T_0 = 1.298T_0$, that is, by 30% of the base operating life.

Conclusions

This paper reports the devised method for determining the entropy of the ballast layer as an element of the railway track using the calculations of mechanical work performed by the ballast as a result of a reaction to an external load. The main part of the devised method is supplemented with the procedure for estimating the entropy of the system according to the results of measuring deviations in its geometric line.

Thus, the tasks of forecasting and managing the lifetime of the ballast have been advanced. The use of entropy has made it possible to simulate ballast degradation as a random process, depending on cyclic stresses and deformations that arise in the ballast due to rolling stock. A procedure for evaluating the quality of track correction through the entropy of the ballast layer has been proposed for the first time.

The built mathematical toolset can be used to compare the resource of ballast operation under different operating conditions, which makes it possible to optimize the correspondence between the track design and train traffic indicators. This is of particular importance under difficult operating conditions: high-speed passenger traffic, excessive weight of freight trains, specialized trains of industrial enterprises. This paper gives a numerical example of comparing the resource of ballast work for two variants of the train flow, which are identical in cargo intensity but significantly differ in the ratio of passenger and freight traffic.

As part of the initial data of the considered example, it was concluded that when passenger traffic dominates, the accumulation of residual deformations occurs 35% slower.

A numerical example of the use of entropy to assess the quality of track correction is also provided. Along the considered section, the correction operation was carried out by the VPR-02 machine according to the procedure proposed in [22]. The assessment showed that after the correction, the entropy of the ballast decreased, which increased the resource of its operation by 30%.

References

- [1] N. Elkhoury, L. Hitihamillage, S. Moridpour, D. Robert. Degradation Prediction of Rail Tracks: A Review of the Existing Literature. *The Open Transportation Journal*, Vol. 12(1), 2018, pp. 88-104, <https://doi.org/10.2174/1874447801812010088>
- [2] A. De Melo, S. Kaewunruen, M. Papaelias, L. Bernucci, R. Motta. Methods to Monitor and Evaluate the Deterioration of Track and Its Components in a Railway In-Service: A Systemic Review. *Frontiers in Built Environment*, Vol. 6, 2020, 118, <https://doi.org/10.3389/fbuil.2020.00118>
- [3] M. Yousefikia, S. Moridpour, S. Setunge, S. Setunge E. Mazloumi. Modeling Degradation of Tracks for Maintenance Planning on a Tram

- Line. *Journal of Traffic and Logistics Engineering*, Vol. 2(2), 2014, pp. 86-91, <https://doi.org/10.12720/jtle.2.2.86-91>
- [4] M. Khosravi, I. Soleimanmeigouni, A. Ahmadi, A. Nissen. Reducing the Positional Errors of Railway Track Geometry Measurements Using Alignment Methods: a Comparative Case Study. *Measurement*, 2021, 109383, <https://doi.org/10.1016/j.measurement.2021.109383>
- [5] N. Papathanasiou, B. Adey. Identifying the Input Uncertainties to Quantify When Prioritizing Railway Assets for Risk-Reducing Interventions. *CivilEng*, Vol. 1(2), 2020, pp. 106-131, <https://doi.org/10.3390/civileng1020008>
- [6] V. Naumov, I. Taran, Y. Litvinova, M. Bauer. Optimizing resources of multimodal transport terminal for material flow service. *Sustainability*, Vol. 12(16), 2020, 6545, <https://doi.org/10.3390/su12166545>
- [7] O. Novytskyi, I. Taran, Z. Zhanbirov. Increasing mine train mass by means of improved efficiency of service braking. *E3S Web of Conferences*, Vol. 123, 2019, 01034, <https://doi.org/10.1051/e3sconf/201912301034>
- [8] D. O. Potapov, V. G. Vitolberg, A. S. Malishevskaya, P. V. Plis, R. M. Trishchun. Predictive assessment of change of basic geometric characteristics of rail track during the operation. *IOP Conference Series: Materials Science and Engineering*, Vol. 708, 2019, 012021, <https://doi.org/10.1088/1757-899X/708/1/012021>
- [9] S. Fischer. Investigation of the Horizontal Track Geometry regarding Geogrid Reinforcement under Ballast. *Acta Polytechnica Hungarica*, Vol. 19(3), 2022, pp. 89-101, <https://doi.org/10.12700/APH.19.3.2022.3.8>
- [10] O. Pshinko, O. Patlasov, V. Andrieiev, M. Arbuzov, O. Hubar, O. Hromova, R. Markul. Research of railway crashed stone use of 40–70 mm fraction. *Transport Means* 2018, pp. 170-178
- [11] S. Fischer. Geogrid reinforcement of ballasted railway superstructure for stabilization of the railway track geometry – A case study. *Geotextiles and Geomembranes*, 2022, <https://doi.org/10.1016/j.geotexmem.2022.05.005>
- [12] D. O. Bannikov, O. L. Tiutkin. Prospecting Directions of the Development of Loose Medium Mechanics. *Science and Innovation*, Vol. 16(2), 2020, pp. 42-50, <https://doi.org/10.15407/scine16.02.042>
- [13] E. Juhasz, S. Fischer. Investigation of railroad ballast particle breakage. *Pollack Periodica*, Vol. 14(2), 2019, pp. 3-14, <https://doi.org/10.1556/606.2019.14.2.1>
- [14] M. Sysyn, V. Kovalchuk, U. Gerber, O. Nabochenko, A. Pentsak. Experimental study of railway ballast consolidation inhomogeneity under vibration loading. *Pollack Periodica*, Vol. 15(1), 2020, pp. 27-36, <https://doi.org/10.1556/606.2020.15.1.3>

- [15] M. Ribeiro, T. Henriques, L. Castro, A. Souto, A. Antunes, C. Costa-Santos, A. Teixeira. The Entropy Universe. *Entropy*, Vol. 23, 2021, 222, <https://doi.org/10.3390/e23020222>
- [16] A. Blagojević, Ž. Stević, D. Marinković, S. Kasalica, S. Rajilić. A Novel Entropy-Fuzzy PIPRECIA-DEA Model for Safety Evaluation of Railway Traffic. *Symmetry*, Vol. 12(9), 2020, 1479, <https://doi.org/10.3390/sym12091479>
- [17] V. A. Mashchenko, O. Ye. Khomenko, V. P. Kvasnikov. Thermodynamic aspect of rock destruction. *Naukovyi Visnyk Natsionalnoho Hirnychoho Universytetu*, Vol. 1, 2020, pp. 25-30, <https://doi.org/10.33271/nvngu/2020-1/025>
- [18] D. M. Kurhan. Accumulated deformation modeling of permanent way based on entropy system. *Science and Transport Progress*, Vol. 58(4), 2015, pp. 99-109, <https://doi.org/10.15802/stp2015/49215>
- [19] R. Avinery, M. Kornreich, R. Beck. Universal and Accessible Entropy Estimation Using a Com-pression Algorithm. *Phys. Rev. Lett.* 123, 2019, 178102, <https://doi.org/10.1103/PhysRevLett.123.178102>
- [20] D. Kurhan, M. Kurhan. Modeling the Dynamic Response of Railway Track. *IOP Conference Series: Materials Science and Engineering*, Vol. 708, 2019, 012013, <https://doi.org/10.1088/1757-899X/708/1/012013>
- [21] D. Kurhan, S. Fischer. Modeling of the Dynamic Rail Deflection using Elastic Wave Propagation, *Journal of Applied and Computational Mechanics*, Vol. 8(1), 2022, pp. 379-387, <https://doi.org/10.22055/JACM.2021.38826.3290>
- [22] D. Kurhan, M. Havrylov. The Mathematical Support of Machine Surfacing for the Railway Track. *Acta Technica Jaurinensis*, Vol. 13(3), 2020, pp. 246-267, <https://doi.org/10.14513/actatechjaur.v13.n3.556>

Railway Load Analysis During the Operation of an Excavator Resting on the Railway Track

Vesna Jovanović¹, Dragoslav Janošević¹, Dragan Marinković^{1,2}, Nikola Petrović¹, Jovan Pavlović¹

¹University of Niš, Faculty of Mechanical Engineering

A. Medvedeva 14, 18000 Niš, Serbia

vesna.nikolic@masfak.ni.ac.rs, dragoslav.janosevic@masfak.ni.ac.rs,

nikola.petrovic@masfak.ni.ac.rs, jovan.pavlovic@masfak.ni.ac.rs

² Technical University Berlin, Institute of Mechanics

17. Juni 135, 10623 Berlin, Germany

Dragan.Marinkovic@TU-Berlin.de

Abstract: Mobile machines perform many functions in the development and maintenance of railway infrastructure. Among them, particular emphasis is on hydraulic excavators. The paper defines a mathematical model of a hydraulic excavator for determining the static and dynamic loads of the railway during the operation of an excavator resting on the railway track. Based on the mathematical model, an excavator simulation program was developed. As an example, using the developed program, the loads of the railway tracks were determined for the operation of an excavator of 17000 kg in mass, equipped with a manipulator with a backhoe bucket of 0.6 m³ in volume.

Keywords: hydraulic excavators; railway transport; load analysis

1 Introduction

Rail transport, as a reliable and efficient means of transporting passengers and goods has been the subject of interest of numerous researchers. The research related to rail transport is quite broad and includes various investigations such as those related to locomotive engines [1], interaction of trains and railways [2], environment protection by reducing the noise emitted from the rails [3] [4], efficient inspection of railways [5], behavior of rails under different conditions [6] [6] [7], to name but a few research directions. There are numerous mobile machines (hydraulic excavators, loaders, graders, dumpers, cranes) (Figure 1a) that are used on railways in performing operational transport functions, but also in the operation and maintenance of railways and other railway infrastructure. Hydraulic excavators weighing from 10000 kg to 25000 kg with a support and

movement mechanism on caterpillars and tires are the most common mobile machines for performing various functions on the railway. Hydraulic excavators move and rest on railway tracks using modular devices with one pair of rail wheels for narrow, standard or wide gauge railway track, installed on the supporting structure of standard support and movement mechanisms in the front and in the rear. According to drivetrains, motion modules can be divided into: a) motion modules with indirect drivetrain, and b) motion modules with direct drivetrain.

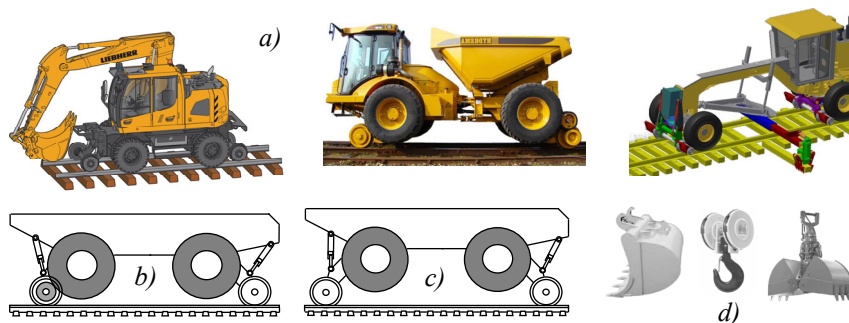


Figure 1

Mobile machines and tools which are used in railway transport

In motion modules with indirect drivetrain, the drive wheel (Figure 1b) in a friction pair transmits drive directly or indirectly to the rail wheel. In motion modules with direct drivetrain (Figure 1c) there are two concepts. The first achieves motion of the machine through the friction pair of the drive wheel and rail stripes. In the second, motion modules have their own hydrostatic transmission, which drives the rail wheels independently of the transmission of the machine movement. Motion modules have a brake system that is derived in the form of hydraulic disc brakes. During operation, resting on railway tracks, hydraulic excavators mostly have a backhoe manipulator, which is equipped with various executive tools in the form of a bucket, hook, or grabber (Figure 1c). Railway track loads are investigated by experimental measurements and theoretical analyses through the development of mathematical models and numerical simulation procedures [8] [9]. Research [10] into railway track loads refer to the experimental simulation of the spectrum of static and dynamic loads, which can occur during the lifetime, with the aim of optimizing and determining the capacity and service life of the elements of the railway track structure. In paper [11], the dynamic relationship between the railway track and the railway vehicle when moving in the curve of the railway track was analyzed using the developed mathematical model. The influence of crawler mobile machines on the moving surface was analyzed in [12] with the aim of determining the parameters of the movement mechanism of a machine, which enables comfortable driving when moving on different surface configurations. The load of a flat surface when a crawler support and movement mechanism of a hydraulic excavator is resting was

analyzed in [13], on the basis of the developed dynamic mathematical model of an excavator with a backhoe manipulator. The analysis of the capacity of hydraulic excavators resting on railway tracks is given in [14], where the permissible capacity of the excavator with a backhoe manipulator, in the entire working space, is determined based on the static stability of the excavator and the hydraulic stability of manipulator drive mechanisms. In what follows, a general mathematical model of a hydraulic excavator is defined to determine the load of the railway track and the dynamic stability during the operation of the excavator resting on the railway track.

2 Mathematical Model

A mathematical model is developed for the general configuration of an excavator kinematic chain composed of: the support and movement mechanism L_1 , (member by which the excavator rests or moves) (Figure 2a), the rotating platform L_2 and the three-plane manipulators with: boom L_3 , stick L_4 and backhoe bucket L_5 , which drives the hydraulic cylinder two-way action c_3, c_4, c_5 . The support and movement member of the excavator is a conventional (standard) movable mechanism with integrated pneumatic modules, having a pair of railway wheels with a mechanism for raising and lowering without stabilizers.

The position of the members of the excavator kinematic chain is defined by the mathematical model in the absolute coordinate system $OXYZ$ with the generalized coordinate θ_i (Figure 2a) determined by the set [15]:

$$\theta = \{\theta_1, \theta_2, \theta_3, \theta_4, \theta_5\} \quad (1)$$

where: θ_1 - the displacement of the support-movement member, θ_2 - the angle of the rotation platform, θ_3 - the angle of the boom position, θ_4 - the angle of the stick position and θ_5 - the angle of the backhoe bucket position.

The mathematical model of the member of the kinematic chain excavator L_i was defined in its local coordinate system $O_i x_i y_i z_i$, with geometric, kinematic and dynamic parameters covered with a set of quantities:

$$L_i = \{\mathbf{e}_i, \mathbf{s}_i, \mathbf{t}_i, m_i, J_i\} \quad (2)$$

where: \mathbf{e}_i - the unit vector of joint axes O_i whose member L_i is linked to the previous member L_{i-1} , \mathbf{s}_i - the position vector of the center joint O_{i+1} , which is the chain member L_i linked with the next member L_{i+1} (intensity vector is the length of the kinematic members) \mathbf{t}_i - the position vector of the center of mass of member L_i , m_i - the mass of member, J_i - the member moment of inertia. The parameters

of the manipulator drive mechanism of the excavator are determined using a set of parameters:

$$P_i = \{ d_{i1}, d_{i2}, a_i, b_i, m_{ci} \} \quad (3)$$

where: d_{i1}, d_{i2} - the diameter of the piston/piston rod in the hydraulic cylinder, a_i, b_i - the vectors, i.e. coordinates, of the position of the centers of the joints in which the hydraulic cylinders are connected to the members of the drive mechanism kinematic pair, m_{ci} - the mass of the hydraulic cylinder.

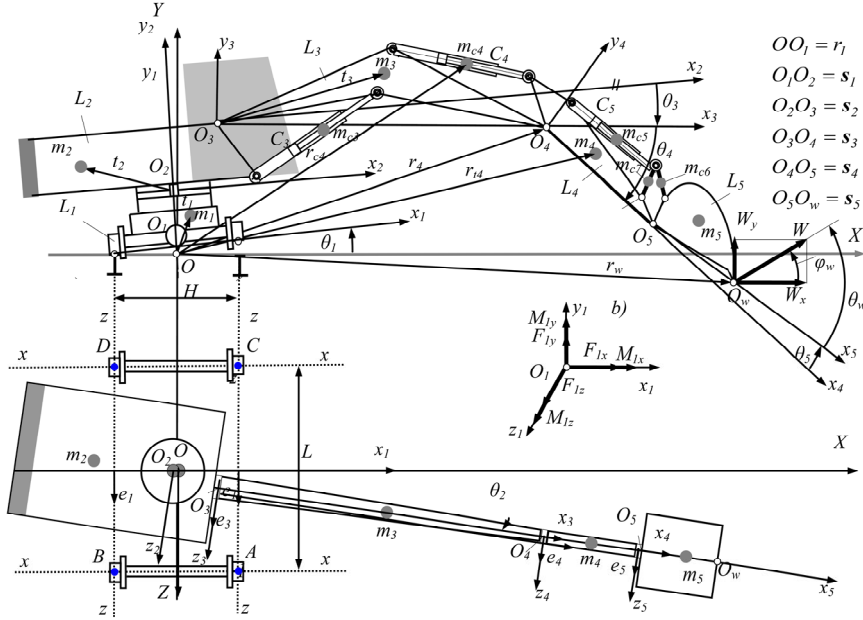


Figure 2

The mathematical model of the hydraulic excavator for determining reaction reliance

The mathematical model of the excavator is based on Newton-Eyler dynamic equations and the following assumptions:

- the support surface and kinematic chain members are modeled using rigid bodies,
- during the manipulation task, gravitational and inertial forces and digging resistance force W act on the members of the kinematic chain,
- the support surface of the excavator lies in the horizontal plane Oxz of the absolute coordinate system,
- the movement of the support-movement member of the excavator is neglected and it is accepted that the generalized coordinate is $\theta_1 = 0^\circ$,
- all excavator loads are transferred to the support surface in the centers A, B, C and D of the contact surfaces of railway wheels and railway tracks,

- connecting lines (x-x and z-z) of the centers A , B , C and D of contact surfaces are potential lines of overturning of excavators, which form a supporting polygon with the center in the coordinate origin O of the absolute coordinate system $OXYZ$ with unit vectors i, j, k .

According to the introduced assumptions, by reducing all the loads of the excavator to the center of the support surface O , the resulting force F_I and the resulting moment M_I , which load the support surface of the excavator, are obtained [15-17]:

$$F_I = W + \sum_{i=1}^5 F_{ui} - j \sum_{i=3}^5 gm_{ci} \quad (4)$$

$$M_I = (r_w \times W) + \sum_{i=1}^5 (r_{ii} \times F_{ui}) + \sum_{i=1}^5 M_{ui} - \sum_{i=3}^5 (r_{ci} \times j) gm_{ci} \quad (5)$$

where: W [kN]- the vector of the digging resistance force, F_{ui} [kN]- the vector of the total force acting in the center of mass of the member of the excavator kinematic chain, M_{ui} [kNm]- the vector of inertial moment of the member of the excavator kinematic chain, r_w - the vector of position of the cutting-edge of the bucket, r_{ii} - the vector of the center of mass of the member of the excavator kinematic chain, m_{ci} - the mass of hydraulic cylinders of the excavator manipulator drive mechanisms, r_{ci} - the vector of the center mass of the hydraulic cylinder.

The vector of the total force F_{ui} acting in the center of mass of the member of the excavator kinematic chain is determined by the following equation:

$$F_{ui} = m_i u_i - gm_i j \quad (6)$$

where: u_i - the vector of linear acceleration of the member.

Components of the vector of the resulting force F_I and the moment M_I in the absolute coordinate system are

$$F_{Ix} = F_I \cdot i; \quad F_{Iy} = F_I \cdot j; \quad F_{Iz} = F_I \cdot k \quad (7)$$

$$M_{Ix} = M_I \cdot i; \quad M_{Iy} = M_I \cdot j; \quad M_{Iz} = M_I \cdot k \quad (8)$$

Horizontal forces in the centers A , B , C and D of the support surface which load the railway track in the OX direction have the value:

$$F_{Ax} = \frac{F_{Ix}}{2} - \frac{M_{Iy}}{L} \wedge F_{Bx} = 0 \vee \frac{F_{Ix}}{2} - \frac{M_{Iy}}{L} > 0 \quad (9)$$

$$F_{Ax} = 0 \wedge F_{Bx} = \frac{F_{Ix}}{2} - \frac{M_{Iy}}{L} \vee \frac{F_{Ix}}{2} - \frac{M_{Iy}}{L} < 0 \quad (10)$$

$$F_{Cx} = \frac{F_{Ix}}{2} + \frac{M_{Iy}}{L} \wedge F_{Dx} = 0 \vee \frac{F_{Ix}}{2} + \frac{M_{Iy}}{L} > 0 \quad (11)$$

$$F_{Cx} = 0 \wedge F_{Dx} = \frac{F_{Ix}}{2} + \frac{M_{Iy}}{L} \vee \frac{F_{Iy}}{2} + \frac{M_{Iy}}{L} < 0 \quad (12)$$

where: L - the range of railway wheels of the excavator movement mechanism.

Vertical forces in the centers A , B , C and D of the support surface which load the railway track in the OY direction have the value:

$$F_{Ay} = \frac{F_{Iy}}{4} - \frac{M_{Ix}}{2L} + \frac{M_{Iz}}{2H} \quad F_{By} = \frac{F_{Iy}}{4} - \frac{M_{Ix}}{2L} - \frac{M_{Iz}}{2H} \quad (13)$$

$$F_{Cy} = \frac{F_{Iy}}{4} + \frac{M_{Ix}}{2L} + \frac{M_{Iz}}{2H} \quad F_{Dy} = \frac{F_{Iy}}{4} + \frac{M_{Ix}}{2L} - \frac{M_{Iz}}{2H} \quad (14)$$

where: H - the width of the railway track of railway wheels of the excavator movement mechanism.

Based on the set mathematical model, a program was developed for dynamic simulation of the excavator and, among other things, determination of dynamic loads of the railway during the operation of the excavator resting on the railway track. During the simulation, the conditions of movement of the kinematic chain of the excavator and technological resistances of movement during the manipulation task of the excavator were set.

3 Example

As an example, using the mathematical model and program, the railway load analysis was performed during the operation of an excavator, weighing 17000 kg , resting on the railway track with a support and movement mechanism with railway wheels, longitudinal wheel range L (Table 1) and wheel width H . The numerical simulation procedure was used to analyze the configuration of a kinematic chain with a backhoe manipulator with a boom, stick and bucket with a volume of $0,6 \text{ m}^3$ (Table 1). The manipulation task of the excavator was simulated with the following operations: capturing (digging), transfer and unloading of material of specific mass $\gamma_z = 1500 \text{ kg/m}^3$ and returning to the new digging position (Table 1). During the simulation, the conditions of movement of the members of the excavator kinematic chain during the manipulation task were given, as defined in the set of the following simulation parameters:

$$U = \{ \theta_2, c_3, c_4, c_5, p_{21}, p_{22}, p_{31}, p_{32}, p_{41}, p_{42}, p_{51}, p_{52} \} \quad (17)$$

where: θ_2 [°]- the angle of the rotation platform (Figure 3), c_3 [m]- the length of the boom cylinder (Figure 3), c_4 [m]- the length of the stick cylinder, c_5 [m]- the length of the bucket cylinder, p_{21}, p_{22} [MPa]- the pressures in the hydraulic motor lines to turn the platform (Figure 4), p_{31}, p_{32} [MPa]- the pressures in the hydraulic cylinder lines of the boom (Figure 4), p_{41}, p_{42} [MPa]- the pressures in the hydraulic cylinder lines of the stick (Figure 5), p_{51}, p_{52} [MPa]- the pressures in the hydraulic cylinder lines of the bucket (Figure 5). The given parameters of simulation of the excavator were determined by measuring a physical model of the hydraulic excavator weighing 17000 kg with a backhoe manipulator, when operating in exploitation conditions [18]. Based on the given simulation parameters, the developed program determined: the coordinates of the position of the members of the kinematic chain, the linear and angular velocities and accelerations, the gravitational and inertial forces and inertial moments of the members, the components of the resistance of the digging force and the static and dynamic loads of the railway.

Tabele 1
Parameters of kinematics chain of excavator (Figure 2)

Title	Symbol	Values [m]	Mass[kg]
Support and movement member L_1	L/H	4,610 /1,435	7040
Rotation platform L_2	-	-	6765
Boom L_3	s_3	5,0	1270
Stick L_4	s_4	1,8	430
Bucket L_5	s_5	1,3	540
Hydraulic motor of rotation platform $1xC_2$	d_{21}/d_{22}	75/75 cm^3	25
Boom hydraulic cylinder $2xC_3$	d_{31}/d_{32}	0,115/0,080	205
Stick hydraulic cylinder $1xC_4$	d_{41}/d_{42}	0,140/0,090	280
Bucket hydraulic cylinder $1xC_5$	d_{51}/d_{52}	0,115/0,080	190

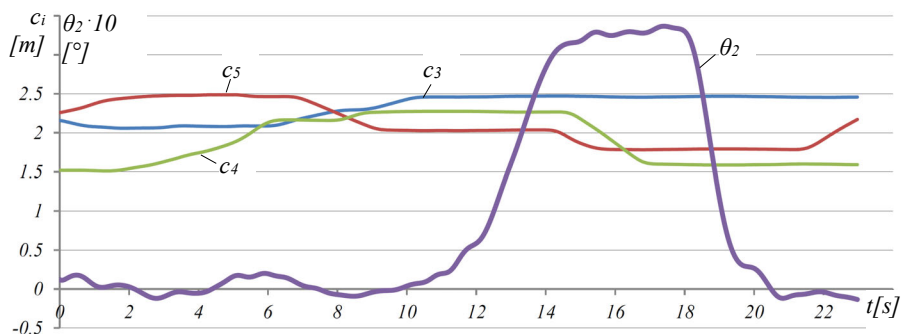


Figure 3

Given simulation parameters for the angle of the rotation platform θ_2 , and the lengths (strokes) of the hydraulic cylinder of the boom c_3 , stick c_4 and bucket c_5

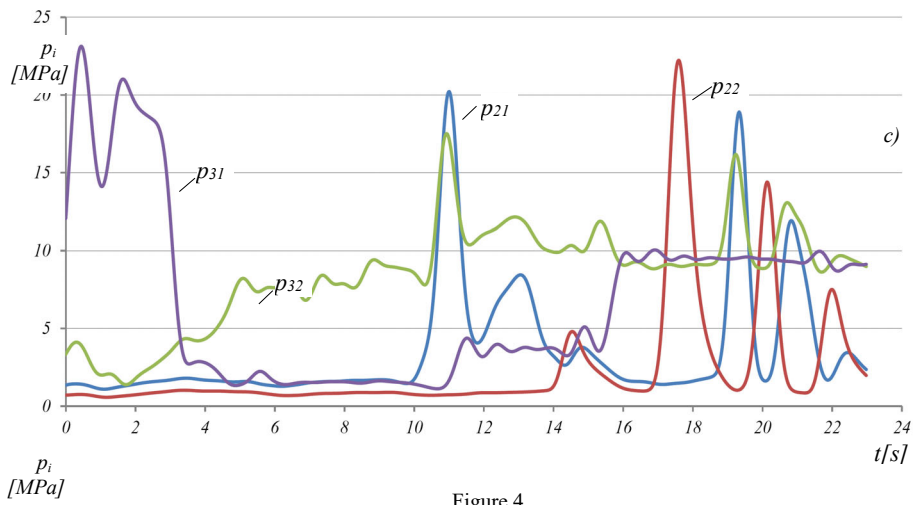


Figure 4

The parameters of simulation: pressures in the hydraulic motor lines to turn the platform p_{21} , p_{22} and pressures in the hydraulic cylinder lines of the boom p_{31} , p_{32}

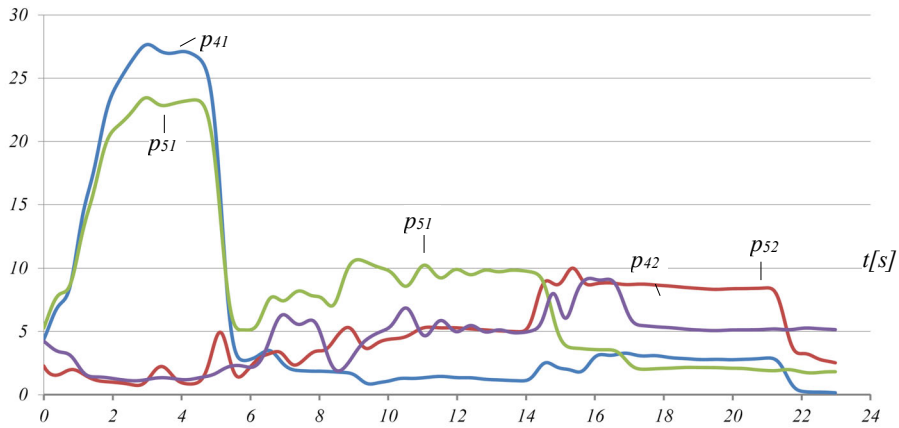


Figure 5

The parameters of simulation: pressures in the hydraulic cylinder lines of the stick p_{41} , p_{42} and bucket p_{51} , p_{52}

4 Analysis

The obtained simulation results show that during the capture operation ($\theta_2 = 0^\circ$) the maximum digging depth is $Y_w = -1,5 \text{ m}$ (Figure 6a), and during the unloading operation ($\theta_2 = 30^\circ$) the maximum unloading height is around $Y_w = 4 \text{ m}$.

During the capturing of materials ($t=0-5,8 \text{ s}$), the components of vector W (Figure 6b) of the digging resistance force change differently.

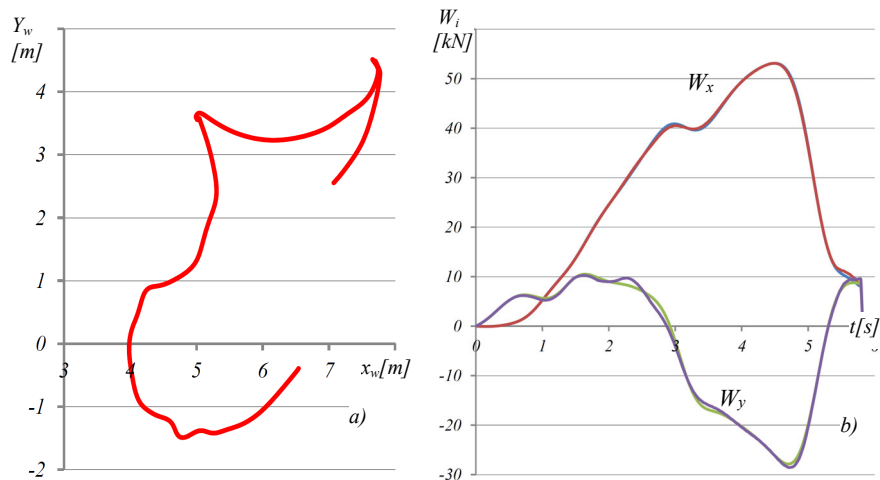


Figure 6

The parameters of the manipulation task of the excavator: a) the center path of the bucket cutting edge, b) the components of the digging resistance force W vector

The horizontal component W_x has a variable one-way action, while the vertical component W_y has a variable intensity and a variable direction of action. The lateral component is of insignificant intensity in relation to other components of the digging resistance force W .

It is characteristic that the magnitude of the total force F_l (Figure 7a) and the total moment M_l (Figure 7b) obtained by reducing all excavator loads to the center of the excavator support surface during the manipulation task possesses, in addition to gravitational forces, inertial loads of kinematic chain members. A comparison of total (F_l, M_l) with static loads (F_{ls}, M_{ls}) shows that the highest inertial loads occur at the beginning ($t=6\text{s}$) of the material transfer operation, when the manipulator is abruptly lifted from the material capture channel.

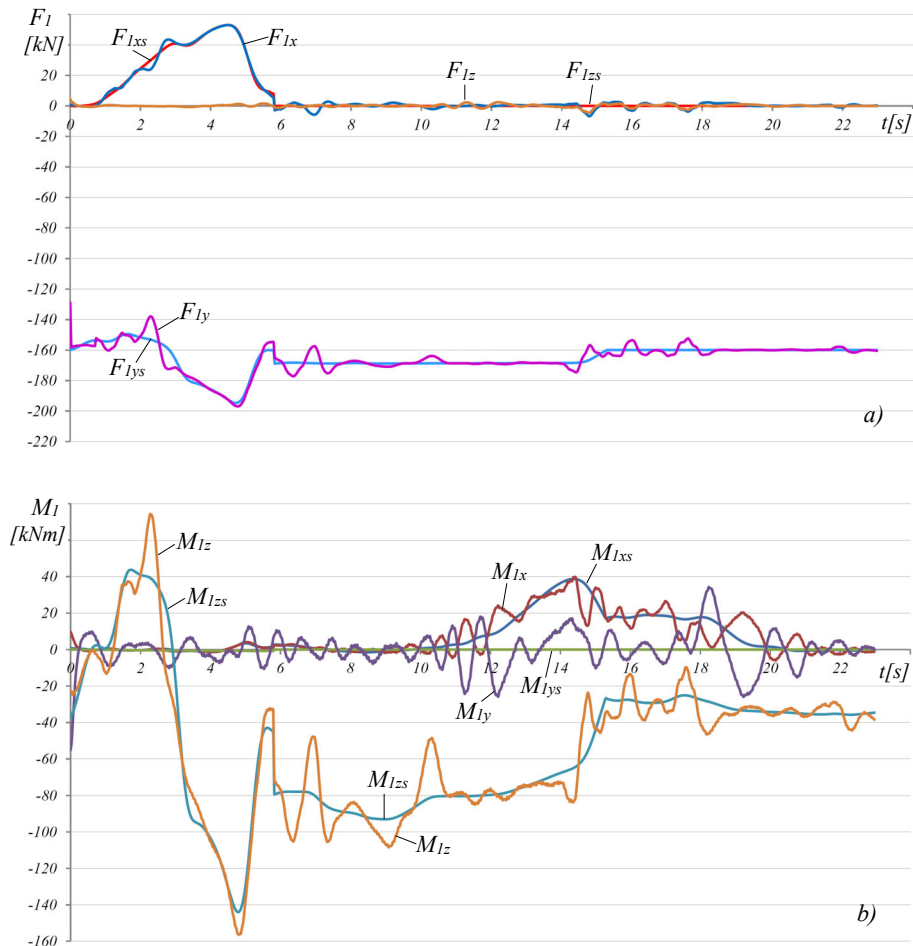


Figure 7

Load vector components: a) forces F_I and b) moment M_I in the center of the excavator support surface

Slightly smaller inertial loads occur ($t=5$ s) at the beginning of the accelerated rotation of the platform with the manipulator from the digging plane ($\theta_2 = 0^\circ$) to the unloading plane ($\theta_2 = 36^\circ$). The increase in inertial loads occurs again ($t=15$ s) due to abrupt stopping of the platform with the manipulator in the unloading plane of material. Inertial loads of lower intensity also occur during the unloading operation due to an abrupt change in the mass of the captured material when emptying the bucket.

The lowest intensity of inertial loads occurs during the operation of capturing (digging) the material due to the relatively slow and not so abruptly changing movement of the members of the kinematic chain of the excavator.

By decomposing the total force F_I and the moment M_I , significantly variable loads of the railway track were obtained during the manipulation task in the centers A , B (Figure 8) C , D (Figure 9) of the support surface of the railway wheels of the support and movement mechanism of the excavator on the railway track.

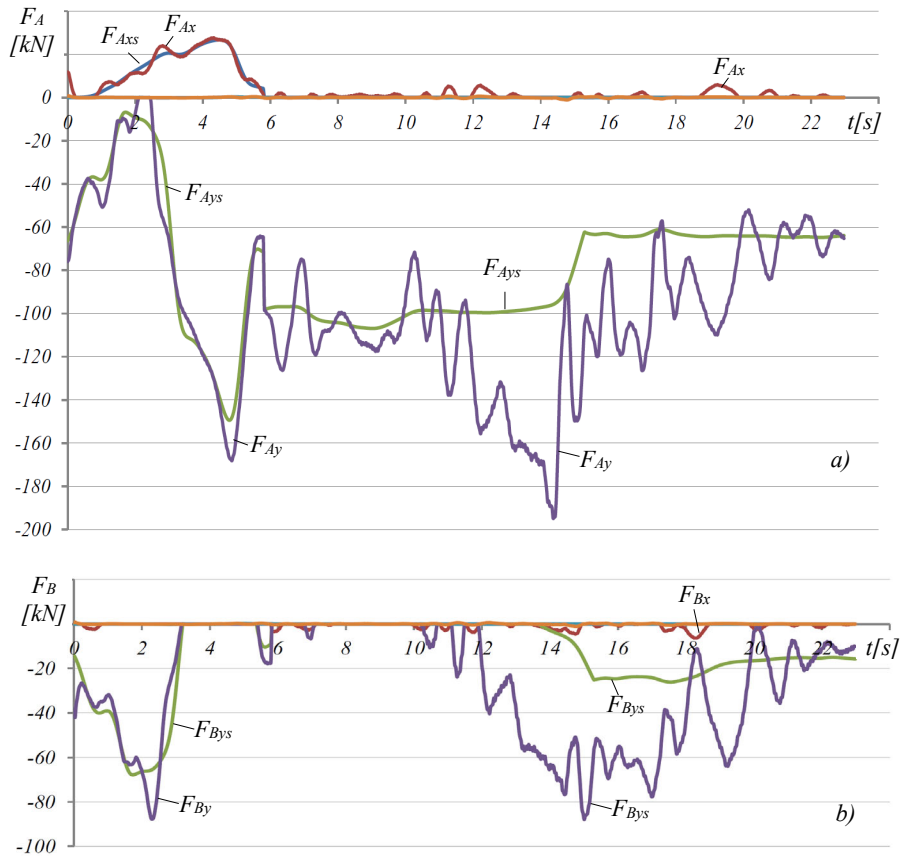


Figure 8

Forces loading the railway track in the X and Y directions in supports: a) A , b) B

According to the given conditions of the excavator simulation, the railway track is most loaded in supports A (Figure 8a) and C (Figure 9a), while in supports B (Figure 8b) and D (Figure 9b) minimal loads occur during the highest period of the manipulation task, especially in support D .

During the operation of capturing (digging) ($t=0-5,8$ s), the railway track is most loaded in supports A and C due to static loads - the resistance of digging and gravitational forces of the members of the kinematic chain of the excavator, while

inertial loads are small. During the same operation, the horizontal railway track loads F_{Ax} and F_{Cx} (Figures 8, 9) occur due to the action of the horizontal component W_x of the digging resistance force, while the railway track is unloaded in the same direction $F_{Bx}=F_{Dx}=0$ (Figures 8, 9).

The vertical loads F_{Ay} and F_{Cy} of the railway track in supports A and C , at the beginning ($t = 0-2,5$ s) of the digging operation, decrease due to the increase in the positive value of the vertical component W_y of the digging resistance force, up to ($t = 2,5$ s) of unloading ($F_{Ay}=F_{Cy}=0$) of the railway track in that direction. In the same period, loads F_{By} and F_{Dy} (Figures 8b, 9b) of the railway track in supports B and D increase and reach the maximum value during the digging operation.

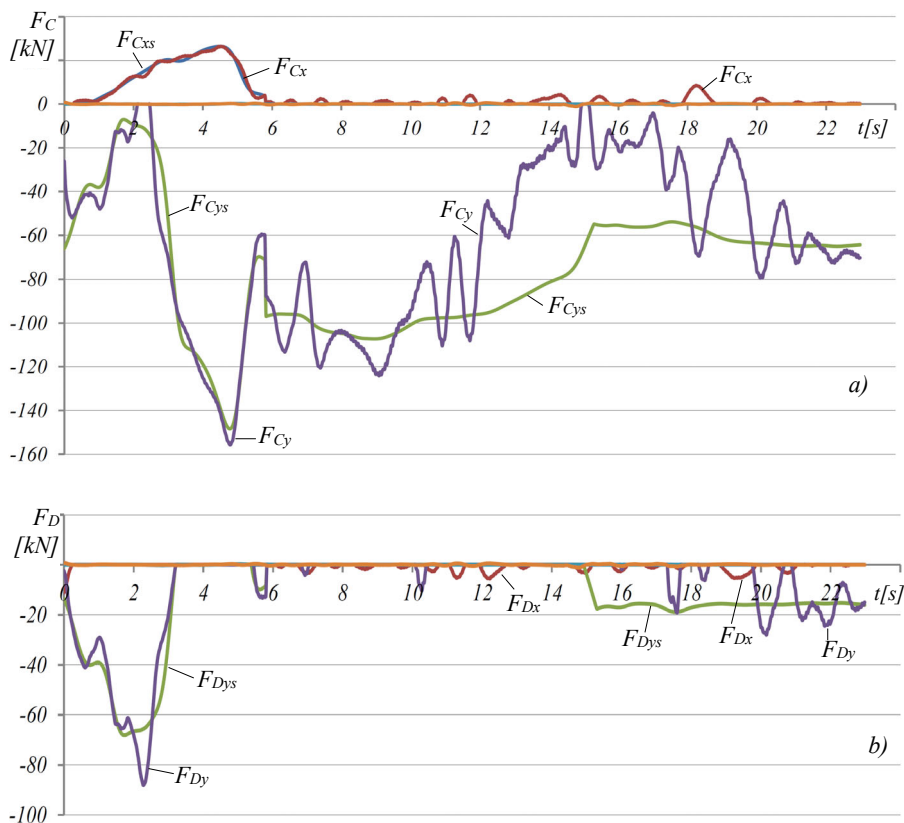


Figure 9

Forces loading the railway track in the X and Y directions in supports : a) C, b) D

In other operations of the manipulation task, the maximum vertical load of the F_{Ay} of the railway track occurs ($t = 14$ s) in support A due to the occurrence of the maximum inertial loads at the end of the material transfer operation due to abrupt stopping of the platform with the manipulator in the unloading plane.

In the same period ($t = 12-15$ s) there is an increase in the vertical load F_{By} (Figure 8b) of the railway track in support B and a decrease ($t = 10-15$ s) in the vertical load F_{Cy} to unload the railway track ($F_{Cy}=0$) in support C . The increase in vertical loads of the F_{Cy} , F_{Dy} railway track in supports C and D occur during the operation of returning the manipulator by turning the platform to a new digging plane ($t=18-23$ s). Slight horizontal loads F_{Ax} and F_{Cx} (Figure 8a, 9a) of the railway track, in relation to the same loads during the digging operation, occur at the beginning ($t = 13$ s) of the material transfer operation and at the beginning ($t = 18$ s) of the manipulator return operation to the new digging position.

The results of the analysis show that the vertical loads of the railway track in the supports are significantly higher than the horizontal loads. Comparing the static vertical loads of the railway track (F_{Asy} , F_{Bsy} , F_{Csy} , F_{Dsy}), caused by the action of the digging resistance force and gravitational forces of the kinematic chain of the excavator and material in the bucket, with the total vertical loads (F_{Ay} , F_{By} , F_{Cy} , F_{Dy}), indicates that the maximum inertial forces of the railway track occur due to lifting the manipulator with the captured material from the digging channel, then at the beginning and end of the operation of material transfer by turning the platform with the manipulator, and at the end of the operation of returning to a new digging plane.

Conclusion

Mobile machines (hydraulic excavators, loaders, cranes, ...) have found great application on the railway in performing operational functions of transmission and transport, but also in the development and maintenance of infrastructure - especially railway tracks. For performing functions on the railway track, mobile machines are equipped with special support and movement mechanisms, with two - axle railway wheels, which enable them stable support and movement.

Hydraulic excavators weighing $10000-25000$ kg, equipped with various manipulators and tools (buckets, hooks, grapples, ...) are used on the railway to perform various manipulative tasks. In the paper, a general mathematical model of a hydraulic excavator was developed for determining the dynamic loads of the railway during the operation of an excavator resting on the railway track.

The mathematical model includes the configuration of a kinematic chain of an excavator, weighing 17000 kg, with a support and movement mechanism, with two - axle railway wheels and a backhoe manipulator. The numerical simulation procedure of the excavator yielded the results which show that during the operation of the excavator resting on the railway track, dynamic loads of the railway track occur.

Loads depend on the position and character of the change in the movement of the members of the kinematic chain of the excavator during the manipulation task. During the capture operation, the static loads of the railway track are primary due to the action of the digging resistance force and the gravitational forces of the members of the kinematic chain of the excavator.

During the material transfer operation, in addition to static forces, the railway track is significantly loaded by inertial forces occurring due to the abrupt movement and stopping of the rotating platform with the manipulator when moving from the digging plane to the material unloading plane. The obtained research results, in addition to the analysis of the railway track load, can be used to assess the dynamic stability of excavators.

Acknowledgement

This research was financially supported by the Ministry of Education, Science and Technological Development of the Republic of Serbia (Contract No. 451-03-9/2021-14/200109).

References

- [1] Sinyavski, V., Shatrov, M., Kremnev, V., & Pronchenko, G. Forecasting of a boosted locomotive gas diesel engine parameters with one- and two-stage charging systems. *Reports in Mechanical Engineering*, 1(1), 2020, 192-198
- [2] Kovalchuk, V., Sysyn, M., Gerber, U., Nabochenko, O., Zarour, J., & Dehne, S. Experimental investigation of the influence of train velocity and travel direction on the dynamic behavior of stiff common crossings. *Facta Universitatis, Series: Mechanical Engineering*, 17(3), 2019, pp. 345-356
- [3] Tigh Kuchak, A. J., Marinkovic, D., Zehn, M. Finite element model updating - Case study of a rail damper. *Structural Engineering and Mechanics*, 73(1), 2020, pp. 27-35
- [4] Kuchak, A. J. T., Marinkovic, D., Zehn, M. Parametric Investigation of a Rail Damper Design Based on a Lab-Scaled Model. *Journal of Vibration Engineering and Technologies*, 9(1), 2021, pp. 51-60
- [5] Banić, M., Miltenović, A., Pavlović, M., Ćirić, I. Intelligent machine vision based railway infrastructure inspection and monitoring using uav. *Facta Universitatis, Series: Mechanical Engineering*, 17(3), 2019, pp. 357-364
- [6] Szalai, S., Eller, B., Juhász, E., Movahedi, M. R., Németh, A., Harrach, D., Baranyai, G., & Fischer, S. Investigation of deformations of ballasted railway track during collapse using the Digital Image Correlation Method (DICM). *Reports in Mechanical Engineering*, 3(1), 2022, pp. 258-282
- [7] Sysyn, M., Gerber U., Kovalchuk V., Nabochenko O. The Complex Phenomenological Model For Prediction Of Inhomogeneous Deformations Of Railway Ballast Layer After Tamping Works, *Archives Of Transport* 47(3), 2018, pp. 91-107
- [8] Fischer, S. Investigation of the Horizontal Track Geometry regarding Geogrid Reinforcement under Ballast, *Acta Polytechnica Hungarica* 19(3) 2022, pp. 89-101

-
- [9] Jóvér, V., Gáspár, L., Fischer, S. Investigation of Tramway Line No. 1, in Budapest, Based on Dynamic Measurements, *Acta Polytechnica Hungarica* 19(3), 2022, pp. 65-76
- [10] Kaewunruen, S., Remennikov, A. Investigations of static and dynamic performance of railway prestressed concrete sleepers, 6th ECCOMAS Thematic Conference on Computational Methods in Structural Dynamics and Earthquake Engineering, Greece, 15-17 June 2017
- [11] Bettaieba, H. Analytical dynamic and quasi-static model of railway vehicle transit to curved track, *Mechanics & Industry* 13, 2012, pp. 231-244
- [12] Matej, J. Tracked mechanism simulation of mobile machine in MSC.ADAMS/View, *Research In Agricultural Engineering*, 56(1), 2010, pp. 1-7
- [13] Mitrev, R., Janošević, D., Marinković, D. Dynamical modelling of hydraulic excavator considered as a multibody system, *Technical Gazette* 24, Suppl. 2, 2017, pp. 327-338
- [14] Janošević, D., Pavlović, J., Jovanović, V. Application of the mobile machines in railway transport, XVI International Scientific-expert Conference on Railways, Serbia, Niš, October 09-10, 2014, pp. 241-244
- [15] Jovanović, V. A contribution to the synthesis of the slewing platform drive mechanism of hydraulic excavators, PhD dissertation, (in Serbian), University of Niš, Faculty of Mechanical Engineering, 2018
- [16] Janošević, D. Optimal Synthesis of Drive mechanisms in Hydraulic Excavators. PhD dissertation, (in Serbian), University of Niš, Faculty of Mechanical Engineering, 1997
- [17] Jovanović, V., Janošević, D., Pavlović, J. Analysis of the influence of the digging position on the loading of the axial bearing of slewing platform drive mechanisms in hydraulic excavators, *Facta Universitatis series: Mechanical Engineering*, 19(4), 2021, pp. 705-718
- [18] Mitrev, R., Marinković, D. Numerical study of the hydraulic excavator overturning stability during performing lifting operations. *Advances in Mechanical Engineering*, 11(5), 2019, doi: 10.1177/1687814019841779

Reversible Planetary Gearsets Controlled by Two Brakes, for Internal Combustion Railway Vehicle Transmission Applications

**Milan Tica¹, Željko Vrcan², Sanjin Troha²,
Dragan Marinković^{3,4}**

¹University of Banja Luka, Faculty of Mechanical Engineering, Vojvode Stepe Stepanovića 71, BA-78000 Banja Luka, Bosnia and Herzegovina
milan.tica@mf.unibl.org

²University of Rijeka, Faculty of Engineering, Vukovarska 58, HR-51000 Rijeka, Croatia
zeljko.vrcan@riteh.hr, sanjin.troha@riteh.hr

³University of Niš, Faculty of Mechanical Engineering,
Aleksandra Medvedeva 14, RS-18000 Niš, Serbia

⁴Technische Universität Berlin, Department of Structural Mechanics and Analysis,
Strasse des 17. Juni 135, 10623 Berlin, Germany
dragan.marinkovic@tu-berlin.de

Abstract: Internal combustion powered railway vehicles require extremely rugged and reliable transmissions. While high-powered applications use electric or complex hydrodynamic transmissions, in the low to medium power range of railway vehicles, transmissions derived from ordinary highway truck or bus automatic transmissions and hydromechanical transmissions, are used. Modern railway vehicles must be able to operate in both directions at the same speed, which is particularly important when units from the same series are connected in a multiple unit lash-up. Simple hydrodynamic and mechanical transmissions are commonly used in such vehicles, but planetary gear trains are also suitable for the application, either as an output gearbox or as the main transmission gearbox in the case of simpler vehicles. This planetary gearbox is designed to provide two equal transmission ratios, however with the output shaft rotating in different directions. Design priority should be given to clutch-type brakes for compactness and reliability, however band brakes should have priority for ease of maintenance is a priority. Additionally, the gearbox design should give priority to boxes that do not experience power circulation, and do not require hollow shafts or complex planet carrier arrangements. The application of planetary gearbox designed according to the guidelines laid out in this paper would simplify the design and manufacture of hydrodynamic, hydromechanical and mechanical transmissions for railway vehicles.

Keywords: Railway vehicle; mechanical power transmission; reversible planetary gearbox

1 Introduction

Internal combustion engines (ICEs), whether using spark or compression ignition, have been in railway use since the early 1930s as an improvement over steam technology. However, as the crankshaft of an ICE cannot be connected directly to the wheels as in the case of a steam engine, it requires a transmission which will transfer power to the wheels while matching the speed and torque range of the engine to the requirements of the wheels [1]. It must also enable the ICE to disconnect from the wheels when the vehicle is stationary, so that the ICE can idle or be started up from standstill.

As the ICE is a constant power machine, the transmission must provide an amplification of the output torque in the range of 10:1 to 5:1, depending on the application, with an adequate number of transmission ratios to enable the whole power range of the engine to be used. Furthermore, the internal efficiency of the transmission must be as high as possible to meet environmental demands and reduce operating costs [2-8]. The transmission must also change gears without reducing or interrupting the engine power output. It must also be reversible, and in some special applications (e.g., shunting) it must be even able to reverse under load. The transmission should be robust, reliable, and low maintenance [9]. Finally, the transmission should be unaffected by climatic extremes and exposure to snow.

Currently, mechanical, hydrostatic, hydrodynamic, electrical, and combined hydro-mechanical transmissions are in use, depending on the application. Modern electrical transmissions are highly reliable, but their weight and size make them applicable only to power ranges beyond 500 kW. Hydrodynamic transmissions have been successfully applied up to 2 MW, although the transmissions tend to become large and heavy in the higher power ranges. Hydrostatic transmissions are simple, reliable and offer continuously variable transmission ratios, however oil cooling issues limit them to approximately 150 kW. Mechanical transmissions use simple, robust, and reliable automotive-derived solutions. Designs using friction and dog clutches are applicable up to 200 kW, however they are usually limited to lightweight maintenance vehicles. More robust designs using planetary gearsets must be coupled to a torque converter and can be used up to 600 kW.

Modern railway vehicles must be able to operate in both directions at the same speed, especially when operated in multiples, as they might end up coupled “head to head” or “tail to tail” and still need to move in the same direction. Furthermore, the transmission should have the same efficiency in both directions. Electrical and hydrostatic transmissions achieve this easily, however on hydrodynamic, mechanical, and hydro-mechanical transmissions a separate gearbox or gearbox stage is required, however this solution creates a slightly different transmission ratio in one direction of travel.

This can be resolved with the application of a two-carrier reversible planetary gearbox controlled by two brakes, which will have the same transmission ratio in

each of its directions of rotation, preferably with the same or very similar efficiency [10-18]. This gearbox can be used on its own with a torque converter for low powered applications, as the output box for a main planetary gearbox in medium powered applications, or as the output stage of high-powered hydrodynamic transmissions.

It is known that the application of planetary gear trains (PGTs) offers considerable advantages in relation to conventional gear train solution, resulting in expanded possibilities for application in mechanical engineering solutions. Some areas of application have been mentioned in [19-22], with railway vehicles being another area of application as they are required to move both forwards and backwards and in multiple at the same speed. Hydrodynamic and PGT transmissions are commonly used in such vehicles, however an additional mechanical stage is required to reverse. This mechanical stage can be easily replaced by an output planetary gearbox consisting of a compound two-speed PGT created by appropriately linking the shafts of the elements of its component planetary gear trains (stages). For the purposes of the research presented in this article, two-speed two-carrier PGTs with four external shafts composed of two PGTs of the basic type were considered. The internal structures of the researched gear trains were laid out. As there is a considerable number of all possible schemes and layout variants, a systematization was performed, and appropriate labelling was devised. A software program for numerical simulation and calculation of PGT parameters was developed to determine the structure and important basic parameters of the component gear trains and the whole gear train, based on the application constraints. The explanation of the operation of this software is followed by a numerical example in which the optimal two-speed planetary gear train that meets predefined transmission requirements is selected and then defined by the numbers of teeth of the component PGT sun gears, gear modules and transmission ratios. The position of the PGT in the transmission chain and the operating conditions of railway vehicles determine the input data for the computer program that defines the structure and important parameters of the component planetary gear trains. The acceptable transmission solutions for the selected application were generated using this specially developed computer program. The final selection between the solutions generated by the program, is performed by comparative analysis [23] [24].

2 Planetary Gear Boxes

The two-carrier compound PGT (compound train) is the simplest form of compound PGT (Fig. 1).

This simplest form of compound PGT has two component trains and four external shafts (Fig. 1).

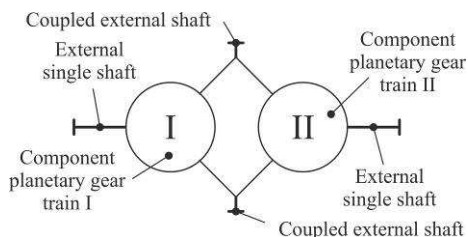


Figure 1

Planetary gear train with four external shafts (compound train)

It is created by connecting two shafts of one component PGT with two shafts of the other component PGT. The resulting four external shafts can then be subdivided to two coupled shafts and two single external shafts. Both component PGTs are planetary gear trains of the basic type consisting of a sun gear 1, planet gear 2, ring gear 3 and planet carrier h, as shown in Fig. 2. The simple and compound PGTs discussed in this paper will be described by means of Wolf-Arnaudov symbols (Figure 2) [12, 15, 18]. This is the most common type of PGT, and it is commonly used in engineering applications as a single stage transmission, or as a building block for higher compound planetary gear trains. The application of this component PGT offers several advantages over other types, notably its efficiency, small overall dimensions and mass, and relatively low manufacturing costs due to the relatively simple production process.

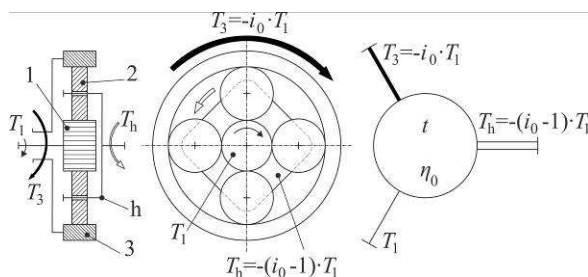


Figure 2

Wolf-Arnaudov symbol and torque ratios of the basic type of PGT [8]

The torque loads on the planetary gear train shafts are indicated in Fig. 2. The torque on the ring gear shaft T_3 and the torque on the carrier shaft T_h are given as functions of the ideal torque ratio t and the torque acting on the sun gear shaft T_1 . The ideal torque ratio is defined as

$$t = \frac{T_3}{T_1} = \left| \frac{z_3}{z_1} \right| = -i_0 > +1 \tag{1}$$

where i_0 is the basic transmission ratio, z_1 is the number of teeth of the sun gear and z_3 is the number of teeth of the ring gear. The transmission ratio depends on

whether the sun gear, ring gear or carrier is the locked element. It is possible to connect two component trains in a total of 36 possible ways (schemes) [12, 15], however this is reduced by isomorphism to only 12 different schemes resulting in PGTs with four external shafts, Fig. 3. In every presented scheme it is possible to put brakes as well as the driving or the operating machine on external shafts in 12 different configurations (layout variants), the cardinal directions of the input and output shafts being used for naming (Fig. 4). The power flow and kinematic characteristics of the gearbox are influenced by the placement of brakes on different shafts, enabling their use as multiple-speed gearboxes.

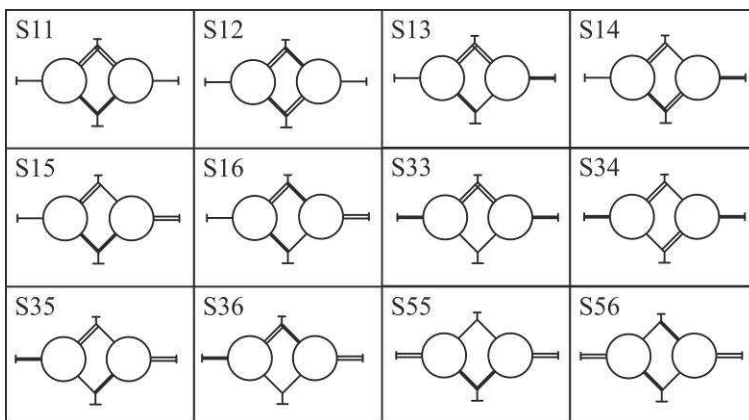


Figure 3

Systematization of all schemes of two-carrier PGTs with four external shafts [10, 15]

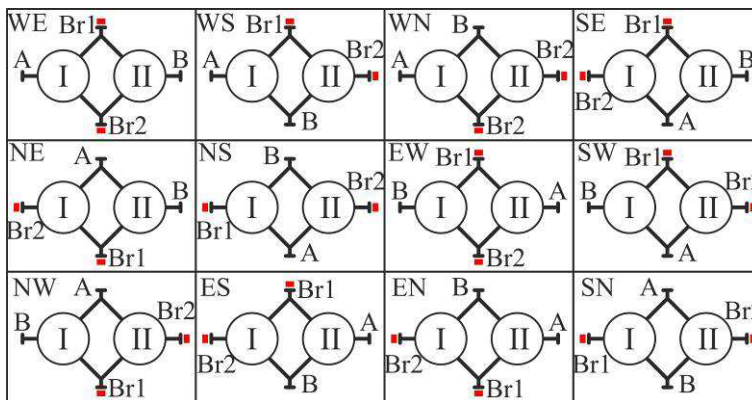


Figure 4

Layout variants of two-carrier planetary gear trains with four external shafts [15] [16]

3 Numerical Example and Discussion

The computer program DVOBRZ is used to select the optimal variant from similar multispeed PGTs, and it operates by synthesizing two-speed PGTs [14]. The program can determine the values of the parameters of valid component PGTs, such as basic gearset efficiency η_0 , gear pitch diameters $d_{1,2,3}$, gear modules m etc. for every valid combination of gear tooth numbers $z_{1,2,3}$, as functions of the ideal torque ratios $t_{I,II}$. Furthermore, for every valid combination of component PGTs for the selected scheme and layout variant, the parameters of the component PGT, such as i_{Br1} , i_{Br2} (transmission ratios with the respective brake Br1 or Br2 activated), η_{Br1} and η_{Br2} (efficiencies with the respective brake activated), are also calculated as functions of the ideal torque ratios t_I and t_{II} and then stored (Fig. 5). Every layout variant has two separate functions relating the transmission ratios as i_{Br1} , i_{Br2} to the ideal torque ratios t_I and t_{II} (Fig. 5, left). The program effectively seeks the ideal torque ratios that will place the overall transmission ratios of the compound PGT into the desired range (Fig 5, right).

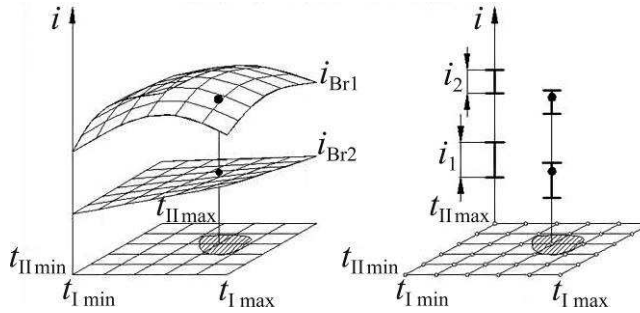


Figure 5

Operating principle of the DVOBRZ program

All valid solutions are compared according to the defined relevant criteria, such as minimal radial dimensions, maximum equivalent efficiency etc. [9]. In this case, a railway vehicle transmission will be used to demonstrate the selection of two-speed PGTs. Considering that the required transmission ratios are $i_1 = -4.5$ and $i_2 = 4.5$, solutions have been found with transmission ratios in the ranges $-4.6 \leq i_1 \leq -4.4$ and $4.4 \leq i_2 \leq 4.6$. The important outer input datum is the frequency of operation of each transmission ratio: $\alpha_{1i} = 0.5$ (50%) and $\alpha_{2i} = 0.5$ (50%). The program is now tasked with finding the optimal solution according to efficiency, while considering the operating conditions of the vehicle. The DVOBRZ program then lists six possible solutions for two-speed PGTs, using the previously listed requirements and assumptions. The main solution parameters are summarized in Table 1 while the kinematic schemes of acceptable solutions are shown in Figs. 5-10. The main parameters include the numbers of teeth of all gears and ideal torque ratios for both component gear trains.

The program DVOBRZ determines the ideal torque ratios for both gear trains. The tooth numbers of all gears were adopted based on the ideal torque ratios [17] and presented in Table 1. All tooth numbers respect the assembly conditions of coaxiality, adjacency and conjunction. Component gearsets have either 3 or 4 (z_2 marked in bold in Tab. 1) planets. The transmission ratios and efficiencies have been calculated for all acceptable solutions for cases of either brake being active. The results are presented in Table 1, with transmission ratios i_{Br1} and i_{Br2} defined by means of the using the adopted tooth number. Also, the basic efficiency η_0 was calculated as a function of the tooth numbers of all gears [14] [18]. The efficiency with active brake Br1 η_{Br1} and the efficiency with active brake Br2 η_{Br2} were calculated as a function of ideal torque ratios and basic efficiencies [13]. It was determined that all solutions provide the required transmission ratios and present high efficiency values in both directions of output shaft rotation.

Table 1
Main parameters of both component gear trains

Mark	t_I	t_{II}	i_{Br1}	i_{Br2}	Z _{1I}	Z _{2I}	Z _{3I}	Z _{1II}	Z _{2II}	Z _{3II}	η_{Br1}	η_{Br2}
S36SN	4.053	5	5.053	-5	19	29	77	16	32	80	0.986	0.982
S16WE	2	1.553	-5.106	4.932	24	12	48	47	13	73	0.953	0.969
S33SE	2	5	-5	5	24	12	48	16	32	80	0.982	0.948
S13WN	2	4.053	5.053	-4.923	24	12	48	19	29	77	0.986	0.922
S12WS	5	1.52	-5	4.947	16	30	80	50	13	76	0.981	0.966
S55NE	4.053	2	5.053	-5.102	19	29	77	24	12	48	0.986	0.945

The valid solutions are presented in Figs. 6-11, showing the general kinematic layout and power flow for cases of brake Br1 or brake Br2 being on. The power flow is marked by the red line, while A denotes power input and B denotes power output. The kinematic layouts shown in Figs. 6-11 have been obtained using computer simulation and torque method analysis combined with appropriate transformations. A diagram linking the ideal torque ratios t_I and t_{II} of the component PGTs (ring to sun gear tooth number ratio) to the required transmission ratio i_{rev} is provided for each valid solution. The torque ratios can then be used to determine the required tooth numbers for both component PGTs by just inverting the assembly conditions. Design constraints (bearing solutions, planet gear rotational speed, noise etc.) place the acceptable values of i_{rev} into an area where the ideal torque ratios exceed 1.5.

The operation of the S36SN gearbox is shown in Figure 6. The gearbox is idle with both brakes off (Fig. 6a). With brake Br1 on, a positive transmission ratio is obtained with only component PGT I active, while component PGT II is idle (Fig. 6b). With brake Br2 on, a negative transmission ratio is obtained, only component PGT II is active, while component PGT I is idle (Fig. 6c). The ideal torque ratios for transmission ratio $i_{rev} = +/- 5$, are $t_I = 4$ and $t_{II} = 5$ (Fig. 6d). The acceptable transmission ratio range is $i_{rev} = +/- 2.5... +/- 12$.

The operation of the S16WE gearbox is displayed in Figure 7. The gearbox is idle with both brakes are off (Fig. 7a). With brake Br1 on, a negative transmission ratio is obtained with both component PGTs in active operation (Fig. 7b). With brake Br2 on, a positive transmission ratio is obtained, also with both component PGTs in active operation (Fig. 7c). The ideal torque ratios for transmission ratio $i_{rev} = +/- 5$, are $t_I = 1.5$ and $t_{II} = 2$ (Fig. 7d). The acceptable transmission ratio range is $i_{rev} = +/- 4... +/- 5$.

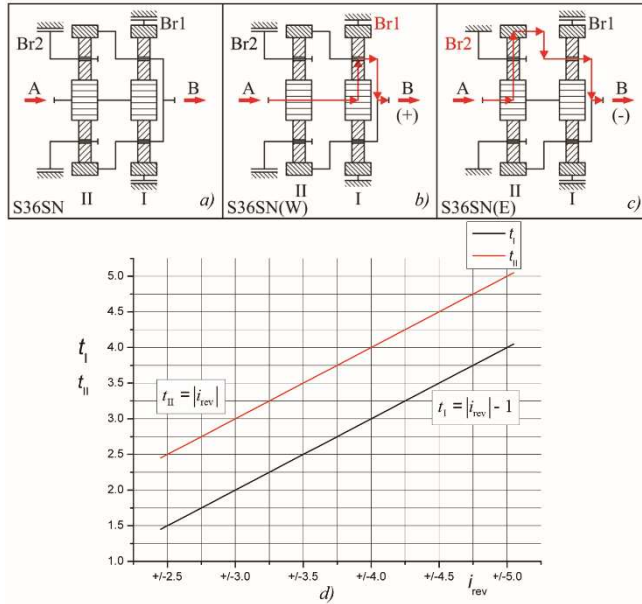


Figure 6

Kinematic arrangement and power flow (top row), and relation of transmission ratio i_{rev} to ideal torque ratios t_I and t_{II} (bottom) for S36SN gearbox

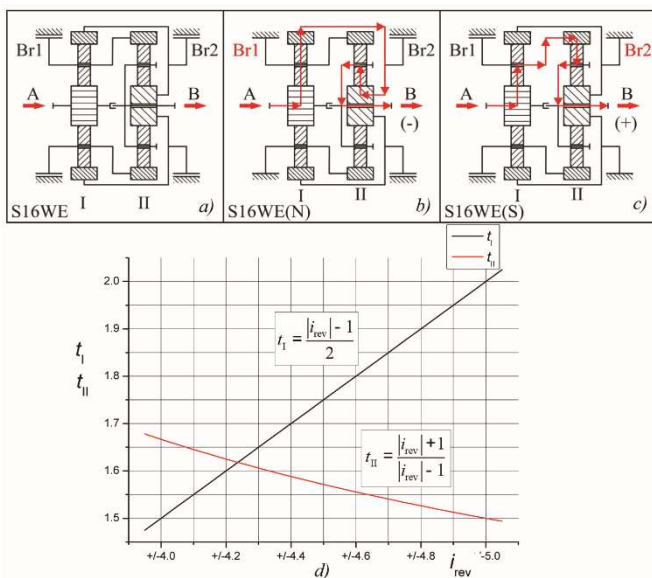


Figure 7

Kinematic arrangement and power flow (top row), and relation of transmission ratio i_{rev} to ideal torque ratios t_I and t_{II} (bottom) for S16WE gearbox

The operation of the S33SE gearbox is seen in Figure 8. The gearbox is idle with both brakes off (Fig. 8a). With brake Br1 on, a negative transmission ratio is obtained with only component PGT II in active operation, while component PGT I remains idle (Fig. 8b). With brake Br2 on, a positive transmission ratio is obtained, with both component PGTs in active operation (Fig. 8c). The ideal torque ratios for transmission ratio $i_{rev} = +/- 5$, are $t_I = 2$ and $t_{II} = 5$ (Fig. 7d). The acceptable transmission ratio range is $i_{rev} = +/- 4... +/- 12$.

The operation of the S13WN gearbox is shown in Figure 9. The gearbox is idle with both brakes off (Fig. 9a). With brake Br1 on, a positive transmission ratio is obtained with only component PGT I active, while component PGT II is idle (Fig. 9b). With brake Br2 on, a negative transmission ratio is obtained with both component PGTs active. The power flow goes from A to B, with power circulation inside the gearbox as shown in the figure (Fig. 9c). The ideal torque ratios for transmission ratio $i_{rev} = +/- 5$, are $t_I = 4$ and $t_{II} = 1.5$ (Fig. 19d). The acceptable transmission ratio range is $i_{rev} = +/- 2.5... +/- 5$.

The S12WS gearbox is shown in Figure 10. With both brakes off, the gearbox is idle (Fig. 10a). With brake Br1 on, a negative transmission ratio is obtained with only component PGT I active, while component PGT II idles (Fig. 10b). With brake Br2 on, a positive transmission ratio is obtained with both component PGTs in active operation. Power flows from A to B, with power circulation inside the

gearbox as shown in the figure (Fig. 10c). For example, for a transmission ratio of ± 5 , the ideal torque ratios are $t_I=5$ and $t_{II}=1.5$. The ideal torque ratios for transmission ratio $i_{rev} = +/- 5$, are $t_I = 5$ and $t_{II} = 1,5$ (Fig. 10d). The acceptable transmission ratio range is $i_{rev} = +/- 1.5... +/- 5$.

The operation of the S55 NE gearbox is seen in Figure 11. The gearbox is idle with both brakes off (Fig. 11a). With brake Br1 on, a positive transmission ratio is obtained with only component PGT II active, while component PGT I is idle (Fig. 11b). With brake Br2 on, a negative transmission ratio is obtained with both component PGTs active. The power flows from A to B, with power circulation inside the gearbox as shown in the picture (Fig. 11c). The ideal torque ratios for transmission ratio $i_{rev} = +/- 5$, are $t_I = 2$ and $t_{II} = 4$ (Fig. 11d). The acceptable transmission ratio range is $i_{rev} = +/- 4... +/- 5$.

The optimal solution is then selected by the designer according to technological and economical demands, such as manufacturing costs. This is achieved by analyzing the kinematic diagrams, (Figs. 6a to 11a). Priority is given to designs which do not require drilled shafts or complex planet carrier arrangements, and layout S36SN satisfies both conditions. In this design, both brakes are acting on single external shafts, and it is obvious that in both situations, i.e. with any of two brakes activated only component PGT is operational (two-shaft operating mode), while the other remains idle. Because of this, power wastage occurs in only one PGT stage and there is only one power sink.

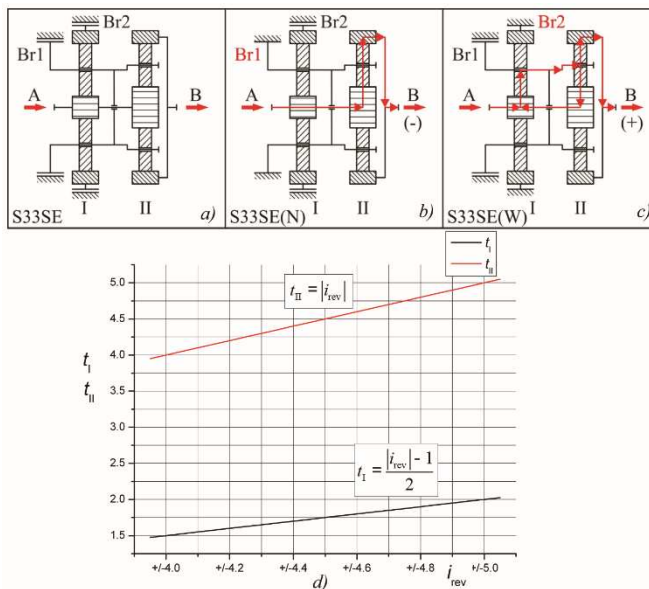


Figure 8

Kinematic arrangement and power flow (top row), and relation of transmission ratio i_{rev} to ideal torque ratios t_I and t_{II} (bottom) for S33SE gearbox

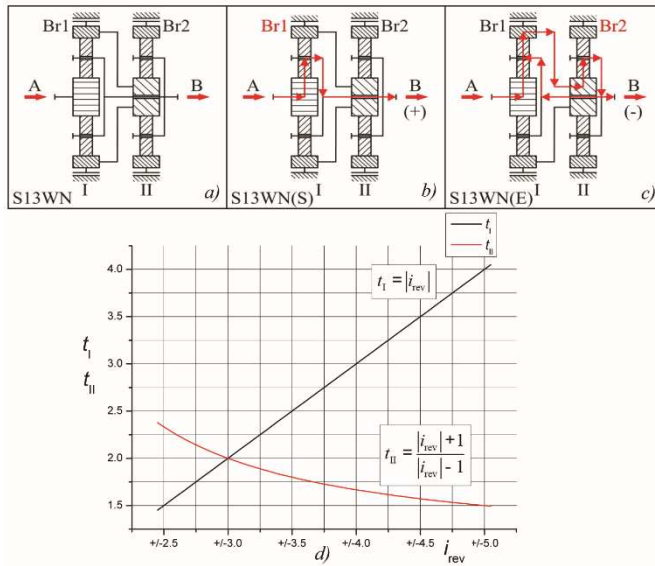


Figure 9

Kinematic arrangement and power flow (top row), and relation of transmission ratio i_{rev} to ideal torque ratios t_I and t_{II} (bottom) for S13WN gearbox

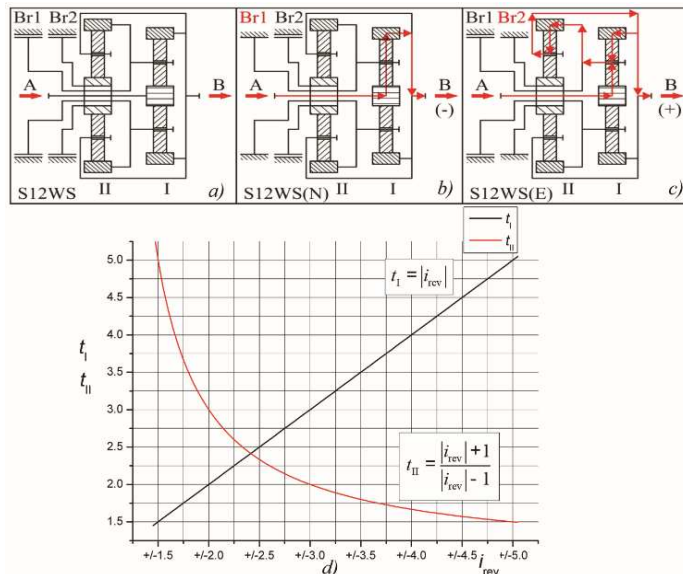


Figure 10

Kinematic arrangement and power flow (top row), and relation of transmission ratio i_{rev} to ideal torque ratios t_I and t_{II} (bottom) for S12WS gearbox

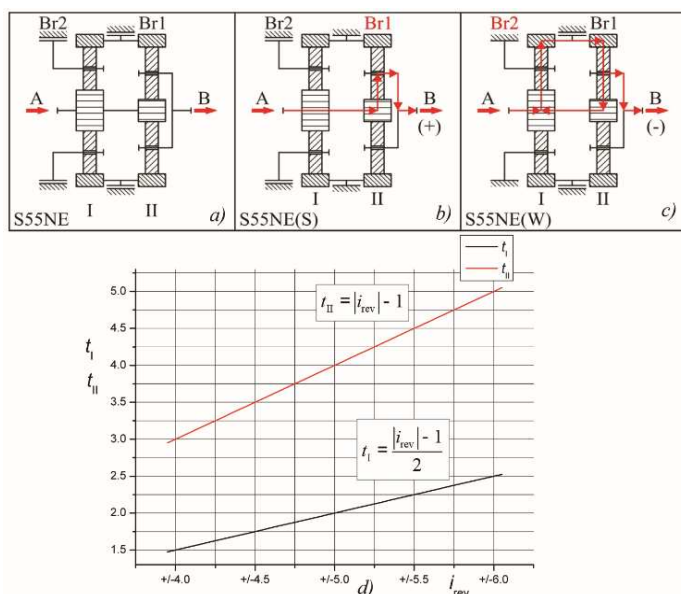


Figure 11

Kinematic arrangement and power flow (top row), and relation of transmission ratio i_{rev} to ideal torque ratios t_I and t_{II} (bottom) for S55NE gearbox

Conclusions

This paper covers two-speed planetary gear trains, with four external shafts controlled by two brakes, composed of two simple component PGTs, complete with a systematization of their kinematic structures and layout variants. Due to their characteristics, such gear configurations are applicable in systems which require the transmission ratio to be change under load, or without disconnecting the prime mover from the transmission. A concise determination of the structure and important basic parameters of two-speed planetary gear trains is also presented, enabled by the application of DVOBRZ, a computer program developed for the research of two-speed planetary gear trains. The procedure is explained by a numerical example dealing with the application for a railway vehicle, where two directions of rotation, at the same speed are necessary. All possible schemes obtained by program are then analyzed and the main parameters are defined. The most appropriate scheme is selected by ranking the obtained systems according to technological demands.

References

- [1] Syzrantsev, V., Syzrantseva, K.: The Arc Teeth Semi-rolled Cylindrical Gear Meshing Geometry, Acta Polytechnica Hungarica, Vol. 19, No. 2, 2022, pp. 173-192

-
- [2] Milovančević, M., Milčić, D., Andjelkovic, B., Vračar, Lj.: Train Driving Parameters Optimization to Maximize Efficiency and Fuel Consumption, *Acta Polytechnica Hungarica*, Vol. 19, No. 3, 2022, pp. 143-154
- [3] Tigh Kuchak A. J., Marinkovic D., Zehn M.: Finite element model updating - Case study of a rail damper, *Structural Engineering and Mechanics*, Vol. 73, No. 1, 2020, pp. 27 -35
- [4] Bhagat, P. R., Naz, F., Magda, R.: Role of Industry 4.0 Technologies in Enhancing Sustainable Firm Performance and Green Practices, *Acta Polytechnica Hungarica*, Vol. 19, No. 8, 2022, pp. 229-248
- [5] Kuchak, A. J. T., Marinkovic, D., Zehn, M., 2021, Parametric Investigation of a Rail Damper Design Based on a Lab-Scaled Model, *Journal of Vibration Engineering and Technologies*, 9(1), pp. 51-60
- [6] Fischer, S.: Geogrid reinforcement of ballasted railway superstructure for stabilization of the railway track geometry – A case study, *Geotextiles and Geomembranes*, Vol. 50, 2022, pp. 1036-1051
- [7] Macura, D., Laketić, M., Pamučar, D., Marinković, D.: Risk Analysis Model with Interval Type-2 Fuzzy FMEA – Case Study of Railway Infrastructure Projects in the Republic of Serbia, *Acta Polytechnica Hungarica*, Vol. 19, No. 3, 2022, pp. 103-118
- [8] Jover, V., Fischer, S.: Statistical analysis of track geometry parameters on tramway line no. 1 in Budapest, *The Baltic Journal of Road and Bridge Engineering*, Vol. 17, No. 2, 2022, pp. 75-106
- [9] Jovanović, V., Janošević, D., Pavlović, J: Analysis of the Influence of the Digging Position on the Loading of the Axial Bearing of Slewing Platform Drive Mechanisms in Hydraulic Excavators, *Facta Universitatis-Series Mechanical Engineering*, Vol. 19, No. 4, 2022, pp. 705-718
- [10] Müller, H. W.: *Die Umlaufgetriebe*. 2. Auflage. Springer Verlag, Berlin, 1998
- [11] Kudriavtsev, V. N., Kirdyiashev, I. N.: *Planetary Gears Handbook*. Leningrad: Mashinostroenie, Leningrad, 1977
- [12] Tkachenko, V.: *Planetary Mechanisms. Optimal Design*, Harkov: HAI, 2003 (in Russian)
- [13] Arnaudov, K., Karaivanov, D.: The torque method used for studying coupled two-carrier planetary gear trains, *Transactions of FAMENA*, Vol. 37, No. 1, 2013, pp. 49-61
- [14] Troha, S.: *Analysis of a planetary change gear train's variants* (in Croatian), PhD Thesis. Rijeka: Faculty of Engineering – University of Rijeka, 2011
- [15] Jelaska, D. T.: *Gears and Gear Drives*. Wiley & Sons, Chichester, 2012
- [16] Looman, J. *Zahnradgetriebe*. 3. Auflage. Berlin: Springer Verlag, 1996

- [17] Troha, S., Vrcan, Ž., Karaivanov, D., Isametova, M.: The Selection of Optimal Reversible Two-speed Planetary Gear Trains for Machine Tool Gearboxes, *Facta Universitatis-Series Mechanical Engineering*, Vol. 18, No. 1, 2020, pp. 121-134
- [18] Arnaudov, K., Karaivanov, D.: *Planetary Gear Trains*, 1st edition, CRC Press, Boca Raton, 2019
- [19] Stefanović-Marinović, J., Vrcan, Ž., Troha, S., Milovančević, M.: Optimization of two-speed planetary gearbox with brakes on single shafts, *Reports in Mechanical Engineering*, Vol. 3, No. 1, 2022, pp. 94-107
- [20] Pavlovic, A., Fragassa C.: Geometry optimization by FEM simulation of the automatic changing gear, *Reports in Mechanical Engineering*, Vol. 1, No. 1, 2020, pp. 195-205
- [21] Vrcan, Ž.; Stefanović-Marinović, J., Tica, M., Troha, S.: Research into the Properties of Selected Single Speed Two-Carrier Planetary Gear Trains, *Journal of Applied and Computational Mechanics*, Vol. 8 No. 2, 2022, pp. 699-709
- [22] Karaivanov, D., Troha, S.: Optimal Selection of the Structural Scheme of Compound Two-Carrier Planetary Gear Trains and their Parameters in: *Recent Advances in Gearing: Scientific Theory and Applications*, Radzevich, S. P. (ed.). Springer International Publishing, Basel, 2021, pp. 339-403
- [23] Kurhan D., Fischer S.: Modeling of the Dynamic Rail Deflection Using Elastic Wave Propagation, *Journal of Applied and Computational Mechanics*, Vol. 8, No.1, 2022, pp. 379-387
- [24] Franulović, M., Marković, K., Trajkovski, A.: Calibration of Material Models for the Human Cervical Spine Ligament Behaviour Using a Genetic Algorithm, *Facta Universitatis-Series Mechanical Engineering*, Vol. 19, No. 4, 2021, pp. 751-765

Numerical Investigation of Glue Laminated Timber Beams considering Reliability-based Design

Harrach Dániel, Muayad Habashneh, Majid Movahedi Rad*

Department of Structural and Geotechnical Engineering, Széchenyi István University, Egyetem tér 1, 9026 Győr, Hungary
e-mail: harrach.daniel@sze.hu, habashneh.muayad@hallgato.sze.hu, majidmr@sze.hu

Abstract: Structural models and their related parameters, are most often considered as deterministic, in numerical analysis. However, according to test results, one can see the existence of uncertainties, in most cases, due to various reasons, such as, natural variabilities and ignorance. Thus, dealing with uncertainty has gained massive attention, due to its importance in structural analysis and anticipating the performance of models. In fact, in some cases of special structure components, like glue laminated timber beams, it appears to be, that there is an absence of information concerning uncertainties. Therefore, the main objective of this study is to inspect uncertainties that facing designers and their role in glue laminated timber beams behavior, by considering different material parameters as random variables. In addition, four-point bending tests are conducted and finite element analysis is conducted, using ABAQUS software, to model the nonlinear behavior of GLT beams. For purposes of numerical model calibration, Hill yield criterion constitutive model is considered based on the obtained data from the experimental test. The results of this study provide a better outline for understanding the effect of uncertainties on glue laminated timber beams.

Keywords: Glue laminated timber beams; Hill yield criterion; Reliability-based design; Finite element analysis

1 Introduction

Timber has been greatly considered as a construction material since centuries in various structural projects, due to its benefits such as its low cost, well mechanical properties, durability, lightweight material, and its ability to respond to seismic and high wind events without occurring of critical failure [1-3]. Moreover, timber is considered as anisotropic material which shows various constitutive relationship in tension and compression which categorized according to the direction of grain by three distinct directions: longitudinal, radial, and tangential [4] [5]. A composite doubly-curved laminated shells were investigated in the study of Monge et al. [6]

by utilizing kinematic models, where a simply supported shell was subjected to various loads. Also, in the study of Le *et al.* [7], an analytical technique was adopted to expect the nonlinear buckling behavior of graphene-reinforced composite laminate shells considering thermal environment. Taking into consideration that one of the most structural timber product is glued laminated timber (GLT) which can be effectively used in cases curved shapes production.

Glue laminated beams could be either horizontally or vertically laminated. Also, these configurations can illustrate the fact that the horizontal method can produce curved members efficiently [8].

Glued laminated timber nowadays is considered as one of most common building material since it has shown efficient behavior and saving energy properties. Thus, glue laminated timber is widely used in industrial projects.

Recently, GLT has been utilized in uncovered applications like vaulted roofs and huge open spaces. Also, glulam is utilized when you look for a mixture of aesthetic and structural qualities. This incorporates a scope of engineering applications, such as glulam gallery which was built in Johor Bahru [9], an arched glulam timber bridge in Sheshan golf court of Shanghai in China [10] and Grandstand of Kulm Hotel in St. Moritz [11].

Different constitutive models have been developed during last decades to represent the nonlinear behavior of timber, which can be classified into three categories: elasto-plastic material models, elastic-damage models and combination of elasto-plastic material with damage model [12] [13]. Thus, finite element models have been considered recently to simulate the behavior of timber.

Currently, the Hill yield criterion and Tsai-Hill criterion are widely used to model the timber behavior. For instance, Xu *et al.* [14] presented in their study a nonlinear finite element model to simulate the strength of GLT. A constitutive elasto-plastic model of timber beam with openings was introduced in the study of Guan and Zhu [15].

The existence of randomness such as in material, loadings, and geometry properties that might reduce the strength of timber, lead engineers to deal with uncertainties. Thus, a stochastic models of timber structures are required for designs. In fact, with contrary to deterministic approach, the probabilistic method improves design reliability where it provides several benefits to designers such as improve sensitivity analysis and allow designers to determine the crucial parameters of uncertain models [16].

Numerical investigations have turned into a significant common methodology for analyzing various designing systems. Simulations are normally depicted as the means for supplanting the actual world according to a combination of theories as well as envisioned models of reality.

Monte Carlo simulation technique was created to be a probabilistic way to deal with complex deterministic complications as computers simply simulate a large number of exploratory tests which yield random results [17]. In the study of Corradi et al. [18], the uncertainty in strength of reinforced timber was modelled and various bending tests were carried to illustrate the effect of reinforcement on timber strength. The randomness of longitudinal strength of timber beam according to the existence of knots was analyzed by Czmocho [19] where Monte Carlo technique was adopted to find the statistics of a specified timber elements. Jenkel et al. [20] investigated and analyzed two timber structures by considering stochastically models of material parameters.

The goal of this study is to examine the effect of reliability indices on the GLT beams using probabilistic finite element analysis. Thus, the novelty of the article is about considering the probabilistic design in order to make the model more reliable and safer in which the designer must deal with the existence of uncertainties to make the method more practical. Moreover, this paper presents the results of an experimental program of 4-point bending tests of GLT beams. A written code is used to pursue the required goal by considering the reliability index as a limit when the material parameters for both tension and compression sides of timber are considered as random variables. Moreover, Monte Carlo sampling method has been adopted to calculate the reliability indices depending on statistics of material parameters. Finally, determination of corresponding load, displacement, and mean stresses values.

The rest of this paper is structured as: Section 2 introduce the used model of timber material behavior while Section 3 illustrates the reliability-based analysis. Furthermore, Section 4 introduces the experimental program and numerical model validation. Finally, Sections 5 and 6 represent the discussion of the results and conclusions respectively.

2 Behavior of Timber Material

The behavior of timber in compression parallel to grain exhibits some strain relaxing as a rule, it tends to be roughly viewed as elastic perfectly plastic. The fundamental anisotropic yield criterion which can be applied in evaluating timber is the Hill yield criterion.

The Hill yield criterion can be used in the numerical analysis of wooden elements. The theory is based on the generalization of the Huber-Mises-Hencky hypothesis for anisotropic materials where a connection is allowed between the anisotropic directions and material strengths. This can be adopted in modelling of materials, such as metals in rolling processes, which display partial orthotropic behavior or composite materials.

In case of using this criterion along the isotropic hardening option, the yield function is expressed by [21]:

$$f(\sigma) = \sqrt{(\sigma)^T \cdot [M] \cdot (\sigma)} - \sigma_0^{(\varepsilon^p)} \quad (1)$$

where σ_0 is the reference yield stress, ε^p is the equivalent plastic strain and $[M]$ represents mass matrix. While in case of use it with kinematic hardening option, the yield function will have the following expression:

$$f(\sigma) = \sqrt{((\sigma) - (\alpha))^T \cdot [M] \cdot ((\sigma) - (\alpha))} - \sigma_0 \quad (2)$$

where α is the yield surface translation vector. The Hill yield stress potential within a coordinate system which is aligned with anisotropy coordinate system can be formulated as following:

$$f(\sigma, \sigma_y) = F(\sigma_{22} - \sigma_{33})^2 + G(\sigma_{33} - \sigma_{11})^2 + H(\sigma_{11} - \sigma_{22})^2 + 2L\sigma_{23}^2 + 2M\sigma_{31}^2 + 2N\sigma_{12}^2 - \sigma_y^2 = 0 \quad (3)$$

where F, G, H, L, M and N are constants calculated experimentally [21] of the material in various orientations.

$$F = \frac{1}{2} \cdot \left(\frac{1}{R_{22}^2} + \frac{1}{R_{33}^2} - \frac{1}{R_{11}^2} \right) \quad (4)$$

$$G = \frac{1}{2} \cdot \left(\frac{1}{R_{33}^2} + \frac{1}{R_{11}^2} - \frac{1}{R_{22}^2} \right) \quad (5)$$

$$H = \frac{1}{2} \cdot \left(\frac{1}{R_{11}^2} + \frac{1}{R_{22}^2} - \frac{1}{R_{33}^2} \right) \quad (6)$$

$$L = \frac{3}{2 \cdot R_{23}^2} \quad (7)$$

$$M = \frac{3}{2 \cdot R_{13}^2} \quad (8)$$

$$N = \frac{3}{2 \cdot R_{12}^2} \quad (9)$$

where R_{ij} are anisotropic yield stress ratios.

Furthermore, this criterion can be used in modelling wood and processed wood products, fiber matrix composites, zirconium alloys and titanium alloys.

3 Reliability-based Analysis

The fundamental concept of reliability analysis can be presented, by assuming X_R which indicates the non-negative limit for X_S , thus the failure could be estimated through $X_R \leq X_S$. Supposing that X_R and X_S independent random variables having

probability density functions $f_R(X_R)$ and $f_S(X_S)$. The probability of failure P_f could be estimated according to following expression [22]:

$$P_f = P[X_R \leq X_S] = \iint_{X_R \leq X_S} f_R(X_R) f_S(X_S) dX_R dX_S \quad (10)$$

A possible definition of the previous formulation can be given in terms of the so-called limit-state function which is identified by:

$$g(X_R, X_S) = X_R - X_S \quad (11)$$

Taking into consideration that $g \leq 0$ identifies the failure domain D_f . Thus, P_f is expressed by:

$$P_f = F_g(0) \quad (12)$$

Additionally, P_f can be determined as:

$$P_f = \int_{g(X_R, X_S) \leq 0} f(X) dX = \int_{D_f} f(X) dX \quad (13)$$

Monte-Carlo sampling method involves realizations generating x of the random vector X upon their probability joint density function $f_X(x)$ and examining if failure occurs or not according to a given realization. The failure probability can be estimated according to the ratio of total number of points within the failure domain to the entire number of generated points. The number of points in the failure domain with respect to the total number of generated points is an estimator of the probability of failure. This concept could be formulated by initiating an indicator function of D_f [23]:

$$\chi_{D_f}(x) = \begin{cases} 1 & \text{if } x \in D_f \\ 0 & \text{if } x \notin D_f \end{cases} \quad (14)$$

Then equation (13) can be rewritten as:

$$P_f = \int_{-\infty}^{+\infty} \dots \int_{-\infty}^{+\infty} \chi_{D_f}(x) f_X(x) dx \quad (15)$$

Consequently, function $\chi_{D_f}(X)$ is a random variable having two points distribution:

$$\mathbb{P}[\chi_{D_f}(X) = 1] = P_f \quad (16)$$

$$\mathbb{P}[\chi_{D_f}(X) = 0] = 1 - P_f \quad (17)$$

where $P_f = \mathbb{P}[X \in D_f]$. The mean value and variance of $\chi_{D_f}(X)$ are expressed by:

$$\mathbb{E}[\chi_{D_f}(X)] = 1 \cdot P_f + 0 \cdot (1 - P_f) = P_f \quad (18)$$

$$\text{Var}[\chi_{D_f}(X)] = \mathbb{E}[\chi_{D_f}^2(X)] - (\mathbb{E}[\chi_{D_f}(X)])^2 = P_f - P_f^2 = P_f(1 - P_f) \quad (19)$$

In Monte-Carlo sampling method, to determine P_f , the following estimator of mean value is applied:

$$\mathbb{E} \left[\chi_{D_f}(X) \right] = \frac{1}{Z} \sum_{z=1}^Z \chi_{D_f}(X^{(z)}) = \hat{P}_f \quad (20)$$

Where $X^{(z)}$ are random independent vectors (where $z = 1, \dots, Z$) accompanied with probability density functions which can be determined by $f_X(x)$. Due to the uncertainties, the material properties are defined as a random variables and it follows the Gaussian distribution with mean value \mathbb{E} and variance Var . Accordingly, the mean value and the variance of the estimator can be simply determined as the following:

$$\mathbb{E}[\hat{P}_f] = \frac{1}{Z} \sum_{z=1}^Z \mathbb{E} \left[\chi_{D_f}(X^{(z)}) \right] = \frac{1}{Z} Z P_f = P_f \quad (21)$$

$$\text{Var}[\hat{P}_f] = \frac{1}{Z^2} \sum_{z=1}^Z \text{Var} \left[\chi_{D_f}(X^{(z)}) \right] = \frac{1}{Z^2} Z P_f (1 - P_f) = \frac{1}{Z} P_f (1 - P_f) \quad (22)$$

Therefore, the reliability constraint can be illustrated by considering the reliability index β as:

$$\beta_{target} - \beta_{calc} \leq 0 \quad (23)$$

To calculate β_{target} and β_{calc} , the following equations are used:

$$\beta_{target} = -\Phi^{-1}(P_{f,target}) \quad (24)$$

$$\beta_{calc} = -\Phi^{-1}(P_{f,calc}) \quad (25)$$

4 Numerical Model Validation

4.1 Experimental Program

In this research, four-point bending tests are conducted similar to de Jesus [24]. Based on this experimental work, three beams of 2500 mm long GLT beams having a cross-sectional area of 100 × 240 mm are tested. Adhesion test of timber was performed before the start of the tests. Commercial glulam available beams are used, the properties of which were defined by the producer. Table 1 represents the experimental properties of the used materials. Furthermore, the layout of the laboratory experimental test is shown in Figure 1.

Table 1
Material properties

<i>Material</i>	<i>Flexural strength</i> [N/mm ²]	<i>Compression strength</i> [N/mm ²]	<i>Tensile strength</i> [N/mm ²]	<i>Shear strength</i> [N/mm ²]	<i>Elastic modulus</i> [N/mm ²]
<i>Timber</i>	$f_{m,k} = 50.0$	$f_{c,0,k} = 29.0$ $f_{c,90,k} = 3.2$	$f_{t,0,k} = 30.0$ $f_{t,90,k} = 0.4$	$f_{v,k} = 4.0$	$E_{0,mean} = 9400$ $E_{90,mean} = 390$



Figure 1
Layout of the experiment

4.2 Material and Methods

Finite element analysis is considered to model the nonlinear behavior of GLT beams. 8-node solid element (C3D8) is considered for modeling the laminated beams. While the contact between lamellas is assumed perfectly bonded. At points of loading, steel bearing plates with dimensions of length = 150 mm, width = 100 mm and thickness = 30 mm are installed to avoid local failure which might be caused by crushing.

The geometry, loading and supporting conditions of the beams are presented in Figure 2, where the whole beams are tested under monotonic loading up to failure, with two concentrated load acting on the top of the beams.

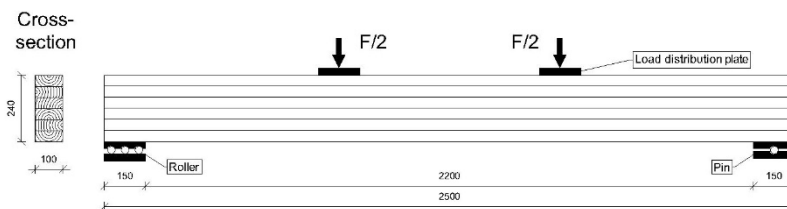


Figure 2
Beams geometry and loading condition

The boundary conditions are roller as a left support to produce rotation and horizontal movement and pin set as the right support to produce rotation. Two vertical concentrated loads are given on the distribution plates which are placed at the top of the beam and these applied loads are distributed by the coupling effect. Furthermore, a fine mesh is considered to obtain results with sufficient accuracy, where the number of total elements is approximately 60000. Figure 3 shows the considered numerical model, while Tables 2 and 3 show the numerical specimen's properties.

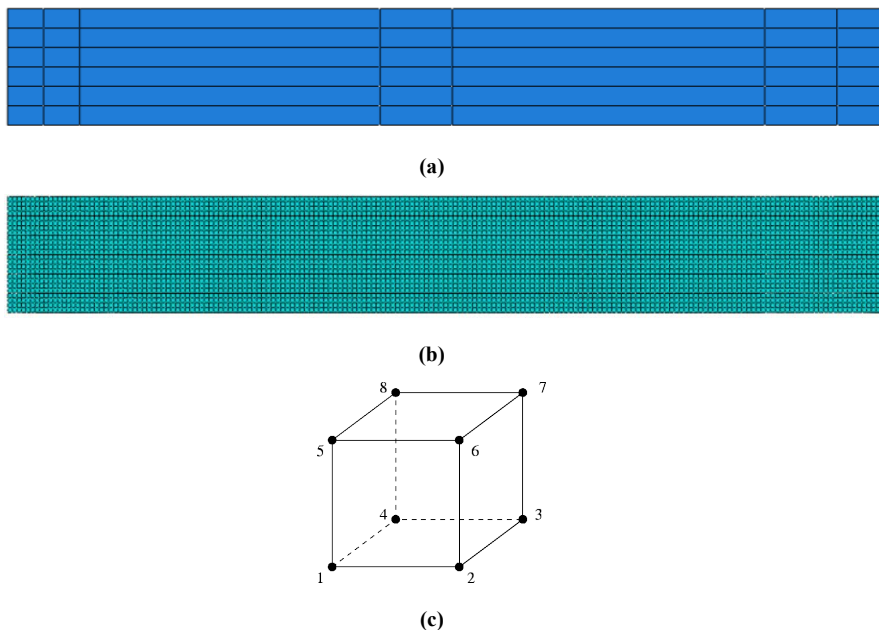


Figure 3

Considered numerical model: (a) assembly of the model (b) finite element mesh of the model (c) the considered elements for FEA

Table 2
Material properties for numerical modelling of timber (compression side)

Elasticity			Plasticity		
$E_1=9400$ MPa	$E_2=0.53$ GPa	$E_3=0.53$ GPa	$\sigma_{\text{yield}}=f_{c,0,k}=29.0$ MPa		
$G_{12}=0.72$ GPa	$G_{13}=0.24$ GPa	$G_{23}=0.24$ GPa	$R_{11}=5.800$	$R_{22}=0.640$	$R_{33}=0.640$
$\nu_{12}=0.40$	$\nu_{13}=0.40$	$\nu_{23}=0.40$	$R_{12}=1.386$	$R_{13}=1.386$	$R_{23}=1.386$

Table 3
Material properties for numerical modelling of timber (tension side)

Elasticity			Plasticity		
$E_1=9400$ MPa	$E_2=0.39$ GPa	$E_3=0.39$ GPa	$\sigma_{\text{yield}}=f_{t,0,k}=30.0$ MPa		
$G_{12}=0.72$ GPa	$G_{13}=0.24$ GPa	$G_{23}=0.24$ GPa	$R_{11}=6.000$	$R_{22}=0.080$	$R_{33}=0.080$
$\nu_{12}=0.40$	$\nu_{13}=0.40$	$\nu_{23}=0.40$	$R_{12}=1.386$	$R_{13}=1.386$	$R_{23}=1.386$

Figure 4 show the deflections of the middle cross section of the validated model compared to the average experimental test.

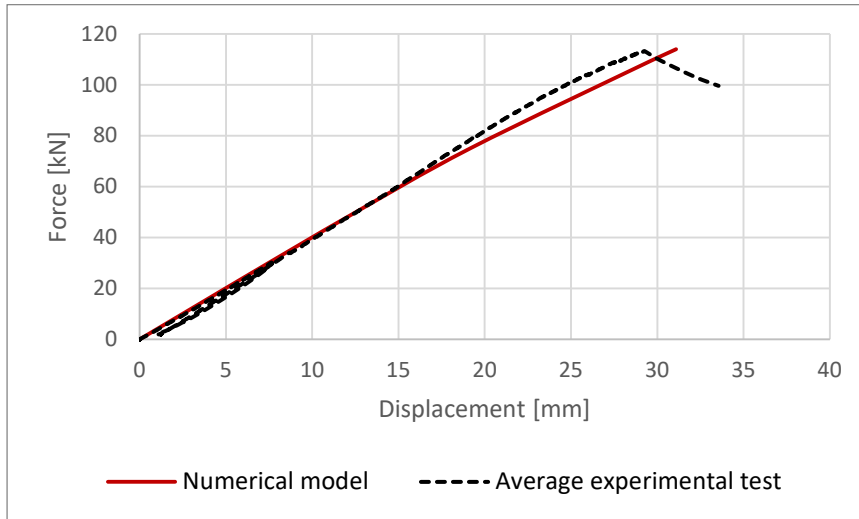


Figure 4

Comparison of experimental and numerical results

5 Results and Discussion

In order to validate the numerical model, finite element software (ABAQUS) is used based on the collected data from experimental tests. Afterward, a code is written and connected to ABAQUS to begin the analysis considering the reliability index as a limit and timber properties as random variables with mean values and standard deviations. Table 4 represents the considered random variables for timber material.

Table 4
Considered random variables of material properties

Parameter	$f_{c,0,k}$	$f_{c,90,k}$	$f_{v,k}$	$f_{t,0,k}$	$f_{t,90,k}$	E_0	E_{90}	G	ν
	N/mm^2	N/mm^2	N/mm^2	N/mm^2	N/mm^2	N/mm^2	N/mm^2	GPa	
Mean	29.00	3.20	4.00	30.00	0.40	9400	390	0.72	0.40
Std. Dev.	5%								

The Monte Carlo simulation technique is used to analyze the samples according to various material properties to examine the effect of reliability index on the behavior of the timber beam by assuming the number of sample point ($Z = 3 \times 10^6$). For illustration, Table 5 shows results of three different considered reliability index.

The effect of reliability index (β) as it works as a limit is obvious on the results alongside the variation of the material properties to show the corresponding loads (F) and displacements (U). Furthermore, adopting small values of β will produce higher loads, thus greater values of displacements too, so a small value β will involve more applied loads to be achieved. However, assuming the material properties with a variance, will cause the operation to produce random material properties, for each cycle and this explains how the role of uncertainties, is considered in this paper.

Table 5
Results of beam analysis

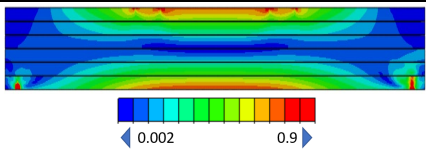
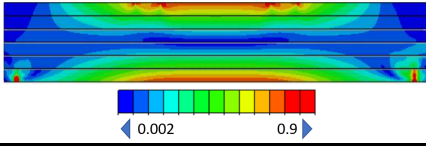
β	$f_{c,0,k}$ N/mm ²	$f_{c,90,k}$ N/mm ²	$f_{v,k}$ N/mm ²	$f_{t,0,k}$ N/mm ²	$f_{t,90,k}$ N/mm ²	E_0 N/mm ²	E_{90} N/mm ²	G GPa	ν	U mm	F kN
4.83	27.44	3.35	4.02	31.40	0.41	9308	384	0.71	0.42	22.07	88
4.28	30.19	3.42	3.78	30.06	0.38	8478	386	0.68	0.41	23.16	90
3.32	26.02	3.14	3.83	26.60	0.45	9271	411	0.71	0.39	23.39	92

Moreover, the variation of material properties which showed in Table 4, indicates that the performance of the applied 5% standard deviation on those values and the results are changed accordingly where the material properties are directly affecting the load and displacement values alongside with the inserted β values.

Another comparison is made to show the stress distribution of the model according to three different β values as shown in table 6. Besides, Table 7 shows the deterministic results which obtained by applying the ultimate load (F_u). Also, the mean stress value and the corresponding displacement (U) are presented.

As three different models having different β values were considered, it can be noticed that the value of mean stress increases as β decreases, also the yielding stresses distribution which presented by the red color are more intense in the deterministic case than the probabilistic case.

Table 6
Stress distribution according to probabilistic analysis

β	F (kN)	Displacement (mm)	Mean stress (MPa)	Stress distribution
4.83	88	22.07	12.04	
4.28	90	23.16	12.35	

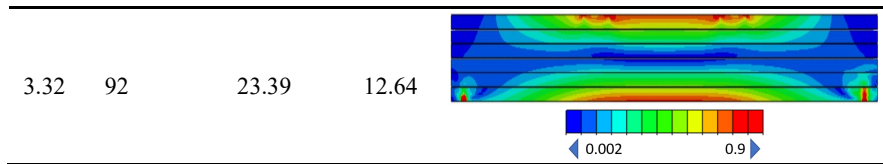
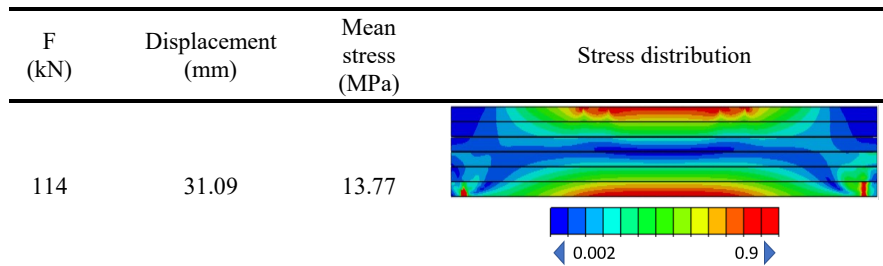


Table 7

Stress distribution of according to deterministic analysis



From the obtained results of introducing the probabilistic analysis, it can be noticed that that the values of mean stresses in case of deterministic design are higher than which are obtained in probabilistic design. Hence, we can say that the β is working as a bound for a safe design controlling the yielding status in the model, where the intensity of the stress is graded from maximum red to minimum blue as seen in tables.

Conclusions

In this paper, the effect of considering the reliability index, for glue laminated timber beams, is examined, by using deterministic and reliability-based finite element analysis. Justification of the numerical model has been proposed using the Hill yield criterion constitutive model after recording the necessary data according to the experimental tests. In addition, a written code was utilized to achieve the aim of considering the reliability index as a limit while material properties of timber are considered as random variables with mean values and standard deviation for each parameter. Hence, according to what have been mentioned previously, the following key points are noted:

- 1) The effect of considering β is obvious on the results as it works as a limit together with the varied material properties to provide the corresponding loads and displacements.
- 2) It can be noticed according to the obtained results that as β decreases, the corresponding values of mean stresses increases.
- 3) Choosing smaller values of β will produce greater loads, thus greater displacements.

- 4) The considered standard deviation and mean values of timber properties causes random varied results since the timber properties are directly affecting the load and displacement values collaborating with the inserted β values.
- 5) Yield stress distributions are less intensive in the probabilistic cases in comparison to the deterministic cases, thus we can say that β works as a bound parameter controlling the yield state in the model.

References

- [1] Kasal B, Leichti RJ. State of the art in multiaxial phenomenological failure criteria for wood members. *Progress in Structural Engineering and Materials* 2005;7:3–13. <https://doi.org/10.1002/pse.185>.
- [2] Yeomans DT. *The development of timber as a structural material*. Routledge; 2017. <https://doi.org/10.4324/9781315240305>.
- [3] Kurhan D, Fischer S. Modeling of the Dynamic Rail Deflection using Elastic Wave Propagation. *Journal of Applied and Computational Mechanics* 2022;8:379–87. <https://doi.org/10.22055/JACM.2021.38826.3290>.
- [4] Eslami H, Jayasinghe LB, Waldmann D. Nonlinear three-dimensional anisotropic material model for failure analysis of timber. *Engineering Failure Analysis* 2021;130:105764. <https://doi.org/10.1016/j.engfailanal.2021.105764>.
- [5] Frontmatter. *Structural Timber Design to Eurocode 5*, John Wiley & Sons, Ltd; 2007, p. i–xii. <https://doi.org/https://doi.org/10.1002/9780470697818.fmatter>.
- [6] Monge JC, Mantari JL, Yarasca J, Arciniega RA. On Bending Response of Doubly Curved Laminated Composite Shells Using Hybrid Refined Models. *Journal of Applied and Computational Mechanics* 2019;5:875–99. <https://doi.org/10.22055/JACM.2019.27297.1397>.
- [7] Le NL, Nguyen TP, Vu HN, Nguyen TT, Vu MD. An Analytical Approach of Nonlinear Thermo-mechanical Buckling of Functionally Graded Graphene-reinforced Composite Laminated Cylindrical Shells under Compressive Axial Load Surrounded by Elastic Foundation. *Journal of Applied and Computational Mechanics* 2020;6:357–72. <https://doi.org/10.22055/JACM.2019.29527.1609>.
- [8] How S, Sik HS, Anwar UMK, others. An Overview of Manufacturing Process of Glue-laminated Timber. *Timber Technology Bulletin* 2016.
- [9] Shing Sik H, Khairun Anwar Uyup M. An Overview of Manufacturing Process of Glued-Laminated Timber n.d.
- [10] Cheng X, Liu W, Lu W, Yang H, Yue K. Engineering Application of Glued Laminated Timber Structures in China. *Applied Mechanics and Materials*

- 2011;71–78:577–82.
<https://doi.org/10.4028/WWW.SCIENTIFIC.NET/AMM.71-78.577>.
- [11] Glavinić IU, Boko I, Torić N, Vranković JL. Application of hardwood for glued laminated timber in Europe. *Journal of the Croatia Association of Civil Engineers* 2020;72:607–16. <https://doi.org/10.14256/JCE.2741.2019>.
- [12] Hoffman O. The Brittle Strength of Orthotropic Materials. *Journal of Composite Materials* 1967;1:200–6. <https://doi.org/10.1177/002199836700100210>.
- [13] Benvenuti E, Orlando N, Gebhardt C, Kaliske M. An orthotropic multi-surface damage-plasticity FE-formulation for wood: Part I – Constitutive model. *Computers & Structures* 2020;240:106350. <https://doi.org/https://doi.org/10.1016/j.compstruc.2020.106350>.
- [14] Xu B-H, Bouchaïr A, Taazount M, Racher P. Numerical simulation of embedding strength of glued laminated timber for dowel-type fasteners. *Journal of Wood Science* 2013;59:17–23. <https://doi.org/10.1007/s10086-012-1296-0>.
- [15] Guan ZW, Zhu EC. Finite element modelling of anisotropic elasto-plastic timber composite beams with openings. *Engineering Structures* 2009;31:394–403. <https://doi.org/10.1016/j.engstruct.2008.09.007>.
- [16] Choi S-K, Grandhi R, Canfield RA. *Reliability-based structural design*. Springer Science & Business Media; 2006.
- [17] Kottegoda Rosso, Renzo., Kottegoda, N. T., NT. *Applied statistics for civil and environmental engineers*. Oxford, UK; [Malden, MA]: Blackwell Pub.; 2008.
- [18] Corradi M, Borri A, Righetti L, Speranzini E. Uncertainty analysis of FRP reinforced timber beams. *Composites Part B: Engineering* 2017;113:174–84. <https://doi.org/https://doi.org/10.1016/j.compositesb.2017.01.030>.
- [19] Czmocho I. Probabilistic Modelling of Bending Strength of Timber Beams with the Help of Weak Zones Model. *Periodica Polytechnica Civil Engineering* 2021;65:1295–1305. <https://doi.org/10.3311/PPci.19228>.
- [20] Jenkel C, Leichsenring F, Graf W, Kaliske M. Stochastic modelling of uncertainty in timber engineering. *Engineering Structures* 2015;99:296–310. <https://doi.org/https://doi.org/10.1016/j.engstruct.2015.04.049>.
- [21] Hill R. *The mathematical theory of plasticity* n.d.:356.
- [22] Haldar Achintya, Mahadevan Sankaran. *Probability, reliability, and statistical methods in engineering design* 2000:304.
- [23] Choi SK, Canfield RA, Grandhi R v. *Reliability-based structural design. Reliability-Based Structural Design* 2007:1–306. <https://doi.org/10.1007/978-1-84628-445-8/COVER>.

- [24] de Jesus AMP, Pinto JMT, Morais JLL. Analysis of solid wood beams strengthened with CFRP laminates of distinct lengths. *Construction and Building Materials* 2012;35:817–28. <https://doi.org/https://doi.org/10.1016/j.conbuildmat.2012.04.124>.
- [25] Smith M. ABAQUS/Standard User's Manual, Version 6.9. United States: Dassault Systèmes Simulia Corp; 2009.

Experimental and Statistical Analysis of the Vertical Temperature Gradient, for Ballastless Railway Track, in Alpine and Plateau Environs

Ping Lou^{1,2}, Tao Shi¹, Weiqi Zheng¹, Xingwang Sheng¹,
Chuanshu Li³, Szabolcs Fischer⁴

¹School of Civil Engineering, Central South University, Changsha 410075, China

²MOE Key Laboratory of Engineering Structures of Heavy-haul Railway, Central South University, Changsha 410075, China

³China Railway fifth Bureau Group, Changsha 410000, China

⁴Széchenyi István University, Egyetem tér 1, H-9026 Győr, Hungary

e-mail: pinglou@csu.edu.cn, shitao@csu.edu.cn, wqzheng@csu.edu.cn,
shengxingwang@csu.edu.cn, fischersz@sze.hu

Abstract: Temporal temperature evolution of ballastless railway track is a random process caused by complex environmental actions. The vertical temperature gradient (VTG), varying continuously with time, has significant effects on the repeated deformation of ballastless track. However, few researchers have considered the statistical analysis of VTGs in alpine and plateau environs characterized by high altitude, strong solar radiation and high diurnal temperature differences. In this study, a temperature field test platform of ballastless track was established in Shannan City, Tibet and the temperature field of ballastless track was measured. Based on four statistical methods, a Monte Carlo simulation (MCS), Gaussian mixture model (GMM), Generalized Pareto distribution (GPD) and a third-order polynomial normal transformation technique (TPNT), the VTGs of ballastless track in alpine and plateau areas, are statistically analyzed. The results show that the applied statistical methods, used for predicting the VTG representative value, in ballastless track, are feasible within different application conditions. The recommended positive and negative representative values of the VTG of ballastless track are 91.58 °C/m and -40.15 °C/m, and 82.83 °C/m and -35.03 °C/m, with failure probabilities of 1% and 5% respectively, in alpine and plateau areas. The research results can provide a reference for the design and maintenance of ballastless track used in alpine and plateau environs.

Keywords: Ballastless track; Temperature distribution; Long-term field test; Vertical temperature gradient; alpine and plateau environs; Statistical analysis

1 Introduction

The high-speed railways, due to their high transportation capacity, environmental friendliness, and safe operation, have been the latest trend for railway developments all over the world [1] [2]. Among them, the Southwest Plateau Railway is of great significance to China's 13th Five-Year Plan, which subsequently climbs 5000 m and runs across the Tibetan plateau [3] [4]. The alpine and plateau environs generally experience high levels of solar radiation, low rainfall, and large diurnal temperature variation [5]. The effects of the complex alpine plateau climatic environment on the construction of the Southwest Plateau Railway should not be ignored.

Ballastless tracks with high stability, small settlements, and low maintenance have been widely utilized and developed in the construction of the Southwest Plateau Railway, but the damage of them cannot be avoided during their service life. Ballastless tracks with large material property differences and complex climatic variations, were vulnerable to various degrees of damage in the complex service environment [6]. The effects of temperature loads on the interface damage evolution process of ballastless tracks have been analyzed [7] [8]. The damage characteristics of ballastless track structures were related to deformation imbalance caused by thermal loads, and various degrees of the arch at the joints between prefabricated slabs were produced under non-uniform temperature distributions [9]. The problems of ballastless track structures have been analyzed combined with the effect of temperature increase and positive temperature gradient [10]. The damage of ballastless tracks under time-varying service environments was closely related to the effects of temperature gradients. Therefore, the study of temperature gradients has significant effects on the optimization design, maintenance, and damage control of ballastless tracks in alpine and plateau environs.

Many pieces of research focused on temperature distributions in concrete structures exposed to various environmental actions [11]. The heat transfer analysis of ballastless tracks has been conducted to calculate the non-uniform temperature distributions and vertical temperature gradients based on meteorological data such as solar radiation and environmental temperature [6] [12]. The vertical temperature gradient and temperature variation of ballastless tracks in natural environment have been investigated, based on field test and temperature simulation [13] [14]. The variation trend of temperature field evolution and temperature gradient of ballastless tracks has been studied considering the geographical locations and environmental conditions [15] [16]. Based on the meteorological data, the nonlinear temperature distribution and temperature gradients of ballastless tracks obey certain statistical regularity [17]. Because meteorological conditions change all the time, the statistical characteristics of temperature gradients of ballastless tracks are varied. Thus, the statistical analysis of the temperature gradient in ballastless tracks exposed to alpine plateau climatic conditions deserves to be studied in detail.

The statistical analysis of temperature gradients, in different structures considering environmental conditions, has been concerned by many researchers. Effective extreme value analysis has been proposed to establish the most unfavourable temperature gradient of concrete-filled steel tubes [18]. The statistical characteristic of maximum or minimum temperature differences has been described by the Gaussian mixture model of flat-steel-box girders and truss girders [19]. Temperature action representative values in a bridge-track system have been researched through a statistical method of a virtual distribution built by high-order moments of data [20]. Based on the stationary binomial probability model, the vertical temperature gradient models and transverse temperature gradient models of concrete box girder have been determined [21] [22]. In the existing studies, the statistical analysis of a certain mathematical model applied to VTG in different structures has been concerned [23]. However, the application of different statistical methods is various under different monitoring periods and analysis objectives. The comparative analysis of different statistical methods for predicting VTG of ballastless track in alpine and plateau environs warrants further detailed study.

In this study, based on the long-term temperature field test of ballastless track in Shannan City, Tibet, the statistical methods including MCS, GMM, GPD, and TPNT, are used to investigate the VTG variation trend of ballastless track considering complex alpine plateau climatic. The VTG representative values with different failure probabilities are analyzed based on the four statistical methods. Furthermore, the recommended positive and negative representative values of VTG of ballastless track are determined.

2 Experimental Program

2.1 Experimental Setup

The temperature distribution of ballastless track influenced by atmospheric temperature, wind speed, altitude, and climatic conditions vary continuously with time. The site construction of the ballastless track located in Gongga County, Shannan City, Tibet Autonomous Region, China (N29.25°, E92.21°) was shown in Figure 1. The ballastless track is situated in the plateau climatic zone (mountainous area), with an air pressure of 61.3 kPa and an altitude of 3535 m.

The length and width of the ballastless track were 4.0 m and 2.8 m, respectively, and the interval between supporting block tracks was 0.65 m. The centerline of the ballastless track was in the direction of northeastern 23°, and the plane layout of the ballastless track was described in Figure 2. Section A-A was the middle section of the ballastless track, where temperature measuring sensors were arranged.



)a) Concrete pouring of ballastless track



)b) Concrete maintenance of ballastless track

Figure 1

The ballastless track used on site

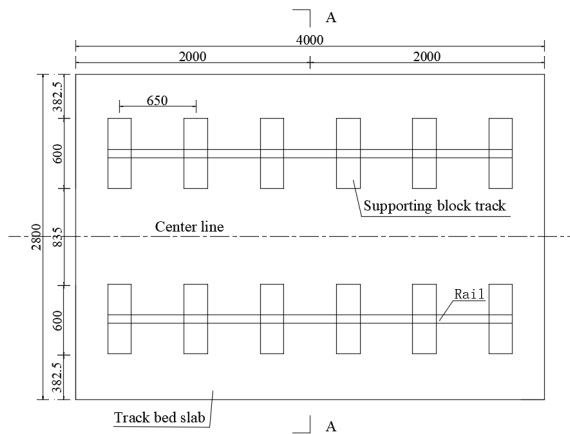


Figure 2

The plane layout of ballastless track (unit: mm)

2.2 Experimental Procedure

The monitoring period of the long-term field test was from 00:19:10 on January 31, 2021 to 03:19:10 on March 1, 2022, with a sampling frequency of 0.5 hours. Thermometers were arranged on the A-A section of ballastless track, to obtain the temperature variation trend of ballastless track in Gongga County. The VTGs of ballastless track were analyzed, and the VTG representative values of ballastless track with different failure probabilities were determined. Structural dimensions and layout of thermometers of ballastless track were shown in Figure 3.

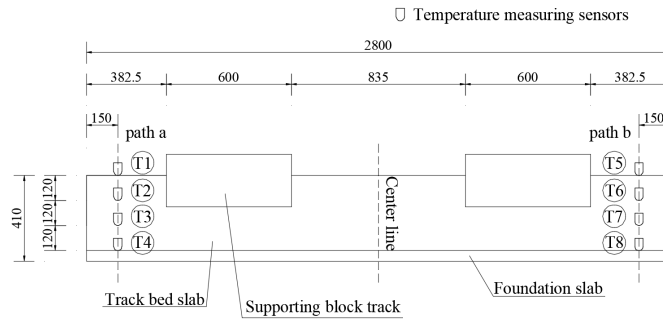
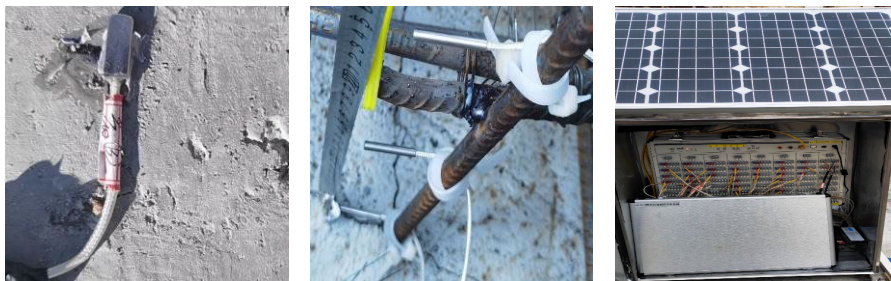


Figure 3

Structural dimensions and layout of thermometers (unit: mm)

From Figure 3, the thermometers T1, T2, T3, and T4 were arranged on the path a of ballastless track, and the thermometers T5, T6, T7, and T8 were arranged on path b of ballastless track. The thermometers T1 and T5 were arranged on the top edge of ballastless track, and the thermometers T4 and T8 were arranged on the bottom edge of ballastless track. The arrangement of thermometers and the data acquisition system were shown in Figure 4.



(a) Thermometers on the top edge of the ballastless track

(b) Thermometers embedded in the ballastless track

(c) Data acquisition system powered by solar energy

Figure 4

The arrangement of thermometers in ballastless track and data acquisition system

From Figure 4, thermometers were arranged on the top edge of ballastless track and embedded in ballastless track, respectively, to obtain the temperature distribution of ballastless track. Thermometers YC-PT1000/3 with the accuracy ± 0.1 °C and measurement ranging from -85 °C to 300 °C, were used to monitor the temperature variations of ballastless track and atmospheric. Based on the temperature monitoring data of ballastless track, the non-uniform temperature distribution, and the temporal and spatial temperature variation of ballastless track were put forward.

2.3 Experimental Results

In this experiment, the temperature variations along path a and b of the ballastless track from January 31, 2021 to March 1, 2022 were investigated. Except for several data missing due to instrumental failure, most of the temperature data has been obtained via the monitoring system. The temperature evolutions along path a and b of the ballastless track were shown in Figure 5.

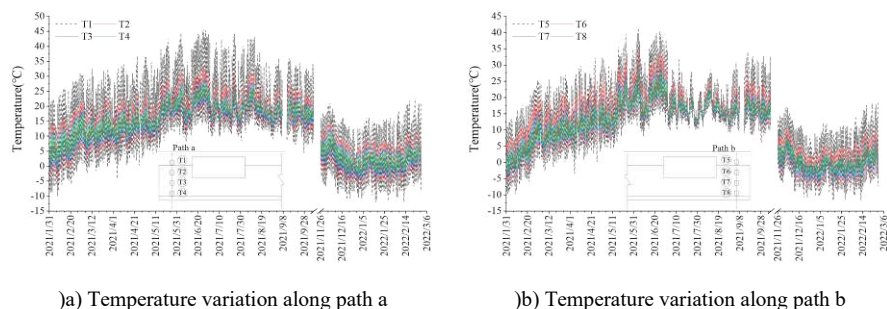


Figure 5
Temperature variations of the ballastless track

From Figure 5, the temperature variation trend along path a and b of the ballastless track were almost the same. The temperature variation of sensor T1 along path a ranged from -12.06 °C to 45.61 °C, and the temperature variation of sensor T5 along path b ranged from -11.76 °C to 41.45 °C. The temperature variation trend along path a varied more drastically than that of path b. Due to the heat transfer laws of concrete materials, the evolution of the internal temperature of the ballastless track lags behind the edge temperature of the ballastless track [24]. The VTG of the track slabs is $(T_{\phi} - T_{\beta}) / D$, where T_{ϕ} is the temperature of the top edge in the track slabs; T_{β} is the temperature of the bottom edge in the track slabs; and D is the track slabs thickness (0.24 m). The VTG of ballastless track can provide an important reference for their design and maintenance, and the variation trend of VTGs (path a) and air temperature were shown in Figure 6.

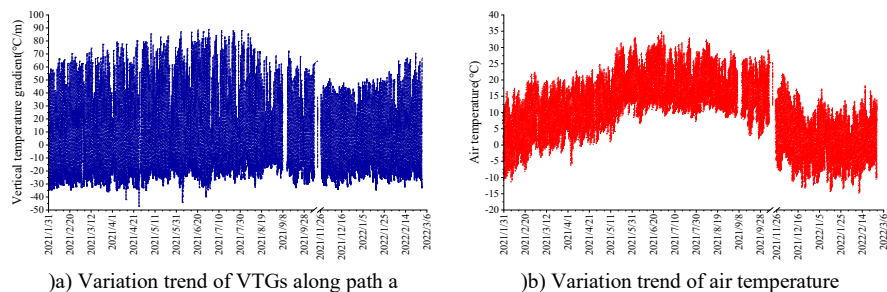


Figure 6
Comparison of the VTG in the ballastless track

From Figure 6, the variation characteristics of VTGs and air temperature were almost the same. The VTGs of ballastless track varied from $-47.16\text{ }^{\circ}\text{C}/\text{m}$ to $88.88\text{ }^{\circ}\text{C}/\text{m}$, and the atmospheric temperature varied from $-13.81\text{ }^{\circ}\text{C}$ and $35.09\text{ }^{\circ}\text{C}$. Furthermore, the distribution characteristics of VTGs were described and the VTG representative values with different failure probabilities were predicted based on various statistical methods.

3 Statistical Analysis

Because the most unfavourable VTGs of ballastless track occurred in the summer and winter of the long-term field test period from January 31, 2021 to March 1, 2022, the temperature experiment could reflect the statistical characteristics of a year. The temperature distribution of ballastless track showed temporal and spatial variation characteristics with the change of measured position and time, and the VTG representative values could be analyzed using statistical methods. Positive and negative daily extreme VTG along path a obtained from the long-term temperature field test were set as random variables, respectively. Statistical methods including MCS, GMM, GPD, and TPNT were used to describe the distribution characteristics of ballastless track' VTGs and predict the VTG representative value R_q with a failure probability q of 5%.

3.1 Monte-Carlo Simulation

Monte Carlo simulation is a method of repeated random sampling based on Bernoulli's law of large numbers, to predict the VTG representative values in ballastless track with different failure probabilities [25]. The positive daily extreme VTG sample set S , with a size of n_p ($n_p = 339$) was sampled randomly for W ($W=10^9$) times, and the sample set S^* could be obtained, where $S^* = \{S_1^*, S_2^*, \dots, S_W^*\}$. The performance function was defined as $G_i^* = R - S_i^*$, where R was the initial ultimate value; and the set G^* was determined by sampling randomly, where $G^* = \{G_1^*, G_2^*, \dots, G_W^*\}$. The VTG positive representative value R_q with different failure probabilities q of the ballastless track could be expressed in Eq. (1):

$$q = \frac{\sum_{i=1}^W L(G_i^*)}{W} \quad (1)$$

where: $L(x) = \begin{cases} 1 & x \leq 0 \\ 0 & x > 0 \end{cases}$; and W is the number of random experiments.

The failure frequency of VTG in the ballastless track was conducted in

W ($W=10^9$) random experiments, and the VTG positive representative value R_q with different failure probabilities q of the ballastless track could be calculated and shown in Figure 7.

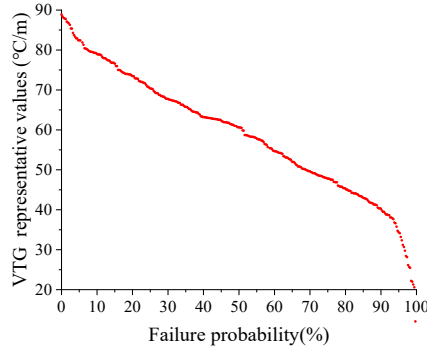


Figure 7

The VTG positive representative values with different failure probabilities

From Figure 7, the VTG positive representative values decreased with the increase of the failure probabilities. When the number of random experiments was large enough, the failure frequency of VTG was convergent to the failure probability of VTG. The VTG representative values showed nonlinear characteristics when the failure probability was less than 5% and more than 95%, because the statistical analysis of MCS was sensitive to the tail data of VTG sample. When the failure probability was between 5% and 95%, the VTG representative values were linearly correlated with failure probabilities. The VTG representative value with a failure probability of 5% was calculated in Eq. (2):

$$\frac{\sum_{i=1}^{10^9} L(R_{5\%} - S_i^*)}{10^9} = 5\% \quad (2)$$

Based on this, the VTG positive representative value of ballastless track in alpine and plateau environs was 82.41 °C/m with a failure probability of 5%. According to the same calculation principle, the VTG negative representative value of ballastless track was -34.13 °C/m with a failure probability of 5%.

3.2 Gaussian Mixture Model

The temperature distribution of ballastless track can be accurately described by GMM defined in Eq. (3), which is a statistical method composed of several Gaussian distributions [26].

$$f(X|\theta) = \sum_{l=1}^L \alpha_l \phi(X|\theta_l) \quad (3)$$

where α_i is the weight coefficient of the l^{th} Gaussian distribution ($\alpha_i \geq 0$ and $\sum_{i=1}^L \alpha_i = 1$); L is the number of combinations of Gaussian distribution; and $\phi(X | \theta_i)$ is the probability density function of the l^{th} Gaussian distribution, described in Eq. (4).

$$\phi(X | \theta_i) = \frac{1}{\sqrt{2\pi}\sigma_i} \exp\left(-\frac{(X - \mu_i)^2}{2\sigma_i^2}\right) \quad (4)$$

where θ_i is equal to (μ_i, σ_i^2) ; μ_i is the mean of the l^{th} Gaussian distribution; and σ_i^2 is the variance of the l^{th} Gaussian distribution. Based on the Expectation-maximization algorithm and Kolmogorov-Smirnov test, the parameters of the GMM $\theta=(\alpha_1, \alpha_2, \dots, \alpha_L; \theta_1, \theta_2, \dots, \theta_L)$ were estimated [27, 28]. When L was 4, significance level α was 0.05 and sample size was n_p , KS statistic D in Eq. (5) was 0.019 smaller than the critical value $D(n, \alpha)$, and the null hypothesis where the sample random variable X came from GMM failed to be rejected [29]. The statistical characteristics of VTG sample were described using GMM in Eq. (6):

$$D = \max_{1 \leq j \leq n} |F_N(X_j) - F_{N0}(X_j)| \quad (5)$$

Where X_j is the j^{th} VTG sample (with $j=1, 2, \dots, n$); F_N is the empirical cumulative distribution function; and F_{N0} is the cumulative distribution function of the VTG sample.

$$f(X|\theta) = \alpha_1\phi(X|\theta_1) + \alpha_2\phi(X|\theta_2) + \alpha_3\phi(X|\theta_3) + \alpha_4\phi(X|\theta_4) \quad (6)$$

where $\alpha_1=0.251$, $\alpha_2=0.098$, $\alpha_3=0.332$, $\alpha_4=0.320$; and $\theta_1=(77.70, 31.06)$, $\theta_2=(34.55, 91.14)$, $\theta_3=(63.34, 22.70)$, $\theta_4=(47.59, 30.10)$.

Based on this, the probabilistic histogram and probability density function of GMM was obtained as shown in Figure 8.

From Figure 8, the variation trend of probabilistic histogram and probability density function of GMM was almost the same, so the statistical characteristics of VTG in the ballastless track could be described by the GMM. Based on the trial algorithm and probability density function of the GMM, the VTG positive representative value R_q with different failure probabilities q in the ballastless track could be defined in Eq. (7):

$$q = \frac{\int_{R_q}^{+\infty} f(X)dX}{\int_0^{+\infty} f(X)dX} \quad (7)$$

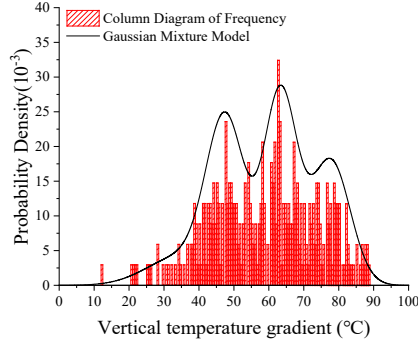


Figure 8
Distribution of vertical temperature gradient

Based on this, the VTG positive representative value of ballastless track in alpine and plateau environs was 82.41 °C/m with a failure probability of 5%. According to the same calculation principle, the VTG negative representative value of ballastless track was -34.56 °C/m with a failure probability of 5%.

3.3 Generalized Pareto Distribution

The GPD is a function of predicting the tail data of test sample that is beyond a position parameter, which can be expressed in Eq. (8):

$$P(X > u) = \begin{cases} 1 - (1 + \xi \frac{X-u}{\sigma})^{-1/\xi} & \xi \neq 0 \\ 1 - \exp(-\frac{X-u}{\sigma}) & \xi = 0 \end{cases} \quad (8)$$

where u is the position parameter; ξ is the shape parameter; and σ is the scale parameter [30]. The VTG representative values of different failure probabilities of the ballastless track could be predicted by GPD [31]. In detail, the VTG samples were divided into m ($m = 399$) groups of independent samples according to the interval of Δt (1 day). The maximum VTG value X_i in each group was determined, which belonged to the maximum value set $\{X_i\} (i = 1, 2, \dots, m)$, and the set of order statistics $\{X_i^*\}$ could be obtained by sorting the maximum value set, where $X_1^* \leq X_2^* \leq \dots \leq X_m^*$. The empirical cumulative probability function of order statistics was defined in Eq. (9):

$$\hat{F}(X_i^*) = F(X \leq X_i^*) = i / (m + 1) = i / 400 \quad (1 \leq i \leq 400) \quad (9)$$

Based on Minimum Squared Error, BoostStarp Method, and Trial Method, the size k of tail order statistic set was obtained and the sample S_1 was composed of tail order statistic, where $S_1 = \{X_{m-k+1}^* - u, X_{m-k+2}^* - u, \dots, X_m^* - u\}$. The position

parameter u was described in Eq. (10), and the shape parameter ξ_0 of the sample S_1 was calculated in Eq. (11):

$$u = X_{m-k}^* \quad (10)$$

$$\xi_0 = 0.5 \left(1 - \frac{E^2(S_1)}{\text{var}(S_1)} \right) \quad (11)$$

The sample-set Z was determined by repeated random sampling for k numbers from the sample S_1 , which was carried out p times, and the shape parameter ξ_z of sample set Z was computed, where $\xi_z = \{\xi_1, \xi_2, \dots, \xi_p\}$. The bias, variance, and mean square error of the shape parameter ξ_z were expressed from Eq. (12) to Eq. (14), respectively:

$$\text{bias}(\xi_z) = E(\xi_z) - \xi_0 = \frac{1}{p} \sum_{i=1}^p \xi_i - \xi_0 \quad (12)$$

$$\text{var}(\xi_z) = \frac{1}{p-1} \sum_{i=1}^p (\xi_i - \frac{1}{p} \sum_{j=1}^p \xi_j)^2 \quad (13)$$

$$\text{MSE}(\xi_z) = \text{bias}^2(\xi_z) + \text{var}(\xi_z) \quad (14)$$

When the size k , position parameter u , shape parameter ξ , and empirical cumulative probability $\hat{F}(u)$ of the tail order statistic set were 20, 81.88, -0.61, and 0.94, respectively, the mean square error of the tail order statistic set was the minimum, where $\text{MSE}(\xi) = 0.23$, and k , u , ξ , and $\hat{F}(u)$ were the optimal estimation results. When the shape parameter ξ is less than zero, the real shape parameter ξ tends to be zero. Thus, the shape parameter ξ was revised to zero with the modified GPD determined, and the scale parameter σ of the tail order statistic set was described in Eq. (15):

$$\sigma = 0.5 E(S_1) \left(\frac{E^2(S_1)}{\text{var}(S_1)} + 1 \right) \quad (15)$$

Based on this, the cumulative probability function of the random variable X of VTG, and the VTG representative value R_q with different failure probabilities q ($q \leq 11\%$) of the ballastless track were computed in Eq. (16) and Eq. (17):

$$F(X) = \begin{cases} \hat{F}(X) & X \leq u \\ \hat{F}(u) + [1 - \hat{F}(u)] [1 - \exp(-\frac{X-u}{\sigma})] & X > u \end{cases} \quad (16)$$

$$R_q = u - \sigma \ln \left(1 - \frac{(1-q) - \hat{F}(u)}{\hat{F}(u)} \right) \quad (17)$$

where $u = 81.88$, $\sigma = 5.48$, and $\hat{F}(u) = 0.94$. Based on this, the probabilistic histogram and probability density function of GPD with the random variable X larger than 81.88 were expressed and shown in Figure 9.

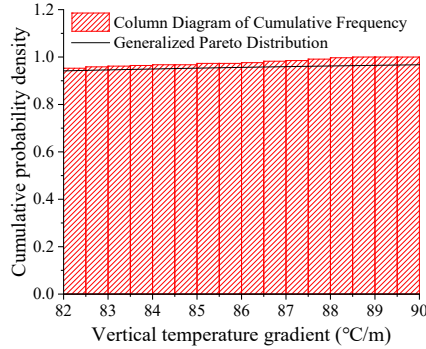


Figure 9
Distribution of vertical temperature gradient

From Figure 9, the probabilistic histogram and probability density function of GPD with the random variable X larger than 81.88 were almost the same, and the statistical characteristics of VTGs in the ballastless track were described by GPD ($X > u$). The VTG representative values were conservative because the probability density function of GPD was lower than the probabilistic histogram of VTG. Based on this, the VTG positive representative value of ballastless track in alpine and plateau environs was 82.77 °C/m with a failure probability of 5%. According to the same calculation principle, the VTG negative representative value of ballastless track was -34.25 °C/m with a failure probability of 5%.

3.4 Third-Order Polynomial Normal Transformation Technique

The evolution characteristics of VTGs in the ballastless track are described by the third-order polynomial normal transformation method, based on the definition of the probability moment without empirical judgment [32]. The first four moments (i.e., the mean, standard deviation, skewness, and kurtosis) of the VTG sample S of the ballastless track were calculated in Eq. (18) and Eq. (19) [33]:

$$\mu_s = \frac{1}{n} \sum_{j=1}^n X_j, \sigma_s = \sqrt{\frac{1}{n-1} \sum_{j=1}^n (X_j - \mu_s)^2} \quad (18)$$

$$\alpha_{rs} \sigma_S^r = \frac{1}{n-1} \sum_{j=1}^n (X_j - \mu_S)^r, r = 3, 4 \quad (19)$$

where μ_S , σ_S , α_{3S} , and α_{4S} were the mean, standard deviation, skewness, and kurtosis of the VTG sample S , respectively. The distribution variation of VTGs was analyzed, and the first four moments of the VTG samples of μ_S , σ_S , α_{3S} , and α_{4S} were 59.096, 15.123, -0.218, and 2.546, respectively. The first four moments (μ_G , σ_G , α_{3G} , and α_{4G}) of the performance function $Z = G(X) = R - S$ can be obtained by μ_S , σ_S , α_{3S} , and α_{4S} , which can be described in Eq. (20):

$$\mu_G = R - 59.096, \sigma_G = 15.123, \alpha_{3G} = -0.218, \alpha_{4G} = 2.546 \quad (20)$$

The performance function $Z = G(X)$ can be standardized using its mean and standard deviation, and the standardized performance function Z_G was approximated by a third-order polynomial of the standard normal random variable u , which was expressed in Eq. (21) and Eq. (22) [34]:

$$Z_G = \frac{G(X) - \mu_G}{\sigma_G} \quad (21)$$

$$Z_G = F(u, \mathbf{M}) = a_1 + a_2 u + a_3 u^2 + a_4 u^3 \quad (22)$$

where \mathbf{M} was the vector denoting the first four moments of the performance function $Z = G(X)$. The coefficients of a_1 , a_2 , a_3 , and a_4 were described from Eq. (23) to Eq. (26) [35] [36]:

$$a_1 + a_3 = 0 \quad (23)$$

$$a_2^2 + 2a_3^2 + 6a_2 a_4 + 15a_4^2 = 1 \quad (24)$$

$$6a_2^2 a_3 + 8a_3^3 + 72a_2 a_3 a_4 + 270a_3 a_4^2 = \alpha_{3G} \quad (25)$$

$$3(a_2^4 + 20a_2^3 a_4 + 210a_2^2 a_4^2 + 1260a_2 a_4^3 + 3465a_4^4) + 12a_3^2 (5a_2^2 + 5a_3^2 + 78a_2 a_4 + 375a_4^2) = \alpha_{4G} \quad (26)$$

With the skewness α_{3G} and kurtosis α_{4G} of the performance function known, the standardized performance function Z_G was expressed in Eq. (27), and the distribution characteristics of u and Z_G were shown in Figure 10:

$$Z_G = F(u, \mathbf{M}) = -0.045 + 1.097u + 0.045u^2 - 0.035u^3 \quad (27)$$

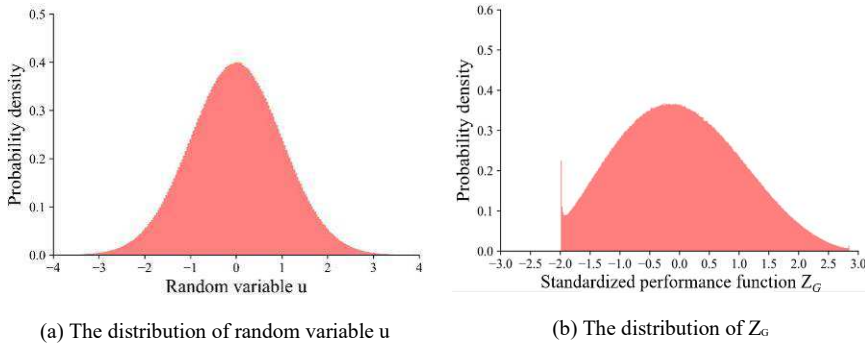


Figure 10

The distribution of random variable u and standardized performance function Z_G

From Figure 10, the distribution variation of the standardized performance function Z_G was different from that of the random variable u . The distribution of Z_G was asymmetric, and the probability density of negative Z_G was higher than that of positive Z_G . The ballastless track was in the limit or failure state when the performance function Z was less than or equal to zero. The VTG representative value R_q with different failure probabilities q can be determined in Eq. (28):

$$\begin{aligned}
 q &= \text{Prob}(G(X) \leq 0) = \text{Prob}(\sigma_G Z_G + \mu_G \leq 0) \\
 &= \text{Prob}(Z_G \leq -\frac{\mu_G}{\sigma_G}) = \text{Prob}(Z_G \leq -\beta_{2M})
 \end{aligned} \tag{28}$$

where β_{2M} equal to μ_G / σ_G was the second-order second-moment reliability index [37]. Based on Trial Method, the VTG positive representative value of ballastless track in alpine and plateau environs was 82.83 °C/m with a failure probability of 5%. According to the same calculation principle, the VTG negative representative value of ballastless track was -35.03 °C/m with a failure probability of 5%.

4 Discussions

In this study, MCS, GMM, GPD, and TPNT have been conducted to analyze the VTG representative values with the failure probability of 5% of the ballastless track. The VTG representative values with different failure probabilities were obtained, and the comparisons of the four statistical methods are shown in Table 1 and Table 2.

Table 1
VTG positive representative values (unit: °C/m)

Failure probability (%)	Recommended values	MCS	GMM	GPD	TNPT
1	91.58	87.82	87.47	91.58	87.89
2	87.78	86.66	85.54	87.78	86.32
5	82.83	82.41	82.41	82.77	82.83
10	79.14	78.90	79.14	78.97	78.79
Average relative error (%)			0.50	1.53	0.28

Table 2
VTG negative representative values (unit: °C/m)

Failure probability (%)	Recommended values	MCS	GMM	GPD	TNPT
1	-40.15	-40.15	-39.71	-38.98	-39.63
2	-37.69	-36.04	-37.38	-36.77	-37.69
5	-35.03	-34.13	-34.56	-34.25	-35.03
10	-32.87	-32.86	-32.72	-32.60	-32.87
Average relative error (%)			1.62	1.52	2.14

Based on large random experiments (10^9 times), the VTG representative values in MCS tend to be accurate. From Table 1 and Table 2, the average relative error (ARE) of the VTG representative values in GMM, GPD, and TPNT was 1.26% compared with MCS, verifying that these statistical methods can predict the VTG representative values with different failure probabilities.

The deviation of statistical results was influenced by the different calculation principles of these statistical methods. MCS has high requirements for the discretization degree and the data scale of VTG sample. When the accuracy of MCS was required to be less than 0.1%, the number of repeated random sampling of the VTG sample needs to be more than 10^5 times. The calculation accuracy of GMM was high (ARE of 1.06%), but the statistical automation of GMM (subjective randomness inevitable) cannot be realized with the prediction process being complex and tedious. The statistical results of GPD were sensitive to the tail data of VTG samples and difficult to be stable. Furthermore, the calculation accuracy of TNPT depended on the distribution of standardized performance function, and it was an automatic computation technique avoiding haphazard and subjectivity.

The VTG representative values obtained by the four statistical methods were deviated, and the recommended representative values of VTG should be conservative, considering the safety and reliability of ballastless track. As seen in Table 1 and Table 2, the recommended representative values of VTG were the maximum representative values among these statistical methods. The positive and

negative VTG representative values of 91.58 °C/m and -40.15 °C/m are larger than that of 90 °C/m and -45 °C/m in China High Speed Railway Design Code. The positive VTG value in China High Speed Railway Design Code is not conservative for ballastless track design in alpine and plateau areas. Based on this, the recommended positive and negative representative values of VTG of ballastless track were 91.58 °C/m and -40.15 °C/m, and 82.83 °C/m and -35.03 °C/m, with failure probabilities of 1% and 5% respectively in alpine and plateau environs.

Conclusions

In this study, various statistical analysis tools were employed, using MCS, GMM, GPD and TPNT, to describe the evolution characteristics of the VTGs in a ballastless railway track system, based on the long-term temperature field test of ballastless track in Shannan City, Tibet. The VTG representative values with various failure probabilities are investigated and the statistical results from the above mentioned statistical tools, are examined. The main conclusions are as follows:

- 1) Based on the long-term temperature field test, the temperature variation of ballastless track in alpine and plateau environs has been studied. The temperature variation of the ballastless track ranged from -12.06 °C to 45.61 °C, and the VTG of the track slab ranged from -47.16 °C /m to 88.88 °C /m from January 31, 2021 to March 1, 2022, in alpine and plateau environs.
- 2) These statistical methods are feasible to predict the representative value of VTG of the ballastless track with different failure probabilities. The deviation of these statistical results is caused by the different calculation principles and application conditions of these statistical methods.
- 3) MCS has high requirements for the discretization degree and the data scale of VTG sample. The statistical automation of GMM cannot be realized with subjective randomness inevitable and prediction process tedious. The statistical results of GPD are sensitive to the tail data of VTG samples. Furthermore, TPNT is an automatic computation technique avoiding haphazard subjectivity.
- 4) The recommended positive and negative representative values of VTG of ballastless track are 91.58 °C/m and -40.15 °C/m, and 82.83 °C/m and -35.03 °C/m, with failure probabilities of 1% and 5% in alpine and plateau areas. The positive VTG value in China High Speed Railway Design Code is not conservative for ballastless track design, in alpine and plateau environments.

Acknowledgments

The authors are grateful to projects (52078501, 52078490, 52078488) supported by the National Natural Science Foundation of China, and the Natural Science Foundation of Hunan Province (2022JJ40628).

References

- [1] Chen L. K., Kurtulus A., Dong Y. F., Taciroglu E., Jiang L. Z.: Velocity pulse effects of near-fault earthquakes on a high-speed railway vehicle-ballastless track-benchmark bridge system, *Vehicle System Dynamics*, 2021; 1-25, <https://doi.org/10.1080/00423114.2021.1933546>
- [2] Kurhan M. B., Kurhan D. M., Husak M. A., Hmelevska N.: Increasing the efficiency of the railway operation in the specialization of directions for freight and passenger transportation, *Acta Polytechnica Hungarica*, 2022; 19(3): 231-244, <https://10.12700/APH.19.3.2022.3.18>
- [3] Lu C. F., Cai C. X.: Challenges and countermeasures for construction safety during the Sichuan-Tibet railway project, *Engineering*, 2019; 5(5), <https://doi.org/10.1016/j.eng.2019.06.007>
- [4] Fischer S.: Investigation of the horizontal track geometry regarding geogrid reinforcement under ballast. *Acta Polytechnica Hungarica*, 2022; 19(3): 89-101, <https://10.12700/APH.19.3.2022.3.8>
- [5] Xue Y. G., Kong F. M., Li S. C., Zhang Q. S., Qiu D. H., Su M. X., Li Z. Q.: China starts the world's hardest "Sky-High Road" project: Challenges and countermeasures for Sichuan-Tibet railway, *The Innovation*, 2021; 2(2): 100105, <https://doi.org/10.1016/j.xinn.2021.100105>
- [6] Song L., Liu H. B., Cui C. X., Yu Z. W., Li Z. G.: Thermal deformation and interfacial separation of a CRTS II slab ballastless track multilayer structure used in high-speed railways based on meteorological data, *Construction and Building Materials*, 2020; 237: 117528, <https://doi.org/10.1016/j.conbuildmat.2019.117528>
- [7] Zhu S. Y., Cai C. B.: Interface damage and its effect on vibrations of slab track under temperature and vehicle dynamic loads, *International Journal of Non-Linear Mechanics*, 2014; 58: 222-232, <https://doi.org/10.1016/j.ijnonlinmec.2013.10.004>
- [8] Zhang J. W., Zhu S. Y., Cai C. B., Wang M. Z., Li H. L.: Experimental and numerical analysis on concrete interface damage of ballastless track using different cohesive models, *Construction and Building Materials*, 2020; 263: 120859, <https://doi.org/10.1016/j.conbuildmat.2020.120859>
- [9] Cai X. P., Luo B. C., Zhong Y. L., Zhang Y. R., Hou B. W.: Arching mechanism of the slab joints in CRTSII slab track under high temperature conditions, *Engineering Failure Analysis*, 2019; 98: 95-108, <https://doi.org/10.1016/j.engfailanal.2019.01.076>
- [10] Li Y., Chen J. J., Wang J. X., Shi X. F., Chen L.: Study on the interface damage of CRTS II slab track under temperature load, *Structures*, 2020; 26: 224-236, <https://doi.org/10.1016/j.istruc.2020.04.014>

-
- [11] Sheng X. W., Zhou T. M., Huang S. J., Cai C. Z., Shi T.: Prediction of Vertical Temperature Gradient on Concrete Box-girder Considering Different Locations in China, *Case Studies in Construction Materials*, 2022; e01026, <https://doi.org/10.1016/j.cscm.2022.e01026>
- [12] Sheng X. W., Shi T., Zheng W. Q., Lou P.: Time-varying non-uniform temperature distributions in concrete box girders caused by solar radiation in various regions in China, *Advances in Mechanical Engineering*, 2022; 14(2): 16878140221076458, <https://doi.org/10.1177/16878140221076458>
- [13] Shi T., Lou P.: Optimized machine learning approaches for identifying vertical temperature gradient on ballastless track in natural environments, *Construction and Building Materials*, 2023; 367: 130321, <https://doi.org/10.1016/j.conbuildmat.2023.130321>
- [14] Shi T., Lou P., Zheng W. Q., Sheng X. W.: A hybrid approach to predict vertical temperature gradient of ballastless track caused by solar radiation, *Construction and Building Materials*, 2022; 352: 129063, <https://doi.org/10.1016/j.conbuildmat.2022.129063>
- [15] Fu J., Qin Y., You Y. Y., Meng J. Y., Lian X. L.: Temperature field analysis on CA mortar ballastless track of high-speed railway, *Key Engineering Materials*, 2013; 531: 163-167, <https://doi.org/10.4028/www.scientific.net/KEM.531-532.163>
- [16] Yang R. S., Li J. L., Kang W. X., Liu X. Y., Cao S. H.: Temperature characteristics analysis of the ballastless track under continuous hot weather, *Journal of Transportation Engineering*, 2017; 143(9): 04017048, <https://doi.org/10.1061/JTEPBS.0000076>
- [17] Yu Z. W., Xie Y., Tian X. Q.: Research on mechanical performance of CRTS III plate-type ballastless track structure under temperature load based on probability statistics, *Advances in Civil Engineering*, 2019; 2019, <https://doi.org/10.1155/2019/2975274>
- [18] Liu J., Liu Y. J., Zhang G. J.: Experimental analysis of temperature gradient patterns of concrete-filled steel tubular members, *Journal of Bridge Engineering*, 2019; 24(11): 04019109, [https://doi.org/10.1061/\(ASCE\)BE.1943-5592.0001488](https://doi.org/10.1061/(ASCE)BE.1943-5592.0001488)
- [19] Wang G. X., Ding Y. L., Liu X. W.: The monitoring of temperature differences between steel truss members in long-span truss bridges compared with bridge design codes, *Advances in Structural Engineering*, 2019; 22(6): 1453-1466, <https://doi.org/10.1177/1369433218815436>
- [20] Lou P., Zhu J. P., Dai G. L., Yan B.: Experimental study on bridge-track system temperature actions for Chinese high-speed railway, *Archives of Civil and Mechanical Engineering*, 2018; 18(2): 451-464, <https://doi.org/10.1016/j.acme.2017.08.006>
-

- [21] Song Z. W., Xiao J. Z., Shen L. M.: On temperature gradients in high-performance concrete box girder under solar radiation, *Advances in Structural Engineering*, 2012; 15(3): 399-415, <https://doi.org/10.1260/1369-4332.15.3.399>
- [22] Cai C. Z., Huang S. J., He X. H., Zhou T. M., Zou Y. F.: Investigation of concrete box girder positive temperature gradient patterns considering different climatic regions, *Structures*, 2022; 35: 591-607, <https://doi.org/10.1016/j.istruc.2021.11.030>
- [23] Shi T., Sheng X. W., Zheng W. Q., Lou P.: Vertical temperature gradients of concrete box girder caused by solar radiation in Sichuan-Tibet railway, *Journal of Zhejiang University-SCIENCE A*, 2022; 23(5): 375-387, <https://doi.org/10.1631/jzus.A2100401>
- [24] Sheng X. W., Yang Y., Zheng W. Q., Zhou B., Li S., Huang L. C.: Study on the time-varying temperature field of small radius curved concrete box girder bridges, *AIP Advances*, 2020; 10(10): 105013, <https://doi.org/10.1063/1.5133992>
- [25] Zio E.: *The Monte Carlo simulation method for system reliability and risk analysis*, London: Springer, 2013; 19-58
- [26] McLachlan G. J., Rathnayake S.: On the number of components in a Gaussian mixture model, *Wiley Interdisciplinary Reviews: Data Mining and Knowledge Discovery*, 2014; 4(5): 341-355, <https://doi.org/10.1002/widm.1135>
- [27] Chen Y. H., Gupta M. R.: *Em demystified: An expectation-maximization tutorial*, Electrical Engineering, 2010
- [28] Do C. B., Batzoglou S.: What is the expectation maximization algorithm, *Nature biotechnology*, 2008; 26(8): 897-899, <https://doi.org/10.1038/nbt1406>
- [29] Frank J., Massey J.: The Kolmogorov-Smirnov test for goodness of fit, *Journal of the American statistical Association*, 1951; 46(253): 68-78
- [30] Fan Z. Y., Huang Q., Ren Y., Xu X., Zhu Z. Y.: Real-time dynamic warning on deflection abnormality of cable-stayed bridges considering operational environment variations, *Journal of performance of constructed facilities*, 2021; 35(1): 04020123, [https://doi.org/10.1061/\(ASCE\)CF.1943-5509.0001537](https://doi.org/10.1061/(ASCE)CF.1943-5509.0001537)
- [31] Xu X., Ren Y., Huang Q., Fan Z. Y., Tong Z. J., Chang W. J., Liu B.: Anomaly detection for large span bridges during operational phase using structural health monitoring data, *Smart Materials and Structures*, 2020; 29(4): 045029, <https://doi.org/10.1088/1361-665X/ab79b3>
- [32] Zhao Y. G., Ono T.: Moment methods for structural reliability, *Structural safety*, 2001; 23(1): 47-75, [https://doi.org/10.1016/S0167-4730\(00\)00027-8](https://doi.org/10.1016/S0167-4730(00)00027-8)

- [33] Zhao Y. G., Ono T.: New point estimates for probability moments, *Journal of Engineering Mechanics*, 2000; 126(4): 433-436, [https://doi.org/10.1061/\(ASCE\)0733-9399\(2000\)126:4\(433\)](https://doi.org/10.1061/(ASCE)0733-9399(2000)126:4(433))
- [34] Chen X. Y., Tung Y. K.: Investigation of polynomial normal transform, *Structural Safety*, 2003; 25(4): 423-445, [https://doi.org/10.1016/S0167-4730\(03\)00019-5](https://doi.org/10.1016/S0167-4730(03)00019-5)
- [35] Zhao Y. G., Lu Z. H.: Cubic normal distribution and its significance in structural reliability, *Structural Engineering and Mechanics*, 2008; 28(3): 263-280, <https://doi.org/10.12989/sem.2008.28.3.263>
- [36] Zhao Y. G., Lu Z. H.: Fourth-moment standardization for structural reliability assessment, *Journal of Structural Engineering*, 2007; 133(7): 916-924, [https://doi.org/10.1061/\(ASCE\)0733-9445\(2007\)133:7\(916\)](https://doi.org/10.1061/(ASCE)0733-9445(2007)133:7(916))
- [37] Lu Z. H., Hu D. Z., Zhao Y. G.: Second-order fourth-moment method for structural reliability, *Journal of Engineering Mechanics*, 2017; 143(4): 06016010, [https://doi.org/10.1061/\(ASCE\)EM.1943-7889.0001199](https://doi.org/10.1061/(ASCE)EM.1943-7889.0001199)

Evaluation of Topology Description Models in Road Network Formats

János Máté Lógó, Árpád Barsi

Department of Photogrammetry and Geoinformatics, Faculty of Civil Engineering, Budapest University of Technology and Economics
Műegyetem rkp. 3, H-1111 Budapest, Hungary
E-mail: logo.janos.mate@emk.bme.hu; barasi.arpad@emk.bme.hu

Abstract: Topology is a particular feature of road networks. Topology refers to properties, such as the connection of roads, but not only through their axes or reference lines, but also at the level of lanes. The map topology of road networks does not currently have procedures that can be expressed in mathematical formulas (or only to a minimal extent), but can only be implemented by algorithms. Our research, therefore, aimed at observing such topological regularities and then developing a method of investigation, by constructing rules and additional algorithms. To test this work, we used synthetic and real data, focusing on the case of map content embodied in four formats. In this paper, we present the test methods for the data models, the results of our test runs and finally, we point out that topological checks are extensively justified to determine the quality of the produced map. In the future we plan to develop an automatic correction mechanism based on this.

Keywords: road network; topology analysis; autonomous vehicle simulation

1 Introduction

One of the most promising developments of our time is the automation of transport. Computers are increasingly being used in the development of self-driving vehicles, through simulation techniques [1] [2]. Simulations need an accurate and detailed representation of reality, which can be provided by specific map content [3-8]. These maps have “grown out” of traditional navigation products, but have some unique features.

Self-driving vehicles are expected to make autonomous decisions on how to control the vehicle as it moves through traffic. By making safe choices, they can select and follow the best and safest route. This requires support from maps in which the true geometric characteristics of the road infrastructure are given. Beyond pure geometry, however, the importance of topology was recognized very early.

Topology is the science of the invariant properties of objects that are preserved during various deformations or transformations. Examples of such properties are the connection of surfaces without gaps or overlaps, the connection of lines and line chains, or the inclusion of points on them.

In this paper, we will discuss various theoretical and practical implementations of map topology, their analysis and verification, the errors that occur, and how to correct them. In the second section of the paper, we describe the theoretical background of map topology. In the third section, we present four realizations found in practice. The fourth section is devoted to the investigation of the road network topology. We close our study with a conclusion.

2 Topology Models

Map topology is most often described using graphs. By definition, a graph G consists of its vertices and the edges that connect them: $G = (V, E)$, where V is the set of vertices (alternative names are nodes, points) and E is the set of edges (or alternatively arcs, links, lines). For the latter, we define the following relation, which makes sense of the edge fit of the vertices:

$$E \subseteq \{(x, y) \mid (x, y) \in V^2 \text{ and } x \neq y\} \quad (1)$$

Instead of storing the data in the above-unordered list format, it is often more appropriate to use the matrix notation, which also helps to keep track of the data. The simplest matrix is the adjacency matrix for the vertex-to-vertex collocation, which is $n \times n$ for n nodes. Its elements take values according to the following rule:

$$A_{ij} = \begin{cases} 1 & \text{if edge } (V_i, V_j) \\ 0 & \text{if no edge} \end{cases} \quad (2)$$

The second matrix representation is the edge-vertex representation, called also as incidence matrix. By definition, it is the following:

$$B_{ij} = \begin{cases} -1 & SP \\ 1 & EP \\ 0 & \text{otherwise} \end{cases} \quad (3)$$

where SP is the starting point, EP is the endpoint. The edge-edge representation is defined as

$$C_{ij} = \begin{cases} -1 & P \\ 1 & S \\ 0 & \text{otherwise} \end{cases} \quad (4)$$

where P means, that the predecessor of V_i is V_j , whilst the successor S of V_i is the vertex V_j .

The above matrix forms can be interleaved with mathematical expressions, i.e. the edge-vertex matrix can be used to calculate the other two matrices:

$$\mathbf{A} = \mathbf{B}^T \cdot \mathbf{B} \quad (5)$$

$$\mathbf{C} = \mathbf{B} \cdot \mathbf{B}^T \quad (6)$$

This is of paramount importance in storing data and maintaining and monitoring data consistency [9].

The strongest connection between geometry and topology is revealed in topological errors. The main types of errors are shown in Figure 1.

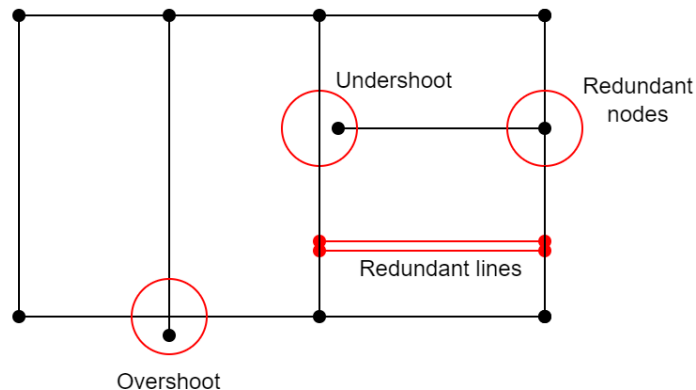


Figure 1
Topological errors

For the road network, directed graphs (digraphs) are preferred, where the edges are oriented.

3 Data Formats for Road Network Storage

Graphs are implemented in concrete formats in order to manage real road networks in geographic information systems (GIS). These realizations consist not only of a data model, i.e. a way of describing the elements of the graph, but also of an application environment. The essential components of the latter are the procedures and operations that can be performed on the data stored in the data model.

Our approach describes four types of solutions. The first is specific to one of the most common GI systems. The developer, ESRI (Environmental Systems Research Institute) **ArcGIS** handles line elements by storing points with their coordinates and then creates an “Arc-Node Topology”, the concrete form of which, is the Arc Attribute Table (AAT). This table contains the edge identifiers (ID), start point (From-node), end point (To-node), and may be extended with the identifiers of the

polygons on the left and right sides (Lpoly and Rpoly). The storage organized in coverage requires strict rules: 6 points, 15 lines, 10 polygons, and 1 line/polygon basic rules are defined.

Our second example is **OpenStreetMap** (OSM), a map database based on community data collection and mapping. OSM has been created as a collaborative project by Steve Coast in the UK in 2004, initially inspired by the success of Wikipedia. OSM is community-owned, but supported by the OpenStreetMap Foundation. OSM data is stored in a PostgreSQL database with PostGIS extension. For data transfer, dumps are created, which are available in two formats: XML and Protocol Buffer Binary Format (PBF). There are further data providers (e.g., the German Geofabrik), where also ESRI shape (SHP) format data is available [10] [11].

OSM's topological data structure is built up from four core elements (also known as data primitives):

- **Nodes:** Points with a geographic position
- **Ways:** Ordered lists of nodes, representing a polyline, or a polygon
- **Relations:** A relation is a multi-purpose data structure that documents a relationship between two or more data elements (nodes, ways, and/or other relations)
- **Tags:** Key-value data pairs

Topology element nodes are twofold in the strict GIS sense: start or end point – called node, and intermediate point – called vertex.

OpenStreetMap has 8.3 million registered users, contains 7.4 billion nodes, have ~4 million map changes/day from 1.75 million different user contributors. The world's uncompressed XML-format OSM database exceeds the size of 1561.5 GB. (Statistics from [12] and [13] on 2022-04-21). The complete Hungarian road network available from Geofabrik has 7.6 million points (1.7 million nodes and 5.9 million vertices) and 864 thousand polylines.

If two polylines are connected at a T-intersection, in a strict topology, the connection point must be a node, which means, that the previously created line must be broken and a node element must be inserted. In contrast, the OSM topology is more permissive: the endpoint of the line starting at the join must be on the other line, but a “simpler” vertex element is sufficient.

The other very important difference from the strict GIS topology is that edges cannot only be directed. This will result in unidirectional and bidirectional elements being “mixed up” in the database, making it difficult for application developers to implement, for example, route planning (Fig. 2).

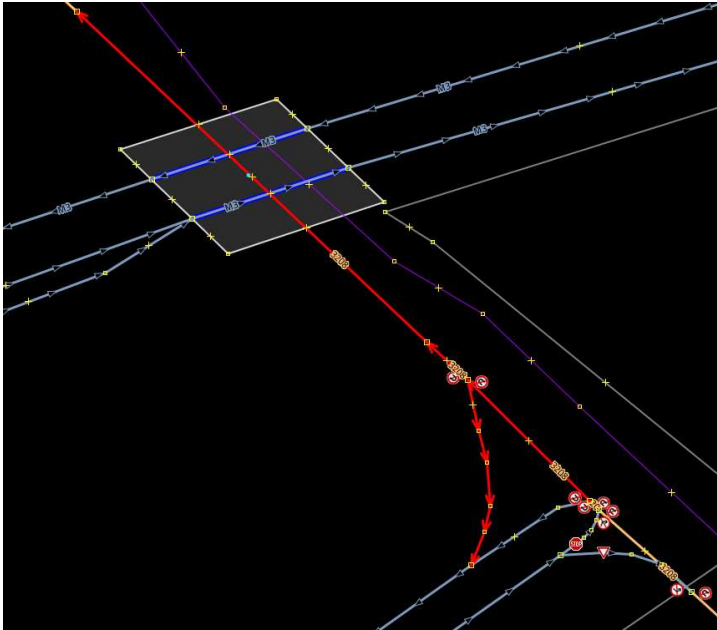


Figure 2

Topology example of a minor road crossing a motorway: both unidirectional and bidirectional edges (see red arrows!) are included in the database (made with the JOSM editor at the junction of the motorway M3 and the rural road 3208)

The third system is the **Navigation Data Standard** (NDS) generally used in the vehicle navigation world [14] [15]. It is a standardized format for automotive-grade navigation databases, jointly developed by automobile manufacturers and suppliers. NDS is also an association registered in Germany with 43 international members of automotive developers, map data providers, and navigation device/application providers.

NDS uses the SQLite Database File Format. An update region represents a geographic area in a database that can be subject to an update. Update regions thus enable incremental and partial updating of defined geographic regions within an NDS database. All navigation data is organized into specific building blocks: 3D objects, Basic map display, Digital terrain model, Full-text search, Junction view, Lane, Name, Natural guidance, Orthoimages, Points of interest, Routing, Shared data, Speech, Traffic information, Volatile data.

In topological terms, NDS is one of the most sophisticated, most mature solutions. It has two data levels: road level and lane level. Fig. 3 illustrates a complex junction with intersecting roads and the corresponding lanes. Roads and lanes are joint with connectors, also numbered and identified in the data model.

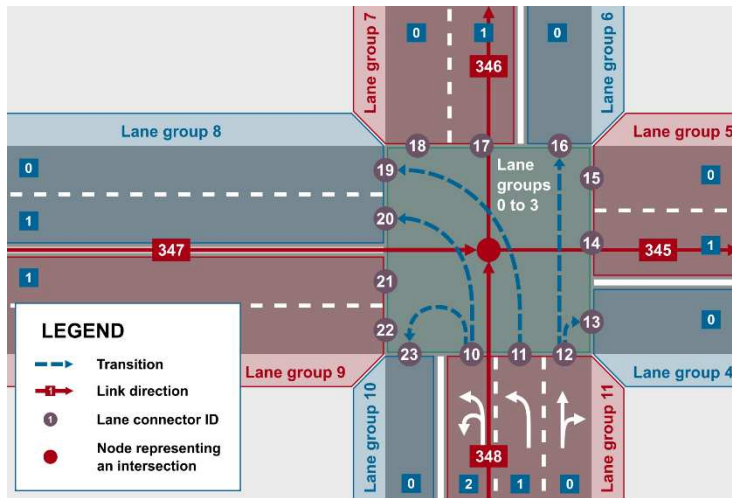


Figure 3

NDS example: A schematic junction with the road and lane level elements [14]

Finally, the last format is **OpenDRIVE**, used in the world of automotive simulators. It was originally a format developed by the German company Vires for various vehicle-oriented simulations to represent real-world map data [3] [4]. It is now standardized; the latest version is 1.7.

OpenDRIVE is used to describe road infrastructure and its environment in 3D. Its XML format provides an inefficient storage for tags encoding many features hierarchically. The format carries the extension XODR.

In terms of topology, the format provides connectivity at the road and lane level using links (Fig. 4). In ambiguous cases (at splitting or merging), a junction must be formed. The road axes are directed, to which the traffic lanes are related. The lanes may point in the same direction as the axis and in the opposite direction (e.g., a bidirectional road). The links of the directional elements can be of predecessor and successor types. From a topological point of view, additional rules can then be introduced, for example, in the case of two connecting roads, taking into account the direction of the axes, the second road can be the successor of the first one, while the second has the first as a predecessor. The possible cases and their implementation are described in detail in the article [9]. It should be emphasized that in OpenDRIVE, we specify the connections not only at the road level but also at the lane level, i.e., the logic of the lane connections must be specified.

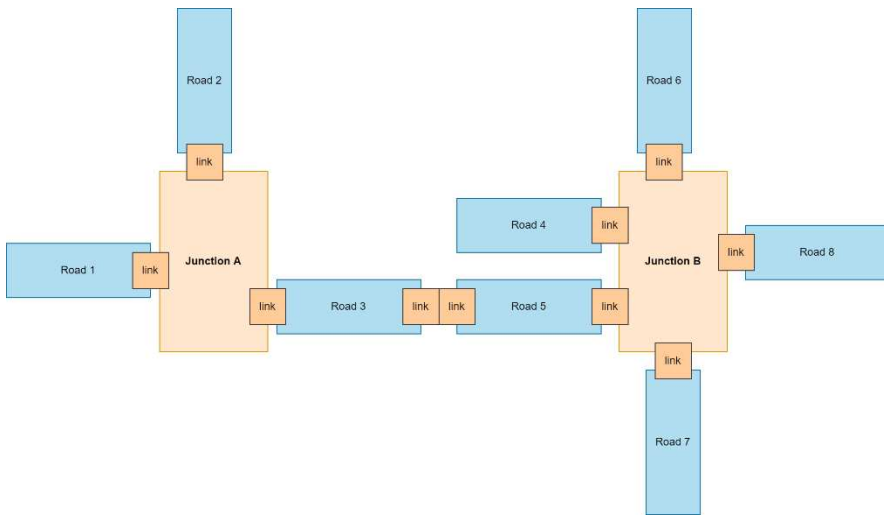


Figure 4

Schema of the OpenDRIVE model with road linkages

4 Evaluation Strategy for Road Topology

The first of the four topological approaches described, the **ESRI** model, is included in this paper because it is considered in GIS as a kind of cord scale; in most cases it is used as a benchmark. Of course, this includes both the topology of coverage and shape formats.

The **OpenStreetMap** model was analyzed in depth with data from 2015. (The analysis software written during the research started a few years ago is outdated due to a change in the data model in 2016; it needs to be rewritten, which is not yet fully completed.) The total road network of the country stored in OSM looked like the following in 2015 (Fig. 5).

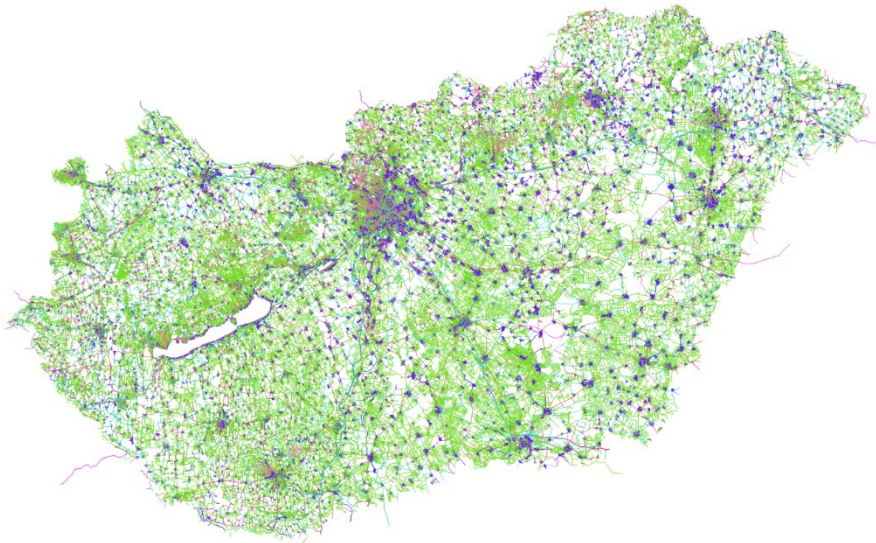


Figure 5

The entire road network of Hungary in 2015 with all 419 076 elements mapped

In the road network, 37 different road categories have been distinguished, but with a huge variation in the number of elements. Fig. 6 displays the frequencies for the eight most important road types. It can be seen that compared to the 140 996 residential types, secondary has only 15 741 items, a difference of almost 9 times (one order of magnitude).

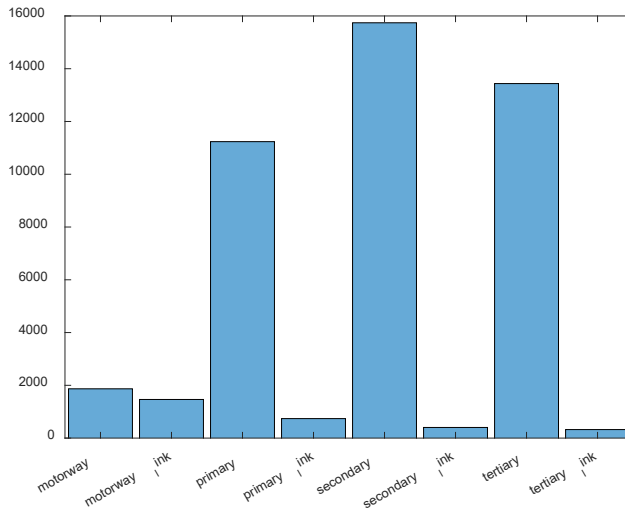


Figure 6

Frequencies of the eight main road categories

The differences in frequency also draw attention to the fact that the interchange between different road categories and connections is of paramount importance for practical use.

If the network is restricted to the element types motorway, motorway link, primary and primary link, i.e., the main road network, the number of polylines downloaded is 15 307, which in the Geofabrik (format-converted) shapefile represents 142 904 points. A small fraction of this set of points (30 614 points, ~21%) is the node, the rest being the vertex (112 290 points).

For topological verification, we defined a geometric tolerance, so that two points occurring within a radius of 5 m were considered as one. This metric was determined based on the size of the lanes and practical experience. While keeping the tolerance in mind, we rebuilt the topology: we gradually added to the model the points that were found to be different and the edges that matched them. In all cases, we followed the strict topology rules of ESRI.

This analysis resulted in 15 208 independent points, 231 282 978 distinct edges. On an average notebook, the topology build-up was about 29 s.

The connectivity of the edges of the path network, the nonzero elements of its primary adjacency matrix, is shown in Fig. 7. It can be seen that there are no prominent nodes, i.e., the network has a largely uniform topological distribution.

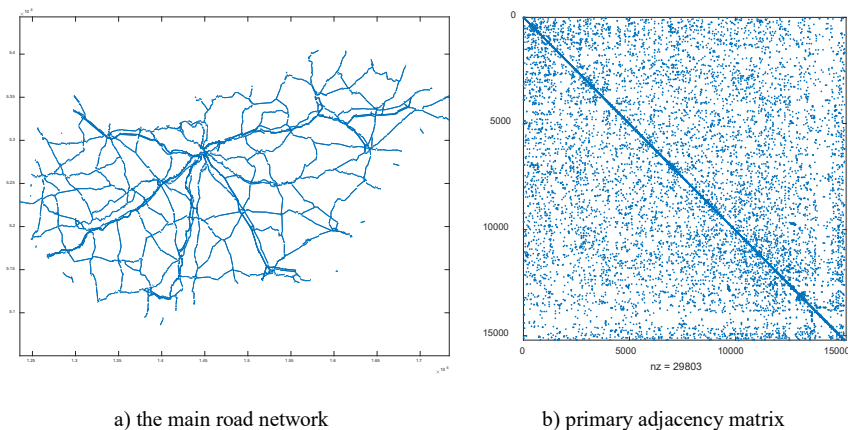


Figure 7

The main road network and the primary adjacency matrix

Very similarly to the adjacency matrix, a distance matrix can be derived, and then by generalizing it to an all-pair type, the distance of each node to each node can be given. Using such an analysis technique, a network reachability analysis can be performed.

To investigate the **NDS** topological model, a sample model of the St. Gellért Square in Budapest was created by orthophoto on-screen digitization (Fig. 8).

The orthophoto was captured in 2019 on behalf of the municipality, from which the mosaics of the working area were merged as Geotiff at a geometric resolution of 0.0625 m in HD72/EOV map projection system. It should also be added that the evaluation was carried out by several independent evaluators. The resulting models were then aggregated and the conflicting positions were discussed and finalized by consensus. The guiding principle for the evaluation was the accurate consideration of traffic rules (e.g., no turning). From the 378 evaluated elements, 9 intersections and 33 lane groups were constructed according to the NDS standard. The generated graph was compared with the data content of the HERE HD map for verification [16]. In the sample area, the complete agreement between the two datasets has proven that the lane design was performed according to the NDS rules. As there are many improvements to the NDS by map data providers, we did not attempt to analyze this model in depth.

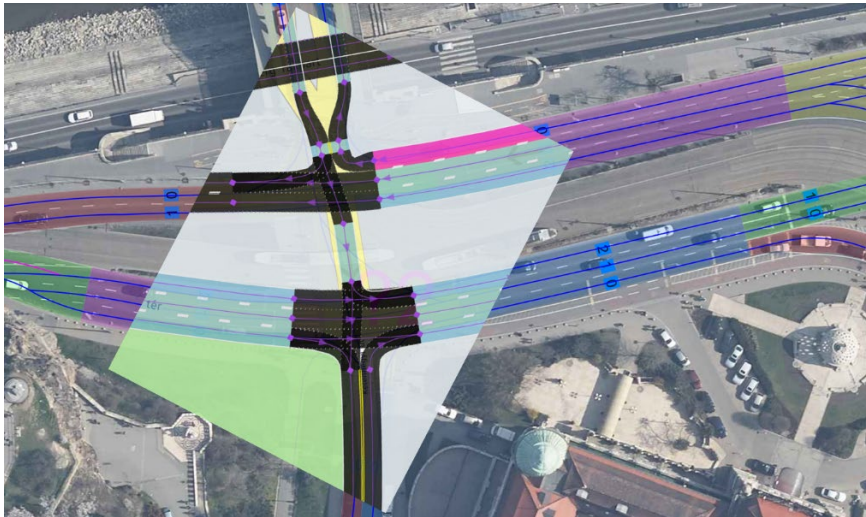


Figure 8

An orthophoto of the sample area with the evaluated NDS elements and a detail of the HERE HD map for comparison

Of the topological models, the **OpenDRIVE** implementation for simulators has received the most attention. This standard is the youngest, has the least experience, and could play a major role in the development of autonomous vehicles. In automotive simulators, standard version 1.4 is the most commonly supported, so we have focused our work on that.

One of the easiest tools to create OpenDRIVE models is the MathWorks RoadRunner software [17]. We used it to create several synthetic test cases and then studied how topology appeared in the models. One of the synthetically designed complex sample spaces (with a roundabout, an X-intersection, and several types of T-intersections) is shown in Fig. 9. It is worth observing how complex the lanes and their relationships can become in turning situations.

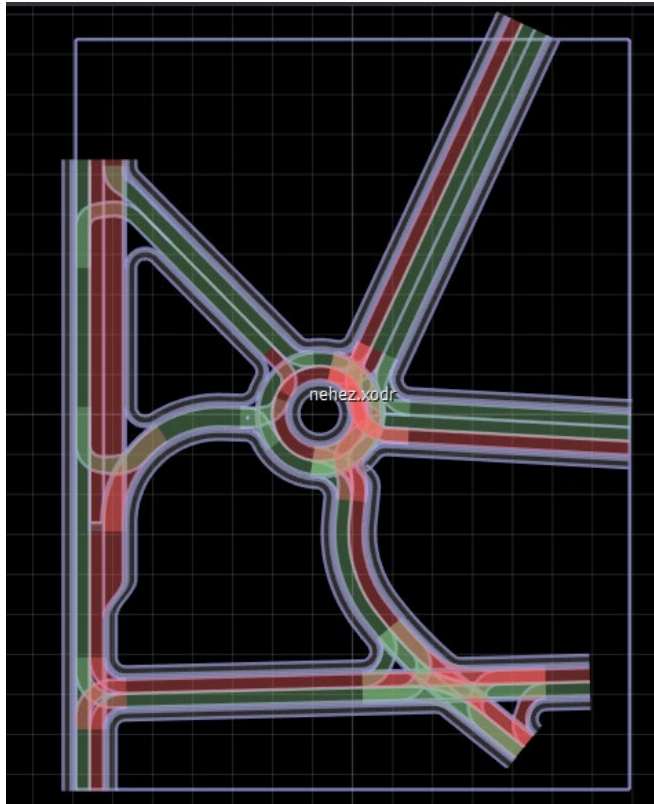


Figure 9

Synthetic OpenDRIVE sample for topological analysis

The sample area shown consists of 83 roads, 258 lanes, 7 intersections, and 117 lanes within them. To study the OpenDRIVE topology, 10 basic rules have been established [9]. An extracted example of the rules: using adjacency matrix equation (2) and incidence matrix equation (3), the following theorem should hold for the endpoints of the path reference lines:

$$\sum_j B_{ij}^{EP} = \sum_j A_{kj} \quad (7)$$

where B_{ij}^{EP} is the endpoint focused incidencies (edge-vertex relations).

OpenDRIVE distinguishes between predecessors and successors of roads and lanes, which are contained in links and junction elements (see Section 3). In addition, inference rules can be defined for these to check the consistency of the database [18]. An excellent example of inference rules [19] is that if for two consecutive roads it is true that the successor of Road 2 is Road 1 and the endpoint of Road 1 is the same as the starting point of Road 2 (a variant of a possible continuation), then the predecessor of Road 2 must be Road 1. Furthermore, the conclusions so applied

can be extended to the numbered lanes of the roads in a sequence, allowing each lane to be uniquely identified and their junctions to be examined. In ambiguous cases, OpenDRIVE requires the use of the standard junction. However, it is very important from a topological point of view that the inference rules can be used to examine the junction lanes and compare them with the links. If they do not match, consistency errors occur, which are reported by the simulators as continuity errors. The synthetic example has one case of a predecessor overlapping error, which is currently only available as an error list and can be corrected manually (Fig. 10a).

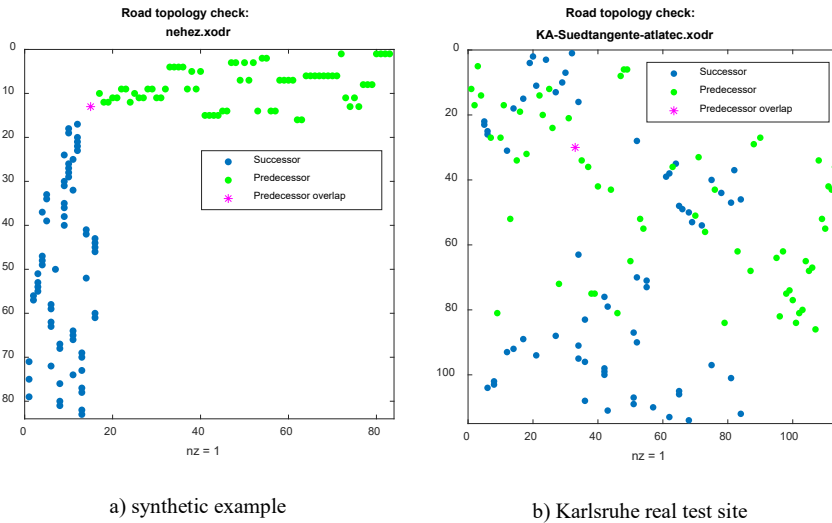


Figure 10

Predecessor-successor verification using synthetic and real examples

In parallel, we also carried out tests with real data. Thus, several models derived from field surveys (e.g., by Atlatec [20]), such as from German motorways, expressways or urban road networks, were analyzed. One of these surveyed models is the motorway near Karlsruhe (“Südtangente”), which consists of 114 roads, 886 lanes, of which 189 are junction lanes and 22 junctions. It is interesting to note that the XODR model from the German A9 motorway survey for international practice is completely flawless, although containing 248 roads, 2 683 lanes, 510 junction lanes, and 63 junctions (Fig. 10b).

Conclusions

In this work, we have reinforced the idea that topology is an extremely important part of the map content in geoinformatics, especially in the world of vehicles and transportation. We examined four different formats in which topology is implemented in different ways. These are, ESRI coverage, OpenStreetMap, Navigation Data Standard and OpenDRIVE respectively. In the course of the research, we found that topology can be embodied in quite different interpretations

in these formats. Accordingly, we tailored our investigations to the data of each implementation: for OSM we focused on the large network connectivity, for NDS we looked at the lane geometry and connectivity appropriate for HD map content, and for OpenDRIVE we looked at the lane connectivity essential for smoothly serving simulations.

Our research required different tools: parsing XML files, populating and interpreting custom topological tables, graph analyzing techniques, establishing topological and inference rules and applying the rule set – to name just a few of the solutions implemented. We have shown that topology, which has been largely neglected, until now, is crucial and needs to be further investigated, verified and sometimes, fixed. Our overall aim is to create a procedure that is as automated as possible and performs the discussed steps, with minimal human intervention. We are therefore designing such a model application, which we intend to implement with the inclusion of Artificial Intelligence.

Acknowledgment

The research reported in this paper and carried out at the Budapest University of Technology and Economics has been supported by the National Research Development and Innovation Fund (TKP2020 Institution Excellence Subprogram, Grant No. BME-IE-MIFM) based on the charter of bolster issued by the National Research Development and Innovation Office under the auspices of the Ministry for Innovation and Technology. The project has been supported by the European Union, co-financed by the European Social Fund. EFOP-3.6.3-VEKOP-16-2017-00001. Supported by the ÚNKP-21-3 New National Excellence Program of the Ministry for Innovation and Technology from the source of the National Research, Development and Innovation Fund.

References

- [1] M. Burg, “Simulation as Tool,” 2019
- [2] “Mechanical Simulation.” [Online] Available: <https://www.carsim.com/> [Accessed: 26-Sep-2019]
- [3] “VTD - VIRES Virtual Test Drive.” [Online] Available: <https://vires.com/vtd-vires-virtual-test-drive/> [Accessed: 26-Sep-2019]
- [4] Vires, “Vires VTD,” 2022 [Online] Available: <https://vires.mscsoftware.com/> [Accessed: 02-Apr-2022]
- [5] “Simulation Technologies - avl.com.” [Online] Available: <https://www.avl.com/hu/web/guest/simulation> [Accessed: 26-Sep-2019]
- [6] “SUMO - Simulation of Urban Mobility.” [Online] Available: <http://sumo.sourceforge.net/> [Accessed: 26-Sep-2019]
- [7] M. T. Horváth, Q. Lu, T. Tettamanti, Á. Török, and Z. Szalay, “Vehicle-In-The-Loop (VIL) and Scenario-In-The-Loop (SCIL) Automotive Simulation Concepts from the Perspectives of Traffic Simulation and Traffic Control,”

Transp. Telecommun. J., Vol. 20, No. 2, 2019

- [8] “CarMaker | IPG Automotive.” [Online] Available: <https://ipg-automotive.com/products-services/simulation-software/carmaker/> [Accessed: 26-Sep-2019]
- [9] J. M. Lógó and A. Barsi, “THE ROLE OF TOPOLOGY IN HIGH-DEFINITION MAPS FOR AUTONOMOUS DRIVING,” *Int. Arch. Photogramm. Remote Sens. Spat. Inf. Sci.*, Vol. XLIII-B4-2022, pp. 383-388, Jun. 2022
- [10] ESRI, “Geodatabase topology rules and fixes for polyline features—ArcGIS Pro | Documentation.” [Online] Available: <https://pro.arcgis.com/en/pro-app/2.8/help/editing/geodatabase-topology-rules-for-polyline-features.htm> [Accessed: 25-Apr-2022]
- [11] OpenStreetMap, “OpenStreetMap,” 2022 [Online] Available: <https://www.openstreetmap.org>. [Accessed: 25-Apr-2022]
- [12] OpenStreetMap, “Stats – OpenStreetMap Wiki,” 2022 [Online] Available: <https://wiki.openstreetmap.org/wiki/Stats>. [Accessed: 25-Apr-2022]
- [13] OpenStreetMap, “Planet.osm – OpenStreetMap Wiki,” 2022 [Online] Available: <https://wiki.openstreetmap.org/wiki/Planet.osm> [Accessed: 25-Apr-2022]
- [14] NDS, “Navigation Data Standard - Wikipedia,” 2022 [Online] Available: https://en.wikipedia.org/wiki/Navigation_Data_Standard [Accessed: 25-Apr-2022]
- [15] NDS, “Navigation Data Standard (NDS) - The worldwide standard for map data in automotive eco-systems,” 2022 [Online] Available: <https://nds-association.org/>. [Accessed: 25-Apr-2022]
- [16] HERE, “HD Maps for Autonomous Driving and Driver Assistance | HERE,” 2018 [Online] Available: <https://www.here.com/products/automotive/hd-maps>. [Accessed: 08-Dec-2019]
- [17] MathWorks, “RoadRunner - MATLAB & Simulink.” [Online] Available: <https://www.mathworks.com/products/roadrunner.html> [Accessed: 02-Apr-2022]
- [18] M. Barsi and A. Barsi, “TOPOLOGICAL ANOMALY DETECTION IN AUTOMOTIVE SIMULATOR MAPS,” in *ISPRS - International Archives of the Photogrammetry, Remote Sensing and Spatial Information Sciences*, 2022, p. 6
- [19] Wikipedia, “Inference engine.” [Online] Available: https://en.wikipedia.org/wiki/Inference_engine [Accessed: 02-Apr-2022]
- [20] A. GmbH, “Atlatec,” 2022 [Online] Available: <https://atlatec.de/en/> [Accessed: 02-Apr-2022]

Evaluating Annual Operation Performance of Serbian Railway System by using Multiple Criteria Decision-Making Technique

**Nikola Petrović¹, Jelena Mihajlović¹, Vesna Jovanović¹,
Dušan Ćirić¹, Tanja Živojinović²**

¹ University of Niš, Faculty of Mechanical Engineering

Aleksandra Medvedeva 14, 18106 Niš, Serbia

petrovic.nikola@masfak.ni.ac.rs, jelena.mihajlovic@masfak.ni.ac.rs,

vesna.jovanovic@masfak.ni.ac.rs, dusan.ciric@masfak.ni.ac.rs

² University of Belgrade, Faculty of Transport and Traffic Engineering

Vojvode Stepe 305, 11010 Belgrade, Serbia

t.zivojinovic@sf.bg.ac.rs

Abstract: The railway is a complex dynamic system, including the railway infrastructure, vehicles and personnel, each of which has its own functions or goals. Evaluating operation performance for freight and passenger railway systems is important for the government, operators and passengers. This paper will use a well-known, Multiple Criteria Decision-Making (MCDM) technique, to evaluate the freight and passenger rail systems operational performance. Initially, the authors will create the evaluation indicator system based on official data, having 5 basic indicators and a total of 18 sub-indicators, for freight transport, as well as passenger transport. Also, these operational data/indicators will be used as the input for the MCDM approach. Next, a formulated approach to obtain the performance evaluation is used as follows: The Entropy weight method is employed to calculate the weight of each sub-indicator; the Technique for Order Preference by Similarity to Ideal Solution (TOPSIS) method, will be used to calculate the comprehensive evaluation values and rankings of performance for each year. Finally, the Serbian railway, with 7 years of data, will be chosen, as the case study, to test the MCDM approach; the related recommendations for freight transport, as well as passenger rail transport, will also be provided.

Keywords: Railway; Entropy; TOPSIS; Operation performance evaluation

1 Introduction

Rail transport is described as a reliable, efficient, safe and complex system of vehicles, infrastructure, equipment and technology, and people. This system is

capable of transporting huge amounts of goods and people, over long distances at high speeds. But, it is less flexible and more expensive, in comparison to road transport, when lower traffic levels are considered. Thus, Rail is more efficient in urban and highly-populated areas. Rail transport has been the second largest block in the modal split, after private motorized transport in Germany in 2018 [1]. Freight transport by rail involves various actors, the most important of which are: Shippers, rail transport companies competing in an open market in the EU since 2007; infrastructure managers and national regulators, and safety authorities. At the European level, the railroad serves an important role in passenger transport. Although the EU has one of the densest railroad networks in the world, the national railroad systems in the EU, have different standards.

In order to modernize and increase efficiency, but simultaneously support cleaner, greener, smarter and sustainable transport, the European Commission adopted, at the end of the last year, a set of proposals [2] [3]. Those proposals refer to the increase of connectivity and the transportation of more passengers and freight to rail and inland waterways. By optimizing performance and greater use of more energy efficient modes of transport, 30% of road freight transport should be redirected to other modes such as rail and water transport by 2030, and more than 50% by 2050, connecting all airports by rail and providing sufficient measure the connection of all seaports to the rail freight and, where possible, inland waterways [2].

The best way of monitoring the performance of some organization or some process is by the properly defined indicator or the set of indicators that are more specifically aimed at the observation area of interest. This way the management could monitor the entire system and make proper decisions to enhance their operations. One of the examples of measuring performance is a key performance indicator (KPI). Actually, a KPI is a universal tool that represents a measurable value that shows the effectiveness of a company in achieving its goals. Consequently, the KPI can be applied to measure railway operation efficiency from available data [4]. In order to make an overall KPI of the railway system, many indicators and sub-indicators must be involved. Those indicators regard reliability, lead time, costs, flexibility and visibility, punctuality performance, mobility, capacity, business and financial performance, safety, etc.

In addition to the proper definition of the KPI and selecting the measuring units for each of them, the data acquisition and the quality of the data, are crucial. The data input could be done digitally, but often, the human factor is the dependent variable. Another perspective of the applied KPI on the railway operation depends on the viewpoint of the stakeholders. This means that the government perspective differs from the passenger perspective or the employee perspective.

The government evaluation of the railway system's performance, mostly favors financial performance and the subventions involved. In this way, proper improvements and optimizations can be applied. The employee process evaluation

defers on the level of the hierarchy and the process itself. But, it is commonly observed as the process performance and whether the goals are achieved on time and on what level. The passenger evaluation of the railway system is based on accessibility, reliability, flexibility, time and money-saving, environmental impact, service quality, and satisfaction, etc.

Today, in addition to the accountable authorities, responsibility is divided between infrastructure managers and transport operators. In the modern rail system, infrastructure management can be independent of the infrastructure owner, although the latter is often responsible for marketing the train tracks. Traditionally, operation covered the entire spectrum from timetabling and dispatching to higher-level transport management. In addition, energy supply, infrastructure maintenance, or the operation of stations and other services can be integrated or located in separate companies or parts of companies. In the EU, these areas are increasingly being taken over by specialized companies that do not belong to the respective former state railroads. Another important role is played by transport service providers. These include transport companies that transport goods or passengers on their own behalf or on behalf of the state, or nowadays also on the basis of municipal orders [5].

The structure of this paper is as follows: The Introduction, discusses the importance and analysis of railway operational performance at the global (state) and local (service users), the second section is devoted to reviewing the literature on the application of approaches and methodologies for evaluating railway performance. There is a wide range of criteria that can be studied when it comes to the efficiency of railways as a system, and for that reason. The third section describes a general mathematical procedure, using multicriteria defining sets of input data, in the form of criteria for passenger and freight rail transport. Next, the fourth section gives a brief overview of the methods used, Entropy for calculating weights and Topsis for ranking the performance of rail transport in the Republic of Serbia, for the time period from 2013 to 2019, based on valid statistics for the railway system, of the Republic of Serbia. At the end of the paper, in fifth section, the main conclusions and an overview of future research tasks are presented.

2 Literature Review

There are a large number of methods and techniques that are applied in certain analyzes [6-8]. Methods of multi-criteria decision-making are most often used because they are based on decision-making when there are several defined and conflicting criteria [9-11]. When reviewing the literature on railway performance analysis, it is seen that in a limited number there are studies that use different decision-making methods with multiple criteria to obtain an assessment of rail transport efficiency. There are two well-known approaches to evaluating and

measuring railway performance. First, parametric approaches are very rarely used because they need certain assumptions to establish the desired function, and second is refers to researchers who prefer using nonparametric approaches that involve fewer assumptions [12].

Various multi-decision making techniques are used to measure and evaluate performance in rail traffic such as AHP (Analytical Hierarchy Process), ANP (Analytical Network Process), DEMATEL (Decision making trial and evaluation laboratory), TOPSIS, SAW (Simple Additive Weighting) and etc. Also, the use of the DEA (Data Envelopment Analysis) method and machine learning can be found in different areas of the railway [13] [14]. DEA method can be used alone or in combination with MCDM methods.

Yu used the DEA method to conduct an efficiency and effectiveness study for a group of 40 large railway systems (passenger and freight) in 2002 [15]. The DEA method is used to evaluate the efficiency of European railway companies, taking into account different input and output configurations [16].

The authors in [17] developed a model for predicting the volume of railway transport that could be applied in different economic contexts and used as a means of transport planning. The model is made using common machine learning techniques that learn from past experience. Indicators defined by the World Bank were used as input parameters in the preparation of the model.

Based on the analysis of publicly available statistical data, taken from Eurostat service at a European level, the authors [18] enabled the identification and comparison of various indicators that affect the performance of the railway system from an infrastructural and operational perspectives. The paper highlights case studies for various parameters that are important for infrastructure managers, railway operators, policymakers and end-users.

A proposed method for the evaluation of service quality for measuring the performances of railway transit lines through passenger satisfaction surveys is given in [19]. Railway transit systems are one of the most desirable modes to avoid traffic congestion, especially during rush hours. The method combines statistical analysis, fuzzy trapezoidal numbers, and the TOPSIS method for estimating service quality levels. In the research conducted in Istanbul in 2012, 2013, and 2014, the authors [19] identified factors that need to be improved, gave recommendations for improving the work of certain lines, and guidance for future investments. Risk analysis is also an important aspect of railways [20].

The paper [21] presents the methodology for the assessment and classification of railway network performance along with the Trans-European Transport Network (TEN-T). Twenty-two infrastructural, economic and technological criteria for evaluating rail transport were used as input data. Based on the adopted criteria, countries are ranked using multi-criteria decision-making methods. The results

show that the eight countries involved in the Orient–East Med corridor can be classified into three groups.

The authors [22] applied MCDM methods in presenting the planning process of an integrated urban transport system where the proposed approach has a universal character and can be applied by urban planners, traffic engineers, and municipal authorities in strategic planning of urban transport systems and design of advanced transport solutions.

The operation performance evaluation of the urban railway system in the Chinese city – Chengdu during 34 months using the Entropy – TOPSIS methods was performed in [23]. The authors created a set of evaluation indicators with 8 indicators and a total of 41 sub-indicators. The operational data of 41 sub-indicators were used as input data for access.

Based on the review of the literature and indicated models and methods, and with the aim of determining the operational performance, a multi-criteria analysis will be conducted for both passenger and freight railway transport of the Republic of Serbia.

3 MCDM Methodology and Input Data

Multi-criteria decision-making methods have been developed as mathematical tools to support decision-makers involved in the decision-making process [24]. Those methods are gaining importance as potential tools for analyzing and solving complex problems due to their inherent ability to evaluate different alternatives with respect to various criteria for possible selection as the best alternative [25]. The choice of the method which will be used for solving the specific multi-criteria analysis problem depends on the nature of the problem, the availability of information concerning a problem, the number of alternatives, as well as the knowledge, previous experience, and preferences of the decision-maker.

Indicators are often defined as quantitative measures that can be used "to simply illustrate and communicate complex phenomena, including trends and progress over time." Indicators can perform different functions. The data collected may be suitable for analysis by those involved in decision-making and thus contribute to better decision-making.

The largest data sources for comparative assessment are statistics and annual reports of companies, however, the main issue under consideration in the last few years is the data availability from privatized and divided transport companies and the fact that many privatized operators find it very difficult to provide some of the details from their business. Although the large number of entities that are vital for transport make the task of collecting data for comparative assessment more complex, their presence on the other hand, should increase the quality and scope of comparative assessment.

The data collected through regular monthly, quarterly and annual statistical reports were taken from [26] and shown in Table 1.

Table 1
Indicators and sub-indicators of rail transport

Indicator	Sub-indicator	Specification of each	Unit of each sub-indicator
Basic indicators of rail transport	f ₁	Passenger transport (locomotive km)	train km, thous.
	f ₂	Freight transport (locomotive km)	train km, thous.
	f ₃	Passenger transport	gross-ton km, mill.
	f ₄	Passenger transport	gross-ton km, mill.
	f ₅	Number of transported passengers	thous.
	f ₆	Realized pkm	passenger-kilometers, thous.
	f ₇	Quantity of goods transported	thous. t
	f ₈	Realized tkm	ton-km, thous.
Employees in rail transport	f ₉	-	number
Generating power of rail transport	f ₁₀	Internal-combustion engines	kW, thous.
	f ₁₁	Electric engines	kW, thous.
Consumption of fuel and electricity in rail transport	f ₁₂	Liquid fuels	thous. t
	f ₁₃	Electricity	thous. MWh
Railway asset	f ₁₄	Effective length of tracks	km
	f ₁₅	Passenger wagon stock and motor trains	number
	f ₁₆		seats thous.
	f ₁₇	Freight wagon stock	number
	f ₁₈		tons of carrying capacity, thous.

The key indicators that are used Basic indicators of rail transport, Employees in rail transport, Generating power of rail transport, Consumption of fuel and electricity in transport and Railway asset. After that, the Entropy method is utilized, for determining weighting factors and the TOPSIS method, for ranking alternatives.

The weight coefficients are values that can be obtained by any of the following methods (Eigenvector method, Least squares weight method, Entropy method, etc.). The entropy method is a method for determining the weighting coefficients of multi-criteria decision-making. The method was invented by Claude Shannon (1984) [27]. Determining the weight of coefficients based on the entropy method consists of normalization of the values of alternatives according to each of the criteria, calculation entropy of all alternatives in terms of criteria, the degree of divergence of the average internal information of each criterion, and the final relative weights of the criteria are obtained by additive normalization [27].

TOPSIS (Technique for the Order Preference by Similarity to Ideal Solution) method was introduced by Hwang and Yoon (1981). The ordinary TOPSIS method is based on the concept that the best alternative should have the shortest Euclidian distance from the ideal solution (positive ideal solution – PIS) and at the same time the farthest from the anti-ideal solution (negative ideal solution – NIS). It is a method of compensatory aggregation that compares a set of alternatives by identifying weights for each criterion [24]. This method can be implemented using develop decision matrix which needs to normalize and weighted then determine the positive ideal and the negative ideal solutions, calculated the distance from the ideal and anti-ideal solutions for each alternative using the two Euclidean distances and calculate the relative closeness of every alternative to the positive ideal solution. The higher values indicate that the rank is better.

Alternatives represent the years of observation, and the criteria are the operational performance of rail freight and passenger transport in the Republic of Serbia.

4 The Approach and Results Discussion for Case Study: The Serbian Railway

To make a good decision, it is necessary to define alternatives by specifying appropriate criteria [28]. It is also necessary to define the values of weight coefficients for each criterion; i.e. the importance of each criterion in relation to the others [29, 30]. Weights will show the importance of the participation of certain criteria in making a decision on the ranking of alternatives (years). Determining the objective weights of criteria according to the Entropy method is based on measuring the uncertainty of information contained in the decision matrix and directly generates a set of weight values of criteria based on the contrast of individual criteria values of alternatives for each criterion and then simultaneously for all criteria using formulas from.

The basic concept of the TOPSIS method is that the chosen alternative should have the smallest distance from the ideal solution and the largest distance from the negative ideal solution, in the geometric sense. During the normalization process, the transformation of minimization into maximization criteria is not performed. For each alternative, the distance from the ideal and negative ideal solution is calculated in relation to each criterion, taking into account the criteria that are minimized and maximized. The weight/significance of each alternative is finally determined based on the relative closeness of the alternatives to the ideal solution [17].

Based on the adopted indicators, for both passenger (Tab. 2) and freight transport (Tab. 3) - Transpose matrix, evaluation of operation performance of the Serbian railway was done by Entropy method for determining weight coefficients and the TOPSIS method for ranking the observed years. The calculation results of weighting coefficients show that for passenger rail transport the Passenger wagon

stock and motor trains (0.1825) and for freight rail transport the Generating power of rail transport - Internal-combustion engines (0.2573) are the two most important indicators (sub-indicator) in the evaluation system.

Railway asset – Effective length of tracks has the smallest weighting coefficient for both passenger (0.0053) and freight (0.0090) rail transport and shows that this indicator has a minor impact in the operation performance evaluation process.

Table 2
Passenger railway transport – indicators, weighting coefficients and ranking

Criteria (Sub-indicator)/ Weight		Year						
f_i	w_i	2013	2014	2015	2016	2017	2018	2019
f_1	0.1306	11531	11170	16256	10930	16644	10417	9030
f_3	0.0201	1745	1666	1624	1957	1529	1727	1486
f_5	0.0676	7158	6443	6258	6092	5638	5062	4190
f_6	0.1469	612	452	509	438	377	347	285
f_9	0.1504	18047	17078	16622	13641	10229	10207	10596
f_{10}	0.0841	190	180	153	191	129	123	133
f_{11}	0.0128	626	626	605	687	585	556	671
f_{12}	0.0256	9	9	10	10	10	11	12
f_{13}	0.0596	148	139	136	120	116	115	90
f_{14}	0.0053	3819	3819	3766	3766	3764	3724	3323
f_{15}	0.1145	786	748	833	883	691	542	467
f_{16}	0.1825	48	45	56	59	48	30	27
Rank		4	5	1	2	3	6	7

Table 3
Freight railway transport – indicators, weighting coefficients and ranking

Criteria (Sub-indicator)/ Weight		Year						
f_i	w_i	2013	2014	2015	2016	2017	2018	2019
f_2	0.0198	5947	5878	5919	5103	4997	5424	5540
f_4	0.0153	5520	5464	5731	4870	5081	5390	5809
f_7	0.0154	10463	10826	11887	11896	12352	12297	11475
f_8	0.0097	3022	2988	3249	3087	3288	3187	2861
f_9	0.2524	18047	17078	16622	13641	10229	10207	10596
f_{10}	0.2573	190	180	153	191	129	89	133
f_{11}	0.0606	626	626	605	687	585	462	671
f_{12}	0.0429	9	9	10	10	10	11	12
f_{13}	0.1055	148	139	136	120	116	110	90
f_{14}	0.0090	3819	3819	3766	3766	3764	3752	3323
f_{17}	0.0921	8452	8486	8486	7277	6781	6589	5661
f_{18}	0.1200	431	432	432	411	342	371	259
Rank		5	4	6	1	2	7	3

By ranking with TOPSIS method on the basis of adopted indicators for passenger transport of the Serbian railways in the time frame from 2013 to 2019, it can be seen that the best operation performances were in 2015, while in 2019 they recorded the worst-case scenario (Tab. 2). When it comes to the obtained results for freight transport of the Serbian railways by ranking the appropriate indicators, it can be seen that the best operation performances were in 2016, while in 2018 they recorded the worst-case scenario (Tab. 3).

Conclusions

Increasingly modern rail transport, provides a more convenient and less expensive mode of daily passenger and goods transport, so the support of the State is necessary. It is important to set operational goals in advance and optimize the allocation of resources. In this paper, based on literature reviews, the evaluation of the railway operation efficiency in the Republic of Serbia is performed, based on data collected by the regular statistical reports, of traffic business entities, with that help, are formed into two sets of indicators, for passenger and for freight transport.

The total number of used indicators is 5 and 18 sub-indicators, i.e. individually for passenger and freight, 5 indicators and 12 sub-indicators, based on which the input matrices were formed in the observed period from 2013 to 2019. The importance of each indicator was calculated by the Entropy method, while the TOPSIS method was used to evaluate operation performance; i.e. to rank the results on an annual basis.

The calculation results of weighting coefficients show that for passenger rail transport the Passenger wagon stock and motor trains (f_{14}) and for freight rail transport the Generating power of rail transport - Internal-combustion engines (f_{10}) are the two most important indicators (sub-indicator) in the evaluation system. Railway asset – Effective length of tracks (f_{14}) has the smallest weighting coefficient for both passenger and freight rail transport and shows that this indicator is the least important indicator (sub-indicator).

Using the TOPSIS method, the adopted indicators, for the passenger rail transport system of the Republic of Serbia, were ranked in the time frame from 2013 to 2019, based on which, it is shown that the best operational performances were in 2015, while in 2019, showed the worst scenario. When it comes to the obtained results for freight transport of the Serbian railways, by ranking the appropriate indicators, it can be seen that the best operational performances were in 2016, while in 2019, showed the worst-case scenario.

Increasing the efficiency and competitiveness of railroads, to promote the market share of environmentally friendly rail, is one of the most important transport policy objectives of the EU and national transport policies are needed to meet the current and future challenges of transport markets, in particular, the increasing demand for long-distance passenger and freight transport.

The framework and goals of future research will be reflected in the use of this approach, to assess the performance of other transport modes or systems, using appropriate indicators.

Acknowledgement

This research was financially supported by the Ministry of Education, Science and Technological Development of the Republic of Serbia (Contract No. 451-03-68/2022-14/ 200109).

References

- [1] Allianz pro Schiene, Marktanteile der Eisenbahn am Personenverkehr in Deutschland (2020) [cited 2022-03-16] Available at: <https://www.allianz-pro-schiene.de/themen/personenverkehr/marktanteile/>
- [2] EU Commission, WHITE PAPER "Roadmap to a Single European Transport Area – Towards a competitive and resource efficient transport system", COM(2011) 144 final, [cited 2022-03-16] Available at: http://ec.europa.eu/transport/strategies/2011_white_paper_en.htm
- [3] Neila, S. B., Rejeb, A., Németh, P., The interplay between the physical internet and logistics: A literature review and future research directions. *Acta Technica Jaurinensis*, Vol. 15, No. 1, 2022, pp. 22-35, <https://doi.org/10.14513/actatechjaur.00638>
- [4] ITF, Efficiency in Railway Operations and Infrastructure Management, ITF Roundtable Reports, No. 177, OECD Publishing, Paris, (2019) [cited 2022-03-16] Available at: https://www.itf-oecd.org/sites/default/files/docs/efficiency-railway-operations-infrastructure_1.pdf
- [5] Salander, C. Akteure und Prozesse der Europäischen Union. In: *Das Europäische Bahnsystem*. Springer Vieweg, Wiesbaden, 2019. https://doi.org/10.1007/978-3-658-23496-6_2
- [6] Andrejić, M., Kilibarda, M., Pajić, V., Measuring efficiency change in time applying Malmquist productivity index: A case of distribution centres in Serbia, *Facta Universitatis-Series Mechanical Engineering*, Vol. 19, No. 3, 2021, pp. 499 - 514. <https://doi.org/10.22190/FUME201224039A>
- [7] Muhammad, L. J., Badi, I., Haruna, A. A., Mohammed, I. A., Selecting the Best Municipal Solid Waste Management Techniques in Nigeria Using Multi Criteria Decision Making Techniques, *Reports in Mechanical Engineering*, Vol. 2, No. 1, 2021, pp. 180-189, <https://doi.org/10.31181/rme2001021801b>
- [8] Pamučar, D., Normalized weighted geometric Dombi Bonferroni mean operator with interval grey numbers: Application in multicriteria decision making. *Reports in Mechanical Engineering*, Vol. 1, No. 1, 2020, pp. 44-52, <https://doi.org/10.31181/rme200101044p>
- [9] Mahmutagić, E., Stević, Ž., Nunić, Z., Chatterjee, P., Tanackov, I., An integrated decision-making model for efficiency analysis of the forklifts in

- warehousing systems, *Facta Universitatis-Series Mechanical Engineering*, Vol. 19, No. 3, 2021, pp. 537-553, <https://doi.org/10.22190/FUME210416052M>
- [10] Durmić, E., Stević, Ž., Chatterjee, P., Vasiljević, M., Tomašević, M., Sustainable supplier selection using combined FUCOM–Rough SAW model, *Reports in Mechanical Engineering*, Vol. 1, No. 1, 2020, pp. 34-43, <https://doi.org/10.31181/rme200101034c>
- [11] Rafat, M., Azadi, S., A Novel Flexible Lane Changing (FLC) Method in Complicated Dynamic Environment for Automated Vehicles. *Journal of Applied and Computational Mechanics*. 2021, DOI: 10.22055/JACM.2021.36276.2818
- [12] Sánchez, I. M. G., Technical and scale efficiency in Spanish urban transport: estimating with data envelopment analysis, *Adv. Oper. Res.* Vol. 2009. <https://doi.org/10.1155/2009/721279>
- [13] Khadem, S. M., *Railway Track Capacity: Measuring and Managing*, Doctoral dissertation, Uni. of Southampton, Faculty of Eng. and the Env., 2012
- [14] Pavelčík, V., Kuba, E., Application of basic machine learning algorithms in railway brake disc temperature prediction, *Transportation Research Procedia*, Vol. 55, 2021, pp. 715-722, <https://doi.org/10.1016/j.trpro.2021.07.040>
- [15] Yu, M. M., Assessing the technical efficiency, service effectiveness, and technical effectiveness of the world's railways through NDEA analysis, *Trans. Res. Part A: Policy and Practice*, Vol. 42, No. 10, 2008, pp. 1283-1294. <https://doi.org/10.1016/j.tra.2008.03.014>
- [16] Kapetanović, M., Milenković, M., Bojović, N., Avramović, Z., Evaluation of European Railway Companies Efficiency: Application of a TwoStage Analysis, *Tehnika – Saobraćaj*, Vol. 64, No. 3, 2017, pp. 403-410, <https://doi.org/10.5937/tehnika1703403K>
- [17] Lazarević, L., Kovačević, M., Popović, Z., Rail traffic volume estimation based on world development indicators, *Facta Universitatis-Series Mechanical Engineering*, Vol. 13, No. 2, 2015, pp. 133-141
- [18] Fraszczyk, A., Lamb, T., Marinov, M., Are railways really that bad? An evaluation of rail systems performance in Europe with a focus on passenger rail, *Transportation Research Part A: Policy and Practice*, Vol. 94, 2016, pp. 573-591, <https://doi.org/10.1016/j.tra.2016.10.018>
- [19] Aydin, N., A fuzzy-based multi-dimensional and multi-period service quality evaluation outline for rail transit systems, *Transport Policy*, Vol. 55, 2017, pp. 87-98, <https://doi.org/10.1016/j.tranpol.2017.02.001>
- [20] Macura, D., Laketić, M., Pamučar, D., Marinković, D., Risk Analysis Model with Interval Type-2 Fuzzy FMEA – Case Study of Railway Infrastructure Projects in the Republic of Serbia, *Acta Polytechnica Hungarica*, Vol. 19, No. 3, 2022, pp. 103-118, <https://doi.org/10.12700/APH.19.3.2022.3.9>

-
- [21] Stoilova, S., Munier, N., Kendra, M., Skrúčaný T., Multi-Criteria Evaluation of Railway Network Performance in Countries of the TEN-T Orient–East Med Corridor, Sustainability, Vol. 12, No. 4, 2020, 1482, <https://doi.org/10.3390/su12041482>
- [22] Fierek, S., Zak, J., Planning of an integrated urban transportation system based on macro-simulation and MCDM/A methods. Procedia- Social and Behav. Sci. 54, 2012, 567-579, <https://doi.org/10.1016/j.sbspro.2012.09.774>
- [23] Huang, W., Shuai, B., Sun, Y., Wang, Y., Antwi, E., Using entropy-TOPSIS method to evaluate urban rail transit system operation performance: The China case, Transportation Research Part A: Policy and Practice, Vol. 111, 2018, pp. 292-303, <https://doi.org/10.1016/j.tr.2018.03.025>
- [24] Shekhovtsov, A., Więckowski, J., Kizielewicz, B., & Sałabun, W., Towards Reliable Decision-Making in the green urban transport domain. Facta Universitatis. Series: Mechanical Engineering, Vol. 20, No. 2, 2021, pp. 381-398, <https://doi.org/10.22190/FUME210315056S>
- [25] Chakraborty, S., Zavadskas, E.,K., Antucheviciene, J., Application of WASPAS method as a multi-criteria decision-making tool, Economic computation and economic cybernetics studies and research, Vol. 49, No. 1, 2015, pp. 5-22
- [26] Statistical Office of the Republic of Serbia, Statistical Yearbook of the Republic of Serbia (2020) Available at: <https://www.stat.gov.rs/en-us/publikacije/publication/?p=12694>
- [27] Dimitrijević, B., Višeatributivno odlučivanje (In Serbian.) University of Belgrade – Faculty of Transport and Traffic Engineering, 2017
- [28] Osintsev, N., Rakhmangulov, A., Baginova, V., Evaluation of logistic flows in green supply chains based on the combined DEMATEL-ANP method, Facta Universitatis Series: Mechanical Engineering, Vol. 19, No. 3, 2021, pp. 473-498, <https://doi.org/10.22190/FUME2105050610>
- [29] Ali, Y, Bilal, M. B., Huzaifa, M., Yasir, U., Khan, U. A., Development of a new hybrid multi criteria decision-making method for a car selection scenario, Facta Universitatis Series: Mechanical Engineering, Vol. 18, No. 3, 2020, pp. 357-373, <https://doi.org/10.22190/FUME200305031A>
- [30] Muhammad, L. J., Badi, I., Haruna, A. A., Mohammed, I. A., Selecting the best municipal solid waste management techniques in Nigeria using multi criteria decision making techniques. Reports in Mechanical Engineering, Vol. 2, No. 1, 2021, pp. 180-189, <https://doi.org/10.31181/rme2001021801b>

Bi-directional Evolutionary, Reliability-based, Geometrically Nonlinear, Elasto-Plastic Topology Optimization, of 3D Structures

Muayad Habashneh, Majid Movahedi Rad, Szabolcs Fischer

Széchenyi István University, Egyetem tér 1, Győr 9026, Hungary

e-mail: habashneh.muayad@hallgato.sze.hu, majidmr@sze.hu, fischersz@sze.hu

Abstract: An extension of bi-directional evolutionary structural optimization, by considering three-dimensional geometrically nonlinear reliability-based elasto-plastic topology optimization, is presented in this study. Due to the important role of the existence of uncertainties to make structural design more practical, this study considers the reliability-based design. Thus, for probabilistic purposes, volume fraction is considered random. The reason of considering the volume fraction as random variable that the application of reliability-based topology optimization shows different topological results comparing to those which are obtained through deterministic designs. By adopting Monte-Carlo technique, the reliability indices are calculated based on the failure probabilities. Different values of volume fractions are considered to explore the effect of changing it on the resultant topologies in case of deterministic design. Furthermore, study the influence of considering different values of reliability indices on the results of probabilistic designs. The plastic-limit analysis is considered in this study in case of elasto-plastic models. A 3D elasto-plastic L-shape beam is considered as a benchmark problem to demonstrate the proficiency of the proposed method. In addition, 3D cantilever beam is considered for deterministic and probabilistic topology optimization designs in cases of elastic and elasto-plastic materials.

Keywords: BESO method; Structural optimization; Geometrically nonlinear analysis; Elasto-plastic deformation; Reliability-based design optimization

Nomenclature

η_{ij}	Total Lagrangian strain	V_i	Element volume
B	Transformation finite element	V^*	Total volume of structure
U	Finite element displacement	V_0	Volume of design domain
s_{ij}	The constituent of second Piola-Kirchhoff stress	V_f	Volume fraction
p_e	Péclet number	N	Number of elements
p	Penalization power	x_i	Binary design variable
C_{ijkl}^0	Solid isotropic material	x	Generated realizations
η_{kl}	The Green-Lagrange strains	X	Random vector
R	Residual vector	$f_X(x)$	Probability joint density

s	Piola-Kirchhoff stress	β	Reliability index
P	The applied load	P_f	Probability of failure
K_T	Tangential stiffness matrix	ν	Poisson's ratio
F_i	Given force	r_{min}	Filter radius
m_s	Load multiplier	ER	Evolutionary volume ratio
F_0	Initial predefined applied forces	τ	Allowable convergence
m_p	Plastic load multiplier	W^c	The complementary work
C	Mean compliance	σ_y	Yield stress
u	Displacement vectors	σ_{HMH}	The Huber-v. Mises-Hencky
K	Global stiffness matrix		

1 Introduction

Topology optimization (TO) is a mathematical approach used to obtain the effectual material distribution within a specified design domain to reach the goal of finding the best structural performance considering fulfilling various constraints. TO has drawn the interest of designers to deal with innovative designs of structures. Thus, the improvement of appropriate applications of (TO) techniques in the construction industry has obtained an increasing consideration [1] [2]. In fact, (TO) can be considered as a promising method to apply in various civil engineering projects such as in concrete and steel structures as well as in case of railway barriers optimization to achieve best designs [3-6]. Besides, (TO) is a powerful technique in finite element analysis of various structures since it allows the designer to identify the parts of the assembly which are unnecessary to satisfy the structure requirements [7-12].

Structural topology optimization has undergone a rapid evolution during last decades. Various tools which facilitate structural optimization in different manners were provided by many authors, for instance, determining load paths in the structures [13], or through determining highly stressed structural areas in a quite effective way [14] [15]. A topology optimization problem of minimizing structural weigh subjected to stress constraints was introduced in the study of Cheng and Jiang [16]. Bi-directional evolutionary structural optimization (BESO) is one of the developed methods which has experienced various improvements recently. In general, the essential idea of (BESO) method is adding and deleting the elements within the design domain at same time according to their sensitivity numbers [17] [18]. A structural topology optimization approach was integrated into laminated composites plates in the study of Chandrasekhar et al. [19] by considering two different goal functions of fundamental frequency and strain energy. Furthermore, Sahithi and Chandrasekhar [20] proposed isogeometric topology optimization based on evolutionary algorithm of swarm intelligence.

Reliability-based topology optimization aims to find a strongly reliable design. Uncertainty topology optimization was considered in the study of Dunning et al. [21] by random assume of the loading magnitude and its direction. Lógó et al. [22] considered uncertainty load condition to develop an updated optimization formulation. Lately, geometrical nonlinearity has been adopted in structural topology optimization by applying it in various problems such as compliant mechanisms and energy absorption. Luo et al. [23] examined in their study topology optimization of structures undergo large displacement. Topology optimization method of elasto-plastic structures was presented in the study of Tazowski et al. [24]. Blachowski et al. [25] proposed a topology optimization method of elasto-plastic materials considering fulfillment of stress constraints. An updated optimization algorithm considering large displacement was introduced in the study of Gomes and Senne [26]. In the case of materially nonlinear analysis, such as elasto-plastic models, one needs to define the material elastic modulus, plastic hardening and the yield stress to perform elasto-plastic topology optimization. The elastoplastic deformation was considered for topology optimization of composite structures in the study of Kato et al. [27]. Gopal and Panchal [28] proposed an integrated technique to examine the reliability and risk problems within uncertain environment of the process of milk industry.

The three-dimensional topology optimization was considered in various scientific papers. In the study of Liu and Tovar [29], three-dimensional models were considered to perform topology optimization by using MATLAB code. A 3D topology optimization with the aim of minimization of the mean compliance was considered in the study of Zuo and Xie [30]. Langelaar [31] presented a self-supporting topology optimization formulation by considering the effect of excluding unprinted geometries from design domain in case of additive manufacturing.

This study is a continues research work of the development of BESO method, which aims to present 3D reliability-based topology optimization of geometrically nonlinear and elasto-plastic problems. The rest of this paper is organized as following: Section 2 represents theoretical background of the problem. Numerical examples which are considered in this paper are included in Section 3. Finally, the work is summarized in Section 4, the Conclusions.

2 Theoretical Background

2.1 Deterministic Elasto-Plastic BESO

Total nonlinear Lagrangian finite element model is considered to perform the analysis of nonlinear large displacements:

$$\eta_{ij} = \frac{1}{2}(u_{i,j} + u_{j,i} + u_{k,i} u_{k,j}) \quad (1)$$

where u is point-wise displacement, and i, j and k represent coordinate axes.

$$d\eta = B(U)dU \quad (2)$$

where B is the finite element matrix which transforms the change in displacement dU into a strain changing, and U is finite element displacement vector. The Hooke's law for material densities can be expressed as:

$$s_{ij} = (p_e)^p C_{ijkl}^0 \eta_{kl} \quad (3)$$

where s_{ij} is the constituent of second Piola-Kirchhoff stress, p_e represents Péclet number, p is penalization power, C_{ijkl}^0 is solid isotropic material constitutive tensor and η_{kl} is the Green-Lagrange strains. Hence, the residual can be defined as the error of the obtained equilibrium.

$$R(U) = P - \int_V B^T s dV \quad (4)$$

where s refers to the vector of Piola-Kirchhoff stress and P represents the applied load. The equilibrium found when the residual vector equal to zero vector. As a rule, the finite element equilibrium (4) is solved by using Newton-Raphson iterative scheme.

$$K_T = - \frac{\partial R}{\partial U} \quad (5)$$

where K_T is the tangential stiffness matrix.

The plastic-limit analysis is considered in this study in case of elasto-plastic models. The theory of this type of analysis is based on assumption indicates that an elasto-plastic body is exposed to a given force F_i which is gradually increased. The relative load is expressed as:

$$F_i = m_s F_0 \quad (6)$$

Where m_s is the load multiplier and F_0 represents the initial predefined applied forces. As m_s increases, plastic zones of the body start to appear until reach extreme intensity which is m_p . Hence, an unrestricted flow of plastic state finally reached. By way of explanation, the corresponding plastic strains and displacements become feasible for the first time during the loading process. According to the definition of plastic limit state, the resultant work of the applied force cannot be negative, therefore, $m_s - m_p \leq 0$.

An extensive explanation of BESO method can be found in various academic papers and literature. Thus, only the applied improvements of BESO method are briefly discussed in this study.

The deterministic elasto-plastic BESO problem can be constructed as following:

$$\text{Minimize: } C = u^T K u \quad (7.a)$$

$$\text{Subjected to: } V^* - \sum_{i=1}^N V_i x_i = 0 \quad (7.b)$$

$$\frac{V^*}{V_0} - V_f \leq 0 \quad (7.c)$$

$$x_i \in \{0,1\} \quad (7.d)$$

$$m_s - m_p \leq 0 \quad (7.e)$$

Where C stands for the mean compliance, u represents displacement vectors and K denotes the global stiffness matrix. Besides, V_i , V^* , V_0 and V_f represent element volume, total volume of structure, volume of design domain and volume fraction respectively. N is the number of entire elements, and x_i is binary variable which indicates the presence of the solid element. Here, Eq. (7.e) introduces the plastic-limit constraint. Based on the static principle, any statically allowable load multiplier m_s is less or equal the plastic limit load multiplier m_p for the whole design domain.

2.2 Probabilistic Elasto-Plastic BESO

The reliability-based design is considered in this study by applying Monte-Carlo technique. The very basic concept of Monte-Carlo technique is generating of realizations \mathbf{x} of the random vector \mathbf{X} from their probability joint density function $f_{\mathbf{X}}(\mathbf{x})$. Consequently, the reliability indices β is determined by estimating the probability of failure P_f according to the number of the points inside failure domain with respect to the number of total generated points [32]. It should be mentioned that V_f is considered as a random variable having probabilistic characteristics of mean value and standard deviation.

Accordingly, the reliability constraint can be formulated considering the reliability index β as:

$$\beta_{target} - \beta_{calc} \leq 0 \quad (8)$$

where β_{calc} is the calculated reliability index for each iteration and when it reaches the target value of reliability index β_{target} , the program will be terminated since that this constraint is satisfied.

To calculate β_{target} and β_{calc} , the following equations are used:

$$\beta_{target} = -\Phi^{-1}(P_{f,target}) \quad (9)$$

$$\beta_{calc} = -\Phi^{-1}(P_{f,calc}) \quad (10)$$

Thus, the probabilistic optimization problem can be illustrated as:

$$\text{Minimize: } C = \mathbf{u}^T \mathbf{K} \mathbf{u} \quad (11.a)$$

$$\text{Subject to: } V^* - \sum_{i=1}^N V_i x_i = 0 \quad (11.b)$$

$$x_i \in \{0,1\} \quad (11.c)$$

$$m_s - m_p \leq 0 \quad (11.d)$$

$$\beta_{target} - \beta_{calc} \leq 0 \quad (11.e)$$

Here Eqs. (11.a), (11.b) and (11.c) have same roles as Eqs. (7.a), (7.b) and (7.d). While Eq. (7.e) presents the reliability boundary condition on the V_f .

2.3 The Procedure of the Improved BESO

After the brief description of the mathematical technique of the new method, the algorithm can be assembled as shown in Figure 1 for both deterministic and probabilistic designs.

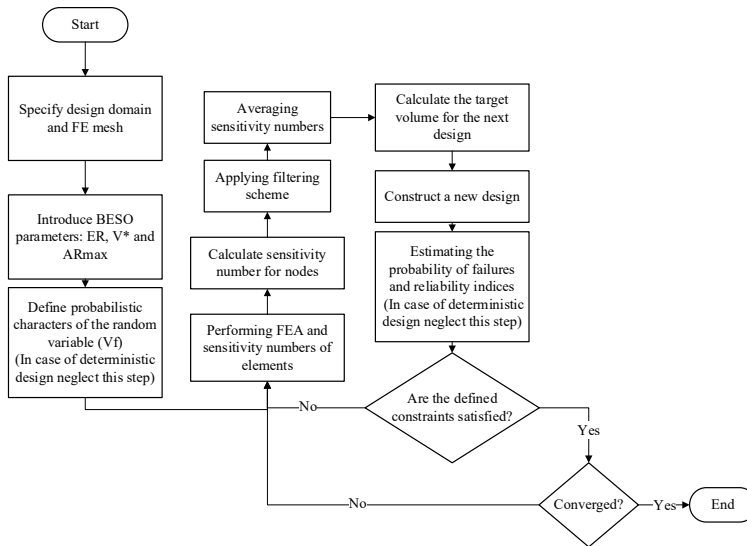


Figure 1

Flow chart of reliability-based geometrically nonlinear elasto-elastic BESO

The algorithm steps can be summed as following:

- 1) Specify the design domain and FE mesh
- 2) Introducing BESO parameters
- 3) Defining mean value and standard deviation (for probabilistic problem)
- 4) Carrying out finite element simulation
- 5) Calculate sensitivity numbers for elements and nodes then applying filter and average schemes
- 6) Calculate the target volume for the next iteration
- 7) Constructing new design

- 8) Estimation of the \mathbf{P}_f and $\boldsymbol{\beta}$ values (for probabilistic problem)
- 9) Repeat steps 4-8 until fulfillment of the specified constraints as well as the solution is converged

3 Numerical Examples

In this section, two 3D numerical models are considered for the improved bi-directional evolutionary structural optimization (BESO) method. The first example is a 3D cantilever beam fixed at one end. A 3D L-shape beam model is considered as the second example, to demonstrate the efficiency of the proposed method, the results of this example are compared with a benchmark example which was done by Rad et al. [33]. For purpose of evaluating probabilistic nature, Monte-Carlo technique as well as V_f is considered as random variable with mean value and standard deviation.

3.1 3D Cantilever Beam Model

The first example in this study is 3D cantilever model. At the beginning, reliability-based topology optimization of elastic linear and geometrically nonlinear models is considered. Then, reliability elasto-plastic topology optimization is considered for the same model. The design domain of the model is represented in Figure 2. The common parameters for both optimization processes are Young's modulus of 70.2 GPa with Poisson's ratio $\nu = 0.25$. BESO parameters are $r_{min} = 3 \text{ mm}$, $ER = 3\%$, and $\tau = 0.1\%$. In addition, volume fraction V_f is assumed random and has probabilistic properties of mean value 10% and standard deviation 5%. Finally, Monte-Carlo technique is considered with number of simulations 3.0×10^6 .

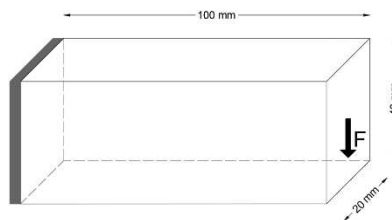


Figure 2
3D cantilever beam model

3.1.1 Elastic Topology Optimization Problem

Elastic reliability-based topology optimization of linear and geometrically nonlinear models is considered in this part. Considering that the applied load at the free end as shown in Figure 2 has a magnitude of $F = 1 \text{ kN}$.

The resulted topological designs of linear and geometrically nonlinear analysis beside the complementary work W^c of different volume fraction values of deterministic design are shown in Table 1. It can be noted from Table 1 that there is a significant decrease in the complementary work from linear design to geometrically nonlinear designs for each value of volume fraction. By considering $V_f = 0.16$, the complementary work value dropped down by 22.2% from 1.35 kJ in linear case to 1.05 kJ in geometrically nonlinear case. Also, for $V_f = 0.10$, the complementary work value declined by 37.3% from 1.93 kJ in linear case to 1.21 kJ in geometrically nonlinear design. Thus, the optimal resulted topologies in case of nonlinear designs are stiffer than those which are obtained in case of linear design. Besides, according to the obtained results, it should be mentioned that as V_f declines the complementary work raises for elastic linear and geometrically nonlinear models.

Table 1
Resulted topological designs and complementary work in case of deterministic design

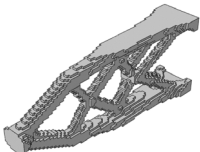
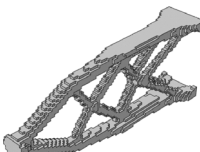
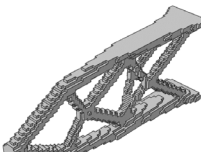
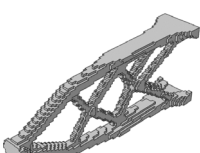
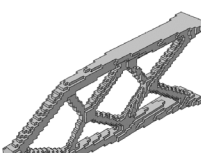
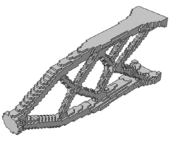
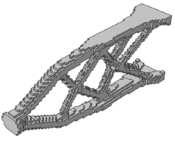
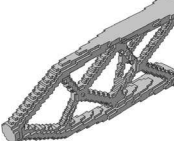
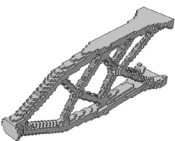
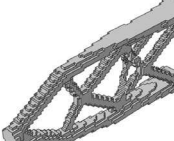
	V_f	Optimized shape	W^c		V_f	Optimized shape	W^c
	Deterministic linear designs from BESO	0.16			1.35	Deterministic geometrically nonlinear designs from BESO	0.16
	0.12		1.72		0.12		1.13
	0.10		1.93		0.10		1.21

Table 2 shows the resulted topological designs of probabilistic linear and geometrically nonlinear analysis beside the complementary work W^c considering different β_{target} values. It can be noted that there are significant differences in the complementary work between linear design and geometrically nonlinear designs for each case of volume fraction. By considering $\beta_{target} = 4.37$, the complementary work value dropped by 13.01% from 1.69 kJ in linear case to 1.47 kJ in geometrically nonlinear case. In addition, for the lowest value of target reliability index $\beta_{target} = 3.05$, the complementary work value fallen by 10.28% from 1.75 kJ in linear case to 1.57 kJ in geometrically nonlinear design. In other words,

in case of geometrically nonlinear designs, the resulted topologies are stiffer from which are obtained in case of linear designs. Also, it can be said that as β_{target} become less the complementary work raises for elastic linear and geometrically nonlinear models.

Table 2
Resulted topological designs and complementary work in case of probabilistic design

	β_{target}	Optimized shape	W^c		β_{target}	Optimized shape	W^c
	Probabilistic linear designs from BESO	4.37			1.69	Probabilistic geometrically nonlinear designs from BESO	4.37
	3.64		1.71		3.64		1.52
	3.05		1.75		3.05		1.57

3.1.2 Elasto-Plastic Topology Optimization Problem


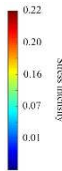
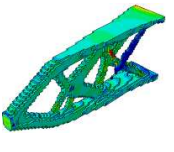
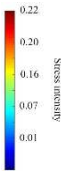
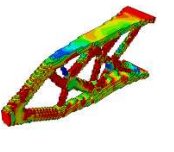
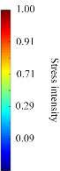
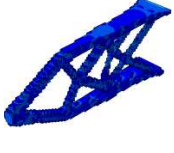
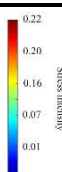
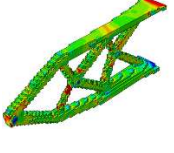
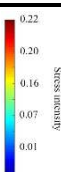
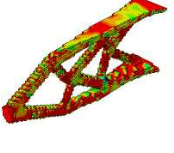
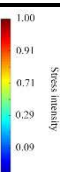

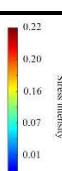
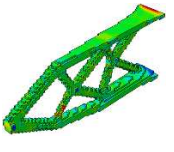
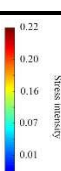
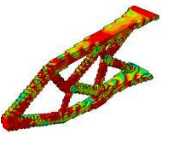
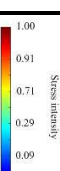
Deterministic and probabilistic geometrically nonlinear topology optimizations of elasto-plastic 3D cantilever model are considered in this part. The yield stress equals $\sigma_y = 135 \text{ MPa}$. The plastic-limit load multiplier m_p is assumed 5.0, the initial load is assumed to be $F_0 = 0.5 \text{ kN}$ and the ultimate load is $F_{ult} = 2.6 \text{ kN}$. To demonstrate the effect of load multiplier, three load cases are considered: $F_1 = 0.5 F_0$, $F_2 = 2.5 F_0$, $F_3 = 5 F_0$.

Table 3 represents the Huber-v. Mises-Hencky (*HMH*) stresses of deterministic resulted topological optimum designs of geometrically nonlinear analysis for different values of V_f considering three different values of load multiplier F_1 , F_2 and F_3 .

According to the results which are included in Table 3, it can be noticed that in case of lowest applied load ($F_1 = 0.5 F_0$), the mean stress is increased by 18.27% from 10.96 MPa in case of $V_f = 0.16$ to 13.41 MPa when $V_f = 0.10$. Corresponding to the highest load multiplier ($F_3 = 5.0 F_0$), the mean stress is raised by 10.37% from 90.36 MPa in case of $V_f = 0.16$ to 100.81 MPa when $V_f = 0.10$. Thus, according to these results, we can say that as V_f decreases, that the mean stress increases for each loading case.

Table 3

Resulted topological designs and *HMH* stresses according to various V_f considering F_1, F_2 and F_3

V_f	$F_1 = 0.5 F_0$	$\frac{\sigma_{HMH}}{\sigma_y}$	$F_2 = 2.5 F_0$	$\frac{\sigma_{HMH}}{\sigma_y}$	$F_3 = 5.0 F_0$	$\frac{\sigma_{HMH}}{\sigma_y}$
0.16						
Mean stress (MPa)	10.96		54.41		90.36	
0.12						
Mean stress (MPa)	11.26		55.68		96.92	
0.10						
Mean stress (MPa)	13.41		67.05		100.81	


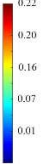
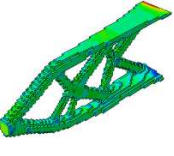
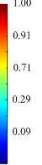
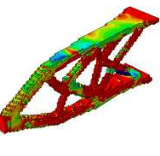


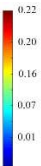
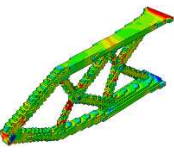
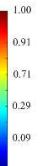
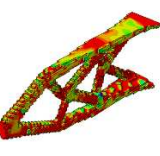


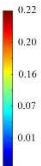
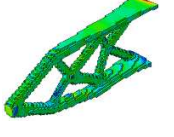
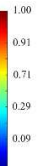
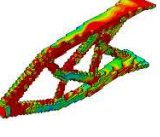

Furthermore, it can be observed from the obtained results that in case of first load multiplier there is almost no plastic regions. While, in case of highest load multiplier, plastic zones are obtained largely.

The corresponding Huber-v. Mises-Hencky (*HMH*) stresses of different load cases $F_1 = 0.5 F_0$, $F_2 = 2.5 F_0$ and $F_3 = 5 F_0$ according to the resulted probabilistic geometrically nonlinear topological designs are shown in Table 4. Considering that three values of β_{target} are considered.

According to Table 4, it is well noticed that in case of lowest load case ($F_1 = 0.5 F_0$), the mean stress is increased by 6.20% from 10.74 MPa in case of $\beta_{target} = 4.37$ to 11.45 MPa when $\beta_{target} = 3.05$. Corresponding to the highest load multiplier ($F_3 = 3.05 F_0$), the mean stress is raised by 5.92% from 89.77 MPa in case of $\beta_{target} = 4.37$ to 95.42 MPa when $\beta_{target} = 3.05$.

Table 4

Resulted topological designs and HMH stresses according to various β_{target} considering F_1, F_2 and F_3

β_{target}	$F_1 = 0.5 F_0$	$\frac{\sigma_{HMH}}{\sigma_y}$	$F_2 = 2.5 F_0$	$\frac{\sigma_{HMH}}{\sigma_y}$	$F_3 = 5.0 F_0$	$\frac{\sigma_{HMH}}{\sigma_y}$
4.37						
Mean stress (MPa)	10.74		53.72		89.77	
3.64						
Mean stress (MPa)	11.08		55.56		92.20	
3.05						
Mean stress (MPa)	11.45		57.32		95.42	

In other words, the mean stress increases as β_{target} decreases for each loading case. Also, the effect of load multiplier can be observed from the obtained results since that in the case of first load multiplier there is almost no plastic regions. While, in case of the highest load multiplier, plastic zones are obtained largely.

3.2 3D L-Shape Beam Model

3D L-shape model is the considered as the second example in this study. Figure 3 represents the design domain of this problem. This work has implemented deterministic and probabilistic geometrically nonlinear elasto-plastic topology optimization. An applied load F is acting at the top of the free end. Material properties are assumed 200 GPa of Young's modulus and 0.25 of Poisson's ratio. Considering that BESO parameters are $r_{min} = 18mm$, $ER = 1\%$, and $\tau = 0.1\%$.

Volume fraction V_f has the probabilistic properties of mean value 21% and standard deviation 5%. The number of Monte-Carlo simulation is assumed 3.0×10^6 .

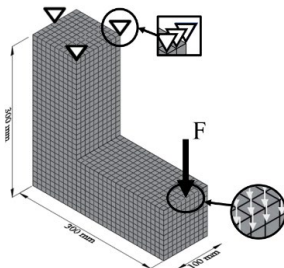
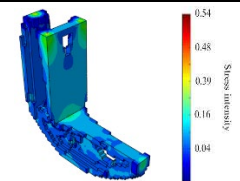
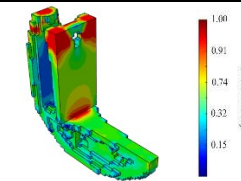
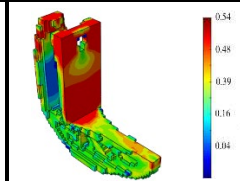
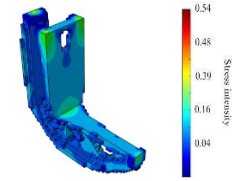
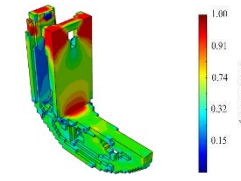
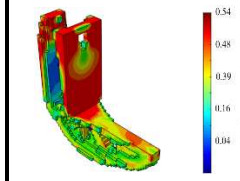
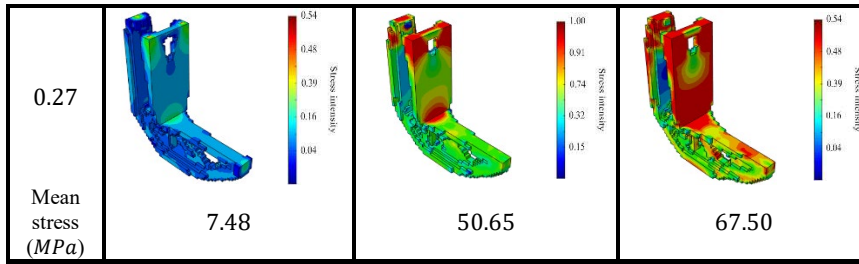


Figure 3
3D L-shaped beam model

For purposes of considering plastic-limit analysis, the initial load is assumed $F_0 = 10 \text{ kN}$ and the value of yield stress $\sigma_y = 93 \text{ Mpa}$. In addition, the limit of plastic load is $m_p = 3.48$. consequently, four load cases are considered in this problem: $F_1 = 0.348F_0$, $F_2 = 2.262F_0$, $F_3 = 3.30F_0$. Finally, as mentioned previously, the results of this work are compared with the study of Rad et al. [33]. Similar to the previous problem, Table 5 shows the results of deterministic topological optimum designs of elasto-plastic geometrically nonlinear analysis for different values of V_f according to $F_1 = 0.348F_0$, $F_2 = 2.262F_0$ and $F_3 = 3.30F_0$.

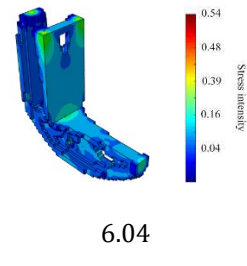
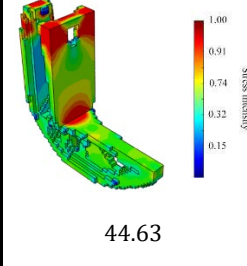
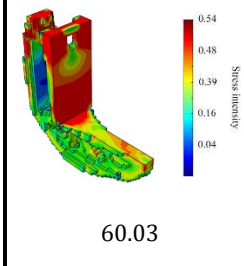
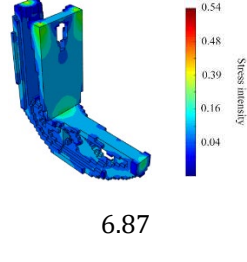
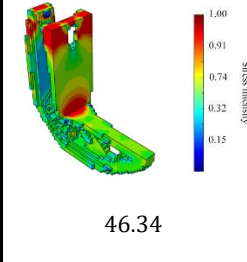
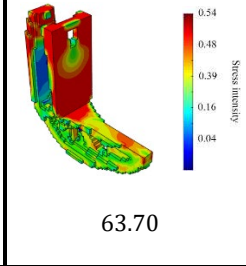
Table 5
Resulted topological designs and HMH stresses according to various V_f by considering F_1, F_2 and F_3

V_f	$F_1 = 0.348F_0$ $\frac{\sigma_{HMH}}{\sigma_y}$	$F_2 = 2.262F_0$ $\frac{\sigma_{HMH}}{\sigma_y}$	$F_3 = 3.30F_0$ $\frac{\sigma_{HMH}}{\sigma_y}$
0.30 Mean stress (MPa)	 6.71	 45.41	 60.21
0.28 Mean stress (MPa)	 7.19	 48.63	 64.67



Similarly, to the results of previous problem, it can be noticed that the mean stress increases as V_f decreases for each loading case. As obtained from the results of lowest load case ($F_1 = 0.348 F_0$), the mean stress is increased by 10.29% from 6.71 MPa in case of $V_f = 0.30$ to 7.48 MPa when $V_f = 0.27$. Also, for the highest load multiplier ($F_3 = 3.30 F_0$), the mean stress is increased by 10.80% from 60.21 MPa in case of $V_f = 0.30$ to 67.50 MPa when $V_f = 0.27$. Besides, here again the significant effect of load multiplier can be noticed from the obtained results since that in the case of first load multiplier there is almost no plastic regions. While the plastic zones are obtained largely in case of the highest load multiplier. Table 6 represents the corresponding Huber-v. Mises-Hencky (HMH) stresses of load multiplier $F_1 = 0.348 F_0$, $F_2 = 2.262 F_0$ and $F_3 = 3.30 F_0$ in case of probabilistic elasto-plastic geometrically nonlinear topological designs. By considering three different values of β_{target} .

Table 6
Resulted topological designs and HMH stresses according to various β_{target} by considering F_1, F_2 and F_3

β_{target}	$F_1 = 0.348F_0$ $\frac{\sigma_{HMH}}{\sigma_y}$	$F_2 = 2.262F_0$ $\frac{\sigma_{HMH}}{\sigma_y}$	$F_3 = 3.30F_0$ $\frac{\sigma_{HMH}}{\sigma_y}$
4.97			
Mean stress (MPa)	6.04	44.63	60.03
4.16			
Mean stress (MPa)	6.87	46.34	63.70

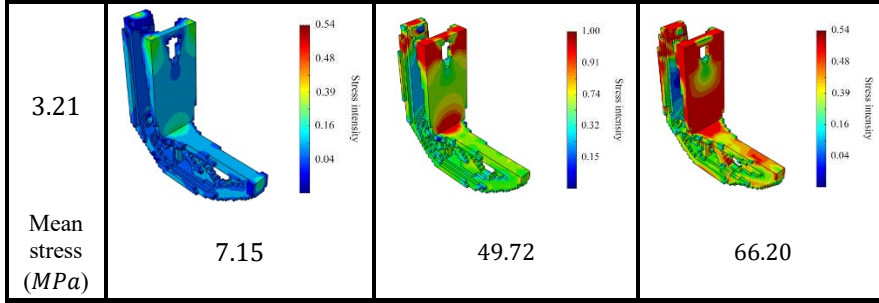


Table 6 shows that the increasing percentage of the mean stress is 15.52% from 6.04 MPa in case of $\beta_{target} = 4.97$ to 7.15 MPa when $\beta_{target} = 3.21$ according to the lowest load case ($F_1 = 0.348 F_0$). Also, 9.32% is the increasing percentage of the mean stress from 60.03 MPa in case of $\beta_{target} = 4.97$ to 66.20 MPa in case of $\beta_{target} = 3.21$ according to the highest load case ($F_3 = 3.30 F_0$). Thus, we can say that the mean stress increases as β_{target} decreases for each loading case. Again, here we can notice that in the case of first load multiplier there is no obtained plastic zones. On the other hand, by increasing the applied load, plastic zones can be obtained sufficiently until reach the plastic-limit load.

Conclusions

This work concerns the expansion of a reliability-based, geometrically nonlinear, elasto-elastic topology optimization, of 3D structures, by considering an extended BESO method. Due to the existence of uncertainties, V_f is treated as a random variable during the optimization process. The reliability-based design is performed, by adopting Monte-Carlo simulation method, by determining the reliability indices according to the values of failure probabilities. In the case of elasto-plastic structures, the plastic-limit analysis method is considered. The proposed method can be considered as an effective structural optimization method, for solving the three-dimensional design problems, associated with a goal of mean compliance minimization. The results of the benchmark problem, obviously validate the efficiency of the proposed method.

The work done in this study, can be summarized, by the following points:

- 1) In case of deterministic design, when multiple V_f values are considered, there is a negative correlation between V_f and complementary work. Also, between V_f and the values of mean stresses.
- 2) In case of Probabilistic design, when multiple values of β_{target} are considered, it can be noted that as β_{target} decreases, the complementary work and the values of mean stresses increase.
- 3) For both deterministic and probabilistic designs, the complementary work values of geometrically nonlinear designs are smaller than which obtained in case of linear designs.

- 4) It is noted, that in elasto-plastic design for both deterministic and probabilistic cases, there is almost no plastic regions obtained corresponding to the lowest acting load, while the plastic zones are clearly visible in case of highest acting load.

This paper can be considered as a huge improvement, towards a more sensible and more extensive framework, for three-dimensional geometrically nonlinear elastic and elasto-plastic topology optimization, by adopting the plastic-limit analysis considering reliability constraint. Thus, based on the noted examples, the proposed approach can be considered as a valuable work in the work associated with finding the optimal topologies, in the design of structures, as compared to other methods. The proposed BESO method has the fundamental advantages of the basic BESO algorithm, exactly, effectiveness and simplicity. In addition, according to the obtained results, we can say that the optimum solutions are firmer in the case of geometrically nonlinear designs, than in the case of linear designs. However, the main concern of the proposed model is related to the global optimum. Thus, it is herein recommended to validate the loading and boundary conditions for each iteration. Nonetheless, additional research is planned to include other nonlinear designs.

References

- [1] Błachowski B, Świercz A, Ostrowski M, Tauzowski P, Olaszek P, Jankowski Ł. Convex relaxation for efficient sensor layout optimization in large-scale structures subjected to moving loads. *Computer-Aided Civil and Infrastructure Engineering* 2020;35:1085–100. <https://doi.org/10.1111/mice.12553>.
- [2] Duysinx P, Bendsøe MP. Topology optimization of continuum structures with local stress constraints. *International Journal for Numerical Methods in Engineering* 1998;43:1453–78. [https://doi.org/10.1002/\(SICI\)1097-0207\(19981230\)43:8<1453::AID-NME480>3.0.CO;2-2](https://doi.org/10.1002/(SICI)1097-0207(19981230)43:8<1453::AID-NME480>3.0.CO;2-2).
- [3] Kurhan D, Kurhan M, Husak M. Impact of the variable stiffness section on the conditions of track and rolling stock interaction. *IOP Conference Series: Materials Science and Engineering*, vol. 985, 2020, p. 12005. <https://doi.org/10.1088/1757-899X/985/1/012005>.
- [4] Kurhan M, Kurhan D, Novik R, Baydak S, Hmelevska N. Improvement of the railway track efficiency by minimizing the rail wear in curves. *IOP Conference Series: Materials Science and Engineering*, vol. 985, 2020, p. 12001. <https://doi.org/10.1088/1757-899X/985/1/012001>.
- [5] Mahmood T, Haleemzai I, Ali Z, Pamucar D, Marinkovic D. Power Muirhead Mean Operators for Interval-Valued Linear Diophantine Fuzzy Sets and Their Application in Decision-Making Strategies. *Mathematics* 2022;10:70. <https://doi.org/10.3390/math10010070>.

-
- [6] Kuchak AJT, Marinkovic D, Zehn M. Parametric Investigation of a Rail Damper Design Based on a Lab-Scaled Model. *Journal of Vibration Engineering & Technologies* 2021;9:51–60. <https://doi.org/10.1007/s42417-020-00209-2>.
- [7] He CH, Liu C, He JH, Mohammad-Sedighi H, Shokri A, Gepreel KA. A fractal model for the internal temperature response of a porous concrete. *Appl Comput Math* 2021;20. <https://doi.org/10.1016/j.ijheatmasstransfer.2018.09.072>.
- [8] Saberi Varzaneh A, Naderi M. Experimental and Finite Element Study to Determine the Mechanical Properties and Bond Between Repair Mortars and Concrete Substrates. *Journal of Applied and Computational Mechanics* 2022;8:493–509. <https://doi.org/10.22055/jacm.2020.32921.2101>.
- [9] Di Re P, Addressi D. Computational Enhancement of a Mixed 3D Beam Finite Element with Warping and Damage. *Journal of Applied and Computational Mechanics* 2022;8:260–81. <https://doi.org/10.22055/jacm.2021.37948.3120>.
- [10] Pavlovic A, Fragassa F. Geometry optimization by fem simulation of the automatic changing gear. *Reports in Mechanical Engineering* 2020;1:199–205. <https://doi.org/10.31181/rme200101199p>.
- [11] Wu F, Wang Z, Song D, Lian H. Lightweight design of control arm combining load path analysis and biological characteristics. *Reports in Mechanical Engineering* 2022;3:71–82. <https://doi.org/10.31181/rme2001210122w>.
- [12] Fragassa C. Lightning structures by metal replacement: from traditional gym equipment to an advanced fiber-reinforced composite exoskeleton. *Facta Universitatis, Series: Mechanical Engineering* 2021;19:155–74. <https://doi.org/10.22190/FUME201215043F>.
- [13] Zhao S, Mao L, Wu N, Karnaoukh S. LOAD PATH VISUALIZATION USING U* INDEX AND PRINCIPAL LOAD PATH DETERMINATION IN THIN-WALLED STRUCTURES. *Facta Universitatis, Series: Mechanical Engineering* 2022;0.
- [14] Strzalka C, Manfred Z. The influence of loading position in a priori high stress detection using mode superposition. *Reports in Mechanical Engineering* 2020;1:93–102. <https://doi.org/10.31181/rme200101093s>.
- [15] Strzalka C, Marinkovic D, Zehn MW. Stress Mode Superposition for a Priori Detection of Highly Stressed Areas: Mode Normalisation and Loading Influence. *Journal of Applied and Computational Mechanics* 2021;7:1698–709. <https://doi.org/10.22055/jacm.2021.36637.2878>.
- [16] CHENG G, JIANG Z. STUDY ON TOPOLOGY OPTIMIZATION WITH STRESS CONSTRAINTS. *Engineering Optimization* 1992;20:129–48. <https://doi.org/10.1080/03052159208941276>.
-

- [17] Li Y, Huang XD, Xie YM, Zhou SW. Bi-Directional Evolutionary Structural Optimization for Design of Compliant Mechanisms. *Advances in Engineering Plasticity XI*, vol. 535, Trans Tech Publications Ltd; 2013, p. 373–6. <https://doi.org/10.4028/www.scientific.net/KEM.535-536.373>.
- [18] Radman A. Combination of BESO and harmony search for topology optimization of microstructures for materials. *Applied Mathematical Modelling* 2021;90:650–61. <https://doi.org/10.1016/j.apm.2020.09.024>.
- [19] Chandrasekhar KN v, Bhikshma V, Bhaskara Reddy KU. Topology Optimization of Laminated Composite Plates and Shells using Optimality Criteria. *Journal of Applied and Computational Mechanics* 2022;8:405–15. <https://doi.org/10.22055/jacm.2019.31296.1858>.
- [20] Sahithi NSS, Chandrasekhar KN v. Isogeometric Topology Optimization of Continuum Structures using an Evolutionary Algorithm. *Journal of Applied and Computational Mechanics* 2019;5:414–40. <https://doi.org/10.22055/jacm.2018.26398.1330>.
- [21] Dunning PD, Kim HA, Mullineux G. Introducing loading uncertainty in topology optimization. *AIAA Journal* 2011;49:760–8. <https://doi.org/10.2514/1.J050670>.
- [22] Lógó J, Ghaemi M, Rad MM. Optimal topologies in case of probabilistic loading: the influence of load correlation. *Mechanics Based Design of Structures and Machines* 2009;37:327–48. <https://doi.org/10.1080/15397730902936328>.
- [23] Luo Y, Wang MY, Kang Z. Topology optimization of geometrically nonlinear structures based on an additive hyperelasticity technique. *Computer Methods in Applied Mechanics and Engineering* 2015;286:422–41.
- [24] Tazowski P, Blachowski B, Lógó J. Topology optimization of elastoplastic structures under reliability constraints: A first order approach. *Computers & Structures* 2021;243:106406. <https://doi.org/10.1016/j.compstruc.2020.106406>.
- [25] Blachowski B, Tazowski P, Lógó J. Yield limited optimal topology design of elastoplastic structures. *Structural and Multidisciplinary Optimization* 2020:1–24. <https://doi.org/10.1007/s00158-019-02447-9>.
- [26] Gomes FAM, Senne TA. An algorithm for the topology optimization of geometrically nonlinear structures. *International Journal for Numerical Methods in Engineering* 2014;99:391–409. <https://doi.org/10.1002/nme.4686>.
- [27] Kato J, Hoshihara H, Takase S, Terada K, Kyoya T. Analytical sensitivity in topology optimization for elastoplastic composites. *Structural and Multidisciplinary Optimization* 2015;52:507–26. <https://doi.org/10.1007/s00158-015-1246-8>.

- [28] Gopal N, Panchal D. A STRUCTURED FRAMEWORK FOR RELIABILITY AND RISK EVALUATION IN THE MILK PROCESS INDUSTRY UNDER FUZZY ENVIRONMENT. *Facta Universitatis, Series: Mechanical Engineering* 2021;19:307–33. <https://doi.org/10.22190/FUME201123004G>.
- [29] Liu K, Tovar A. An efficient 3D topology optimization code written in Matlab. *Structural and Multidisciplinary Optimization* 2014;50:1175–96. <https://doi.org/10.1007/s00158-014-1107-x>.
- [30] Zuo ZH, Xie YM. A simple and compact Python code for complex 3D topology optimization. *Advances in Engineering Software* 2015;85:1–11. <https://doi.org/https://doi.org/10.1016/j.advengsoft.2015.02.006>.
- [31] Langelaar M. Topology optimization of 3D self-supporting structures for additive manufacturing. *Additive Manufacturing* 2016;12:60–70. <https://doi.org/https://doi.org/10.1016/j.addma.2016.06.010>.
- [32] Stanton A, Wiegand D, Stanton G. *Probability reliability and statistical methods in engineering design* 2000.
- [33] Rad MM, Habashneh M, Lógó J. Elasto-Plastic limit analysis of reliability based geometrically nonlinear bi-directional evolutionary topology optimization. *Structures*, vol. 34, 2021, p. 1720–33. <https://doi.org/10.1016/j.istruc.2021.08.105>.

Experimental and Numerical Analysis of Vibrations Induced by a Twin Tunnel, Underground Railway

Ramin Heidary, Morteza Esmaeili, Morteza Gharouni Nik

School of Railway Engineering, Iran University of Science and Technology, Malekloo str, 16846, 77451500 Tehran, Iran. r_heidary@rail.iust.ac.ir, m_esmaeili@iust.ac.ir, gharouni@doctor.com

Abstract: Many underground railway lines around the world consist of twin tunnels. One of the environmental vibration problems caused by these subways is the effect of the existence of loads in the two tunnels simultaneously. For example, measurement of the vibrations induced by two trains simultaneously in the field tests is rare. In this study, a 3D finite element model was built to investigate the ground vibrations induced by the subway twin tunnels and was verified against field measurements. A site measurement was performed on Line 1, Tabriz Metro. Furthermore, the influence of the second tunnel with various separation distances in the soil layer containing the different elastic modulus (for 3 values of 60, 150, and 400 MPa) on the surface vibrations is examined. The results show that when the elastic modulus of the soil decreases, the distance between two tunnels which the effect of the second tunnel disappears increases. So that, for the soil layer with an elastic modulus of 60, 150, and 400 MPa, the separation distance is obtained about 8, 9, and 10 times of the tunnel radius. In addition, a correction factor of +6 dB has been proposed for the field measurement data of the twin tunnels, which was determined from one of the trains.

Keywords: twin tunnels; railway vibration; situ measurement; numerical analysis

1 Introduction

Subway structure is undergoing increases in many cities in order to reduce the urban traffic. Subways usually run beneath the space of residential areas, which may cause disturbances to nearby buildings and their residents. The interaction between the wheel and the rail induces dynamic force, and causes vibrations, which that propagate through the tunnel and the surrounding soil into buildings. The induced vibration from the underground railway causes vibrations in the frequency range of 1–80Hz and re-radiated noise in the range of 1-200 Hz. [1]. To design a new railway or checking the vibrations from existing lines, the

induced vibrations must be determined and compared with the standards. Then, according to the obtained values, vibration reduction solutions should be taken. In addition, the mitigation effects of the proposed methods need to be evaluated. However, the prediction model is necessitated to achieve the above goals [2].

In the past decade, several numerical and analytical models have been established to predict ground vibrations induced by underground railways. These studies have investigated vibration in single and twin tunnels. Numerous prediction models and field measurements have been performed for assessments of vibration induced by single tunnel and isolated systems [3-9]. While a common simplifying assumption adopted in these studies is to neglect the presence of a neighboring tunnel. However, most underground railway lines around the world consist of twin tunnels: one for the outbound direction and one for the inbound direction. For example, in London, Copenhagen, Washington DC, Shiraz, and Isfahan the metro lines are included twin tunnels. To date, few numbers of models are available in the literature, which accounts for the effect of second tunnel on induced vibration by another tunnel.

Kuo *et al.* have presented the formulation of a model for underground-railway vibration induced from twin tunnels based on the single-tunnel Pip in Pip model. The superposition method has been used to determine of interaction between neighboring tunnels [10]. Hamad *et al.* have investigated the vibration response of the twin tunnels by two different methods, a fully coupled approach, and a superposition approach. The accuracy of the two methods is assessed [11]. He *et al.* present a 2.5D theoretical model for the solution of dynamic interaction between two parallel tunnels in a multi-layered half-space. The influence of soil layering and the stiffness of the soil above the tunnels were investigated [12]. Yuan *et al.* have proposed an analytical method for calculating vibrations from a twin tunnel in a saturated poroelastic half-space. The results show that the surface vibration from the half-space model is larger than those of the full-space model [13]. In another study, Yuan *et al.* have presented an analytical solution for estimating twin tunnels vibrations, which considers the multiple scattering effects between the two tunnels. The second tunnel has a small influence on the soil displacement at the low frequencies, while in the high frequencies the neighboring tunnel has significant scattering effects [14]. Heidary *et al.* have investigated the effect of axle load and speed of trains on the ground surface vibration, while two trains passed each other in the opposite direction in the twin tunnels [15]. Heidary *et al.* have studied the effect of surrounding soil layers and lens properties on the ground-borne vibration induced from twin tunnels. In the following, the results of the twin tunnels model have been compared with the single tunnel model [16].

Because of complexity of vibration source, uncertainty of transmission path and existing of different materials, study on vibration needs of reliable experimental data for the verification of numerical or analytical models. To date, several field studies of the single tunnel have conducted in previous works, but the evidence in the literature of a field measurement, which accounts for the vibrant interaction

between neighboring tunnels, does not exist. In this study, measurements are carried out to study the influence of the twin tunnels-induced vibration on the ground surface. At Tabriz, Iran, microtremor instrumentations on the ground surface and inside the underpass tunnel were carried out in order to evaluate train-induced vibrations. These results were used to verify the 3D numerical model in the time domain. The effects of the existence of the second active tunnel and tunnels separation distance on the ground vibration were then investigated. The goal of this study is to determine the minimum separation distance of the two tunnels, that the effect of the second tunnel on the ground surface vibration is eliminated. Also, one of the study gaps in the field measurement of the twin tunnels has been investigated in this study. The possibility of recording vibrations from both trains simultaneously in the field measurements is very low. Therefore, in this study, the correction factor for this issue is determined.

The outline of the paper is as follows. Section 2 introduces the test site in Tabriz (Iran) and addresses the determination of the soil, train and track characteristics. The 3D finite element model is presented in Section 3, and the experimental results are compared to results obtained by 3D FE modeling. Additional simulations are performed for the investigating of the tunnels separation distance effect in section 4. Also, the effect of a neighboring tunnel on the propagation of surface ground-borne vibrations is studied in Section 5.

2 In-situ Measurements

Underground Line 1 in Tabriz, Iran was designed in about 2002 to allow connection west to east with a length of 17.2 km and 17 stations. This line consists of twin tunnels, used for the outbound and inbound directions, respectively. The tunnel on this line is a deep-bored tunnel with a concrete lining and a single track in each tunnel. The tunnels were excavated in a clay stone and tuff soils, using a tunnel boring machine (TBM) at a depth of about 15-25 m below the surface. In the test site, the two tunnels are built as circular section with inner radius 3 m, outer radius 3.3 and burial depths 15 m. The two tunnels are separated by a transverse distance 13 m (Figure 1).

2.1 Track and Train Specifications

The rails are placed on the slab with rail pads, and the slab is connected to the tunnel invert by rubber mat. The distance between the rail pads is 0.6 meters, and the rail type is a S49.

The line 1 trains are a normal passenger train, consisting of 5 cars: a driving motor car, three non-driving motor cars, and a driving motor car. The length of a motor

car is 21 m, while the length of a trailer car is 19.5 m. The bogie and axle distances on all cars are 12.6 and 2.2 m, respectively. The total length of the test train is 100 m (Figure 2). Considering the mass of a wagon and the bogies, the axle load is 9.5 tons.

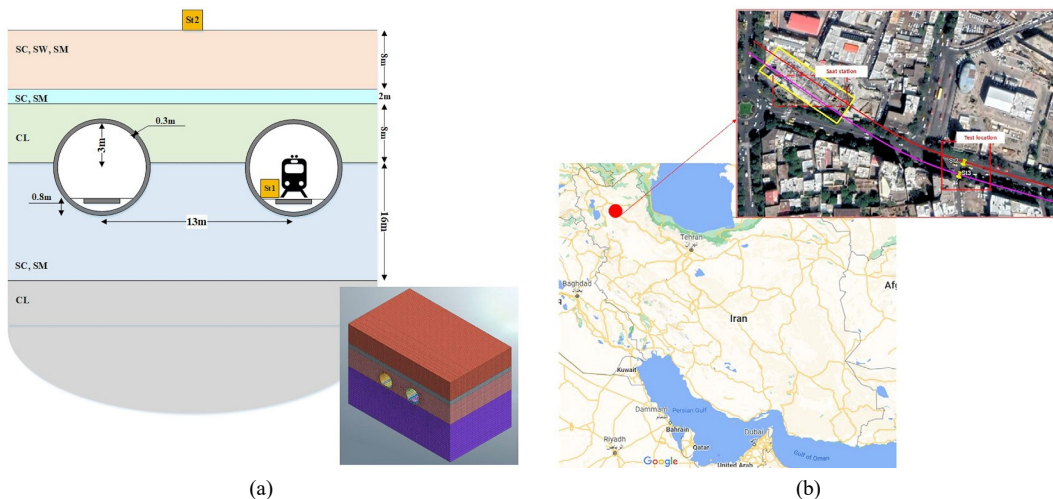


Figure 1

(a) Cross section of the tunnels on line 1 and FE model, (b) location of field measurement

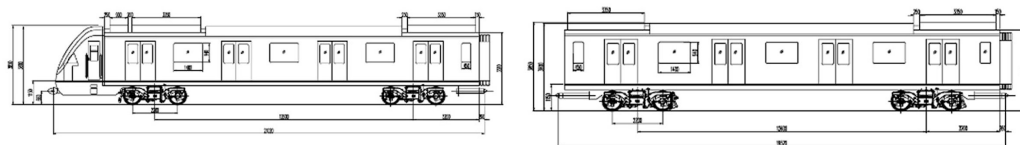


Figure 2

The configuration of the train

2.2 Geodynamic Characterization

The test site is located on line 1 of the Tabriz metro, between the Beheshti and Saat stations. The mechanical characteristics of the surrounding soil were determined using the Downhole seismic test.

Figure 1 shows the locations of two parallel tunnels through the scheme of soil layers. The soil is defined as a superposition of seven horizontal layers. Soil layers include silty sand and silty clay upper the clay soil, the uppermost layer is formed by a sand mixture. The soil parameters are summarized in Table 1, for the 5

layers, in terms of Young's modulus E , density ρ , Poisson's ratio ν and wave velocity V_s .

Table 1
Dynamic soil characteristics

Layer	E (Mpa)	ν	ρ (kg/m ³)	V_s (m/s)
1	300	0.39	1600	250
2	500	0.37	1800	300
3	700	0.37	1800	370
4	1350	0.36	1800	500

2.3 Measurements and Data Processing

The experimental measurements were carried out with the three vertical velocimeters (microtremor). These velocimeters were established on the ground surface and tunnel inside. The connected equipment includes a data recorder, power supply, and GPS are shown in Figure 3.

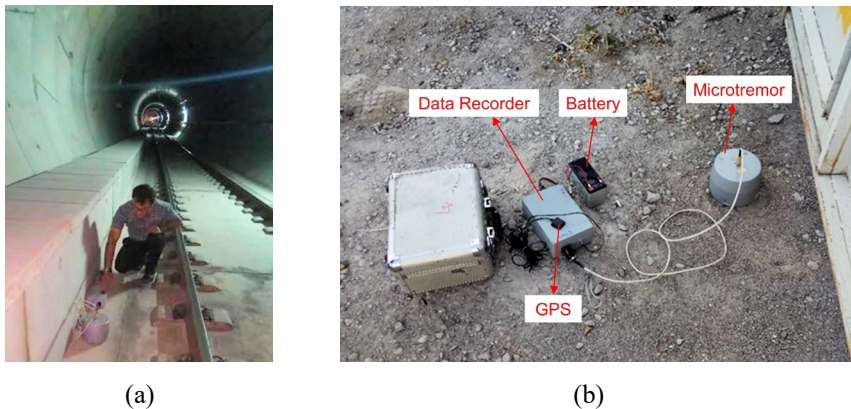


Figure 3

(a) Railway track, (b) Microtremor equipment

The velocity responses were obtained at the tow points on the ground surface and one point on the slab. Points on the ground surface were located above the active tunnel and between a distance of the two tunnels. Three detection points were defined and are shown in Figure 1.

Field measurements were performed at the time with lowest passing surface road traffic. Nevertheless, data processing was implemented which includes eliminating noise signals, baseline correction, and the appropriate frequency range. The frequency range for the recorded data was set between 0 to 100 Hz.

3 Numerical Modeling

To predict the vibration responses, two 3D FE models were built with the FE code Midas GTS NX, one used for verification and the other used for other paper objectives. The model includes the soil layers, twin tunnels, and train load. To keep the model as simple as possible, also to decrease the model run time, superposition principle is applied for trainload. For this purpose, it is necessary to know the axle distribution and the train speed [17-19]. To simplify the cross-section of the rail in the numerical model, it is considered as a rectangle section with a contact surface equal to the width of the original rail foot. Moreover, the inertia must be equal to that of the original rail. [18].

The dimensions of the 3D model are considered to be 35*35*30 m. In addition, the mesh size of the soil layers surrounding the tunnels is 0.5 m. The sensitivity analyses were performed in another paper by the same authors to study the effect of model dimensions, mesh size, and time increment [15]. The absorbing boundary was used to prevent the wave reflection from the model boundaries.

Rayleigh damping theory used in the model includes a damping matrix $[C]$ which can be calculated as is shown in Equation 1:

$$[C] = \alpha [M] + \beta [K] \quad (1)$$

Here α and β are the Rayleigh coefficients, and $[M]$ and $[K]$ are the mass and stiffness matrix, respectively. The damping ratio coefficients α and β have a relation with fundamental frequency and damping ratio. The fundamental frequency is determined by solving the free vibration equation of the system. The calculated α and β are 2.159 and 0.00115, respectively.

3.1 Verification of the FE Model

In the present section, the response to a train moving at a speed of 32 km/h is predicted with 3D FE model, and compared to the experimental results. Figure 4 shows the comparison of measurement and calculation results, in time history and frequency content on the slab.

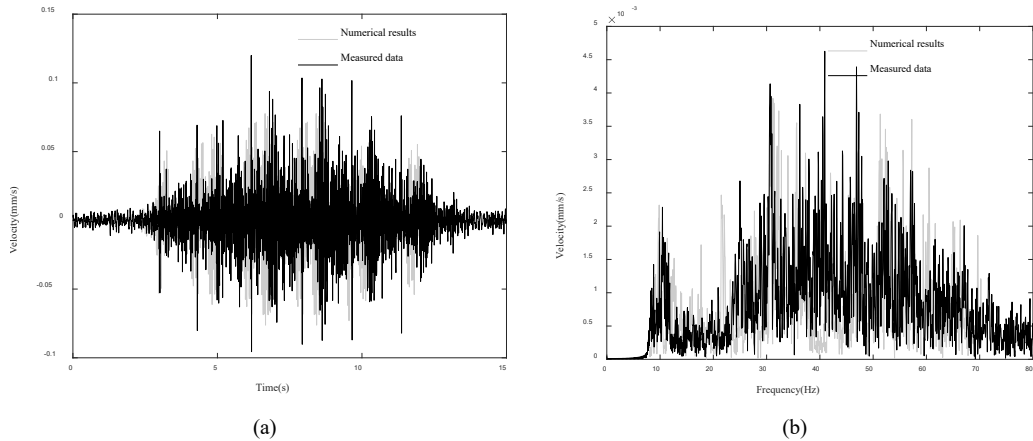


Figure 4

The experimental and numerical: (a) time history and (b) frequency content of the station 1 response

The general agreement between both results is acceptable. However, some discrepancy are existence, which this could be due to the underestimation of the dynamic forces and the influence of the train suspensions, which has been disregarded in the FE model.

Vibration measurements have also been performed in above the Tabriz line tunnels on the surface as well as at the slab in tunnel. Figure 5 compares the experimental and computed ground surface vibration at the distance between the two tunnels. Both the experimental and numerical results show a relatively good agreement at the observation point. The difference between the predicted and experimental results could probably be due to background noise, soil layers damping or inhomogeneities in the soil layers.

4 Effect of Separation Distance of Two Tunnels

In this section, the influence of separation distance of the two tunnels on the responses at the ground surface is investigated. The single tunnel model and the present model under different separation twin tunnels distances have been compared. The goal is to determine the distance, which the induced vibration from the two tunnels does not affect each other. The cross sections of the two models, and the observation point at the ground surface are presented in Figure 6.

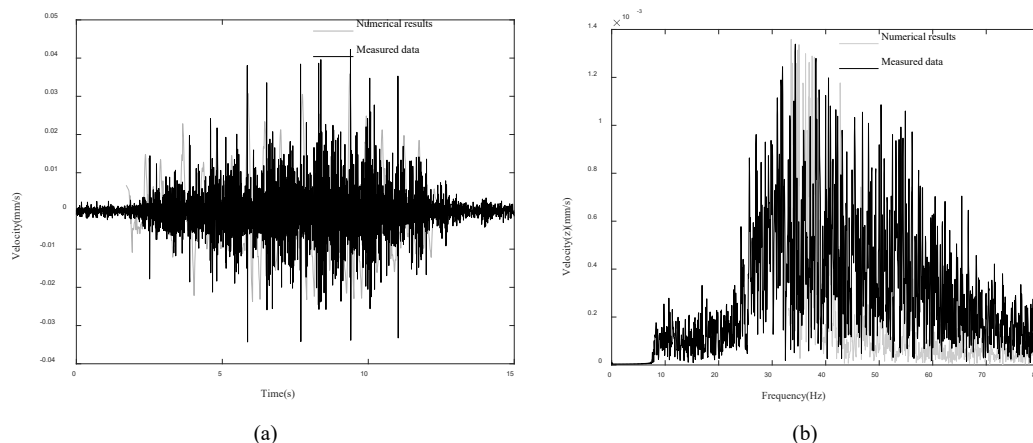


Figure 5

The experimental and numerical: (a) time history and (b) frequency content of the station 2 response

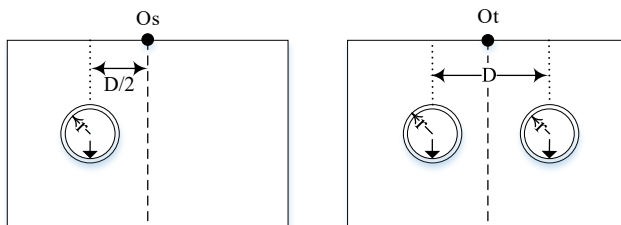


Figure 6

Cross sections of single tunnel and twin tunnel and observation point location

For a complete study, a homogeneous single layer with 3 different elastic modulus, 60, 150 and 400 MPa are considered. The comparison of the results between the single and twin tunnels is shown in Figure 7 for layer elastic modulus 150 MPa.

As shown in Figure 7, the responses at the ground surface above the twin tunnels are greater than those of the single tunnel. This is because the values obtained above the twin tunnels are the sum of the vibrations from the active tunnel and reflected waves from the adjacent tunnel lining. However, the dynamic responses at point O_s are only from the active tunnel. Also, the tunnels separation increases, the differences of the responses at observation points (O_t , O_s) decrease. Figure 7 shows that, when the distance between the two tunnels is more than $9r$, the vibrations on the ground surface are equal to those of the single tunnel.

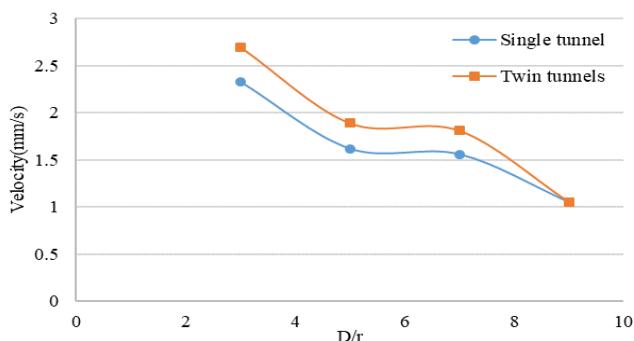


Figure 7

The effect of the separation distance of twin tunnels on the induced vibration and comparison with a single tunnel ($E_{soil}=150$ MPa)

The comparison between the single and twin tunnels models is shown in Figure 8 under different layer elastic modulus. The difference between the results is represented as a percentage, which is determined from the following equation (Equation 2).

$$DV\left(\frac{D}{r}\right) = \frac{Velocity(Ot) - Velocity(Os)}{Velocity(Os)} \times 100 \quad (3)$$

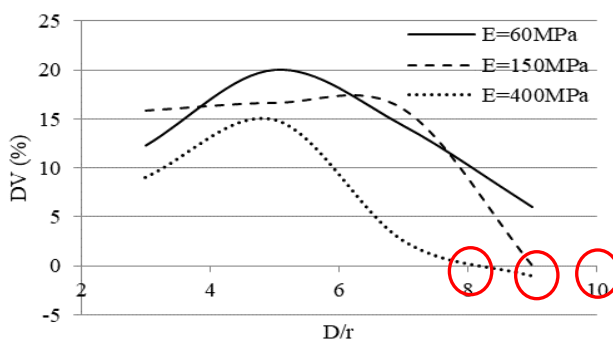


Figure 8

Comparison between the single tunnel and the twin tunnels model for different tunnels spacing and soil layer elastic modulus

As can be seen, the differences increase first, because of second tunnel effect, and then decrease to zero by the increase of the D/r ratio. From the results Figure 8 it can be concluded that The effect of the second tunnel for the soil layer with Young's modulus 60, 150, and 400 MPa disappears at a D/r ratio of 8, 9, and 10, respectively. In other words, as the soil layer becomes softer, the second tunnel affects the response at the ground surface at a larger distance.

5 Effect of Twin Active Tunnels on Surface Vibrations

During field measurements in twin tunnels, one of the trains usually passes through a tunnel. This is because as the second tunnel is not finished to the operation, or during measurement, two trains do not pass simultaneously. Therefore, if the measurement results are used to design the structure at ground surface above the tunnels, it is not completely correct. Because it is possible that during the structure lifespan, both trains pass each other through the tunnels at several times while daytime. To the author’s knowledge, this correction factor has not reported in any published work. This section aims to present the effect of second active tunnel on the free field response for soil layer with different elastic modulus 60, 150 and 400 MPa. In additional this parameter is investigated to different twin tunnel separation distance (Figure 9). Insertion Gain (IG) concept (Equation 3) is used to assess determined results [4]:

$$IG = 20 \log \left(\frac{x_2}{x_1} \right) \tag{3}$$

where x_1 is the reference case results (twin tunnel with one active tunnel), and x_2 is result after changes (twin tunnel with two active tunnels). IG represents the changes in the vibration response and expresses in decibel (dB).

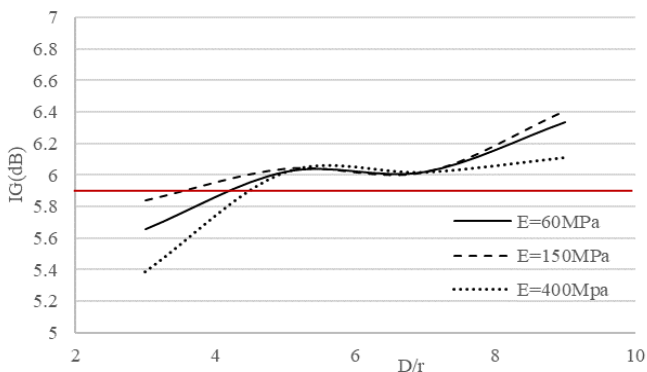


Figure 9

IG due to the existence of the load in the second tunnel compared to the passive tunnel model

As can be seen, in all cases, the IG is positive, which means that the existence of the load in the second tunnel causes an increase the vibration at the ground surface. Figure 9 shows that as the distance between the tunnels increases, the effect of the load in the second tunnel on the induced vibrations increases. But this effect is small and can be ignored. Also, the influence of the stiffness of the soil beneath the tunnels on the response is small. therefore, the improvement factor +6 dB (on average) have been suitable for the measurement of the field vibrations.

Conclusions

In this paper, a 3D twin-tunnel model is presented to evaluate the vibrations induced by trains. In continuation, a 3D FE model is validated with filed measurement data. Then the effects of two tunnels separation distance and existence of second tunnel on the vibration response are investigated. The present work includes field measurements of twin tunnels, which do not exist in previous studies. Field measured data can be used for future works as a reference. With the increase of the separation distance of two tunnels, the response of the active tunnel on the ground surface decreases. In addition, the elastic modulus of the soil layer influences the obtained results. The response on the ground surface increases with the decrease of the Yang's modulus of the soil layer. In other words, the distance between the tunnels, which the effect of the active tunnel disappears, for the soil layer with an elastic modulus of 60, 150, and 400 MPa, is equal to 8, 9, and 10 times the tunnel radius, respectively. In the field measurements of twin tunnels, if measured data do not include the vibrations induced from the two trains that pass each other simultaneously, according to the results of this paper, +6 dB should be added to the obtained values. In addition, this value does not depend on the distance between the tunnels and the elastic modulus of the soil layer.

References

- [1] Forrest, J. A., & Hunt, H. E. M. (2006) Ground vibration generated by trains in underground tunnels. *Journal of Sound and Vibration*, 294(4-5), 706-736
- [2] Yuan, Z., Boström, A., Cai, Y., & Cao, Z. (2019) Analytical solution for calculating vibrations from twin circular tunnels. *Soil Dynamics and Earthquake Engineering*, 117, 312-327
- [3] Andersen, L., & Jones, C. J. C. (2006) "Coupled boundary and finite element analysis of vibration from railway tunnels—a comparison of two- and three-dimensional models". *Journal of sound and vibration*, 293(3-5), 611-625
- [4] Gupta, S., Degrande, G., & Lombaert, G. (2009) "Experimental validation of a numerical model for subway induced vibrations". *Journal of sound and vibration*, 321(3-5), 786-812
- [5] Gupta, S., Stanus, Y., Lombaert, G., & Degrande, G. (2009) "Influence of tunnel and soil parameters on vibrations from underground railways". *Journal of Sound and Vibration*, 327(1-2), 70-91
- [6] Real, T., Zamorano, C., Ribes, F., & Real, J. I. (2015) "Train-induced vibration prediction in tunnels using 2D and 3D FEM models in time domain". *Tunneling and Underground Space Technology*, 49, 376-383
- [7] Ruiz, J. F., & Rodríguez, L. M. (2015) "Application of an advanced soil constitutive model to the study of railway vibrations in tunnels through 2D

- numerical models: a real case in Madrid (Spain)". *Revista de la Construcción. Journal of Construction*, 14(3), 53-61
- [8] Németh, A., & Fischer, S. (2018) Investigation of glued insulated rail joints with special fiber-glass reinforced synthetic fishplates using in continuously welded tracks. *Pollack Periodica*, 13(2), 77-86
- [9] Fischer, S. (2021) Investigation of effect of water content on railway granular supplementary layers. *Naukovyi Visnyk Natsionalnoho Hirnychoho Universytetu*, 2021(3), 64-68
- [10] Kuo, K. A., Hunt, H. E. M., & Hussein, M. F. M. (2011) The effect of a twin tunnel on the propagation of ground-borne vibration from an underground railway. *Journal of Sound and Vibration*, 330(25), 6203-6222
- [11] Hamad, W. I., Hunt, H. E., Talbot, J. P., Hussein, M. F., & Thompson, D. J. (2015) "The dynamic interaction of twin tunnels embedded in a homogeneous half-space". *COMPADYN 2015, Greece*. 13 pp.
- [12] He, C., Zhou, S., Guo, P., Di, H., Zhang, X., & Yu, F. (2019) Theoretical modelling of the dynamic interaction between twin tunnels in a multi-layered half-space. *Journal of Sound and Vibration*, 456, 65-85
- [13] Yuan, Z., Boström, A., Cai, Y., & Cao, Z. (2019) Analytical solution for calculating vibrations from twin circular tunnels. *Soil Dynamics and Earthquake Engineering*, 117, 312-327
- [14] Yuan, Z., Boström, A., & Cai, Y. (2019) An analytical model for calculating vibrations from twin tunnels in a saturated poroelastic half-space. *Soil Dynamics and Earthquake Engineering*, 120, 23-27
- [15] Heidary, R., Esmacili, M., & Gharouni Nik, M. (2021) Effects of train operational parameters on ground-borne vibrations induced by twin metro tunnels. *International Journal of Rail Transportation*, 9(2), 144-156
- [16] Heidary, R., Esmacili, M., & Gharouni Nik, M. (2021) Evaluation of the soil layering and soil lens effect on the ground-borne vibrations induced by twin metro tunnels. *European Journal of Environmental and Civil Engineering*, 1-20
- [17] El Kacimi, A., Woodward, P. K., Laghrouche, O., & Medero, G. (2013) Time domain 3D finite element modelling of train-induced vibration at high speed. *Computers & Structures*, 118, 66-73
- [18] Real Herráiz, J. I., Zamorano, C., Hernández, C., Comendador, R., & Real, T. (2014) Computational considerations of 3-D finite element method models of railway vibration prediction in ballasted tracks. *Journal of vibroengineering*, 16(4), 1709-1722
- [19] Wu, T. X., & Thompson, D. J. (2001) Vibration analysis of railway track with multiple wheels on the rail. *Journal of Sound and Vibration*, 239(1), 69-97

Method of Railway Subgrade Diseases (defects) Inspection, based on Ground Penetrating Radar

Yaonan Li¹, Hengbai Liu¹, Shilei Wang¹, Bo Jiang¹, Szabolcs Fischer²

¹Infrastructure Inspection Research Institute, China Academy of Railway Sciences Corporation Limited, Beijing, China, 100081

²Széchenyi István University, Egyetem tér 1, H-9026 Győr, Hungary
e-mail: liyaonan@rails.cn, liuhengbai@rails.cn, wangshilei@rails.cn, pjiang@rails.cn, fischersz@sze.hu

Abstract: Due to the impact of climatic and natural factors, the normal-speed railway subgrade is vulnerable to mud pumping, water accumulation, subsidence and other defects, hereafter called diseases, that frequently occur, after a period of service. It is imperative to quickly detect subgrade diseases. On the basis of studying the law of geological radar electromagnetic signal propagation along the railway subgrade, according to the results of site excavation and verification, this paper proposes a method for railway subgrade disease inspection based on ground penetrating radar. In addition, radar image features of typical subgrade diseases are clarified herein. Practical application results show that this inspection method is effective to accurately identify subgrade diseases. In particular, it is of great significance to the rapid inspection of hidden subgrade diseases. In addition, an analysis of inspection results and distribution of subgrade diseases along the line is conducive to determining the key section for treatment of subgrade diseases.

Keywords: ground penetrating radar; subgrade disease; denoising; radar image; subgrade inspection device

1 Preface

The railway industry in China has undergone a rapid development. For example, the total mileage of railways in operation reached up to about 150,000 kilometers by the end of 2021 ("Statistical Bulletin on the Development of the Transportation Industry in 2021", The Ministry of Transport of China). The railway subgrade directly bears and transfers the track gravity and the dynamic load of the train, and is also affected by geological conditions, construction and other factors, so that it is vulnerable to more and more subgrade diseases year by year [1]. In fact, in-situ excavation is one of the traditional methods for discovering subgrade diseases.

Although this method is intuitive, it is inefficient and hard to be rolled out at the railway network level because it will interfere with the normal operation of trains.

As a subgrade inspection technology, ground penetrating radar technology has been developing rapidly in recent years. Many research institutions in the world have carried out various research projects and practices in this regard. In 1998, J. Hugenschmidt successfully applied geological radars to railway subgrade inspection for the first time [2]. From then on, many countries including China carried out related experiments [3-8]. For example, Szalai S, used image methods to study the deformation of ballasted railway tracks [9]. Trong Vinh Duong *et al.* conducted the physical modeling and in-depth research and analysis on the elements of mud pumping at the interface of railway ballast/subgrade, including particle distribution, water content, pore water pressure, and hydraulic conductivity [10]. Xu Xinjun studied the deep learning and target inspection of geological radar image features of mud pumping through the fast regional convolutional neural network [11]. Yang Xin'an proposed a method for identifying the development, distribution forms and diseases of mud pumping according to radar images in 2004 [12]. In 2010, Du Panfeng proposed to classify the mud pumping diseases according to geological radar waveform stacking diagram [13]. In 2015, Hou Zhezhe explored a typical subgrade disease classification method based on radar image features through the study of actual detection data and theoretical analysis [14]. Sysyn proposed a non-destructive measurement method to investigate the distribution of the ballast consolidation along the sleeper [15, 16]. Liu studied the effect of different tamping operations on the longitudinal vibration transfer characteristics of the track bed and the frequency response function of the track bed under different temperature and humidity conditions [17, 18]. PAY Ibrekk assessed the abilities of a GPR system to detect anomalies like ballast pockets and to map the distribution of water in railway ballast [19].

Thanks to these studies and applications, the role of geological radars in detecting and positioning railway subgrade diseases has been gradually accepted. However, due to the differences in the hardware equipment of geological radars, processing software and processes, there is no unified standard for identifying railway subgrade diseases through geological radars. In order to solve the aforesaid problems, this paper explores a geological radar inspection method for subgrade diseases. Through this method, the distribution state of the subgrade disease along the long trunk line can be evaluated, and the basis for the treatment of subgrade disease can be provided.

2 Inspection Method

2.1 Inspection Principle

The geological radar method is used to detect and locate the target object according to the reflection characteristics of electromagnetic waves and the change law of propagation speed of the interface between the propagation media with different dielectric constants. With high-frequency or ultra-high-frequency electromagnetic waves as the information carrier, this method has the characteristics of real-time display, as well as fast, non-destructive, continuous inspection.

Electromagnetic wave signals are emitted towards the ground through the continuous movement of the antenna. When such signals encounter a medium interface with electrical property differences (such as differences in the dielectric constant) in the process of propagation inside the object, the phenomena of reflection, transmission and refraction will occur. The larger difference in dielectric constants of the media on both sides of the medium interface indicates more electromagnetic wave energy reflected. After the electromagnetic waves to be reflected are received, by the receiving antenna, that moves synchronously with the transmitting antenna, the radar host will accurately record the two-way travel time, amplitude, phase and other motion features of the reflected electromagnetic wave. On this basis, the cross-sectional scanning images of underground media can be obtained. Underground targets can be identified through processing and interpretation of radar images (its working principle is shown in Figure 1).

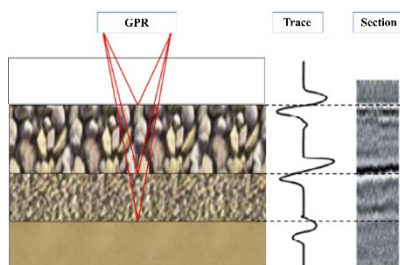


Figure 1

Schematic diagram of geological radar inspection principle

Since the propagation speed of electromagnetic waves in the same medium remains constant, the target object depth H can be calculated based on the two-way travel time t of the electromagnetic wave received and recorded. The specific calculation formula is as follows:

$$H = \frac{vt}{2} \quad (1)$$

Where, $v = C/\sqrt{\varepsilon}$ indicates the propagation speed of electromagnetic waves in the medium, C represents the propagation speed of electromagnetic waves in the air (about 3×10^8 m/s), and ε denotes the relative dielectric constant of the medium.

2.2 Inspection Device

The subgrade condition inspection system adopts IDS SRS system, which comprises a radar host, three IDS TR400 Radar antennas (corresponding to the three measurement lines distributed on the center between lines, ballast shoulders on both sides), a data acquisition instrument, a signal display instrument, a rangefinder, signal transmission cables, a global navigation satellite system(GNSS), etc. This inspection system is mounted on a special inspection vehicle, with the 25T passenger train body as the supporting platform.



Figure 2
Subgrade inspection device

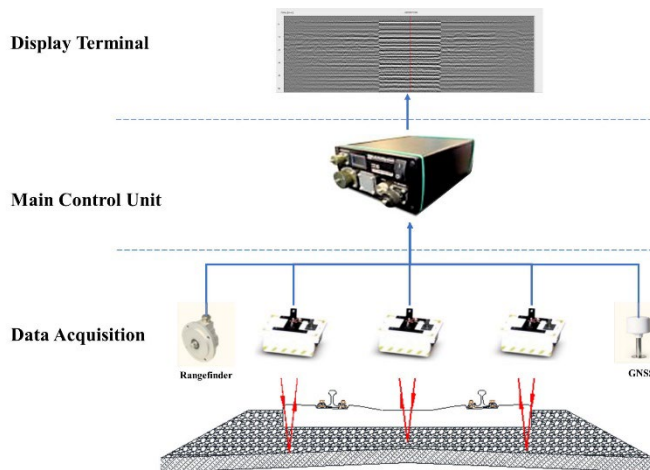


Figure 3
Subgrade inspection system

The inspection device is shown in Figure 2, and the system composition is detailed in Figure 3. The inspection speed reaches up to 120 km/h. After the inspection system is started, the rangefinder will trigger the radar system to transmit pulse signals according to the prescribed interval. Then the data acquisition instrument will receive and record the radar wave signals reflected from the subgrade structure layer, and the display system will display the detected echo signal (namely radar image) in real time. In this way, data on each structural layer of the subgrade can be obtained.

2.3 Inspection Data Processing

Preprocessing of geological radar data constitutes an important part of radar data analysis. In the process of preprocessing, fidelity processing is required to ensure the reliability of subsequent analysis.

Denoising is the most important part of preprocessing. Regarding the geological radar inspection of the railway subgrade, there are two main types of noise, namely external interference noise and background noise. Specifically, external interference noise mainly includes the superimposed noise caused by the influence of signals by railway infrastructures such as Rail Sleeper, rail and catenary, as well as tunnels, bridges, slopes and other structures. In addition, background noise mainly includes the noise generated by the instruments during their operation, and also the interference noise generated in the antenna coupling process.

(1) The external interference noise is usually suppressed through the Complementary Ensemble Empirical Mode Decomposition (CEEMD) method. In 1998, the EMD method was proposed by E. Huang for the first time [20]. In 2010, the EMD method was optimized and upgraded by Yeh et al. [21] Specifically, paired auxiliary noise (positive and negative) was added to eliminate the residual auxiliary noise in the reconstructed signal, which significantly improved the computational efficiency. This new method is renamed as CEEMD. The basic principle is as follows:

Firstly, add the white noise of fixed intensity to the original signal, and decompose the additive noise signal through EMD to obtain an IMF (Intrinsic Mode Function) component; continue to decompose N kinds of white noise newly added for corresponding times, and calculate the overall average of obtained components. The specific calculation formula is as follows:

$$IMF_1 = \frac{1}{N} \sum_{i=1}^N E_i[x + \varepsilon \omega_i] \quad (3)$$

Where, IMF_1 is the first-order IMF component, N represents the number of times of adding different kinds of noise, E_i indicates the i^{th} component generated by EMD decomposition, ε represents the proportion of added noise, and ω_i denotes the added white noise. The residual generated after subtracting the first-order IMF component is calculated as follows:

$$r_1 = x - IMF_1 \quad (4)$$

Then decompose $r_1 + \varepsilon E_1[\omega_1]$, $i = 1, 2, \dots, N$, iteratively decompose to obtain the component meeting the IMF_1 conditions, and then calculate the overall average of all IMF_1 to obtain the second-order IMF_2 of the original signal. The specific calculation formula is as follows:

$$IMF_2 = \frac{1}{N} \sum_{i=1}^N E_i[r_1 + \varepsilon E_i[\omega_i]] \quad (5)$$

Calculate the residual of the k th order ($r_k = r_{k-1} - IMF_k$), extract the first-order IMF components of $r_k + \varepsilon E_k[\omega_1]$ ($i = 1, 2, \dots, N$), and then calculate the overall

average to obtain the $k+1$ th order component IMF_{k+1} of the original signal. The specific calculation formula is as follows:

$$IMF_{k+1} = \frac{1}{N} \sum_{i=1}^N E_i[\tau_k + \varepsilon E_k[\omega_i]] \quad (6)$$

Continue to perform iterative screening until the number of extreme values of residual does not exceed 2.

$$R = x - \sum_{k=1}^K IMF_k \quad (7)$$

Where, R indicates the residual value, and K denotes the number of IMF components.

Finally, the original signal recovered from IMF component and residual sequence can be expressed as follows:

$$x = \sum_{k=1}^K IMF_k + R \quad (8)$$



(a) Radar cross-section with Rail Sleeper interference (b) Radar cross-section after denoising

Figure 4

Rail Sleeper interference removal

Figure 4 shows the effect of Rail Sleeper noise disposal. Figure 4 (a) is a radar cross-section featuring the Rail Sleeper interference, and Figure 4 (b) shows the cross-section generated after decomposition and denoising by CEEMD, with the Rail Sleeper interference removed thoroughly relatively.

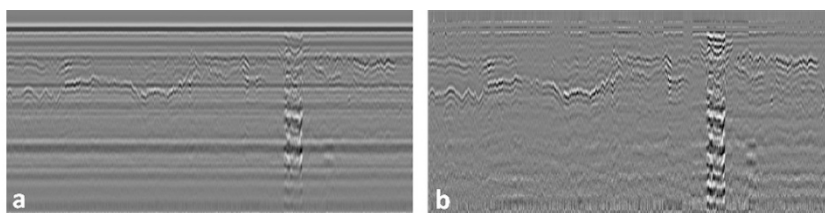
(2) The mean image denoising algorithm is used for the background noise. To enhance the regular horizontal signal and attenuate the irregular reflected signal, the mean of all track data concerning the signal segment on the radar cross-section with obvious inter-track horizontal interference is calculated. This mean can be deemed as an interference signal caused by the instrument, thus needing to be removed from all data channels of the radar cross-section. Also, this mean is regarded as the value of instrument background noise. The background noise can be eliminated by calculating the difference between background noise and all channels of radar cross-section.

The background noise is selected as follows:

$$x_z(t) = \frac{1}{N2 - N1 + 1} \sum_{i=N1}^{N2} x_i(t) \quad N1 < N2 \quad (9)$$

Where, N1 is the starting channel of the cross-section background noise, and N2 represents the ending channel of the cross-section background noise.

Figure 5 shows the effect of background noise disposal. Figure 5(a) is the radar cross-section with background noise, and Figure 5(b) shows the cross-section after mean background denoising. The background noise is removed thoroughly relatively, but valid signals are maintained.



a) Radar cross-section with background noise (b) Radar cross-section after denoising

Figure 5

Background noise removal

3 Radar Image Features of Typical Subgrade Diseases

After data preprocessing, the signal-to-noise ratio (SNR) of geological radar inspection will be improved, and disease signal features will be clearly reflected. In combination with theoretical analysis and site excavation and verification, geological radar signal features of three subgrade diseases (namely mud pumping, water accumulation and subsidence) were analyzed and determined during the study.

(1) The radar image of mud pumping is characterized by continuous flat or undulating strong reflection coaxial axis in the depth range from the ballast bed surface to the subgrade bed surface. Differences in water containing conditions might result in the differences in multiple reflections, and cover the signals reflected from the interfaces of ballast bed and subgrade bed. What's worse, the illusion that the interface of ballast bed and subgrade bed uplifts towards the shallow layer might occur. The distance between the top surface of mud pumping and the top surface of the Rail Sleeper is limited to 25 cm. Mud pumping is further divided into concealed mud pumping (surface depth is less than 25 cm) and exposed mud pumping (surface depth is greater than 25 cm).

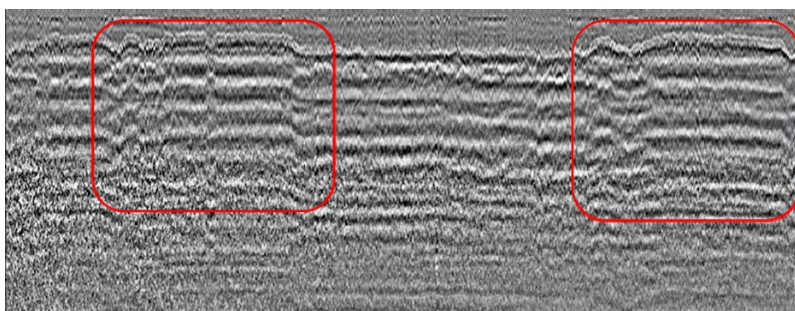


Figure 6

Radar image features of mud pumping

(2) The high water content of the subgrade or foundation might lead to the subgrade quality deterioration and instability, and further cause diseases such as mud pumping and subsidence. The image features of water accumulation are characterized by low frequency strong reflection, large amplitude, reverse phase and multiple reflections at the interface, and the interface is relatively flat.

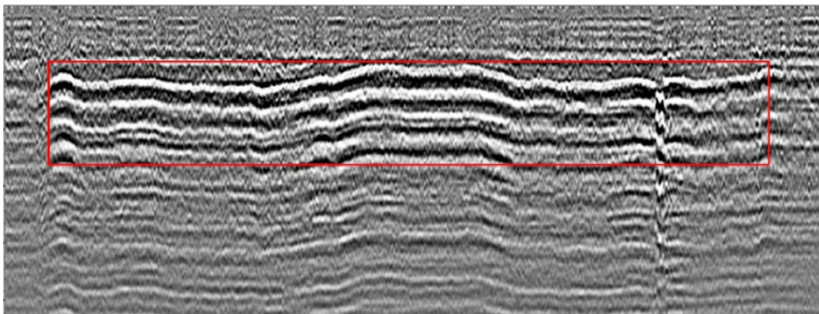


Figure 7
Radar image features of water accumulation along the line

Subsidence refers to the local or relatively large vertical settlement or subsidence deformation under the coupling effect of water, overlying load, self-weight, climate change, dynamic train load and vibration resulting from insufficient compactness of the ballast bed, subgrade, or foundation. It is also called ballast pit, ballast sack or ballast pocket in case of local or small range with the ballast trapped in the subgrade bed. Radar image features of subsidence area as follows: The reflective events of the interface between the ballast bed and the subgrade bed structure, and between the subgrade bed surface and the substratum indicate significant bending, discontinuity or offset of the depth downwards. By the length limit of 10 m, the subsidence diseases are further divided into ballast trap (with a length of less than 10 m) and structural interface fluctuation (with a length of greater than 10 m). The subsidence is identified mainly through one-off inspection, which represents the condition of subgrade at the time of inspection. In contrast, multiple inspections are required for judging the subsequent development trend of subsidence.

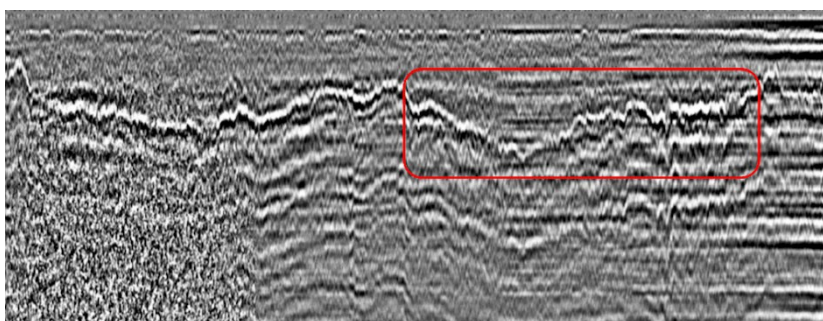


Figure 8
Radar image features of subsidence

4 Case Analysis

The subgrade of a normal-speed railway in Southwest China is vulnerable to relatively serious diseases. Particularly in the rainy season, mud pumping, water accumulation, subsidence and other diseases occur frequently, and it is difficult to maintain the track geometry. In July 2021, the authors of this paper conducted site inspection of the entire railway line using the subgrade inspection method and special inspection device introduced herein. Meanwhile, the work of data processing and interpretation was carried out.

4.1 Summary of Inspection Results

Through inspection, diseases were found in 262 places with a cumulative length of 30,244 m, accounting for 4.50% of the total length (700 km) of subgrade inspected.

Specifically, mud pumping disease was discovered in 36 places with a cumulative length of 5,238 m, accounting for 0.78% of the total length above; water accumulation was found in 217 places with a cumulative length of 22,382 m, accounting for 3.33% of the total length; and subsidence was found in 9 places with a cumulative length of 2,624 m, accounting for 0.39% of the total length.

The distribution and proportions of various subgrade diseases are shown in Fig. 9. Specifically, by the ratio between cumulative length and total length, mud pumping, water accumulation and subsidence accounted 17.32%, 74.00%, and 8.68%, respectively.

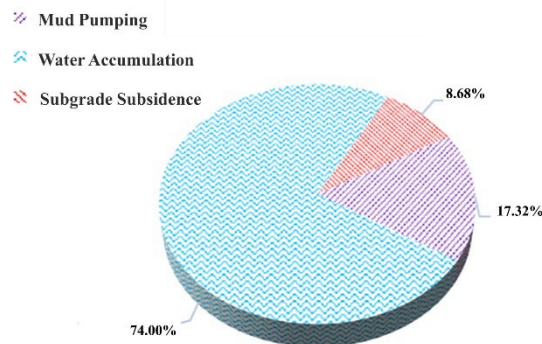


Figure 9
Distribution of subgrade diseases

Statistical analysis was made based on the cumulative length of diseases in the 10 km interval. The results show that the cumulative length of subgrade diseases in the K1230-K1240 segment accounted for 19.70% of the total subgrade length of this segment.

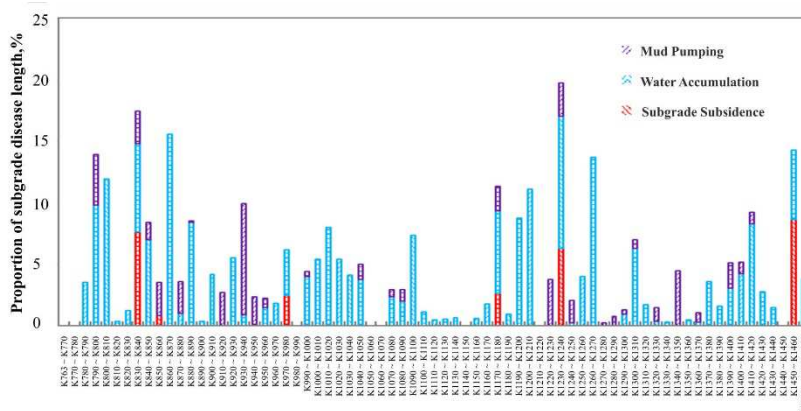


Figure 10
Distribution of diseases along the route

Analysis of inspection data is makes it possible to understand the distribution of three typical diseases by line length (Figure 10) and depth. In particular, it is useful for accurately judging whether mud pumping has occurred inside the ballast bed. In addition, the railway maintenance unit can optimize the ballast bed screening plan according to the distribution of diseases by depth. In order to ensure the long-term effect of ballast bed screening, the key subgrade diseases can be treated together.

4.2 Site Excavation and Verification

To verify the accuracy of inspection through this method, site excavation of 17 sections of subgrade disease development was performed. The results of geological radar recognition are relatively consistent with the in-situ excavation conditions.

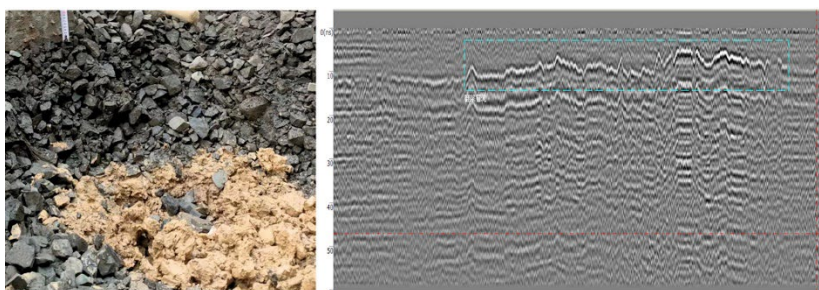


Figure 11
Excavation and verification results of mud pumping disease along the K920+800 line

Figure 11 shows the excavation and verification results of mud pumping disease along the K920+800 line. Radar reflection waveform shows the characteristics of uneven reflections, there are multiple reflections in the underlying layer, and the

mud pumping interface has not reached the surface layer. Therefore, it is deemed as concealed mud pumping. Site excavation findings are consistent with the inspection conclusions. Obvious mud pumping was seen after excavation without access to the rail surface.

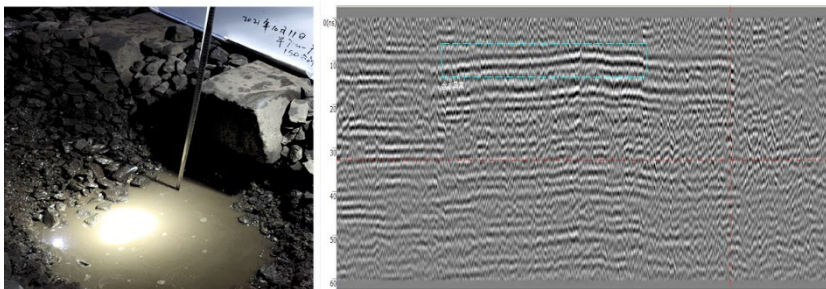


Figure 12

The result of water accumulation test of K1253+400 line

Figure 12 shows the excavation and verification results of water accumulation along the K1253+400 line. The radar reflection waveform in Figure 12 shows parallel strong reflection characteristics, and there are multiple reflections in the underlying layer. Therefore, the line is deemed as water accumulation. Site excavation findings are consistent with the inspection conclusions, and obvious water accumulation was seen after excavation.

Conclusions

This paper proposes a method for railway subgrade disease inspection based on the geological radar. Firstly, radar data were denoised to improve the SNR, and then radar image features of typical subgrade diseases were determined according to the results of site excavation and verification. A special detection device equipment was used for rapid acquisition of geological radar data of subgrade, and effective identification of typical subgrade diseases according to comparison results of radar image features. The subgrade inspection method has been applied to a normal-speed railway in Southwest China. It is demonstrated that this method is effective to realize the rapid inspection and accurate identification of concealed subgrade defects. Conclusions are made as follows:

- (1) The CEEMD method and the mean background denoising algorithm are effective to remove the Rail Sleeper interference and background noise in the radar data, and to improve the SNR of inspection data.
- (2) This paper analyzes and summarizes the radar image features of three typical subgrade diseases, namely mud pumping, water accumulation and subsidence. According to the characteristics of typical subgrade diseases, radar inspection data of subgrade are interpreted, which provides a basis for the identification of concealed subgrade diseases.

- (3) This inspection method makes it possible to understand the distribution of three typical subgrade diseases by line length and depth, so as to support the treatment of such diseases. In particular, it is useful for accurately judging whether diseases have existed inside the ballast bed. In addition, it is conducive to optimizing the ballast bed screening plan, and ensuring the long-term effect of ballast bed screening.

Acknowledgement

This research was funded by the Research and Development Project of China Academy of Railway Sciences Corporation Ltd., under Grant Number [2021JJXM22]: Automatic identification technology of mud pumping disease based on ground penetrating radar.

References

- [1] National Railway Administration of People's Republic of China, "TB/T 2818-2016 Railway Roadbed Disease Classification," 2017
- [2] Hugenschmidt J, "Railway Track Inspection Using GPR," *Journal of Applied Geophysics*, Vol. 43, pp. 147-155, 2000
- [3] Clark M R, Gillespie R, Kem PT, et al., "Electromagnetic properties of railway ballast," *NDT & E International*, Vol. 34, No. 5, pp. 305-311, 2001
- [4] Sussmann T R, Selig E T, Hysli PJ P, "Railway track condition indicators from ground penetrating radar," *NDT & E International*, Vol. 36, No. 3, pp. 157-167, 2013
- [5] Geraads S, Charachon B, Loeffler O, et al. , "Applying a wavenumber notch filter to remove interferences caused by railway Rail Sleepers from a GPR section," *Ninth International Conference on Ground Penetrating Radar. Bellingham, WA : Society of Photo-Optical Instrumentation Engineers*, pp. 715-718, 2002
- [6] Wang S, Liu G, Jing G, et al., "State-of-the-Art Review of Ground Penetrating Radar (GPR) Applications for Railway Ballast Inspection," *Sensors*, Vol. 22, No. 7, pp. 24-50, 2022
- [7] Y. Guo, V. Markine, G. Jing*, "Review of ballast track tamping: mechanism, challenges and solutions," *Construction and Building Materials*, 2021
- [8] Juhász E, Fischer S, "Tutorial on the fragmentation of the railway ballast particles and calibration methods in discrete element modelling," *Acta Technica Jaurinensis*. Vol. 14, No. 1, pp. 104-122, 2021
- [9] Szalai S, Eller B, Juhász E, et al. , "Investigation of deformations of ballasted railway track during collapse using the Digital Image Correlation Method (DICM)," *Reports in Mechanical Engineering*, Vol. 3, No. 1, pp. 258-282, 2022

-
- [10] Trong Vinh Duong, Yu-Jun Cui, et al., "Investigating the mud pumping and interlayer creation phenomena in railway sub-structure," *Engineering Geology*, 2014
- [11] Xinjun Xu, Yang Lei, et al., "Railway Subgrade Defect Automatic Recognition Method Based on Improved Faster R-CNN," *Scientific Programming*, 2018
- [12] Yang Xinan, Gao Yanling, "Ground Penetrating Radar Detection of Slurry Flooring Diseases on Shanghai-Nanjing Railway," *Rock Mechanics and Engineering Journal*, Vol. 23, No. 1, pp. 116-119, 2004
- [13] DU Panfeng, LIAO Lijian, YANG Xin'an, "Intelligent Recognition of Defects in Railway Subgrade," *Journal of the China Railway Society*, Vol. 32, No. 3, pp. 142-146, 2010
- [14] HOU Zhezhe. "Research on GPR Images Recognition for Subgrade Defects in Ballasted Railroad," *Beijing Jiaotong University*, 2016
- [15] Sysyn, Mykola, et al. "Experimental study of railway ballast consolidation inhomogeneity under vibration loading." *Pollack Periodica* Vol. 15, No. 1, pp. 27-36, 2020
- [16] Sysyn, Mykola, et al. "Laboratory evaluation of railway ballast consolidation by the non-destructive testing." *Communications-Scientific letters of the University of Zilina* Vol. 21, No. 2, pp. 81-88, 2019
- [17] Liu, Jianxing, et al. "Influence of a tamping operation on the vibrational characteristics and resistance-evolution law of a ballast bed." *Construction and Building Materials* 239, 117879, 2020
- [18] Liu, Jianxing, et al. "Dynamic characteristics of the railway ballast bed under water-rich and low-temperature environments." *Engineering Structures* 252 .113605, 2022
- [19] PAY Ibrenk. Detecting anomalies and water distribution in railway ballast using GPR [D] Norwegian University of Science and Technology, 2015
- [20] Norden E. Huang, Zheng Shen, et al., "The Empirical Mode Decomposition and the Hilbert Spectrum for Nonlinear and Non-Stationary Time Series Analysis," *Proceedings: Mathematical, Physical and Engineering Sciences* . 1998 (1971)
- [21] Yeh, Jia-Rong, Jiann-Shing Shieh, et al., "Complementary ensemble empirical mode decomposition: A novel noise enhanced data analysis method," *Advances in Adaptive Data Analysis* Vol. 2, No. 2, pp. 135-156, 2010

Research on Risk Control Parameters of a Shielded-Tunnel-enlarged Station, based on Bearing Capacity of Pre-removed Segment

Zhiyong Peng^{1,2}, Xiuren Yang^{1,2}, Weining Liu³,
Majid Movahedi Rad⁴

¹Beijing Urban Construction Design and Development Group Co., Ltd, 100037 Beijing, China; pengzhiyong@bjucd.com; yangxr@bjucd.com

²National Engineering Laboratory for Green & Safe Construction Technology in Urban Rail Transit, Beijing, 100037; pengzhiyong@bjucd.com; yangxr@bjucd.com

³School of Civil Engineering, Beijing Jiaotong University, Beijing, 100044; China; wnliu@bjtu.edu.cn

⁴Department of Structural and Geotechnical Engineering, Széchenyi István University, Egyetem tér 1, H-9026 Győr, Hungary; majidmr@sze.hu

Abstract: A pre-removed segment is a new structure segment applicable to enlarging shield tunnel technology. It can facilitate the removal of the excess partitioned segment, for an enlarged station, by shield tunnel, however, it may cause certain risk of enlarged excavation construction, when a certain construction control limit is exceeded. To study the risk control problem for the removed segment, applicable to the shielded-tunnel-enlarged station, a risk control method, based on the load critical curve of the pre-removed segment is proposed. In this paper, a three-dimensional stratum structure model of the shielded-tunnel-enlarged station is established and variations of forces on the interface of the pre-removed segment are analyzed, under the influences of buried depth and staggered distance, for different enlarged excavation construction stages, as well as different soil properties (elasticity modulus). Combined with the load critical curve of the contact surface concerning the pre-removed segment obtained from the test, the critical construction control surface of buried depth and staggered distance, was obtained to ensure the bearing capacity of the pre-removed segment in different soil properties and in all of the involved enlarged excavation stages. It provides the technical guidance and reference for the construction risk control of the application of pre-removed segment in the shielded-tunnel-enlarged station.

Keywords: pre-removed segment; buried depth; staggered distance; soil properties; enlarged excavation construction; the load critical curve; the critical construction control curve; risk control and shielded-tunnel-enlarged station

1 Introduction

It is a special construction method of underground engineering to enlarge subway station by shield tunnel^[1-4]. The shield equipment passes first, and then the shield tunnel structure is used to enlarge the subway station in combination with other excavation methods^[5-7]. Due to the complex process of segment removal during enlarging, the segment to be removed or cut can be set in the form of pre-removal in advance, which can reduce the difficulty of enlarged construction and shorten the enlarged construction period. Therefore, if the station enlarging plan is carried out in a certain section of shield tunnel in the future, the pre-removed segment can be installed in this section in advance, which can provide great convenience for the station expansion in the later period.

This leads to a question, of whether the internal force changes, of the pre-removed segment, can meet the requirements of the bearing capacity of the pre-removed segment during the shield tunnel, with the pre-removed segment still not enlarged. It is the key to control the construction risk to enlarge subway stations by shield tunnel, with the pre-removed segment, during this period. It should be said that this shielded-tunnel-enlarged station method, is not applicable to any operational stages, so the impact of subway train vibrations, on the shield tunnel structure, has not been considered^[8]. In addition, this method is not suitable for staggered assembled segment tunnels in operation period^[9].

At present, there are some cases concerning enlarged subway stations, with a shield tunnel: In Russia^[10,11], the single-arch station structure was enlarged between two shield tunnels, in which some segments were partially removed and the interior space is poured into arch supports. In Saudi Arabia^[12], open-cut method was used to remove part of large diameter shield tunnel, and the location where the tunnel was removed was enlarged into a station structure. In China, large-diameter shield segments were used to enlarge subway a station combined with a PBA method^[13]. The segments at critical removal locations are also cut directly. In the above cases, segments are directly cut, which ensures the safety of the structure during the enlargement period, in which, segments are not removed. At the same time, it also increases the difficulty of partial demolition of segments during the enlarging of the subway station, especially for the underground construction.

If the segment to be removed is designed in a partitioned form, the construction difficulty of segment removal can be greatly reduced. At the same time, it also increases the safety risks of the structure, during the construction period. This partitioned segment is defined as a pre-removed segment, as shown in the Figure 1. In fact, this segment has been used in the discussion scheme for the shielded-tunnel-enlarged station of Beijing Metro Line 14. The bearing capacity test has also been done especially for this kind of segment^[11]. Although it was not adopted in the final designing scheme, the experiments and related research are still

valuable for similar projects. This paper is one research work, which based on the construction risk control of the shielded-tunnel-enlarged station with a pre-removed segment.

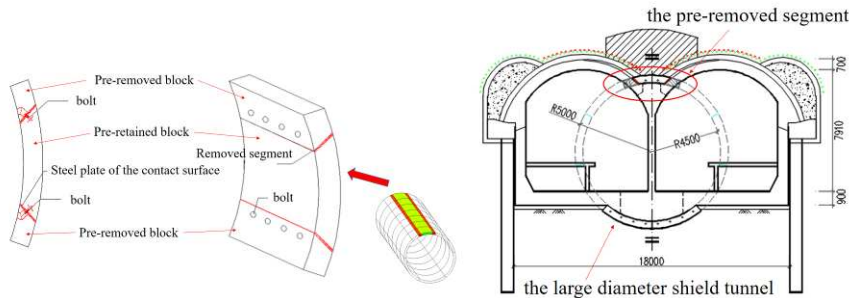


Figure 1

The pre-removed segment

The purpose of this research is to establish a method to analyze the reasonable construction risk control parameters of the shielded-tunnel-enlarged station with the bearing capacity of pre-removed segments, so that designers can quickly predict a reasonable risk range during the preliminary design phase.

In this paper, a three-dimensional stratum structure model for shielded-tunnel-enlarged stations is established to analyze the internal force changes of the pre-removed segment, under different key construction parameters with different soil properties. Based on the test results of the bearing capacity of the pre-removed segment, the reasonable construction key parameters are screened out, so the construction risk control index, of the shielded-tunnel-enlarged station, based on the bearing capacity of the pre-removed segment, was determined.

2 Risk Control Principle Based on Bearing Capacity of Pre-removed Segment

This paper is a research on construction risk control based on the completed bearing capacity test of pre-removed segment^[14]. It was found through test analysis that there are many kinds of critical loading combinations on the contact surface of the same type of pre-removed segment, and these combinations will form the envelope of critical loading combinations, as shown in the Figure 2.

The critical state features of the pre-removed segment are as follows: When the internal force of the pre-removed segment is in a group of critical state combinations. The displacement of the contact surface of the pre-removed segment will increase suddenly. It will cause the bolts connecting the segments to

be locked in place, so that the separation of the pre-removed segment cannot be successfully completed. At this time, the original cutting methods can only be adopted and the original intention of designing the pre-removed segment is invalid.

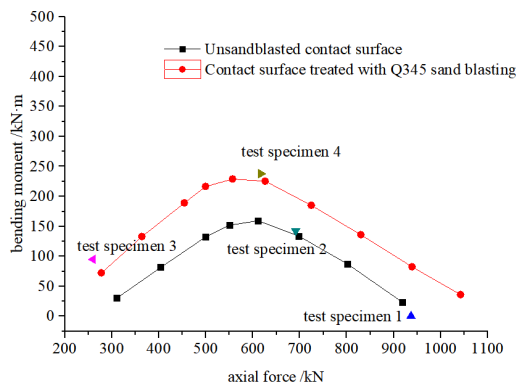


Figure 2

The load critical curve about the pre-removed segment

Therefore, in different enlarged excavation construction stages and under different soil properties (elasticity modulus), the internal force on the pre-removed segment changes with the variation of construction parameters. When the internal force combination value of the removed segment corresponding different construction conditions is within the range of critical curve, the removed segment is in normal condition. Otherwise, the pre-removed segment cannot be removed successfully and it may cause structural safety and stability risks. Therefore, the reasonable risk control parameters can be found through the load-bearing critical curve of the pre-removed segment.

3 Analysis of Major Risk Factors

This paper analyzes the risk factors of the enlarged subway station by the large-diameter shield tunnel combined with the PBA method. From the perspective of the enlarged construction process, the stages in which the pre-removed segment is still in a working state include, as shown in the Table 1:

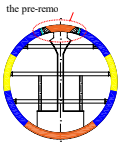
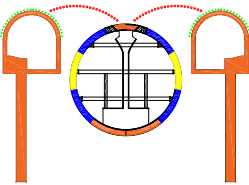
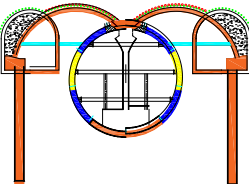
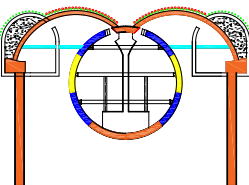
- (1) Initial state of tunnel segment
- (2) Pilot tunnel excavation
- (3) Supporting arch excavation
- (4) The pre-removed segment removed

The main influence of each risk factor on internal force of pre-removed segment is as follows:

- (1) **The buried depth of tunnel:** With the change of buried depth, the ground stress in surrounding rock changes correspondingly, and the internal force on the pre-removed segment also adjusts accordingly.

Table 1

Main factors affecting internal force of pre-removed segment in different construction stages

Enlarged excavation construction stages	Enlarged construction diagram	Main factors affecting the pre-removed segment
Stages 1: Tunnel segment ring		buried depth of tunnel; the soil properties
Stages 2: pilot tunnel excavation		buried depth of tunnel; asymmetric excavation; the soil properties
Stages 3: Supporting arch excavation		buried depth of tunnel; asymmetric excavation; the soil properties
Stages 4: The pre-removed segment removed		The pre-removed segment has been removed and this stage is beyond the analysis scope of this paper

- (2) **Enlarged excavation construction stage:** The construction stages before the pre-removed segment is removed mainly include tunnel segment ring (Stages 1), pilot tunnel excavation (Stages 2) and supporting arch excavation (Stages 3), Shown in table 1. The internal forces on the contact surface of the pre-removed segment will be constantly adjusted in the three main construction stages. Each construction stage has different influence on the internal force of pre-removed segment.

- (3) **Asymmetric excavation:** In fact, it is difficult to complete the synchronous construction of the left and right sides in the pilot tunnel excavation stage and supporting arch excavation stage. When the two sides of the driving length are different, the partial load will be formed on the pre-removed segment, which will cause the change of the internal force of the pre-removed segment.
- (4) **Soil properties:** Numerical analysis shows that the soil properties have a great influence on the internal force of the structure, the influence of elastic modulus of soil is particularly obvious. Considering that this kind of engineering may occur in different soil environments, this paper considers the influence of different elastic modulus of soil on the internal force of the contact surface of pre-removed segment based on the combination of the first three analyses.

These four risk factors are correlated. buried depth is a key factor affecting structural mechanics. The internal force of pre-removed segment is also affected by different enlarged excavation construction stages, which also affect the allowable range of asymmetric excavation at each enlarged excavation construction stage. At the same time, the elastic modulus of soil has a further superposition effect on the internal force of the pre-removed segment. And the value range of internal force is limited by the bearing capacity of the enlarged segment which determines the reasonable range of the four main factors mentioned above.

Therefore, three-dimensional numerical analysis can be used to grasp the influence of different buried depth, enlarged excavation construction stages and asymmetric excavation in different soil environments on the internal force of the pre-removed segment. And the critical line of bearing capacity of pre-removed segment is taken as the control standard. A reasonable parameter selection scheme, for risk control of enlarged subway station, is proposed based on the bearing capacity of the pre-removed segment, as a control standard.

4 Model Analysis

4.1 Establishment of Numerical Model

The ABAQUS software is used to analyze the influence of enlarged excavation construction stages and asymmetric excavation on the internal force of the pre-removed segment, in different buried depths and for different elastic modulus of soil. The simulation is carried out for the shielded-tunnel-enlarged station with the PBA method, which involves a construction process before the pre-removed

segment is removed. The models transverse length is 130 m and longitudinal length is 36 m. The width of each tunnel segment is 1.8 m, the thickness is 0.5 m. The model contains 20 tunnel segment rings. The 20 pre-removed segments will be removed in the model. Main parameters of the model are shown in Table 2.

Table 2
Main parameters of the model

buried depth (m)	Model height (m)	Length difference of asymmetric excavation		
		Pilot tunnel excavation	Supporting arch excavation	Elastic modulus of soil
10	50	The staggered distance is divided into 6 stages, with each stage increasing by 3.6 m and the range is 0-18 m	The staggered distance is divided into 6 stages, with each stage increasing by 3.6 m and the range is 0-18 m	The elastic modulus of soil is divided into three categories: 6 MPa, 30 MPa and 150 MPa
18.5	60			
30	70			
40	80			
50	90			

Note: Because the numerical calculation uses the stratum structure model, the height of the calculation model will be adjusted accordingly with the change of the buried depth of the station roof structure in keeping the thickness of the soil at the bottom of the station constant.

Table 3
Physical and mechanical parameters of materials

Model components	Materials	Density kg/m ³	Elastic modulus /GPa	Poisson's ratio
tunnel segment	toncrete C50	2450	34.5	0.2
bolt	steel	7800	210	0.2
temporary support	steel	7800	210	0.2
Beam, column, primary lining	toncrete C30	2500	30	0.2
Grouting layer	grouting material	2150	0.06	0.3
Soil layer (all soil parameters are considered as a single homogeneous material by weighted average method)	soil	1950	The values of elastic modulus are shown in Table 2. And the cohesion of the soil is 20kPa and the angle of internal friction is 15°.	0.3

Hypothetical conditions: To study the main risk factors, material parameters such as all soil parameters are considered as a single homogeneous material by weighted average method. The cohesion of the soil is 20 kPa and the angle of internal friction is 15°. The cohesion of the grouting material is 50 kPa and the angle of internal friction is 35°. Each stage of the enlarged construction was

completed before the next enlarged construction begins. Pre-removed segment structure is simulated according to actual size. The pre-removed segment consists of three component blocks that are bolted together. These are all solid units. A contact unit is arranged between the blocks. Rigid contact is set in the normal direction of the block contact surface and frictional contact is set in the tangential direction. A binding connection is set between the two surfaces of the bolt and the inner surface of the bolt hole on the corresponding pre-removed segment, and the bolt is set up with a prestressing force of 100 kN. The temporary supports are used for beam units. The physical and mechanical parameters of the materials^[15,16] involved in the calculations for the model, are shown in Table 3.

The 3D model mesh division schematic and the bolt and contact surface detail schematic is shown in Figure 3.

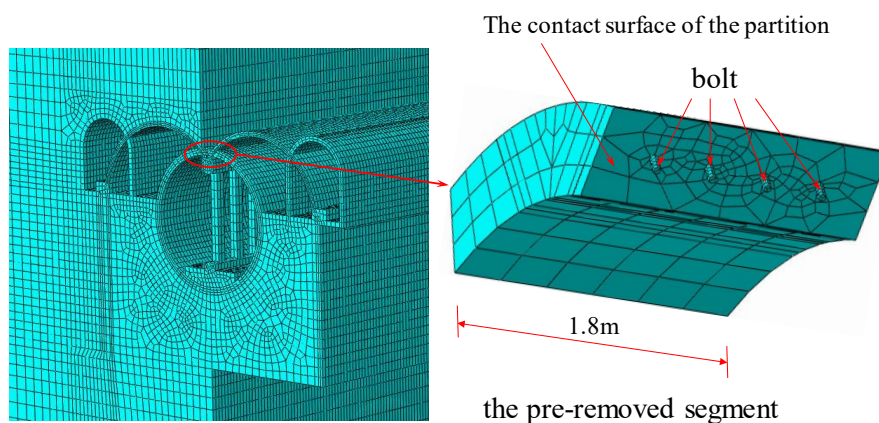


Figure 3

3D model and bolt connection of pre-removed segment

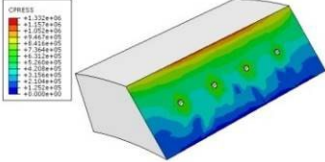
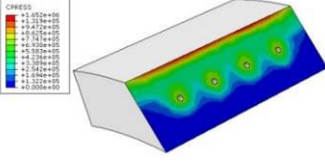
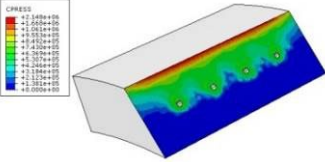
4.2 Analysis of Computing Results

ABAQUS calculation software is used to analyze the influence of enlarged excavation construction stages and asymmetric excavation on the internal force of the pre-removed segment in different buried depths.

Table 4 shows the distribution of CPRESS (compressive stress) on the contact surface of the pre-removed segment in different enlarged excavation construction stages under the condition of 18.5m buried depth and 0m staggered excavation (i.e. symmetrical excavation) which in the elastic modulus of soil is 30 MPa.

As can be seen from Table 4, when the buried depth of the structure is 18.5 m, the staggered distance is 0 m and the elastic modulus of soil is 30 MPa, the characteristics of the contact surface of the pre-removed segment change as follows:

Table 4
Variation of CPRESS on the contact surface at different construction stages

Enlarged excavation construction stages	CPRESS diagram on the contact surface of the pre-removed segment
Stages 1: Tunnel segment ring	
Stages 2: Pilot tunnel excavation	
Stages 3: Supporting arch excavation	

- (1) **Tunnel segment ring (Stages 1):** The CPRESS (compressive stress) distribution on the contact surface of the pre-removed segment is relatively uniform, and the area near the bolt hole of the contact surface is in compressed state, and only the lower edge of the pre-removed segment is in open state.
- (2) **Pilot tunnel excavation (Stages 2):** The CPRESS distribution is basically the same as in the previous stage. However, the degree of pressure on the upper edge area and the degree of opening of the lower edge seam have increased, and the contact surface in the vicinity of the bolt is still under pressure. It indicates that in the pilot tunnel excavation stage, the tension of the lower edge of the contact surface of the pre-removed segment has a gradually increasing trend.
- (3) **Supporting arch excavation (Stages 3):** The CPRESS distribution is basically the same as in the first two stages. The compression degree of the upper edge and the opening degree of the lower edge increase further. Although the contact surface near the bolt is still under pressure, the upper part of the area near the bolt begins to open trend. It is obvious that the largest opening range of the pre-removed segment in this stage which among the previous several stages.

In the same enlarged excavation construction stage, which the elastic modulus of the soil is 30 MPa, the converted axial force and bending moment on the contact

surface with different burial depth conditions and different staggered distances are obtained, as shown in Figure 4 and Figure 5.

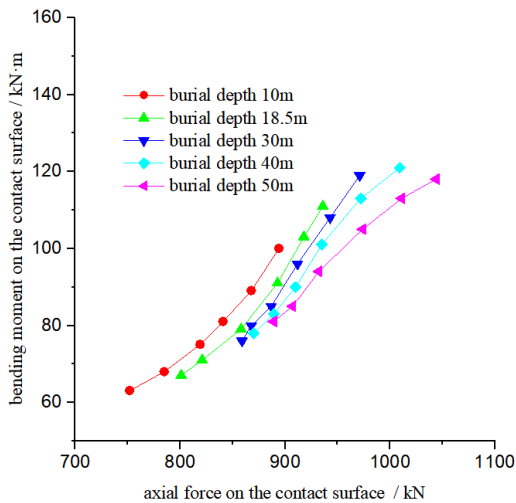


Figure 4

The relationship about the internal force of contact surface of the pre-removed segment in pilot tunnel excavation stage

Note: The calculation points of each burial depth in the figure are calculated in order of the staggered distance 0 m, 3.6 m, 7.2 m, 10.8 m, 14.4 m and 18 m, which the elastic modulus of the soil is 30 MPa.

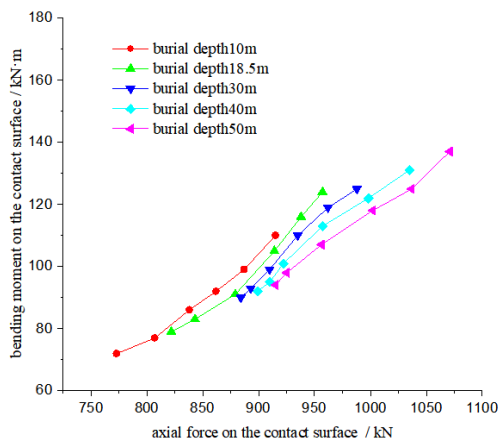


Figure 5

The relationship about the internal force on contact surface of the pre-removed segment in supporting arch excavation stage

Note: The calculation points of each burial depth in the Figure are calculated in order of the staggered distance 0 m, 3.6 m, 7.2 m, 10.8 m, 14.4 m and 18 m, which the elastic modulus of the soil is 30 MPa.

According to Figure 4 and Figure 5, the following rules can be seen.

- (1) In the same buried depth and enlarged construction condition, the internal forces on the contact surface of the pre-removed segment are different due to different staggered distances. The axial force and bending moment of the contact surface gradually increase with the increase of the staggered distance.
- (2) The influence range of the internal force of the contact surface caused by the excavation with the staggered distance of the buckle is greater than that of the excavation with the staggered distance of the small guide tunnel.
- (3) The internal force of the contact surface will increase gradually with the increase of the buried depth under the condition of the same staggered excavation.

5 Construction Risk Control Based on Pre-removed Segment in Normal Service Conditions

5.1 Risk Control in Pilot Tunnel Excavation Stage

The internal force of the contact surface of the pre-removed segment obtained from the previous numerical analysis in pilot tunnel excavation stage was compared with the critical curve of the contact surface internal force obtained by the previous test, the following characteristics can be found, as shown in Figure 6.

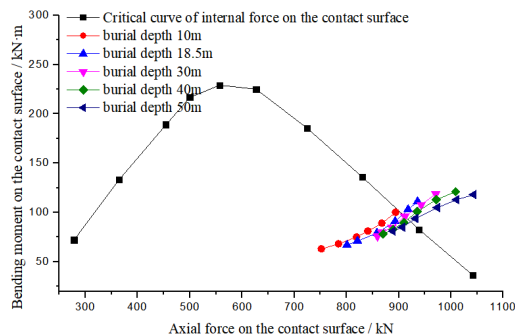


Figure 6

The relationship between internal force of contact surface and critical curve of internal force of contact surface in different buried depth and staggered distance in pilot tunnel excavation stage

As shown in the Figure 6. In the condition of different buried depth and staggered distance and the elastic modulus of the 30 MPa soil layer, the internal force produced by pilot tunnel excavation on the contact surface of pre-removed segment is not all within the critical curve of internal force of contact surface. Therefore, when the combination of parameters beyond a certain buried depth and staggered distance is exceeded, no matter how the excavation is done, it cannot meet the normal use requirements of the pre-removed segment. According to the critical curve of internal force on the contact surface, the critical buried depth and staggered distance that meet the requirements of pre-removed segment should be determined. The analysis results are shown in Table 5.

Table 5
Critical staggered distance of different buried depths

Buried depth (m)	Axial force (kN)	Bending Moment (kN·m)	Conv. of staggered distance / m
10	--	--	--
18.5	907.7	98.1	10.8
30	912.9	95.6	8.3
40	917.6	93.3	6.9
50	921.9	91.1	5.7

According to Table 5, the relationship in pilot tunnel excavation stage between critical buried depth and critical staggered distance excavation in normal use of pre-removed segment is calculated, as shown in Figure 7.

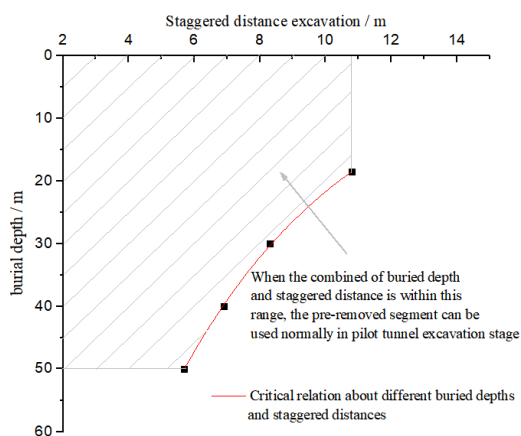


Figure 7

The critical relation about different buried depths and staggered distances in the pilot tunnel excavation stage

In the soil, the elastic modulus of which is 30 MPa, when the combination of the buried depth and staggered distance is within the envelope of the critical curve, the pre-removed segment can meet the requirements of its bearing capacity.

Otherwise, the staggered distance needs to be adjusted to a reasonable range to ensure that the pre-removed segment can be used properly in the pilot tunnel excavation stage.

Furthermore, the corresponding critical burial depth and staggered distance relationship can also be obtained in the pilot tunnel excavation stage for the different elastic modulus (6 MPa, 30 MPa, 150 MPa) of the soil. As shown in Figure 8, the critical relation surface in the pilot tunnel excavation stage can be obtained by combining these critical relationships, which are determined by different buried depths, staggered distances, and elastic modulus of the soil.

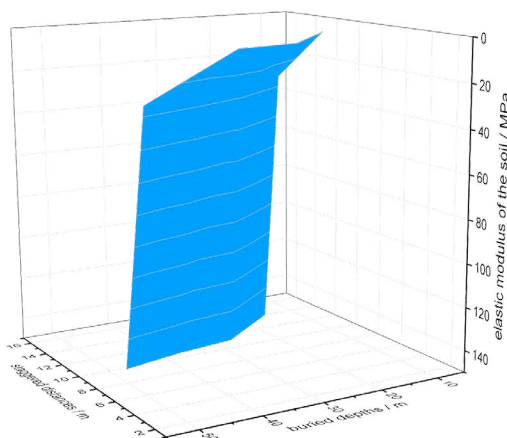


Figure 8

The critical surface about different buried depths, staggered distances, and the elastic modulus of soil in the pilot tunnel excavation stage

In the soil, the elastic modulus of which is 6 MPa, 30 MPa, and 150 MPa, when the combination of the buried depth and staggered distance is within the envelope of the critical surface, the pre-removed segment can meet the requirements of its bearing capacity. Otherwise, the staggered distance needs to be adjusted to a reasonable range to ensure that the pre-removed segment can be used properly in the pilot tunnel excavation stage.

5.2 Risk Control in Supporting Arch Excavation Stage

The internal force of the contact surface of the pre-removed segment obtained from the previous numerical analysis in the supporting arch excavation stage was compared with the critical curve of the contact surface internal force obtained by the previous test, the following characteristics can be found, as shown in Figure 9.

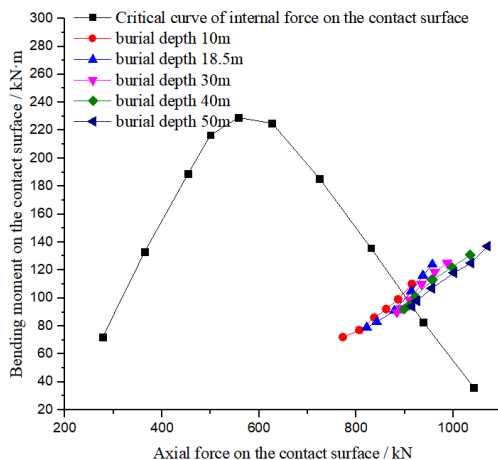


Figure 9

The relation between internal force of contact surface and critical curve of internal force of contact surface under different buried depth and staggered distance in supporting arch excavation stage

As the same data analysis process as 5.1, the corresponding critical buried depth and staggered distance relationship can also be obtained in supporting arch excavation stage for the different elastic modulus (6 MPa, 30 MPa, 150 MPa) of the soil. As shown in Figure 10, the critical relation surface in the pilot tunnel excavation stage can be obtained in supporting arch excavation stage by combining these critical relationships, which are determined by different buried depths, staggered distances, and elastic modulus of the soil.

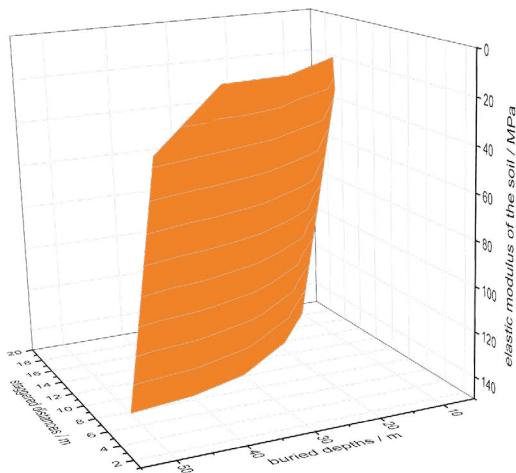


Figure 10

The critical surface about different buried depths, staggered distances, and the elastic modulus of soil in supporting arch excavation stage

In the soil, the elastic modulus of which is 6 MPa, 30 MPa, and 150 MPa, when the combination of the buried depth and staggered distance is within the envelope of the critical surface, the pre-removed segment can meet the requirements of its bearing capacity. Otherwise, the staggered distance needs to be adjusted to a reasonable range to ensure that the pre-removed segment can be used properly in supporting arch excavation stage.

5.3 The Envelope Surface, for a Reasonable Risk Control Range

Considering the actual construction requirements, the new envelope surface can be obtained by superimposing the critical surface of the two construction stages, as shown in Figure 11.

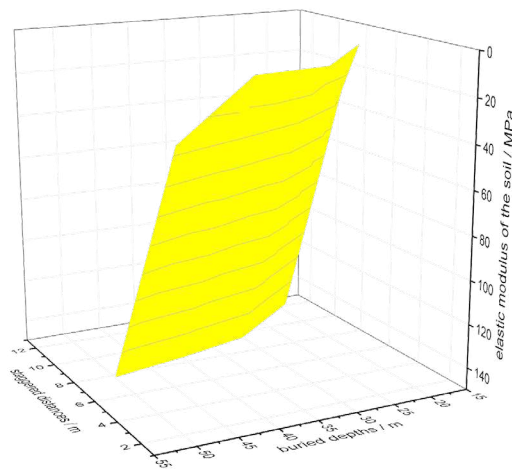


Figure 11

The envelope surface about different buried depths, staggered distances, and the elastic modulus of soil in all enlarged excavation stages

The new envelope surface indicates when the construction parameter combination meets the combination of the station buried depth, staggered distance and elastic modulus of soil corresponding to the critical surface, the pre-removed segment can meet the requirements of its bearing capacity in all enlarged excavation stages prior to the pre-removed segment removed stage.

Conclusions

A risk control method of enlarged subway station construction, using a shield tunnel was proposed, using the bearing capacity of pre-removed segment. In this paper, a three-dimensional stratum structure model of the shielded-tunnel-enlarged

station is established and the internal forces of contact surface are screened in various enlarged construction conditions, different buried depths, staggered distances, and the elastic modulus of the soil. Combined with the critical internal force curve of the contact surface around the pre-removed segment, obtained from the test, the construction control surface of critical buried depth and staggered distance was obtained, to ensure the bearing capacity of the pre-removed segment. This provides a technical reference for the construction risk control of the application of pre-removed segment, in the shielded-tunnel-enlarged station.

The results show that the internal force of the contact surface is largest in the supporting arch excavation stage, followed by the pilot tunnel excavation stage. The compression surface on the contact surface of the pre-removed segment gradually concentrates on the upper region and gradually detaches on the lower region.

With the increase of buried depth, the internal force of the contact surface presents a nonlinear growth and the internal force growth, tends to slow, below 30 m.

In the scenario of equal buried depth and the equal enlarged constructions, the internal force of the contact surface gradually increases with the increase of staggered distance. And the influence range of the internal force of the contact surface, caused by the enlarged excavation with staggered distance in supporting arch excavation stage, is greater than in the pilot tunnel excavation stage.

Acknowledgement

This work was supported by Fund program: National Key R&D Program of China (2017YFB1201104)

References

- [1] Yukinori Koyama, Present status and technology of shield tunneling method in Japan, *Tunnelling and Underground Space Technology*, 2003(18):145-159
- [2] Hiroyuki KAMATA, Yoshio MATSUMOTO. Conceptional Design and Feasibility Study of a New Tunneled Station with Multi-Circular Face Shield (MF Shield). *Quarterly Report of RTRI*, 1992,33(2): 115-123
- [3] LU Meili, Study on schemes and risk analysis of the expanded Metro station under shield running tunnel. Beijing: Beijing Jiaotong University, 2008 (in Chinese)
- [4] JiaoLong Zhang, YiMin Gao, Xian Liu. A shield tunneling method for enlarging the diameter of existing tunnels: Experimental investigations, *Tunnelling and Underground Space Technology*, 2022(128): 104605
- [5] Heidkamp H, Katz C, Hofstetter C. Enlargement of the Marienplatz Metro station: A complex tunnel project beneath Munich City Hall. *Structural Engineer*, 2006, 84 (3): 41-44

-
- [6] Mohammad H. Sadaghiani, Saleh Dadizadeh, Study on the effect of a new construction method for a large span metro underground station in Tabriz-Iran, *Tunnelling and Underground Space Technology*, 2010(25):63-69
- [7] Morteza Abdi Cherlo. Hamid H, Masoud C, Saeed M: Feasibility evaluation for excavation of Naghshe Jahan Square subway station by underground methods, *Journal of Rock Mechanics and Geotechnical Engineering*, 2013(5): 452-45
- [8] Xu L, Ma M, Cao R, Tan X, Liang R. Effect of longitudinally varying characteristics of soil on metro train-induced ground vibrations based on wave propagation analysis. *Soil Dynam Earthq Eng* 2022;152:107020
- [9] Hao Jin et al., Study on vibration propagation characteristics caused by segments joints in shield tunnel, *International Journal of Structural Stability and Dynamics*[J]. DOI: 10.1142/S0219455423501560
- [10] C H Brasov. Essence of subway construction in Russian. Translators: Qian Qihu, Qi Chengzhi. Beijing: China Railway Publishing House, 2002
- [11] HONG Dailing. Design of deep Moscow Metro stations. *Tunnel and Underground Engineering*, 2000(1): 33-39 (in Chinese)
- [12] Mohammad H. Sadaghiani, Saleh Dadizadeh, Study on the effect of a new construction method for a large span metro underground station in Tabriz-Iran, *Tunnelling and Underground Space Technology*, 2010(25):63-69
- [13] LE Guiping, HUANG Qiwu, LI Hongan, Shield Tunneling Technologies and PBA Enlarging Method: A Case Study on Beijing Metro, *Tunnel Construction*, 2016, 36(2): 211
- [14] Peng Zhiyong, The mechanical state of key structure for the shielded-tunnel-enlarged station on operation. Beijing: Beijing Jiaotong University, 2016 (in Chinese)
- [15] YiFeng Yang, ShaoMing Liao, MengBo Liu. A new construction method for metro stations in dense urban areas in Shanghai soft ground: Open-cut shafts combined with quasi-rectangular jacking boxes, *Tunnelling and Underground Space Technology*, 2022(125): 104530
- [16] Xiangyu Guo, Zhengzheng Wang, Ping Geng. Ground surface settlement response to subway station construction activities using pile–beam–arch method, *Tunnelling and Underground Space Technology*, 2021(108): 103729

Comprehensive Laboratory Test Series for Timber-Concrete Composite Structures

Harrach Dániel, Majid Movahedi Rad*

Department of Structural and Geotechnical Engineering, Széchenyi István University, Egyetem tér 1, H-9026 Győr, Hungary
e-mail: harrach.daniel@sze.hu, majidmr@sze.hu

Abstract: Timber-concrete composite structures are not as widespread as traditional steel-concrete fabrications; this structural design still has many critical points that require tests on laboratory specimens. This paper presents the complex testing process of timber-concrete composite structures, which must be followed from the investigation of the possibilities of connecting timber and concrete to each other, through the tests of bended beams acting as timber-concrete composites, to the laboratory tests of full-scale custom-designed timber-concrete composite bridge structures subjected to both concentrated and distributed loads. In this study, to improve the flexural properties of timber beams, carbon fiber-reinforced polymer (CFRP) laminates are attached externally to timber elements. To verify the behavior of the designed structure, we built a full-scale experimental structure and performed a load test. In the laboratory tests, the serviceability limit states, standard loads and load arrangements were investigated. The results of the loading experiments were evaluated. The bridge structures in this article will be placed outdoors after completion of the tests, where they will be used as pedestrian-bicycle bridges. In the case of the examined structures, it was an important aspect, to use elements that are commercially available and suitable for use in the Hungarian design and regulatory systems.

Keywords: — Timber-concrete structures; connections; composite structures; bridge model; static load

1 Introduction

"Composite structures are structures made of several different materials, in which at the moment of assembly, at least one part of the support made of material has considerable stiffness and load capacity. In addition, it is also important that the static characteristics of the structure are calculated according to the rules of elasticity, taking into account changes in stiffness over time.

According to the narrower interpretation, a bent beam or beam grid is called a composites structure, which consists of a steel beam with bending stiffness at the moment of installation, the reinforced concrete slab above it, and sufficiently rigid joint connecting the two structural elements." [1].

Timber-concrete composite (TCC) structures produced using two elements (tensioned wooden beam and compressed reinforced concrete slab) where composite structures can be considered as modern structures [2]. Wood is a natural/renewable building material and reinforced concrete is a modern building material. In this work, the timber beams are located in a protected place under the reinforced concrete slab, which protects the wood from the swelling effects caused by precipitation. [3]

The composite system created from two structure parts with different properties has a significantly higher load capacity and stiffness compared to (purely) wooden structures, and a significantly lower self-weight compared to concrete and reinforced concrete structures. Concrete behaves well against compressive forces, but its tensile strength is low and its self-weight (compared to wood) is significant. Compared to other building materials, wood has a much lower self-weight and a high tensile strength value (the density-strength ratio is very favorable).

In case of outdoor application (e.g.: pedestrian bridge superstructure), an additional advantage is that the concrete layer protects the wooden beams from environmental effects (e.g.: direct rain or sunlight), thus increasing its service life. To use timber and concrete as a composite structure, it is necessary for the elements to work together. Ensuring adequate relationship rigidity is the main goal that is able to transfer shear forces at the connected part of the structure [4] [5]. Figure 1 illustrates the normal stress diagrams that develop depending on the type of connection.

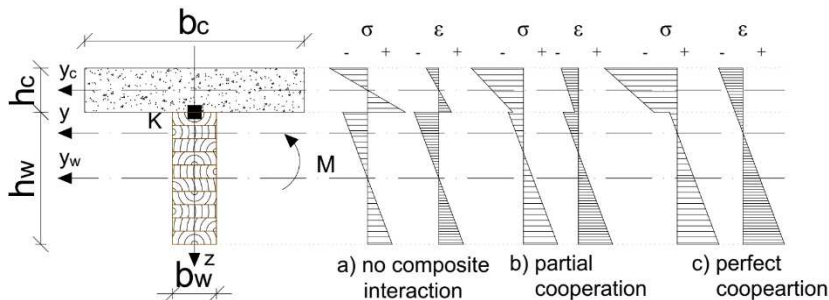


Figure 1

Possible connection levels of timber-concrete structures

The connection stiffness, which can be determined based on the tests, shows the resistance to displacement on the connection surface of the two parts during loading of the structure. K is the connection stiffness, a scalar value that expresses the degree of cooperation between two structural elements. The higher the value, the more cooperation prevails, see Figure 1 [6]:

$K < 5,000 \text{ N/mm}$ - no composite interaction

- $K = 5-100,000 \text{ N/mm}$ - partial cooperation

- $K > 100,000 \text{ N/mm}$ - perfect cooperation

The timber-concrete composite structural system has a history of almost 100 years, the first real-scale experiments on timber-concrete composite beams were conducted between 1938 and 1942, with the aim of comparing the behavior of different connection methods [7].

The analysis of the TCC structures are based on the dimensioning principle of flexibly connected multi-part bent beams, where the entire moment of inertia of the entire cross-section can be calculated, but the deformation of the connecting elements must be taken into account. Most design procedures (e.g. the Eurocode 5's γ -method [8], the stiffness method [9], Girhammar's simplified analysis method [10]) are based on this connection stiffness factor, which must be determined experimentally.

Timber-concrete composite bridges are widespread in the western and northern parts of Europe [5]. In the case of timber bridges with a lifespan of more than 30 years and wooden structures with insufficient load-bearing capacity, the idea to reinforce the wooden beams with a concrete slab first came to light. In the 21st Century, perhaps the most important aspect in bridge construction is no longer applied to meet the requirements of functional needs where the aspects of structure selection do not determine the traffic requirements alone. In addition to load-bearing capacity, durability and economy are the most important design considerations, but aesthetics and environmental awareness have always been important in the design of modern bridges and structures.

In order to achieve an optimal timber-concrete composite behavior, the neutral axis must be located in the vicinity of the contact plane. [11] The stiffness ratio and the strength of the materials show that the ratio of the optimal structural element thickness between timber and concrete should be around 1:10 [12]. However, this ratio is not economical in the case of small bridge structures because the design standards and design regulations prescribe a minimum reinforced concrete slab thickness of 15-20 cm depending on the structural variation in e-UT 07.01.14:2011 [13].

In this paper, we deal with the process from the measurements of the connection between timber and concrete to the static load test of the full-scale (6.0 m span, 2.4 m wide) bridge model in laboratory conditions. The special feature of the designed TCC bridges, that they have been designed in such a way that they can be used as an actual pedestrian-bicycle bridge with minimal reconstruction. During the design of the experimental program, it was important to match the bridge structures to the real traffic loads.

2 Connecting Timber and Concrete

In order to determine the mechanical properties of any composite structure, it is essential to know the strength and deformation characteristics of the joint that connects the different materials. In the case of a timber-concrete composite system, these are influenced by the type of connection. When considering the characteristics of wood and concrete, the initial slip between the two support sections and the effective bending stiffness of the composite system are taken into consideration.

However, it is important to note that joining timber and concrete does not mean joining two perfectly rigid materials. For the Timber-concrete composite (TCC) connection, the difference is that of the steel-concrete composite, so that the coupling element can be moved, pivoted and pushed in both the wood and the concrete [14]. Both wood and concrete have time-dependent properties (shrinkage, swelling, permanent deformation), in the case of design an optimal connection, the coupling element must also be able to absorb the resulting additional stresses [6].

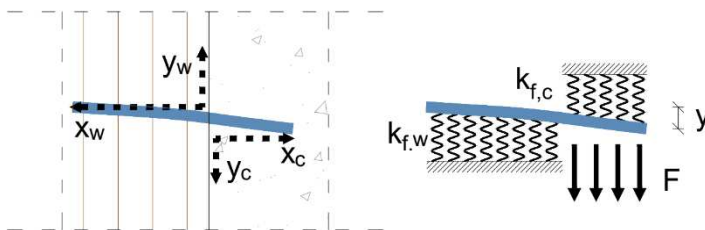


Figure 2

The model of the connection of timber-concrete composite structures [4]

When designing the connections of timber-concrete composite structures, the linear-elastic connection stiffness models only give appreciable results in a very narrow range. The dimensioning procedure that takes into account the non-linear behaviours of the connection exists only at a theoretical level and cannot currently be used for calculations. Its essence is that in the case of relationships and material properties, it calls for a transition from Hooke's linear material model and Winkler's spring model to higher-level theories and functions [14].

The mechanical properties of the connection influence the behaviour of the structure (distribution of stresses, deformations). The classification of shear connections was carried out by Ceccotti [4], who classified the connections, based on their stiffness.

- Class A:** Inexpensive, easy-to-build, low-rigidity connections
- Class B:** Connections with greater stiffness and ductility
- Class C:** Shear wedges reinforced with anchoring units
- Class D:** Connections with the greatest stiffness. There is no slippage between the two structural elements

2.1 Test Method for the Connection between Timber and Concrete

To test the connection between wood and concrete, researchers typically follow the requirements of the EN 26891:1997 [15] and ASTM D5652-21 [16] and EN 1994-1-1:2010 [17] and based on this, they develop their experimental method for examining wood-concrete composite structures. Three different layouts are used for shear testing of wood-concrete composite structures: Pure shear test specimen, Single shear push out test specimen and Double shear push out test specimen. There are two types of the last, when the wood is surrounded between two sides of concrete (CWC concrete-wood-concrete), and when the concrete is located between two wooden parts (WCW wood-concrete-wood). Figure 3 shows the test arrangements for the connection between wood and concrete.

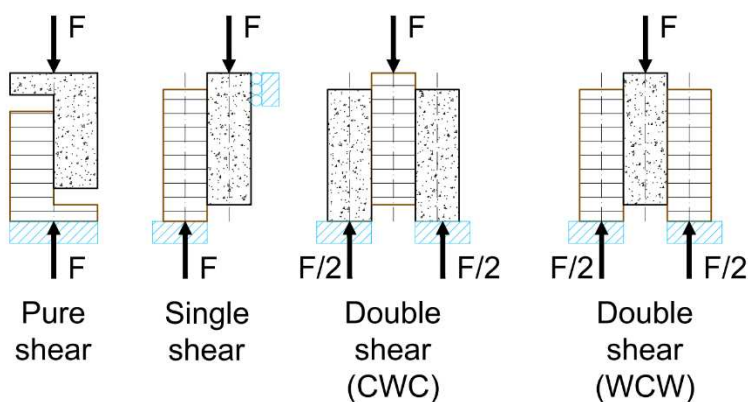


Figure 3

The most common wood-concrete connection test assemblies [18]

2.2 Push-Out Tests

When choosing the test method, I took into account the recommendations of Ceccotti [4] and Holschemacher et al [19], and to determine the connection stiffness, twice sheared push-out wood-concrete-wood (WCW) test specimens I made. The test specimens were designed uniformly with a contact surface of 100x200 mm, because the smaller test specimens can be produced in large quantities and in good quality. The geometry of the test specimens is a 150x100x250 mm wooden beam and a 130x100x250 mm concrete beam adapted to the type of connecting element. A total of 10 different types of connection designs were made, three test specimens per connection type. The characteristics of the test specimens are listed in Table 1.

Table 1

The main characteristics of test specimens for the connection between wood and concrete

Type	Connection method	Contact element quantity
ACS	threaded rod with a tightening torque of 109 Nm	1 pc M20-8.8 – Ø20
ICO	flexible adhesive	Icosit® KC 340/65
RM	epoxy adhesive	Sikadur®-31 CF Normal
FCS90	timber-concrete screw at 90°	1 pc VB-48-7,5x100
FCS45	timber-concrete screw at 45°	1 pc VB-48-7,5x100
FCS±45	timber-concrete screw at ±45°	2 pc VB-48-7,5x100
BB45	bent rebar	1 pc B500B - Ø8 Sikadur®-30 Normal
EA	glued perforated steel plate	1 pc 120x200x3mm Stw. 22, stainless steel Sikadur®-52 Injection Normal
KFCS	glued hardwood dowel	1 pc hardwood dowel: D24 (Ø20) Sikadur®-30 Normal
ICOPL	flexibly embedded perforated steel sheet	1 pc 120x200x3mm Stw. 22, glued hardwood dowel Icosit® KC 340/65

The concrete part is made with non-reinforced construction, uniformly with concrete quality C35/45-XA1-XC4-XD3-XF2-16-F3, while the timber's material quality C24. Figure 4 show the design of the connection test specimens. The tests were performed based on the loading procedure of the MSZ EN 26891:1995 [15] standard.

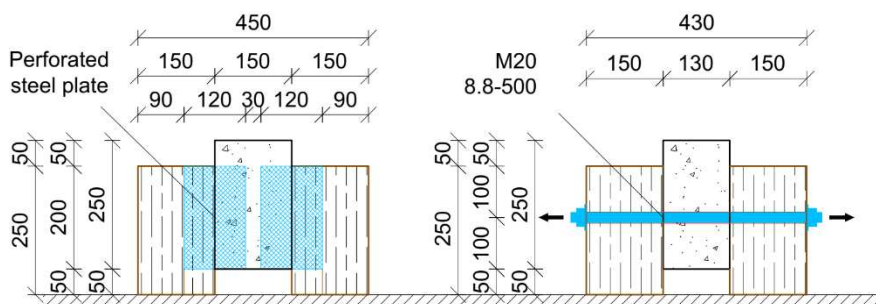


Figure 4

The plans of the test specimens EA and ACS

2.3 Test Results

The main test results are contained in Table 2. The connection stiffness values to be used during linear design methods, i.e. the connection stiffness value for the service

limit state (K_{ser}) and the ultimate limit state (K_u). In addition, the $K(x)$ function of stiffness for the implementation of non-linear design methods was given.

Table 2
The main results of push-out tests

Type	F_{max} [kN]	K_{ser} [kN/mm]	K_u [kN/mm]	$K(x)$ Function of the connection stiffness
ACS	94.9	38.5	23.8	$K(x) = \text{if } x \leq 0.2 \rightarrow 221.97x$ $\text{if } x > 0.2 \rightarrow 4.8145x + 43.431$
ICO	119.4	42.5	32.5	$K(x) = -3.2333x^2 + 40.021x$
RM	125.4	170.0	194.3	$K(x) = 174.76x^{0.8013}$
FCS90	25.8	3.9	2.3	$K(x) = -0.0765x^2 + 2.8122x$
FCS45	10.0	8.7	7.8	$K(x) = 1.1342\ln(x) + 6.8077$
FCS±45	56.3	193.5	121.3	$K(x) = 7.2937\ln(x) + 39.11$
BB45	20.6	41.0	28.2	$K(x) = 1.8245\ln(x) + 13.32$
EA	83.2	73.8	70.0	$K(x) = -9.8284x^2 + 63.371x$
KFCS	36.2	11.0	5.8	$K(x) = -4.7948\ln(x) + 15.412$
ICOPL	56.2	59.0	35.1	$K(x) = 6.2976\ln(x) + 31.573$

The connection type with sufficient connection stiffness and ductile reserve -out of the 10 different connection designs examined - is the shear connection with perforated steel plate glued into the timber part (EA) when using a monolithic reinforced concrete. While using a prefabricated reinforced concrete, the threaded rods (ACS) gives favorable design. Figure 5 shows the typical force-displacement diagram of the various connection types measured during the experiment.

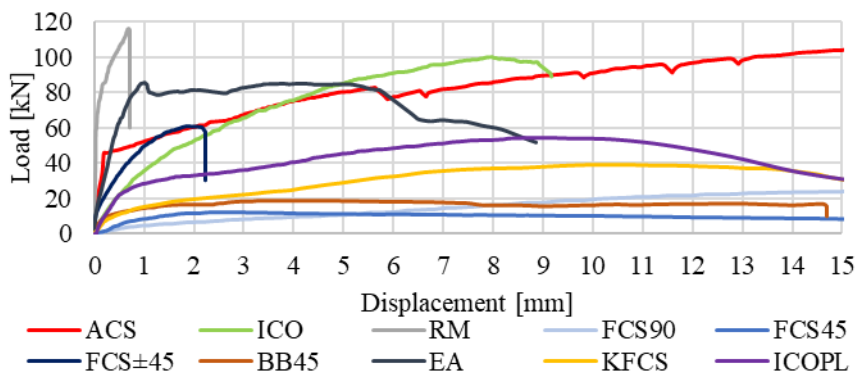


Figure 5
Characteristic force-displacement diagrams

3 Timber-Concrete Composite Beams

Timber-concrete composite structures are most often used as two-support, bent beams. The timber-concrete composite bridges built in Europe were used almost exclusively as simply supported, upper-track beams.

Accordingly, the laboratory measurements of TCC were carried out in all cases by examining the three- or four-point bending of simply supported beams, as was done, for example, by Brazilian researchers in [20], Gutkowski's research team [11], and by the Spanish researchers [12] also. During the tests, experiments were carried out in accordance with the principles of EN 408:2010+A1:2012 [21].

In order to reduce the structural height, the timber beams are provided with carbon fiber reinforcement at the tensioned side and as a result, the beam's height can be significantly reduced [22].

3.1 Test Specimens

During the laboratory test, two series of test specimens were loaded. The test specimens were uniformly made of 360x80 mm C35/45 quality reinforced concrete slab (B500B reinforcing steel), 120x240 mm GL24h quality glue laminated timber beams, and two pieces of Sika CarboDur-S-512 lamellas glued to the lower plane of the timber beams with SikaDur-30. The difference between the two series is the different connection system between the two main elements: for the prefabricated reinforced concrete slab: threaded rods with a tightening torque (**ACS**); for the monolithic reinforced concrete slab: glued perforated steel plate (**EA**) were used.

Table 3
Material parameters for timber-concrete composite beams

	f_c [N/mm ²]	f_t [N/mm ²]	f_v [N/mm ²]	E [kN/mm ²]	ε [N/mm ²]
Concrete	35	3.2		34	0.35
Reinforcement	-	563	-	200	10
CFRP	-	3.100	-	170	1.70
Epoxy	85-95	26-31	16-19	11.2	-
Perforated steel plate	-	510-680		210	-
Injection material	52	37	-	1.8	-

Through Threaded Rods with Friction Connection (1-3)

The threaded rods were M10, material quality 8.8, and were placed in the Ø14 mm sleeves formed in the test specimens. The threaded rods were uniformly tightened with a tightening torque of 49 Nm, thus creating a frictional connection.

Glued Perforated Steel Plate Connection (I-III)

The connection between the concrete and the wooden part is provided by a Qg10-15x3 type Qg10-15x3 square mesh perforated stainless steel plate with a thickness of 3 mm glued to the timber beam with SikaDur-52 Injection.

The cross-sections of the specimens are showed in Figure 6.

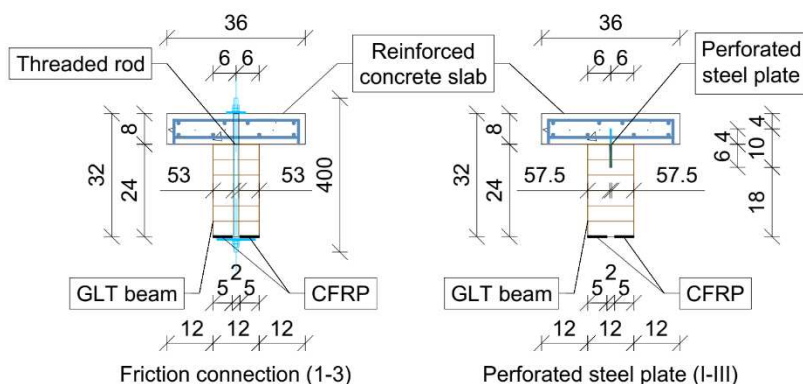


Figure 6

Cross-section of the test specimens (Dimension in cm)

3.2 Test Results

During the tests, three-point loading was carried out, and deformations were measured in three cross-sections (at the center of the support and at the quartering points). At both ends of the beams, fork-shaped, hinged supports were placed. Furthermore, the end plate displacement between the timber and concrete part was examined, with the test layout as can be seen at Figure 7.



Figure 7

The test layout of the three-point bending test of timber-concrete composite beams

Figure 8 shows the deflection of the central cross section of the composite beams during the loading process. On the diagram, I also marked the theoretical deflection function of the timber beam, and the different connection levels "Perfect" and "Partial" based on EN 1995-1-1:2010 [8].

In the case of a frictional connection, based on the measurement of the slippage between the timber and concrete part, no displacement occurs up to a load value of ~30-35 kN, the friction holds the two parts together, but after that the two parts slide in relation to each other. This slippage is permanent, i.e. the two support parts did not return to their original position during or at the end of the load cycles.

The failure of the beams was caused by the fact that the threaded rods were no longer able to prevent the sliding of the timber and concrete elements beyond the friction limit.

In the case of the perforated plate connection, based on the slippage between the wooden and concrete parts, the stiffness of the connection is constant up to a load value of ~60 kN, but after that the behaviour of the connection is no longer linear.

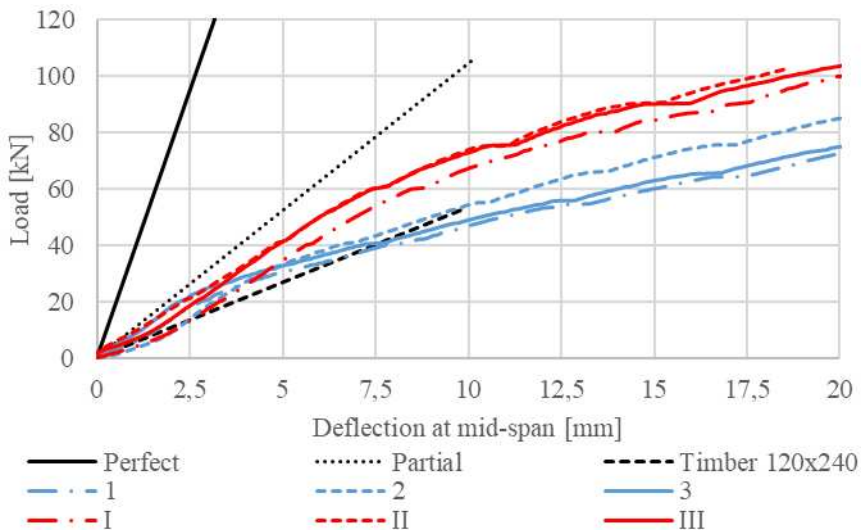


Figure 8

Deflection of the central cross-section as a function of the load force

In the case of the perforated plate specimens, the failure was caused by the fact that the glued-laminated beams were not able to withstand the stresses resulting from bending. The plane of failure occurred above the lower lamella of the laminated glued support, the two lower lamellas were sheared due to horizontal sliding forces, as shown in Figure 9.



Figure 9
Shearing of the last lamella layer

EN 1995-1-1:2010 [8] works with an excessively large error in the cases we examined, as shown in Table 4, the difference in stiffness is almost double - to the detriment of safety. In addition to the fictitious stiffness values (EI_{fikt}), the table below also includes the deflection (e_{30kN}) and the breaking load (F_{max}) corresponding to a load value of 30 kN.

Table 4
Comparison of measured and calculated test results

	“Perfect” EC5B	Perforated steel plate EC5B	Frictional connection EC5B	TEST	TEST	Timber EC5
e_{30kN} [mm]	0.62	1.78	2.01	3.52	3.96	5.08
F_{max} [kN]	176.13	116.80	109.58	105.04	85.49	52.66

It can also be seen from the results presented in the table that the results measured under laboratory conditions and those determined by Eurocode calculations working with the simplified linear elastic theory are not even close to the same. The linearly flexible dimensioning according to Eurocode – in comparison with the experimental results – increases the stiffness, deflection by about twice as much, and the breaking strength by approx. It approximates by 10-30% to the detriment of safety. The main reason for this is the neglect of approximations and material/relational nonlinearities in theoretical calculations.

4 Timber-Concrete Composite Bridge Models

4.1 Models

Two timber-concrete composite (TCC) bridges were made with dimensions of 6.5 m bridge length, 6.0 m span, and 2.4 m track width (without parapet). The first bridge has two glue-laminated timber (GLT) girders design (TC-A), while the second has six GLT girders (TC-B). The shear connection between the timber and the concrete is given by a perforated steel plate connection glued into the timber beams along its entire length and the shear elements were connected to the reinforcement of the reinforced concrete traffic deck. The ends of the timber girders are also connected to the cross girder with the same connection type.

Since the case of a connection between concrete and timber, the wood extracts water from the concrete and reduces the strength of the concrete near the connection, a separation layer was built between the timber and the concrete parts in order to separate the water from the wood during the setting of the concrete. The tensioned side of the timber beams was reinforced with CFRP strips to reduce the required structural height of the bridge models. Table 5 provides the properties of the materials used.

Table 5
Materials properties

<i>Material</i>		<i>Compression strength</i> f_c [N/mm ²]	<i>Tensile strength</i> f_t [N/mm ²]	<i>Modulus of elasticity</i> E [N/mm ²]
Concrete	C35/45	35	3.20	34 000
Rebar	B500B	500	500	200 000
CFRP	CarboDur S-1214	-	3.1000	170 000
Epoxy glue	SikaDur 30	-	26-30	11 200
Perforated steel	Qg 10-15-3 S355J	85-95	510-680	210 000
Injection	SikaDur-52	52	37	1 800

Figure 10, displays the cross-section of the TC-A bridge model which has a 12 cm reinforced concrete desk, and two GLT beams - 16x32 cm, also, two shear connections were placed between the timber beam and the reinforced concrete slab.

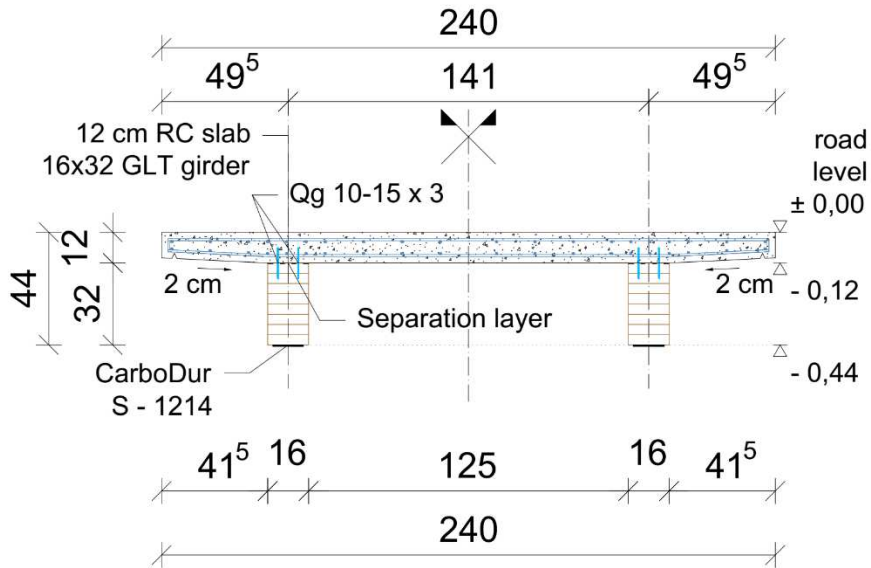


Figure 10

Cross-section of the two girders bridge model (TC-A)

In the case of the six-girders design (TC-B), the thickness of the deck is 8 cm, the timber beams are made with a 12x24 cm cross-sections as shown in Figure 11.

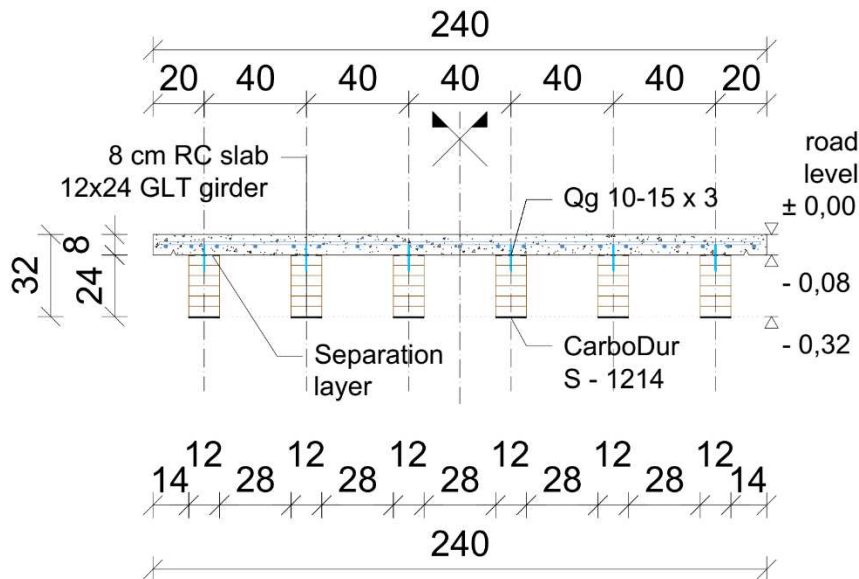


Figure 11

Cross-section of the six girders bridge model (TC-B)

4.2 Loading Process

Several loads were applied to the bridge models in order to simulate the actual behavior. However, the load-bearing limit of the structures could not be reached and the bridges did not load up to failure as the investigation was in operating condition. During the loading process, we followed the regulations of EN 1995-2:2014 [23] and e-UT 07.01.14:2011 [13] standards where the aim was to prove the resistance for the standard loads. The bridge models will be installed in an external site after the laboratory test period as these bridges will be pedestrian-bicycle bridges and according to the planned location, we dealt with the load required for pedestrian-bicycle bridges according to EN 1991-2:2006 [24]

- Distributed load: Load Model No. 1:

Recommended characteristic value for pedestrian traffic areas and bicycle lanes of short or medium-length footbridges:

$$q_{fk} = 5,00 \text{ kN/m}^2 \quad (1)$$

- Concentrated load: Load Model No. 2:

To test the local effects, a vertical force shall be applied to a surface of 0.1 x 0.1 m:

$$Q_{f,wk} = 10 \text{ kN} \quad (2)$$

- Service Vehicle Load: Load Model No. 3:

Figure 12 shows the standard load arrangement of the service vehicle according to EC. The arrow indicates the direction of travel of the vehicle.

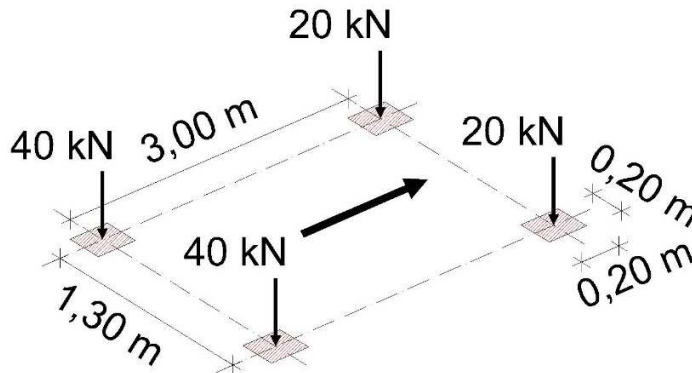


Figure 12
Vertical load model of the service vehicle

Concerning the case of distributed load at an area, different load arrangements have been investigated:

- Full loading (Full)
- Full loading over half the length (Uni)

- One-sided full loading (Lane)
- Checkerboard loading (Chess)

The distributed loading was applied by placing sandbags at the loading area considering load steps of 100 kg/m^2 ($1,00 \text{ kN/m}^2$). Figures 13 and 14 shows typical arrangements for the distributed loads.



Figures 13-14

Load arrangements for distributed load (Chess_1 and Lane_1)

In the case of concentrated forces, the following types were examined separately:

- The total load of the service vehicle at the point of maximum bending stress
- The load on the one-sided wheels of the service vehicle at the point of maximum bending stress, placed on the edge of the console
- The load on the main axle of the service vehicle at the middle of the span
- Load of one-sided wheel of the main axle of the service vehicle in the middle of the span, placed on the edge of the console



Figures 15-16

Axle load arrangements during concentrated load (S_1 and A-4)

Axle and wheel loads were tested with forces acting on standard surfaces. Figures 15 and 16 shows the test setups of the concentrated loading period of the models.

4.3 Test Results

During the load tests, the deflections resulting from the self-weight of the bridges were not measured separately, only the deflections due to overload were recorded. The vertical deflection of the bridges was measured in three different cross-sections at a total of fifteen measuring points during the whole loading process. The load-displacement diagrams obtained during loading showed linear behavior for all measurement points. Besides, the magnitudes of the largest deflection values correspond to the results obtained during the modeling. Figures 17 and 18 shows the shape of the structure as the maximum load value was reached in different representations.

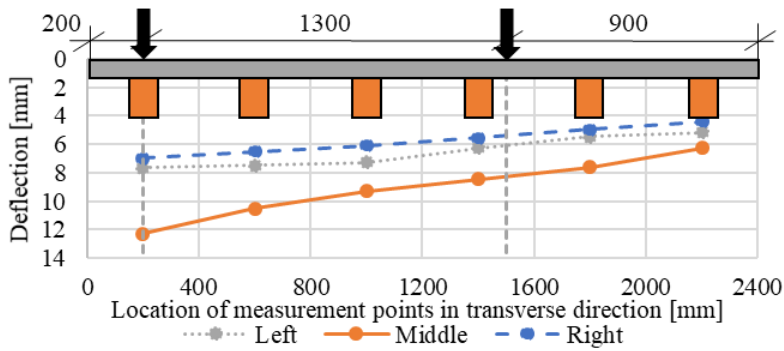


Figure 17

Deflection diagram of the TC-B bridge model under the effect of the total load of the service vehicle in nonsymmetrical arrangements (S_3)

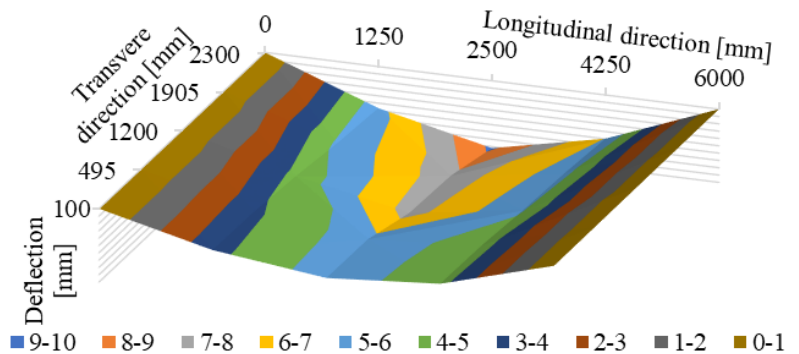


Figure 18

Contour line map of the TC-A bridge model under right-hand eccentric loading at the middle of the bridge (A_2)

Table 6 shows the maximum measured deflection values for TC-A and TC-B bridges under different concentrated loads. The load A_1 to A_4 refers to the asymmetrical load positioning along the bridge model length, the load types S_1 to S_4 refers to the symmetrical concentrated load arrangement.

Table 6
Experimental test results for concentrated load

Load type	Load location d_x [mm]	Eccentricity of load d_y [mm]	Load F_{max} [kN]	Deflection e_{max} [mm]	
				TC-A	TC-B
A_1	2500	0	2x60 kN	7.78	9.66
A_2	2500	+350	2x60 kN	9.21	11.54
A_3	2500	-350	2x60 kN	8.56	12.29
A_4	2500	-1000	1x60kN	5.62	8.67
S_1	3000	0	2x40 kN	5.12	6.62
S_2	3000	+350	2x40 kN	6.11	8.25
S_3	3000	-350	2x40 kN	5.90	8.01
S_4	3000	-1000	1x40kN	3.84	5.88

Table 7 shows the maximum measured deflection values for TC-A and TC-B bridges under different distributed loads. An indexed load of “_2” means an inverse arrangement of an indexed load of “_1”.

Table 7
Experimental test results for distributed loads

Load type	Load q_{max} [kN/m ²]	Deflection e_{max} [mm]	
		TC-A	TC-B
Full	5.00	3.21	3.54
Chess_1	5.00	1.75	1.89
Chess_2	5.00	1.74	1.90
Uni_1	5.00	1.61	1.89
Uni_2	5.00	1.65	1.97
Lane_1	5.00	1.96	2.78
Lane_2	5.00	1.91	2.64

Based on the results of the tests, both bridge structures remained in the operating load level due to the load as no permanent deformations have occurred. Most importantly, it was possible to compare the maximum deflection values by the standards e-UT 07.01.12:2011 [25] and EN 1995:2:2014 [23] prescribes the limit for the maximum deflection of footbridges due to traffic loads as follows:

$$L/400 = 15.625 \text{ mm} > e_{max} \quad (3)$$

Conclusion

This paper presents the tests of wood-concrete composite structures under laboratory conditions.

Small-scale push-out tests of the connections between wood and concrete were carried out in order to find the optimal connection system. For the connection to precast concrete, we considered a prestressed, frictional connection to be the best.

Until the friction caused by the tension force ceases, the connection between the two elements can be taken into account with a high value. The wood is loaded perpendicular to the grain direction, by the tension force. This type of connection system requires subsequent maintenance; the planned tension force must be checked during the operating period.

In the case of the connection to monolithic concrete, the perforated plate connection gave the best results, in terms of the stiffness and ductility of the connection. By connecting the steel plate and the reinforcing bars of the reinforced concrete structures, the problem of concrete splitting can also be treated.

A three-point bending test was performed on the composite beams. Using the results of the connection test specimens, we loaded the beams formed with the ACS and EA connection types. As expected, the two connection designs behaved almost identically in the initial (low load) range. During higher loads, however, in the case of the screw connection, the connecting force disappeared and the two structural parts separated from each other.

In the case of timber-concrete beams, the failure was caused by tensile stresses arising from bending on the stretched side of the wood due to the sizes available on the market and required by the construction rules.

The last tests were static trials of timber-concrete composite models, where the behavior of two and six, main girder structures, under concentrated and distributed loads, was examined.

The main aim of this research was to investigate the bridge models under standard loads. After the investigation, the models will become functional bridges, at an external site. Under the bridge standard loads, the structures were adequate, after conversion to road regulations (placing pedestrian parapets, application of the anti-slip coatings...), are suitable to prove against actual traffic. The bridges will be equipped with a monitoring system at the actual installation site, that will provide an opportunity to compare laboratory tests and on-site results, thus, describing the behavior of the structures, as accurately and completely as possible.

References

- [1] KISS, L. (2012) „Hidépítés 5.” [Online] Available: <https://docplayer.hu/12052901-5-eload-szlo-2012.html>
- [2] FRAGIACOMO, M, (2012) „Experimental behaviour of a full-scale timber-concrete composite floor with mechanical connectors”, *Materials and Structures*, Vol. 45, No. 11, pp. 1717-1735, doi: <http://dx.doi.org/10.1617/s11527-012-9869-3>
- [3] BAJZECEROVÁ, V & KANÓCZ, J, (2016) „The Effect of Environment on Timber-concrete Composite Bridge Deck”, *Procedia Engineering*, Vol. 156, pp. 32-39, doi: <http://dx.doi.org/10.1016/j.proeng.2016.08.264>

- [4] CECCOTTI, A., (1995) „Timber-concrete composite structures”. Timber Engineering-STEP 2, Ed. by H. J. Blass, P. Aune, B. S. Choo, R. Görlacher, D. R. Griffiths, B. O. Hilson et al. Centrum Hout, The Netherlands. ISBN 90-5645-002-6
- [5] RODRIGUES, JN, DIAS, AMPG & PROVIDÊNCIA, P., (2013) „Timber-Concrete Composite Bridges: State-of-the-Art Review”, *BioResources*, Vol. 8, No. 4, doi: <http://dx.doi.org/10.15376/biores.8.4.6630-6649>
- [6] DIAS A. M. P. G., (2005) „Mechanical behavior of timber-concrete joints”, PhD Thesis, University Coimbra, Portugal. ISBN 90-9019214-X
- [7] COSTA, L., (2011) „Timber concrete composite floors with prefabricated fibre reinforced concrete”, Lund Institute of Technology, ISSN: 0349-4969
- [8] EN 1995-1-1:2010: Eurocode 5: Design of timber structures - Part 1-1: General - Common rules and rules for buildings
- [9] CVETKOVIC, R & STOJIC, D, (2003) „Design methods of a timber-concrete T-cross-section”, *Facta universitatis - series: Architecture and Civil Engineering*, Vol. 2, No. 5, pp. 329-338, doi: <http://dx.doi.org/10.2298/fuace0305329c>
- [10] GIRHAMMAR, UA, (2009) „A simplified analysis method for composite beams with interlayer slip”, *International Journal of Mechanical Sciences*, Vol. 51, No. 7, pp. 515-530, doi: <http://dx.doi.org/10.1016/j.ijmecsci.2009.05.003>
- [11] GUTKOWSKI, R, BROWN, K, SHIGIDI, A & NATTERER, J, (2008) „Laboratory tests of composite wood-concrete beams”, *Construction and Building Materials*, Vol. 22, No. 6, pp. 1059-1066, doi: <http://dx.doi.org/10.1016/j.conbuildmat.2007.03.013>
- [12] NEGRÃO, JHJ DE O, MAIA DE OLIVEIRA, FM, LEITÃO DE OLIVEIRA, CA & CACHIM, PB, (2010) „Glued Composite Timber-Concrete Beams.II: Analysis and Tests of Beam Specimens”, *Journal of Structural Engineering*, Vol. 136, No. 10, pp. 1246-1254, doi: [http://dx.doi.org/10.1061/\(asce\)st.1943-541x.0000251](http://dx.doi.org/10.1061/(asce)st.1943-541x.0000251)
- [13] e-UT 07.01.14:2011: Beton, vasbeton és fészített vasbeton hidak. Közúti hidak tervezése (KHT) 4
- [14] AUCLAIR, SC, SORELLI, L & SALENIKOVICH, A, (2016) „Simplified nonlinear model for timber-concrete composite beams”, *International Journal of Mechanical Sciences*, Vol. 117, pp. 30-42, doi: <http://dx.doi.org/10.1016/j.ijmecsci.2016.07.019>
- [15] EN 26891:1997: Timber structures - Joints made with mechanical fasteners - General principles for the determination of strength and deformation characteristics (ISO 6891:1983)

- [16] ASTM D5652-21: Standard Test Methods for Single-Bolt Connections in Wood and Wood-Based Products
- [17] EN 1994-1-1:2010: Eurocode 4: Design of composite steel and concrete structures - Part 1-1: General rules and rules for buildings
- [18] DIAS, A. M. P. G., MONTEIRO, S. R. S., MARTINS, A. G. D, (2013) „Summary of shear connector methods for timber-concrete composites”, Proceedings on Innovative Timber Composites: Improving wood with other materials, Nicosia, Cyp., 17. October 2013. pp. 15-17, ISBN 1 85790 178 9
- [19] HOLSCHEMACHER, K., KLOTZ, S., WEISSE, D., (2002) „Application of steel fibre reinforced concrete for timber-concrete composite constructions”, Leipzig Annual Civil Engineering Report, University of Leipzig, Germany, Lacer No. 7, 2002, pp. 161-170
- [20] MIOTTO, JL & DIAS, AA, (2015) „Structural efficiency of full-scale timber–concrete composite beams strengthened with fiberglass reinforced polymer”, Composite Structures, Vol. 128, pp. 145-154, doi: <http://dx.doi.org/10.1016/j.compstruct.2015.03.054>
- [21] EN 408:2010+A1:2012: Timber structures - Structural timber and glued laminated timber - Determination of some physical and mechanical properties
- [22] KIM, YJ & HARRIES, KA, (2010) „Modeling of timber beams strengthened with various CFRP composites”, Engineering Structures, Vol. 32, No. 10, pp. 3225-3234, doi: <http://dx.doi.org/10.1016/j.engstruct.2010.06.011>
- [23] EN 1995-2:2014: Eurocode 5: Design of timber structures - Part 2: Bridges
- [24] EN 1991-2:2006: Eurocode 1: Actions on structures - Part 2: Traffic loads on bridges
- [25] e-UT 07.01.12:2011: Erőtani számítás. Közúti hidak tervezése (KHT) 2